

Modelling of Transformer and  
Medium Voltage Powerline  
Channels for Data  
Communication on Single Wire  
Earth Return Distribution Grids

Balarabe Nkom

2017

# Modelling of Transformer and Medium Voltage Powerline Channels for Data Communication on Single Wire Earth Return Distribution Grids

Balarabe Nkom

A thesis submitted to Auckland University of Technology in fulfilment of  
the requirements for the degree of Doctor of Philosophy (PhD)

Supervisors:

Dr. Adam P. R. Taylor

Dr. Craig Baguley

School of Engineering

June 2017

# Abstract

Tangible benefits such as remote metering and fault diagnosis may be accrued by the implementation of communication capability alongside distribution grids, especially those that supply power to sparsely populated rural communities. Keeping costs to a minimum is a major concern to the operators of rural grids, as evidenced by the development and regular improvements to specialized distribution systems such as the Single Wire Earth Return (SWER) system.

A possible low-cost option to implementing grid communications is Powerline Communication (PLC), which has a distinct advantage over other options, such as wireless, of the pre-existence of communication infrastructure in the form of power lines. This advantage over wireless becomes more apparent when geographical terrain makes the propagation of wireless signals without line-of-sight strategies difficult.

Previous work on PLC implementation on SWER grids was limited by the available methods for characterizing and modelling the earth return paths at PLC frequencies, which were mostly based on analytical approaches. Therefore, the first original and significant contribution to knowledge outlined in this thesis is the development of a hybrid empirical/analytical method for characterizing and modelling earth paths, inclusive of the earthing system and superfluous components, at narrowband PLC frequencies.

The method was empirically verified by field experiments on a replicated SWER Medium Voltage (MV) line consisting of an industry-standard conductor and earth rods, resulting in a hybrid empirical/analytical per-unit length SWER line model. A Two-wire MV line with conductor properties identical to that of the single conductor used in the SWER experiment was also analytically characterized at narrowband PLC frequencies, for comparison with the SWER MV line.

Data transfer on distribution grids through the exclusive use of PLC is limited by transformers, which create high impedance nodes at the MV/LV grid boundary that tend to attenuate the PLC signals to impractical levels. This high attenuation may be overcome by implementing a bypass channel, where the signal is made to go ‘around’ the transformer. However, this configuration has cost and safety-related disadvantages, which are addressed by implementing a ‘through’ transformer PLC configuration.

A major shortcoming of SWER systems is that they suffer from voltage regulation issues, resulting in voltage fluctuations with bulk loading conditions. Consequently, a study on the effects of energization levels on PLC signals passing through distribution

transformers was also carried out. The study revealed that the mechanism of transformer insulation dielectric polarization causes the cyclic variation of high frequency signals passing through distribution transformers, due to the instantaneous energization levels of the transformer.

These cyclic variations were empirically determined via laboratory experiments that involved passing high frequency constant current signals through a range of single-phase 11 kV/230 V transformers. Models of the unenergized through-transformer channels of some of the transformers used in the experiments were also estimated for PLC simulation.

A general relationship between transformer insulation dielectric polarization and through-transformer PLC data throughput was established, from PLC simulations of the energized through-transformer channel models of one of the transformers. This general relationship forms the second original and significant contribution to knowledge, made through the research outlined in this thesis.

The method used in developing the simulation models of the energized through-transformer channels was based on a hybrid modelling approach. It involved running iterative scripts that directly scaled the outputs of the unenergized through-transformer models, to effect the cyclic high frequency signal magnitude and phase variations associated with the energized channels. The method has not been previously used in creating simulation models for energized through-transformer PLC simulation, therefore forming the third original and significant contribution to knowledge, made through the research outlined in this thesis.

These three original and significant contributions to knowledge demonstrate the feasibility of grid-wide PLC implementation on SWER grids, by considering the various MV/LV configurations that may be implemented across combinations of transformers and MV lines that are found on typical SWER grids, and distribution grids in general.

# Table of Contents

## 1 Introduction

1.1 Thesis Definition of PLC	1
1.2 The Advantage of PLC	1
1.3 Purpose of Research	1
1.4 Research Questions	3
1.5 Contributions to Knowledge	4
1.6 Thesis Outline	5

## 2 Background

2.1 Modern Power Grid Communication Concept	7
2.2 Physical Components of PLC Systems	9
2.3 Common Obstacles to Reliable PLC	10
2.4 PLC Channel Macro-mitigation via the PLC Interface	11
2.4.1 Line traps	12
2.4.2 Couplers	12
2.5 PLC Channel Micro-mitigation via the Communication Module	13
2.6 Impedance Characteristics of MV Lines	14
2.7 2.7 MV/LV Grid Boundary PLC Configurations	16
2.7.1 Around-transformer PLC Configuration	16
2.7.2 Through-transformer PLC Configuration	17
2.8 Impedance Characteristics of Distribution Transformers	19
2.8.1 Transformer Resonance at High Frequencies	20
2.8.2 Transformer Insulation Dielectric Polarization	20
2.9 Power Grid Component Modelling for PLC Applications	22
2.9.1 Traditional Modelling	22
2.9.2 Hybrid Modelling	23
2.10 Chapter Summary	25

## 3 Literature Review

3.1 Introduction	26
3.2 General PLC Channel Characterization, Modelling and Simulation	26
3.3 Through-transformer PLC Channel Characterization, Modelling and Simulation	29
3.4 Influence of Transformer Insulation Properties on Transformer Impedance	31
3.5 Distribution Transformer Hybrid Modelling and Simulation	32
3.6 PLC on SWER Grids	33
3.7 Gaps Identified from Literature	38
3.8 Research Design	39
3.8.1 Research Scope	39

3.8.2	Research Plan	40
3.8.3	Methodological Approach	40
<b>4</b>	<b>Methods</b>	
4.1	Introduction	42
4.2	SWER MV Line NB-PLC Characteristics	42
4.2.1	Description of Earth Path Characterization Method	42
4.2.2	Procedure for Earth Path Characterization	45
4.2.3	Description and Procedure for SWER MV line Characterization	47
4.3	0.5 kVA Transformer NB-PLC Characteristics	49
4.3.1	Description	49
4.3.2	Procedure	50
4.4	1 kVA and 15 kVA Transformer NB-PLC Characteristics	50
4.4.1	MV and LV PLC Interface Design and Implementation	51
4.4.1.1	MV PLC Interface	51
4.4.1.2	LV PLC Interface	53
4.4.2	Experimental Description and Procedure	57
4.5	MV Line and Through-transformer NB-PLC Channel Model Estimation	59
4.5.1	Determination of SWER and Two-wire MV Line FRFs and ILs	59
4.5.2	Determination of 1 kVA and 15 kVA Through-transformer Channel FRFs and ILs	60
4.5.3	Estimation of MV Line and Unenergized Through-transformer PLC Channel Models	60
4.6	MV Line and Through-transformer Channel NB-PLC Simulation	61
4.6.1	MV Line PLC Simulation Set-up	61
4.6.2	Unenergized Through-transformer Channel PLC Simulation Set-up	63
4.6.3	Energized Through-transformer Channel PLC Simulation Set-up	63
4.7	Conclusion	66
<b>5</b>	<b>SWER Medium Voltage Line NB-PLC Characterization Results</b>	
5.1	Introduction	67
5.2	Determination of Rod ZOI	67
5.3	Correlation of Measured Platform Impedances	68
5.4	Derivation of Earth Path Impedance	71
5.5	Derivation of Earth Path Impedance Scaling Factor from $V_{drop}$ Results	73
5.6	Analytical and Hybrid SWER MV Line	

Characterization with Constant Soil Parameters	75
5.7 Analytical and Hybrid SWER MV Line	
Characterization with Frequency-dependent Soil Parameters	78
5.8 Comparison of Squirrel and Flounder Conductors	82
5.9 Conclusion	83
<b>6 Through-transformer NB-PLC Characterization Results</b>	
6.1 Introduction	84
6.2 0.5 kVA Transformer Results	84
6.3 1 kVA and 15 kVA Transformer Results	88
6.3.1 Pre-processing of Results	88
6.3.2 Modal Occurrence of Minimum and Maximum Variations within the 50 Hz Voltage Segments	91
6.3.3 Minimum and Maximum Waveform Variation Values	93
6.3.3.1 Magnitude Variation Values	94
6.3.3.2 Phase Angle Variation Values	97
6.4 Development of Energized Through-transformer PLC Channel Simulation Model from Variation Data	99
6.4.1 Procedure	99
6.5 Conclusion	101
<b>7 NB-PLC Modelling and Simulation Results</b>	
7.1 Introduction	103
7.2 Unenergized Through-transformer Channel FRFs and ILs	103
7.2.1 Unenergized Through-transformer Channel FRFs	103
7.2.2 Unenergized Through-transformer Channel ILs	107
7.3 Energized Through-transformer Channel Simulation Model	109
7.4 MV Line Models	111
7.4.1 SWER and Two-wire MV Line FRFs	111
7.4.2 SWER and Two-wire MV Line ILs	112
7.5 MV Line NB-PLC Simulation	114
7.5.1 BERs for 100 m SWER MV line Simulation	114
7.6 Unenergized Through-transformer Channel NB-PLC Simulation	116
7.6.1 BERs for Unenergized Through-transformer Channel Simulation	116
7.6.2 Unenergized Through-transformer Channel Average Received Bit Power	119
7.7 Energized Through-transformer Channel NB-PLC Simulation	121
7.7.1 Incremental Complex Phase Correlation	121
7.7.2 Incremental BER	123
7.8 Conclusion	127

<b>8</b>	<b>Discussion and Analysis</b>	
8.1	Introduction	129
8.2	Derivation of Expression for Empirical Earth Path Impedance	129
8.3	Evaluation of PLC on SWER MV Lines	132
8.4	Effect of Insulation Dielectric Polarization on Distribution Transformer High Frequency Impedance	133
8.5	Implications of Insulation Dielectric Polarization on Through-transformer PLC	136
8.6	Suitability of Through-transformer Channels from Unenergized and Energized PLC Simulation Data Throughput	138
8.7	Feasibility of Continuous PLC on Distribution Grids	139
8.8	Conclusion	141
<b>9</b>	<b>Conclusion</b>	
9.1	Original and Significant Contributions of Research to Knowledge	142
9.2	Research Shortcomings and Challenges	143
9.3	Recommendations for Further Research	144
9.3.1	Earth Path Characterization	144
9.3.2	Aerial Conductor Characterization	144
9.3.3	Through-transformer PLC	144
9.3.4	Transformer Characterization and Modelling	145
9.3.5	Grid-wide PLC Optimization	146
	<b>References</b>	147
	<b>Appendices</b>	
A.	Design Procedure for Line Traps	162
B.	Design Procedure for Couplers	165
C.	LV Neutral Terminal Bonding to Distribution Transformer Tank	167
D.	Flowchart of Experimental Procedure for Earth Path Characterization Method	168
E.	Squirrel and Flounder Aerial Conductor Datasheets	169
F.	Transformer Magnitude and Phase Angle Variation Plots for Less Significant Cases	171
G.	Flowchart of Energized Through-transformer PLC Simulation Model Program	176
H.	Timing Performance of Energized Through-transformer PLC Simulation Program	177
I.	1 kVA MV to LV Incremental BER Charts	178



# List of Figures

2.1 – Conceptual Illustration of the Smart Grid	8
2.2 – Block Diagram of PLC System in Relation to a Distribution Grid and Communication Module	9
2.3 – Schematic Diagram of Typical SWER Distribution System	15
2.4 – Around-transformer PLC Configuration	17
2.5 – Around-transformer PLC Configurations, with Repeater for High Loss Channels	17
2.6 – Through-transformer PLC Configuration	18
2.7 – Through-transformer PLC Configurations, with Repeater for High Loss Channels	18
2.8 – High Frequency Schematic Diagram of Single Phase Distribution Transformer	24
2.9 – High Frequency Inductor Model Representation of Through-transformer Live Path	24
3.1 – Analytical per-unit length Transmission Line Model Representation of a SWER Line	37
3.2 – Depiction of Power Transmission Line Elements, According to Field Theory of Images	38
3.3 – Multi-Methodological Approach for Constructive Research	41
4.1 – Earth Path Impedance Experimental Platform	43
4.2 – Earth Path Impedance Measurement Schematic Diagram	43
4.3 – SWER Transmission Line Impedance Experimental Platform	48
4.4 – Hybrid per-unit length Transmission Line Model Representation of a SWER Line	49
4.5 – Block Diagram of 0.5 kVA Energized Through-transformer Experimental Platform	50
4.6 – Medium Voltage PLC Interface	51
4.7 – Measured and Simulated Medium Voltage Line Trap Impedance	52
4.8 – Measured and Simulated Medium Voltage Drain Resonator Impedance	53
4.9 – Low Voltage PLC Interface	53
4.10 – Measured and Simulated Low Voltage Line Trap Impedance	54
4.11 – Measured and Simulated Low Voltage Drain Resonator Impedance	55
4.12 – Overhead View of the Assembled 1 kVA and 15 kVA Transformer Experimental Platform	56
4.13 – Control and Measurement Station for the 1 kVA and 15 kVA Transformer Experimental Platform	56
4.14 – Block Diagram of 1 kVA and 15 kVA Energized Through-transformer Experimental Platform	57
4.15 – Flow Direction and Measurement Points for LV to MV Signal Transfer through Analysis Transformer	58

4.16 – Flow Direction and Measurement Points for MV to LV Signal Transfer through Analysis Transformer	58
4.17 – Block Diagram of Experimental Platform with Transformers Bypassed	59
4.18 – Simulink Block Diagram for Medium Voltage Line PLC Simulation	62
4.19 – Simulink Block Diagram for Energized Through-transformer PLC Simulation	64
5.1 – Percent Voltage Drop versus Distance $z$ , with Reference to Rods A and B, for $d = 1.8$ m	68
5.2 – Magnitude (Mag) Plots of Measured (Mea) Platform Impedance for $d = 0.5$ m, 1.0m and 1.8m	69
5.3 – Phase (Ph) Plots of Measured (Mea) Platform Impedance for $d = 0.5$ m, 1.0m and 1.8m	69
5.4 – Magnitude Plots of Measured (Mea) and Simulated (Sim) Platform Impedance for $d = 0.5$ m, 1.0m and 1.8m; 30 kHz - 250 kHz	72
5.5 – Phase Plots of Measured (Mea) and Simulated (Sim) Platform Impedance for $d = 0.5$ m, 1.0m and 1.8m; 30 kHz - 250 kHz	72
5.6 – RMS $V_{drop}$ versus $f$ for 9.5 meter Earth Section for $d = 1.0$ m; 30 kHz to 1 MHz	73
5.7 – RMS $V_{drop}$ versus $f$ for 9.5 meter Earth Section for $d = 1.8$ m; 30 kHz to 1 MHz	73
5.8 – Measured and Simulated $V_{drop}$ versus $f$ ; Simulated Value Scaled by 0.0032; 30 kHz to 250 kHz	75
5.9 – SWER Line $Z_{in}$ (Mag) vs. $f$ ; Measured with Squirrel (S) and Flounder (F); Simulated with Analytical Model for $\rho = 10$ (Sim 10M) and 100 (Sim 100M)	76
5.10 – SWER Line $Z_{in}$ (Phase) vs. $f$ ; Measured with Squirrel (S) and Flounder (F); Simulated with Analytical Model for $\rho = 10$ (Sim 10M) and 100 (Sim 100M)	76
5.11 – SWER Line $Z_{in}$ (Mag) vs. $f$ ; Measured with Squirrel (S) and Flounder (F); Simulated with Hybrid Model for $\rho = 10$ (Sim 10M) and 100 (Sim 100M)	77
5.12 – SWER Line $Z_{in}$ (Phase) vs. $f$ ; Measured with Squirrel (S) and Flounder (F); Simulated with Hybrid Model for $\rho = 10$ (Sim 10M) and 100 (Sim 100M)	78
5.13 – SWER Line $Z_{in}$ (Mag) vs. $f$ ; Measured with Squirrel (Sq); Simulated with Analytical Model Adjusted for Frequency-Dependency with Models S, SL, M, VP, P and VA	79
5.14 – SWER Line $Z_{in}$ (Phase) vs. $f$ ; Measured with Squirrel (Sq); Simulated with Analytical Model Adjusted for Frequency-Dependency with Models S, SL, M, VP, P and VA	79
5.15 – SWER Line $Z_{in}$ (Mag) vs. $f$ ; Measured with Squirrel (Sq); Simulated with Hybrid Model Adjusted for Frequency-Dependency with Model (P+EM)	80
5.16 – SWER Line $Z_{in}$ (Phase) vs. $f$ ; Measured with Squirrel (Sq); Simulated with Hybrid Model Adjusted for Frequency-Dependency with Model (P+EM)	81
5.17 – Measured Line Impedance of Squirrel (S) and Flounder (F) Conductors, Zero – 1 MHz	82

6.1 – Measured 110 kHz Sinusoidal Waveform, plotted with One Cycle of 270 V 50 Hz Waveform	85
6.2 – Plots of Cycle RMS Values and Upper Envelope for Measured 110 kHz Waveform	85
6.3 – High Frequency Signal Magnitude dB Attenuation at Designated 50 Hz Voltage Energizations	86
6.4 – Measured 35 kHz Sinusoidal Waveform, plotted with One 50 Hz Cycle of 255 V Waveform	88
6.5 – Plots of 10-Cycle RMS Values and Upper Envelope for Measured 35 kHz Waveform	89
6.6 – 1 kVA LV to MV Minimum Input RMS Voltage Magnitude Variation	94
6.7 – 1 kVA LV to MV Maximum Input RMS Voltage Magnitude Variation	95
6.8 – 1 kVA LV to MV Minimum Output RMS Voltage Magnitude Variation	96
6.9 – 1 kVA LV to MV Maximum Output RMS Voltage Magnitude Variation	97
6.10 – 1 kVA LV to MV Minimum Phase Angle Variation	98
6.11 – 1 kVA LV to MV Maximum Phase Angle Variation	98
7.1 – FRF (Magnitude) of 15 kVA Through-transformer Channels	104
7.2 – FRF (Phase) of 15 kVA Through-transformer Channels	105
7.3 – FRF (Magnitude) of 1 kVA Through-transformer Channels	105
7.4 – FRF (Phase) of 1 kVA Through-transformer Channels	107
7.5 – IL of 15 kVA Through-transformer Channels	108
7.6 – IL of 1 kVA Through-transformer Channels	108
7.7 – Plot of 1 kVA Transformer LV to MV Voltage Magnitude Variation Applied to 35 kHz Waveform; for Single 255 V 50 Hz Energization Cycle	109
7.8 – Plots of Upper Envelopes for Simulated and Measured 35 kHz Waveform	110
7.9 – Plots of 10-Cycle RMS Values for Simulated and Measured 35 kHz Waveform	110
7.10 – Simulated FRFs of 100 m SWER and Two-wire MV Lines	111
7.11 – Simulated FRFs of 1 km SWER and Two-wire MV Lines, Compared with Equation (9) Magnitude Loss	112
7.12 – Simulated ILs of 100 m SWER and Two-wire MV Lines	113
7.13 – Simulated ILs of 1 km SWER and Two-wire MV Lines	113
7.14 – BER for SWER PLC Channel; $l = 100\text{m}$	114
7.15 – BER for Unenergized 1 kVA Through-transformer Channel, LV to MV Direction	116
7.16 – BER for Unenergized 1 kVA Through-transformer Channel, MV to LV Direction	117
7.17 – BER for Unenergized 15 kVA Through-transformer Channel, LV to MV Direction	118
7.18 – BER for Unenergized 15 kVA Through-transformer Channel, MV to LV Direction	119

7.19 – Average Received Bit Power for Unenergized 1 kVA Transformer; input = 1W	120
7.20 – Average Received Bit Power for Unenergized 15 kVA Transformer; input = 1W	120
7.21 – Incremental Phase Angle Correlation for Signals Passing through Energized 1 kVA Transformer; LV to MV Direction	122
7.22 – Incremental Phase Angle Correlation for Signals Passing through Energized 1 kVA Transformer; MV to LV Direction	123
7.23 – Incremental BER for BPSK Signals Passing through Energized 1 kVA Transformer; LV to MV Direction	124
7.24 – Incremental BER for QPSK Signals Passing through Energized 1 kVA Transformer; LV to MV Direction	125
7.25 – Incremental BER for 8PSK Signals Passing through Energized 1 kVA Transformer; LV to MV Direction	125
7.26 – Incremental BER for 16QAM Signals Passing through Energized 1 kVA Transformer; LV to MV Direction	126
7.27 – Average Incremental BER for 8PSK and 16QAM Signals passing through Energized 1 kVA Transformer	127
 A.1 – Grid Component Impedances at PLC Centre Frequency	162
A.2 – Schematic Diagram of Simple Damped Line Trap	164
A.3 – Schematic Diagram of Improved Damped Line Trap	164
 B.1 – Schematic Diagram of constant-k Bandpass T-Filter	165
 F.1 – 1 kVA MV to LV Minimum Output RMS Voltage Magnitude Variation	171
F.2 – 1 kVA MV to LV Maximum Output RMS Voltage Magnitude Variation	172
F.3 – 1 kVA MV to LV Minimum Phase Angle Variation	172
F.4 – 1 kVA MV to LV Maximum Phase Angle Variation	173
F.5 – 15 kVA LV to MV Minimum Output RMS Voltage Magnitude Variation	174
F.6 – 15 kVA LV to MV Maximum Output RMS Voltage Magnitude Variation	174
 I.1 – Incremental BER for BPSK Signals Passing through Energized 1 kVA Transformer; MV to LV Direction	178
I.2 – Incremental BER for QPSK Signals Passing through Energized 1 kVA Transformer; MV to LV Direction	178
I.3 – Incremental BER for 8PSK Signals Passing through Energized 1 kVA Transformer; MV to LV Direction	179
I.4 – Incremental BER for 16QAM Signals Passing through Energized 1 kVA Transformer; MV to LV Direction	179

# List of Tables

5.1 – Results of Iterations for Deriving Circuit Element Values	71
5.2 – Calculated per-unit length (meter) SWER Line Parameters	75
5.3 – Slope of Line of Best Fit Values for SWER Model Simulation Results	81
6.1 – Variation of Test Signal Output Voltage with Energization	87
6.2 – Modal Occurrence of Minimum and Maximum Input Voltage Magnitude Variations within the 50 Hz Voltage Segments; 30 kHz - 150 kHz	91
6.3 – Modal Occurrence of Minimum and Maximum Output Voltage Magnitude Variations within the 50 Hz Voltage Segments; 30 kHz - 150 kHz	92
6.4 – Modal Occurrence of Minimum and Maximum Phase Angle Variations within the 50 Hz Voltage Segments; 30 kHz - 150 kHz	92

# Abbreviations, Symbols, and Nomenclature

Abbreviations	Meaning
8PSK	Eight Symbol Phase Shift Keying
16QAM	Sixteen Symbol Quadrature Amplitude Modulation
ACSR	Aluminium Conductor Steel Reinforced
AIEE	American Institute of Electrical Engineers
BER	Bit Error Ratio
BPSK	Binary Phase Shift Keying
CENELEC	European Committee for Electrotechnical Standardization
DC	Direct Current
Dyn	Primary Delta-Secondary Star with Neutral Connection
EMI	Electromagnetic Interference
EMTP	Electromagnetic Transients Program
FEM	Finite Element Method
FRA	Frequency Response Analysis
FRF	Frequency Response Function
G3-PLC	PLC Industry Standard
IEEE	Institute of Electrical and Electronics Engineers
IL	Insertion Loss
LC	Inductance-Capacitance Pair
LCR	Inductance, Capacitance, Resistance
LTI	Linear Time-invariant
LV	Low Voltage
MIMO	Multi-input, multi-output
MV	Medium Voltage
NB-PLC	Narrowband Powerline Communication
PWM	Pulse Width Modulation
QPSK	Quadrature Phase Shift Keying\
RMS	Root Mean Square
SWER	Single Wire Earth Return
TF	Transfer Function
USA	United States of America
ZOI	Zone of Influence

Symbols and Units	Description
m	$10^{-3}$ units, or length unit in meters
k	$10^3$ units
M	$10^6$ units
s	Time unit in seconds
pul	Per-unit length in meters
Hz	Frequency Unit in Cycles/s
dB	Decibels
VA	Volt-Ampere
W	Watt
$f$	Frequency

$\omega$	Angular Frequency
$^\circ$	Angle Degree
$e$	Euler's number
$A$	Ampere
$\Omega$	Ohm
$Z$	Impedance
$R$	Resistance
$L$	Inductance
$C$	Capacitance
$E$	Electric Field
$V$	Volt
$\rho$	Resistivity
$\epsilon$	Permittivity
$\chi_e$	Complex Electric Susceptibility
$\mu$	Permeability
$\gamma$	Propagation Constant
$\delta$	Skin depth
$\approx$	Approximately Equal to
$\pi$	Pi
$\ln$	Natural Logarithm

The thesis contains some nomenclature found in the literature; these are reproduced here as a quick reference.

Nomenclature	Description	
$A, B, C, D$	Two-port Transmission Parameters, as complex numbers	
	$A$	$\frac{V_{in}}{V_{out}}$ with $I_{out} = 0$ , i.e. with output open-circuited
	$B$	$\frac{V_{in}}{I_{out}}$ with $V_{out} = 0$ , i.e. with output short-circuited
	$C$	$\frac{I_{in}}{V_{out}}$ with $I_{out} = 0$ , i.e. with output open-circuited
	$D$	$\frac{I_{in}}{I_{out}}$ with $V_{out} = 0$ , i.e. with output short-circuited
$E_b/N_0$	Energy per bit to Noise Power Spectral Density (PSD) Ratio	
	$E_b$	Ratio of carrier power to actual information bit rate = $C/R$
	$N_0$	Noise PSD = $kT$ , where $k$ = Boltzmann's constant and $T$ = receiver noise temperature in Kelvin


# Publications

1. B. Nkom, A. P. R. Taylor, C. Baguley, B. C. Seet, and T. T. Lie, "A Unified Approach to Characterizing Medium to Low Voltage Powerline Communication Channels," in *2016 IEEE International Conference on Power System Technology (POWERCON)*, 2016, pp. 1-6.
2. B. Nkom, A. P. R. Taylor, and C. Baguley, "Narrowband Modeling of Single Wire Earth Return Distribution Lines," *IEEE Transactions on Power Delivery*, vol. PP, no. 99, pp. 1–1, 2017.
3. B. Nkom, A. P. R. Taylor, and C. Baguley, B. Nkom, A. P. R. Taylor, and C. Baguley, "The Impact of Transformer Energization Levels on Powerline Communication Signal Integrity," *IEEE Transactions on Power Delivery*, vol. PP, no. 99, pp. 1–1, 2017.



## Attestation

I hereby declare that this thesis is the result of my personal ideas and efforts and, to the best of my knowledge, does not contain any material that has been previously published by any other person. All complementary sources and efforts have been mentioned in the citations, references and acknowledgements provided. I also declare that the thesis, or any part of it, has not been previously submitted for the award of any other degree in any other institution of higher learning.

Balarabe Nkom\_\_\_\_\_  \_\_\_\_\_

# Acknowledgements

I wish to express my sincere appreciation to my supervisors, Dr Adam P. R. Taylor and Dr Craig Baguley, for their steadfast belief in my research, and my ability to see it through to its expected conclusion. It was a privilege to have two broad academic shoulders to stand on during this unique research experience.

I must also give great thanks to Auckland University of Technology, and the School of Engineering, Computer and Mathematical Sciences, particularly for offering me a PhD fees scholarship and the PhD student stipend. This funding made all the difference. Individual academic and administrative staff were always there, on a professional and personal level, to provide the much-needed grease for moving this research forward when situations threatened to grind it to a halt. In particular, I wish to appreciate Professor Tek Tjing Lie, Professor Zhan Chen, Dr Boon-Chong Seet, Josephine Prasad and her team, and David Crofts and his team of technicians.

I also wish to thank Tony Hollart and his team at The Lines Company, Te Kuiti; they staked significant personal efforts to make this research successful.

Special thanks go to members of Nigerian PhD community, and our mentors Professor Love Chile and Associate Professor James Rotimi; their academic advice and personal support were highly beneficial.

My friends and adopted family here in New Zealand, too many to be named individually but are all aware of the bonds that have now been established, are also greatly appreciated.

My extended family has been immensely supportive and encouraging. Ultimately, I dedicate this thesis to my parents, Professor Andrew and Mrs Magdalene Nkom; you planted, watered and tended; we grew. To my siblings: Always remember, we are highly favoured by the Most High Yahawah.

# **Chapter One – Introduction**

This chapter introduces the thesis. The definition of Powerline Communication (PLC) with respect to the undertaken research is provided in Section 1.1, the advantage of PLC for power grid communication is expressed in Section 1.2, and the purpose of the research is explained in Section 1.3. The research questions and contributions to knowledge are given in Sections 1.4 and 1.5 respectively, while the thesis outline is given in Section 1.6.

## **1.1 Thesis Definition of PLC**

The technology which enables concurrent transfer of information and electrical energy through power conductors is known as Powerline Communication (PLC) [1]. For this thesis, PLC refers to the bi-directional transfer of data through outdoor electrical power grid components, such as bare aerial conductors and distribution transformers.

## **1.2 The Advantage of PLC**

Most power grids require a certain level of remote or automatic measurement of the power system processes, and control of the grid components, for increased reliability and efficiency of power delivery. These capabilities are only possible if communication capability is implemented alongside the power grid.

Due to the pre-existence of the power lines, PLC has an advantage of providing a means of implementing communication capability on existing distribution grids, at less cost than is required to build a fresh communication network alongside the power grid. This advantage is obvious in many urban areas, where costs associated with wireless spectrum licensing and optical fibre right-of-way use are significant.

The cost saving potential of PLC is highlighted in peculiar situations. One of these is the geographical terrain of the distribution grid, such as hilly regions. Another situation is distribution grids that supply sparse locations that are minimally populated. These situations aptly describe many locations in rural New Zealand and other parts of the globe.

## **1.3 Purpose of Research**

Governments worldwide are increasingly deregulating their electricity sectors. Also, there is little incentive for profit-driven power companies to provide service to small, sparsely populated rural communities, especially in developing countries. This situation is due to two main factors; scarce financial and energy resources, and consumer income

levels that do not ensure payment of bills [2, 3]. Providing electricity to small numbers of consumers located in sparsely populated remote locations, using the common 3 phase 3-wire MV/4-wire LV distribution system, is not economical. A single phase 2-wire MV system is more economically viable [4, 5].

A further reduction in the cost of providing electricity to sparsely populated rural communities can be achieved by using the Single Wire Earth Return (SWER) distribution system [6]. As the name implies, only a single aerial conductor is required on the MV grid section, with the literal earth mass serving as the return path for the MV current [7], thereby offering a significantly lower initial capital cost for service roll-out. Running costs are also commensurately low because most of the grid components are low power rated, usually less than 25 kVA per distribution transformer [8, 9].

Some SWER grids currently have communication capabilities based on wireless schemes. However, they suffer from limitations that are mainly due to the two peculiar situations of geographical terrain and sparse populations mentioned in Section 1.2. Improvements to the wireless networks are only possible if line-of-sight antenna arrays are included in servicing a small number of consumers that are spread over large areas.

These peculiar situations are also generally unfavourable to power distribution companies with regards to metering, fault diagnosis, and maintenance. As such, there is an interest in the implementation of alternative communication schemes. With the peculiar situations under consideration, and the objective of a low-cost distribution grid in mind, a viable option for implementing communication capability on SWER grids is PLC. Therefore, the feasibility of PLC implementation on SWER MV grids is of research interest, especially as benchmarks for comparison exist in the form of literature related to PLC on regular single phase Two-wire MV grids.

The need for remote metering is of paramount interest to operators of SWER grids, and therefore the PLC signals need to traverse the transformers located at the MV/LV grid boundary, for this need to be met. PLC signal transfer across MV/LV grid boundaries can be achieved by implementing around-transformer PLC configurations. However, this creates challenges to the low-cost objective of SWER grids because extra coupling and line trapping components are required at each transformer location. The through-transformer MV/LV grid boundary PLC configuration has received much interest in recent times, due to its requirement for minimal communication hardware at the transformer location, which translates to a cost-saving potential. Some commercial implementations of this configuration already exist [10, 11].

For through-transformer PLC on SWER grids, the influence of MV/LV transformer energization levels on PLC signals passing through them is of significant research interest because SWER grids suffer from voltage regulation issues, with voltage sags and swell durations that depend on the load demand cycles being experienced on individual grids.

The effective study of the influence of transformer energization levels on PLC signals passing through them is predicated on suitable PLC simulation models of such transformers. In the absence of such energized transformer PLC simulation models, adequate steps need to be taken to develop them. Therefore, possible methods for developing energized transformer PLC simulation models are of research interest, to evolve a benchmark modelling method.

In summary, the research outlined in this thesis is centered on the evaluation of the general feasibility of PLC implementation on SWER MV grids, in relation to regular single phase Two-wire MV grids. Consequently, the feasibility of low-cost continuous MV/LV PLC on SWER grids will be based on the determination of the most practical MV/LV grid boundary PLC configuration to be used, which depends on cost versus reliability factors. The characterization of earth paths is therefore required for developing SWER line models. Appropriate energized MV/LV transformer PLC simulation models are also required for studying the effects of voltage fluctuations on PLC data throughput. The SWER system is further discussed in Sections 2.6 and 3.6, while distribution transformer characteristics are further discussed in Sections 2.8, 3.3 and 3.4.

## **1.4 Research Questions**

1. What is required for SWER MV lines to be accurately characterized and modelled for PLC applications? How will they perform in comparison to Two-wire MV lines of similar conductor type and length?
2. How does the behaviour of energized distribution transformers at 50 Hz voltage energization levels influence the integrity of PLC signals passing through them?
3. How can a method for developing PLC channel models of transformers be made accurate enough to capture operational phenomena that cause signal changes to occur within a single period of the highest applicable PLC carrier frequency?
4. How can basic building blocks for grid-wide PLC implementation be formed from the integration of MV line and distribution transformer PLC channel models?

## 1.5 Contributions to Knowledge

Challenges for implementing cost-effective data links on SWER grids have been previously encountered because adequate studies on PLC on SWER MV lines had not been carried out, due to the constraint of earth return path characterization. Therefore, the first original and significant contribution to knowledge outlined in this thesis is the development and verification of a method for characterizing earth path impedances, inclusive of the impedances of the earthing system and other superfluous components. The method may be directly applied to modelling a SWER line at NB-PLC frequencies, using minimal resources.

The research outlined in this thesis incorporated a study on continuous MV/LV grid PLC implementation via the propagation of high frequency signals through distribution transformers. The study revealed that dielectric polarization of transformer insulation causes cyclic variation of high frequency signals passing through distribution transformers. This particular phenomenon has not been previously studied in relation to PLC through distribution transformers. Therefore, the second original and significant contribution to knowledge outlined in this thesis is the establishment of a relationship between transformer insulation dielectric polarization and data throughput, when a through-transformer configuration is used for continuous MV/LV grid PLC.

This contribution is important because transformer insulation dielectric polarization is directly proportional to the transformer instantaneous energization level. Voltage regulation is a significant problem in certain types of distribution grids, especially SWER grids, and frequent voltage fluctuations may lead to degraded PLC performance on such grids [12].

The successful implementation of PLC channel micro and macro mitigation strategies are a function of the accuracy of the power grid models used in carrying out the research efforts. The models should be capable of faithfully replicating the power grid conditions in relation to the applied PLC signals. Therefore, the third original and significant contribution to knowledge outlined in this thesis is the development of a hybrid method for creating PLC simulation models of energized distribution transformers. The method was demonstrated by carrying out PLC simulations of the energized through-transformer channel magnitude and phase angle variations, and verified by comparisons with the measured variations.

## 1.6 Thesis Outline

This thesis is arranged as follows:

Chapter Two presents the background material related to the various topics of the research.

Chapter Three presents the literature review for the research. The identified research themes are general PLC channel characterization, modelling and simulation, through-transformer PLC channel characterization, modelling and simulation, the influence of transformer insulation properties on transformer impedance, distribution transformer hybrid modelling and simulation, and PLC on SWER grids. The gaps in scientific knowledge identified from the literature review are also given in this chapter.

Chapter Four presents descriptions of the methods used to carry out the research. These include the methods used to characterize the earth path, SWER MV line, Two-wire MV line, and the 1 kVA and 15 kVA unenergized through-transformer channels. Also provided are descriptions of the methods used to estimate PLC channel models of the SWER MV line, Two-wire MV line, and the 1 kVA and 15 kVA unenergized through-transformer channels. Descriptions of the methods used in carrying out PLC simulations of the estimated PLC channels are also provided.

Chapter Five presents results for the SWER line experiments, which includes the results from the application of the earth path characterization method.

Chapter Six presents results for the 0.5 kVA, 1 kVA and 15 kVA 11 kV/230 V through-transformer channel experiments, and provides a description of the development of the energized through-transformer PLC simulation model, based on the results obtained from the 1 kVA through-transformer channel experiments.

Chapter Seven presents results for the estimation process for the PLC channel models of the SWER and Two-wire MV lines, and the 1 kVA and 15 kVA unenergized through-transformer channels. The method for creating PLC simulation models of energized distribution transformers was verified by comparisons with measured results.

Chapter Eight presents results for the simulations of the PLC channel models of the SWER and Two-wire MV lines, the 1 kVA and 15 kVA unenergized through-transformer channels, and the 1 kVA energized through-transformer channel.

Chapter Nine provides an analysis and discussion of the results obtained from the research. A transfer function for fitting measured capacitance and resistance values of

individual earth path and earthing systems, from the earth path characterization method, was synthesized and presented. A general relationship between energized transformer insulation dielectric polarization and the bit error ratios of its through-transformer channels was also mathematically expressed. The earth path transfer function and generalized transformer polarization-BER relationship thereby establish the research contributions.

Chapter Ten presents the concluding remarks, summarizes the original and significant contributions of this thesis to knowledge, and provides recommendations for further research work.



## **Chapter Two – Background**

This chapter presents the background material related to the various topics of the research. An overview of the modern concept of power grid communication is given in Section 2.1, a description of the physical components of a PLC system is given in Section 2.2, a few obstacles to reliable PLC are given in Section 2.3, the role of the PLC interface in PLC channel macro-mitigation is covered in Section 2.4, and the role of the communication module in PLC channel micro-mitigation is covered in Section 2.5.

An overview of the impedance characteristics of MV lines is given in Section 2.6, some MV/LV grid boundary PLC configurations are given in Section 2.7, an overview of the impedance characteristics of distribution transformers is given in Section 2.8, and an overview of power grid component modelling for PLC applications is given in Section 2.9. The chapter is summarized in Section 2.10.

### **2.1 Modern Power Grid Communication Concept**

A collection of various types of power grids within a defined geographical region, each with communication capabilities that enable them to exchange diverse information, is commonly termed a 'smart grid.' These grids provide tangible benefits that have global significance [13]. Electricity generation, transmission and distribution companies benefit from improved grid efficiency, maintainability, and energy management. Consumers benefit from short interval consumption data for proper planning, automated meter reading, improved outage response, and availability of last-mile data service. Governments and environmental interest groups also benefit from stable socio-economic indices and resource sustainability through improved efficiency in energy conversion and utilization [14].

The smart grid concept is illustrated in Figure 2.1 [15].

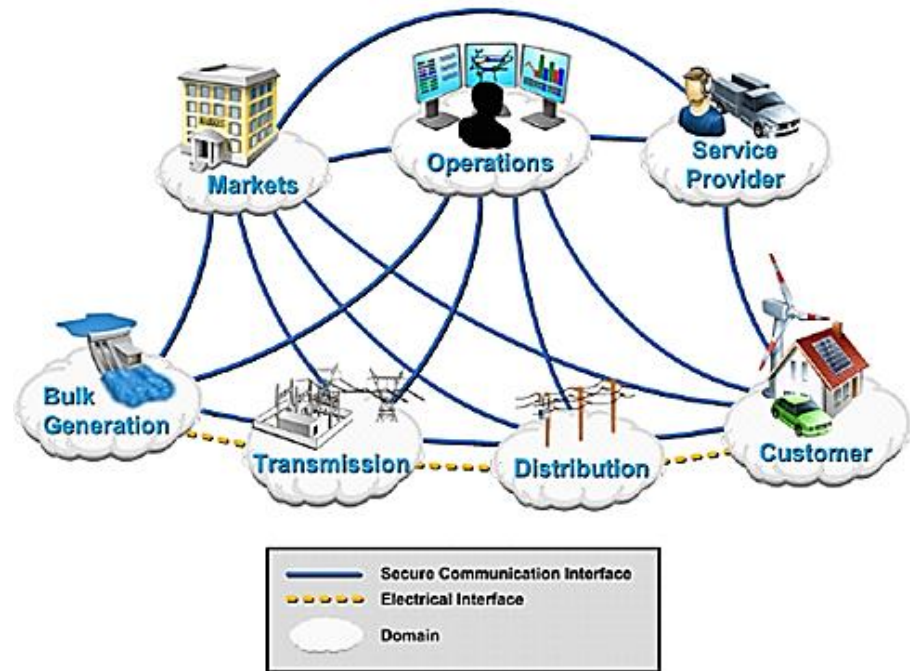


Figure 2.1 – Conceptual Illustration of the Smart Grid [15]

The solid lines represent two-way data flow, while the dotted lines represent power flow, including two-way power flow between the customer and distribution domains of the overall grid. The domains not linked by dotted lines, i.e. non-grid domains, require a diverse mix of expertise and processes that are outside the power engineering domain.

The possibilities for the growth of the smart grid, even in non-traditional aspects of power systems such as distributed generation and energy storage, drive the expansion of communication capabilities for power systems [16]. However, this expansion, in tandem with the expansion of communication capabilities in many other areas of human endeavour such as transportation, law enforcement, and so on, comes at a price. The costs currently associated with wireless spectrum and optical fibre right-of-way use, especially in urban environments, are a significant component of operational costs for mainstream telecommunications companies.

Geographical constraints also exist that make the use of wireless or optical fibre communication links on some distribution grids, such as those supplying sparsely populated settlements on hills, expensive. These constraints place special requirements such as line-of-sight antenna arrays, adding to cost.

Power distribution companies have the option to either engage a backhaul provider to provide the required data links or acquire and control their own communication network, to be smart grid compliant. In order to maintain security and reliability, and avoid third party legal issues, power distribution companies may opt for the latter [17]. PLC offers

such companies the opportunity to acquire and control their own communication networks in a cost-effective manner [18]. This is explained in Section 2.2, in relation to distribution grids.

## 2.2 Physical Components of PLC Systems

A physical PLC system consists of the communication module, the PLC interface, and the PLC channel. These are depicted in the block diagram of Figure 2.2.

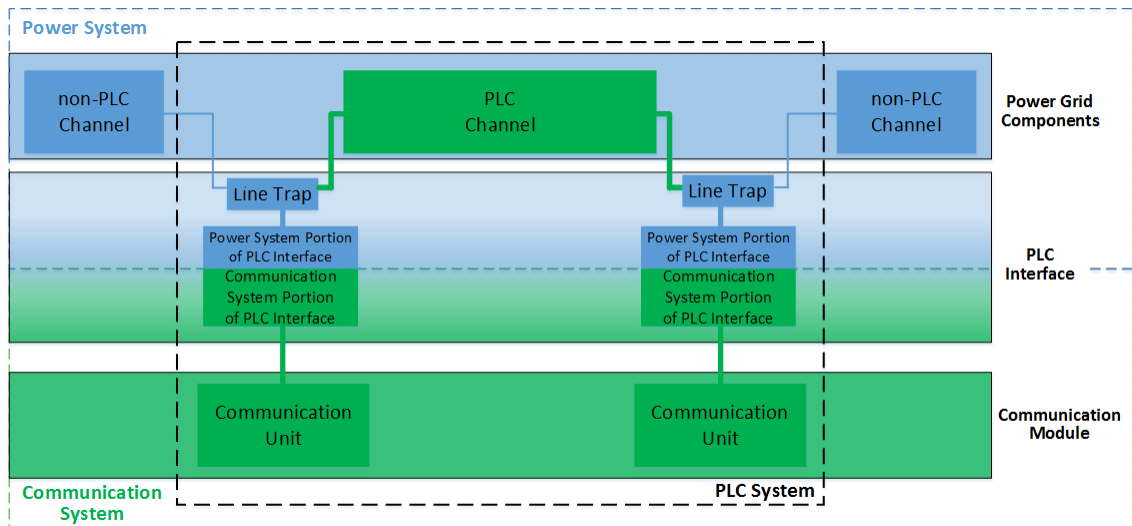


Figure 2.2 – Block Diagram of PLC System in Relation to a Distribution Grid and Communication Module

The communication module is made up of the data modulation, transmission, reception, and demodulation components within each communication unit. The PLC interface is made up of the coupling units, line traps, and protection components. The PLC channel is made up of the power grid components that collectively form the actual signal path.

Power conductors are the principal grid components for PLC implementation. Since they always exist at the location of the electricity end-user, PLC signals may be transferred between a device that is connected to that location, which is termed the end node, and the bulk data source that is connected to another location that usually exists within the same distribution grid, which is termed the root node. For PLC implementation, all that is required in addition to the power lines are the PLC interfaces, as shown in Figure 2.2.

A number of repeaters may also be necessary at line length intervals that depend on the impedance characteristics of the conductors and grid components, as well as the operational conditions of the grid. This is also obtainable for wireless and optical fibre communications schemes, to a lesser extent. As mentioned in Section 2.1, the major

advantage of PLC is that next to no operational costs, such as periodic licenses, are associated with this communication scheme, for the purpose of grid communications.

Therefore, power supply utilities that choose to implement PLC can gain a competitive advantage by reaping the benefits that smart grids have to offer while lowering their operational cost. However, the challenge lies in surmounting the common obstacles to achieving reliable PLC on distribution grids [19]. A few of these obstacles are given in Section 2.3.

### **2.3 Common Obstacles to Reliable PLC**

The transportation of electrical energy over long distances with minimal loss requires much higher voltages than those used in high frequency communication. This has negative safety implications for PLC. Therefore, the use of filtering and protection components are necessary, to prevent the high energy power signals from flowing into the communication equipment. Considering the vast amounts of energy involved, and the strict technical specifications needed for reliability and longevity, many of these schemes need to be customised, and so are expensive to procure and maintain.

The requirements for electric power transfer on distribution grids dictate a hierarchy of different voltage and current combinations, which form MV and LV grid segments. Each of these has similar components with different specifications, such as transformers. These various specifications combine to create diverse impedance profiles, even within small sections of the distribution grid. This situation presents a need for proper impedance matching between the communication module and the PLC channel. Impedance matching is necessary to ensure the filtering and protection schemes work as desired and the signals are mostly confined within the PLC channel.

When static impedance matching is successfully carried out on the basis of the impedances of the power system components alone, it is still difficult to achieve accurate and consistent impedance matching, due to the dynamic nature of power system loads. These loads vary from as low as  $0.5 \Omega$  for heavily loaded LV installations, to as high as  $500 \Omega$  for a lightly loaded LV installation, at 50 Hz. At the elevated PLC frequencies, most LV loads may have different impedances from those at 50 Hz. Depending on the type and scale of the load fluctuations, the impedance changes could affect large sections of the power grid, making long distance PLC unreliable. This situation requires the use of components such as adaptive line traps and coupling systems, to mitigate this obstacle.

Noise is also generated and propagated within the power system, due to rapidly fluctuating loads such as motor commutators and digital electronic loads. These raise the noise threshold on the power lines, thereby reducing the signal-to-noise ratio of PLC signals at the receiver. This situation requires mitigation strategies, such as bandpass filtering, to be implemented on the grid as well as at the receiver.

These obstacles exist because power grids are designed and operated with the primary objective of electrical energy transfer, not communication signal transfer. As such, these obstacles may only be mitigated. There are two broad strategies for PLC channel mitigation. Macro-mitigation involves measures implemented on the physical PLC components through manipulations of their impedance characteristics at the applicable frequencies and power levels, while micro-mitigation involves measures implemented on the PLC signals through manipulations of their properties by modulation, coding, and error correction.

Figure 2.2 shows that PLC channel micro-mitigation strategies are directly implemented by the communication module, while PLC channel macro-mitigation strategies are directly implemented by the PLC interface. The success of both mitigation strategies relies on the impedance characteristics of the power grid components that constitute the PLC channel, as well as those of the power grid components that constitute the non-PLC channel. This is important because one part of a power grid component may constitute a PLC channel, while another part of the same component may not. The separation of the two parts is achieved by the PLC interface.

## **2.4 PLC Channel Macro-mitigation via the PLC Interface**

As mentioned in Section 2.2, the PLC interface is made up of the coupling units, line traps and protection components [20]. Its function is to keep PLC signal attenuation through it at a minimum while mitigating the common obstacles to reliable PLC [19].

PLC interfaces usually consist of coupling, filtering, and impedance matching components, which may be combined into a single unit that is called a coupler [21]. They sometimes also include line traps [22]. PLC interface components are best designed or selected based on the nominal or characteristic impedance of the PLC channel they are to be included in, to provide a tangible parameter for effective PLC signal transmission power [23]. For line traps, this enables the amount of PLC signal that will be lost due to its inclusion to be pre-determined in relation to the loss that will occur due to its exclusion. For couplers, this enables optimal power flow between the transmitter and line.

### 2.4.1 Line Traps

Line traps are usually made up of passive-element LC combinations, which present high impedances at a selected centre frequency, thereby functioning as bandstop filters. The line traps shown in Figure 2.2 are designed or selected to prevent most of the PLC signal current from flowing into the non-PLC channel, while presenting as little impedance as possible at 50 Hz.

If the PLC channel has an impedance  $Z_0$  at the centre frequency of the stipulated PLC bandwidth, which is usually the case for long rural MV power lines with minimal branches [24], then the output impedance of the communication unit, commonly standardized to 50 or 75  $\Omega$ , may be accurately matched to  $Z_0$ . However, the combined high frequency impedance of the line trap and substation also has to be factored into the overall impedance matching scheme [25]. This requires the impedance of these three components to be concurrently matched, which is usually achieved using static components [23, 26]. A suitable method for doing so is described in Appendix A. However, to address the issues of dynamic variations of power system loads, adaptive impedance matching schemes may be implemented [27].

### 2.4.2 Couplers

Capacitive coupling is significantly better than inductive coupling for PLC applications [28, 29]. The coupling capacitor value chosen has to be capable of sufficiently reducing the 50 Hz current to levels suitable for the rest of the interface components and the communication equipment, whilst also presenting a sufficiently low impedance in relation to  $Z_0$ . This presents a challenge because if for instance, a 3 nF capacitance is to be used for coupling the PLC signals to a 11 kV MV line, it will present a reactance of approximately 1.061 M $\Omega$  at 50 Hz. However, it will also present a reactance of approximately 1.77 k $\Omega$  at 30 kHz, which may be too high, depending on the capabilities of the transmitter.

Also, at 11 kV potential, the 50 Hz current that will flow through this capacitive reactance will be approximately 10 mA, bearing in mind tolerances and other practical considerations such as shunt and series resistances associated with the capacitor at any given frequency. If it is considered that PLC signals must be kept at low power levels of usually not more than 4 watts due to EMI regulations, then this value of 50 Hz current may be considered to be acceptable, even if not ideal. Consequently, the choice of

coupling capacitor value is a trade-off between blocking as much of the initial MV current as possible and reducing the total impedance that the PLC signal will encounter.

Supplementary filtering techniques will, therefore, be necessary to prevent the residual 50 Hz power signal that passes through the coupling capacitor from flowing into the communication equipment, and also to improve PLC signal to noise ratios through band-selection [30]. For example, a constant-k T-section filter type may be considered for implementing a simple band pass filter which incorporates a coupling capacitor. This arrangement makes the filter a combined coupling and filtering unit, with an impedance that will need to be matched with that of the communications unit [25]. Details of a constant-k filter and impedance matching design process, based on static components, are provided in Appendix B. To address the issues of dynamic variations of power system loads, adaptive impedance matching schemes may also be implemented [27].

## 2.5 PLC Channel Micro-mitigation via the Communication Module

As mentioned in Section 2.2, the communication module is made up of the data modulation, transmission, reception, and demodulation components. Mitigation of channel impairments that are unfavourable to reliable data transfer may be carried out by these components, using a combination of hardware and software techniques [31]. Channel impairment mitigation is usually performed at the receiver end [32] and mostly involves reducing various types of noise [33], in order to obtain favourable bit error ratios (BERs). Equation (1) may be used to determine the approximate BER for PSK coherent modulation [12].

$$BER \approx \frac{2}{\log_2 M} Q \left( \sqrt{2 \frac{E_b}{N_0} \log_2 M \sin \left( \frac{\pi}{M} \right)} \right) \quad (1)$$

where  $M$  is the modulation order,  $E_b$  is the ratio of carrier power to actual information bit rate, and  $N_0$  is the noise power spectral density (PSD).  $Q$  refers to the q-function, which is a statistical variable related to the cumulative distribution function of a standardized normal random variable.

A special type of channel impairment is dynamic phase variation, whereby the channel phase properties are not constant at any given frequency [34]. This impairment differs from the expected static channel phase shifts with frequency, which causes an imbalance of in-phase and quadrature (I/Q) components of communication signals. Dynamic phase variation is very similar to phase noise in terms of effect on communication signals, however the difference is that phase noise is usually due to communication system

impairments [35], while dynamic phase variation is due to communication channel characteristics, such as multi-input, multi-output (MIMO) characteristics [36, 37].

Dynamic phase variation has negative effects on phase shift-based digital modulation, such as phase shift keying (PSK) and quadrature amplitude modulation (QAM) [38]. Various mitigation schemes exist and have been incorporated into various PLC industry standards [39], but they all have their unique disadvantages with respect to total data throughput [40, 41]. Therefore, knowledge of the dynamic phase variation properties of power grid components is important for achieving reliable PLC data transfer.

## 2.6 Impedance Characteristics of MV Lines

The impedance characteristics of outdoor power lines consisting of aerial conductors are usually determined analytically, using transmission line equations derived from field theory approximations. These equations are used in power line parameter determination because the literal earth is considered to be an imperfect conducting plane, in practical terms. As such, the field interactions between the wave propagating through the power line in transverse electromagnetic (TEM) mode and the earth plane, create additional inductive and capacitive terms which are not due to current flow through the earth path, but are rather due to its role as the zero potential reference of the power grid. These inductive and capacitive terms due to the considered imperfect earth plane are often significant for long power lines [42].

A variety of these equations exist, each set being extended to fit particular purposes, such as high frequency wave propagation and layered earth [43]. However, regardless of the various formulations, they all show that the impedance magnitude of power lines increase with frequency, with phase relationships that largely depend on the spacing between the current-carrying conductor and its return path. This is true of Two-wire MV lines, whereby equations (2) to (4) may be used to obtain its transmission line parameters, for waves under TEM propagation with imperfect earth considered.

The per-unit length resistance of a single conductor is given by:

$$R_{Cpul} = \sqrt{\frac{(R_{DCpul})^2 \cdot s^2}{4\rho} + (R_{ADCpul})^2} \quad \Omega/\text{m} \quad (2)$$

where  $R_{DCpul}$  is the conductor per-unit length DC resistance assuming an all-aluminium cross section,  $R_{ADCpul}$  is the actual conductor per-unit length DC resistance as quoted on its data sheet,  $\rho$  is the conductor resistivity, and  $s$  is the radius of each strand in millimetres



as quoted on its data sheet. The result from (2) is multiplied by 2 to obtain the total per-unit length resistance for the Two-wire line.

The per-unit length inductance of the Two-wire line is given by:

$$L_{Cpul} = 4 \times 10^{-7} \ln \left[ \frac{D}{r'} \right] \quad \text{H/m} \quad (3)$$

where  $D$  is the spacing between the two conductors, from their centre point, and  $r'$  is the geometric mean radius of the conductor, as quoted on its data sheet.

The per-unit length capacitance of the Two-wire line is given by:

$$C_{(C-N)pul} = 10^{-9} / 36 \ln \left[ \frac{D}{r} \right] \quad \text{F/m} \quad (4)$$

However, for SWER MV lines, the situation is more complex due to the peculiarity of the literal earth return path.

The schematic diagram of a typical SWER distribution system is shown in Figure 2.3 [7].

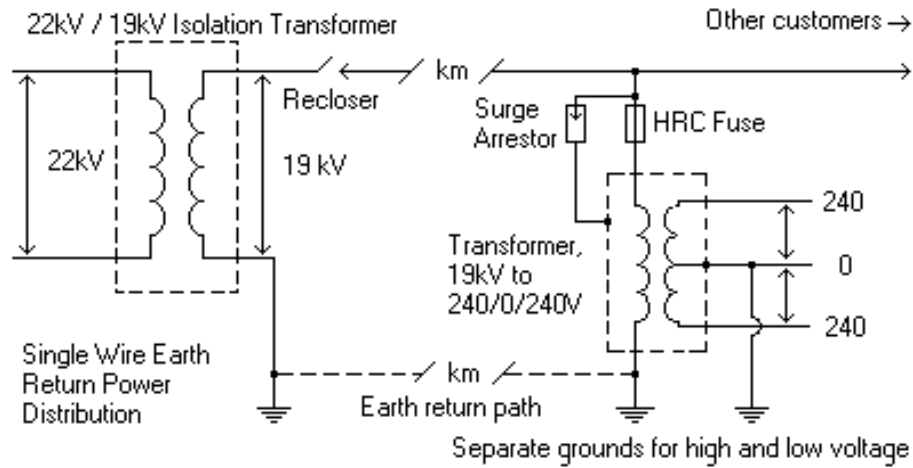


Figure 2.3 – Schematic Diagram of Typical SWER Distribution System [7]

The electrical characteristics of earth return paths are resistive and capacitive in nature, by virtue of the ionic and water retention properties of soil [44, 45]. With rural MV line lengths being up to hundreds of kilometres, the earth return path of long SWER lines create challenges of additional line capacitive reactances at 50 Hz, which causes voltage regulation issues at the loading points [46, 47].

Soil is also inhomogeneous and anisotropic, and therefore its resistivity and permittivity values are frequency-dependent. This means that non-linear variations of impedance with frequency will occur, apart from variations with path length, current injection depth, moisture retention properties, and weather. The implication of this is that purely analytical

methods of characterizing and modelling earth path impedances may not give results that are accurate enough for PLC applications.

As a compromise, established analytical equations for determining earth path properties such as resistivity and permittivity, may be used in conjunction with periodic empirical measurements, in order to obtain and apply correction factors to analytically modelled earth paths. Specifically, if the earth return path impedance of SWER MV lines, inclusive of the impedance of the standard earthing system used throughout the grid, is empirically determined, then this impedance may be combined with the impedance of the aerial conductor.

As SWER MV lines have a literal earth return path, the impedance of the aerial conductor is best determined by using the previously described transmission line parameter equations for waves under TEM propagation with imperfect earth considered, to obtain the required analytical accuracy. The combined conductor and earth path impedance may then be used as a basis for developing a per-unit length transmission line representation of the SWER MV line.

## **2.7 MV/LV Grid Boundary PLC Configurations**

By virtue of their primary function of stepping down distribution grid voltages to their final levels for supply to domestic consumers, distribution transformers represent the boundary between MV and LV grid sections. Figure 2.3 shows that the SWER system is similar to the North American single phase 2-wire MV system. The MV line is used to deliver power as close to the consumer as possible, where a MV/LV transformer is co-located with the bulk LV load, thereby resulting in minimal LV line length. The main difference is that SWER grids are primarily used to supply sparsely located loads, thereby offering very little opportunity for transformer sharing between registered consumers. This indicates that there will be at least as many transformers as there are registered consumers on the SWER grid.

### **2.7.1 Around-transformer PLC Configuration**

The implication of having short LV lines, in combination with dedicated transformers on distribution grids, is that the use of an around-transformer configuration [48] may not be a cost-effective option for PLC implementation. An around-transformer configuration is shown in Figure 2.4.

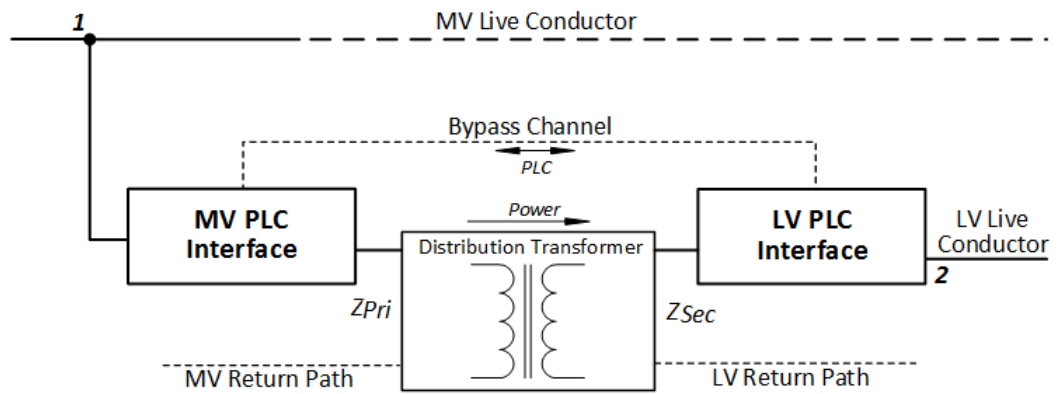


Figure 2.4 - Around-transformer PLC Configuration

A bi-directional bypass channel is created with two PLC interfaces bearing two couplers *1* and *2*, and possibly two line traps to prevent the PLC signal from flowing through the distribution transformer. In this way, the high attenuation of the through-transformer channel is avoided. Another around-transformer PLC configuration that incorporates a repeater [49-51] for high loss PLC channels is shown in Figure 2.5.

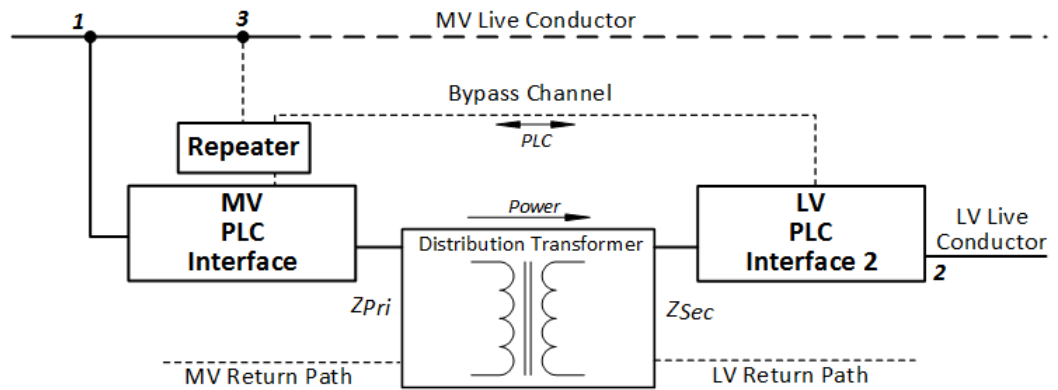


Figure 2.5 – Around-transformer PLC Configurations, with Repeater for High Loss Channels

Along with an unavoidable amount of attenuation [52], wholesale implementation of an around-transformer configuration in distribution grids significantly adds to cost, due to the two extra PLC interfaces required for each transformer. Therefore, to keep the cost of PLC implementation on large SWER grids low, it may be an advantage to adopt a through-transformer PLC configuration, as much as is practically possible.

### 2.7.2 Through-transformer PLC Configuration

Nothing is required to be connected at the MV/LV boundary to achieve PLC signal transfer between MV and LV grid sections when a through-transformer configuration is used, as shown in Figure 2.6.

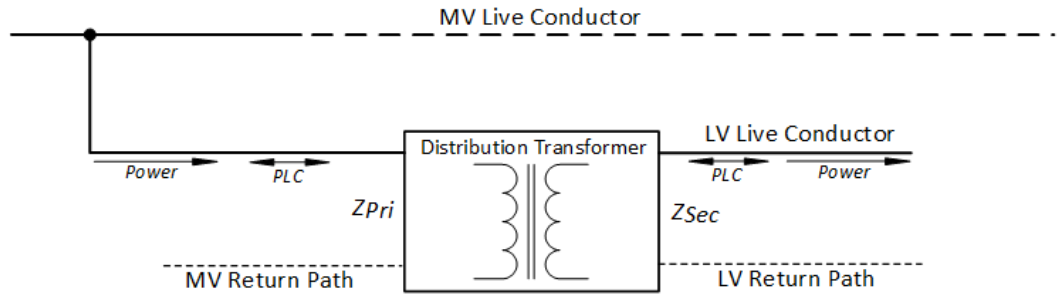


Figure 2.6 – Through-transformer PLC Configuration

The concept is practical in situations where the distribution transformer attenuation is relatively low, especially when modern digital communication techniques are also employed, as explained in Section 2.5.

Two through-transformer PLC configurations that each incorporate a repeater [49-51], for high loss PLC channels that require signal conditioning or data processing [53], are shown in Figure 2.7.

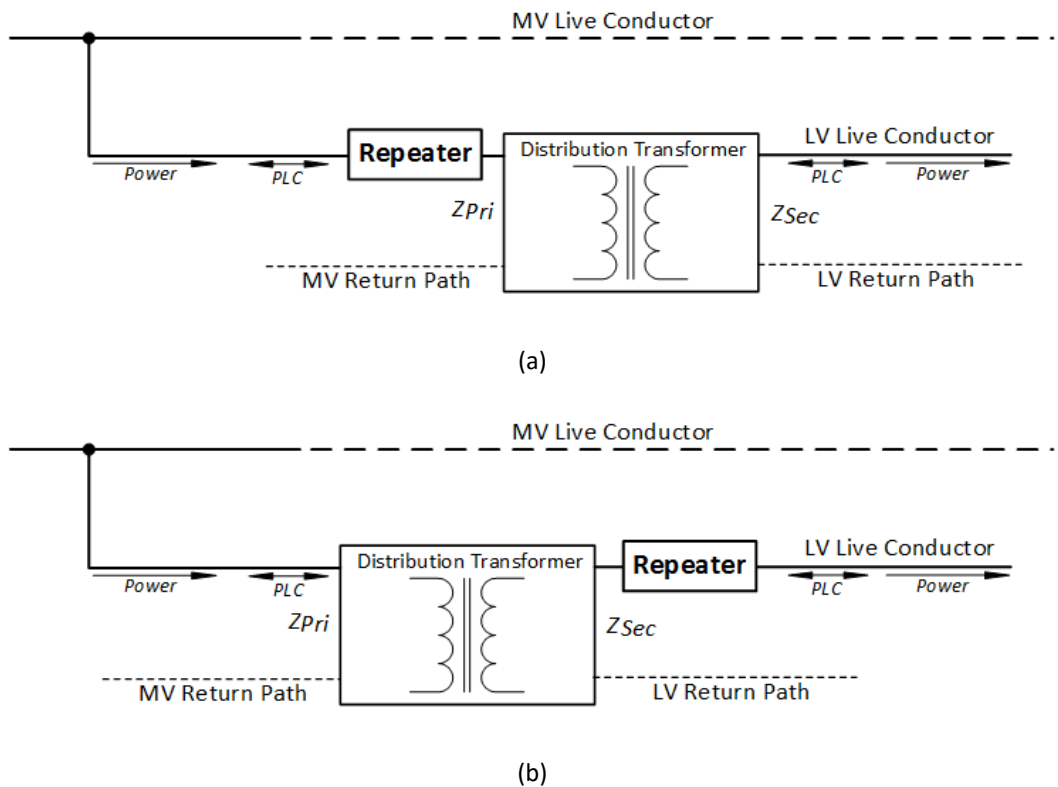


Figure 2.7 – Through-transformer PLC Configurations, with Repeater for High Loss Channels

The configuration which is shown in Figure 2.7 (a) may be used to boost weak PLC signals on the MV line. It may also be used in cases where the communication unit is near the distribution transformer on the secondary side. If the through-transformer PLC channel attenuation in the LV to MV direction is substantial, and there is no need to boost the PLC signals on the MV line, the configuration of Figure 2.7 (b) may be considered.

Both configurations offer the possibility of using only one hybrid PLC coupling unit for the repeater, thereby also providing the opportunity to apply tone masking, with the total exclusion of line traps. This is an additional cost saving measure.

While a through-transformer configuration is a cost-effective means of implementing PLC on distribution grids, if it is assumed that the inherently high inductive reactances of all distribution transformers may be successfully mitigated against, there are a number of constraints that still affect the grid-wide feasibility of this configuration. The two main ones are the type of distribution grid and the overall grid topology. If the lines connected to the transformer are long with numerous branches, reliable through-transformer PLC may be more difficult to achieve, due to signal attenuation and reflection [54]. In addition, if the lines are multi-core underground cables with sheathed/armoured outer conductors, the cable capacitance will further increase signal attenuation.

Consequently, some of the ideal conditions for the through-transformer configuration are minimal line branches and lengths on the LV side, and moderate line branches on the MV side, using aerial conductors. Coincidentally, these conditions best match rural single phase distribution grids, including SWER grids [24]. For SWER, the challenge for PLC implementation lies in the accurate characterization of the earth return path at the applicable frequencies.

## **2.8 Impedance Characteristics of Distribution Transformers**

Early PLC implementation on distribution grids employed most grid components, including transformers, as PLC channels. This was possible because the signal frequencies were low, with high power levels, enabling propagation through the components without significant signal loss. The through-transformer scheme grew in popularity [55-57] and was routinely used to pass PLC signals downstream from MV injection substations to consumers, for applications such as ripple control [58, 59].

Although these systems were successfully applied, with numerous variations such as limited two-way communication [60], in recent times EMI regulations have restricted the amount of signal power that may be placed on power lines, for PLC purposes. This means that the inherently high inductive reactances of through-transformer channels at elevated frequencies will result in high levels of PLC signal attenuation and noise accumulation, at the reduced power levels specified by regulations. As this high inductance is a design property of distribution transformers for the primary function of efficient electrical power transfer, it cannot be changed.

However, through-transformer PLC has re-emerged, as evidenced by recent successfully commercial implementations. This has been made possible by the application of modern PLC channel mitigation strategies [10, 11], thereby showing that it is practical.

### **2.8.1 Transformer Resonance at High Frequencies**

Power transformers possess some amount of capacitance, due to the substantial amounts of insulation material required to restrict current flow within the closed windings. At elevated frequencies, distributed capacitive reactances are developed, which exhibit complex series and parallel resonance phenomena in relation to the inductive reactance. This has the net effect of lowering the impedance of through-transformer PLC channels at a number of frequencies that depend on the individual transformer construction.

In addition, some electrical installation codes, such as those in the New Zealand electrical industry, require the LV terminal of distribution transformers to be bonded to the transformer tank, thereby making the transformer tank a fundamental part of the high frequency signal path. This is shown in Appendix C. Bonding the transformer LV terminal to the transformer tank will increase the distributed capacitance shunt paths and by extension improve the high frequency through-transformer signal transfer.

PLC channel macro-mitigation strategies may be used to exploit resonance phenomena in many ways, such as implementing bandpass filtering with centre frequencies that correspond to these frequencies of minimum attenuation. PLC channel micro-mitigation strategies may also be used to exploit resonance phenomena in many ways, such as implementing tone masks to categorise resonance frequencies into bands that may be allocated to specific groups of PLC nodes.

### **2.8.2 Transformer Insulation Dielectric Polarization**

Power transformer insulation components, such as oil, are non-polar dielectrics by design, although large numbers of permanent dipoles usually develop, due to various factors such as ageing, stress, and contamination [61]. The number of permanent dipoles in a material is directly proportional to its relative permittivity, which translates to capacitance phenomena [62].

Considering that the majority of distribution transformers are immersed in oil and enclosed in a tank, and also that typical transformer oils have relative permittivities between 1.5 and 2.5, highly distributed low capacitive reactance paths are created between the primary and secondary terminals by the oil-paper insulation [63]. This implies that distribution transformers could provide impedance values that are low

enough to make the through-transformer configuration of Figure 2.6 practical at certain frequencies. However, potential issues could arise from the transformer insulation dielectric polarization process.

Firstly, the dielectric polarization process is influenced by the instantaneous value of the electric field due to the 50 Hz voltage, because it is stronger than that of the applied high frequency signal, and so acts as a DC bias to the dielectric polarization process. Therefore, as the applied 50 Hz voltage cycles through a single period, the availability of charge carriers to propagate the high frequency signal through the transformer insulation varies. This implies that there will be commensurate variations in the capacitive reactance of the insulation path, which results in cyclic signal variation that is proportional to the applied 50 Hz voltage.

Secondly, polarization in a material is given by (5) [64]:

$$P(t) = D(t) - \varepsilon_0 \cdot E(t) = \chi_e \varepsilon_0 \cdot E(t) \quad (5)$$

where  $D(t)$  is the electric flux density,  $\varepsilon_0$  is the permittivity of free space,  $\chi_e$  is the complex electric susceptibility of the material, and  $E(t)$  is the applied electric field vector.

As most practical materials are not homogeneous,  $P(t)$  is made up of a rapid polarization part  $Pr$ , and a slow polarization part,  $Ps$ .

The polarization process within the material which closely follows changes in the applied electric field is represented by  $Pr$ ; this is associated with components of the material which possess large numbers of permanent dipoles.  $Ps$  represents the components that are non-polar or have low numbers of permanent dipoles, such as oil-paper insulation. In this case, the polarization process also involves initial dipole allocation, interfacial polarization, and space charge orientation [65]. These processes introduce delayed responses of total polarization to the applied electric field. Therefore, the extent of the delayed response of the transformer insulation dielectric polarization process may lead to dielectric dispersion at high frequencies, which may introduce non-linear and frequency-dependent effects [65].

The implication of transformer insulation dielectric polarization is that a through-transformer PLC channel may exhibit variations in impedance, in accordance with the 50 Hz instantaneous energization. The extent of impedance variation will depend on the condition of the transformer insulation, in terms of its dielectric properties. This further implies that the integrity of PLC signals passing through a distribution transformer will depend on the variable of frequency due to resonance phenomena, and also depend on the

variable of 50 Hz voltage energization due to transformer insulation dielectric polarization phenomena. While the former variable may be selected to an extent, the latter unfortunately may not.

## 2.9 Power Grid Component Modelling for PLC Applications

ABCD parameters are a good choice for determining the frequency response function (FRF) of power grid components for PLC applications, especially at narrowband PLC (NB-PLC) frequencies, because they are already widely used in the power industry for determining the characteristics of power lines at 50 Hz.

The expression for calculating FRFs from **ABCD** parameters is given by (6).

$$FRF = \frac{Z_L}{A.Z_L + B + Z_S(C.Z_L + D)} \quad (6)$$

where  $Z_L$  = load impedance,  $Z_S$  = source impedance, and **A**, **B**, **C**, and **D** are the two-port parameter matrices. The FRF is a dimensionless quantity in complex number format, which may be converted to its equivalent polar coordinate representation if desired.

The Insertion Loss (IL) is also a useful parameter for obtaining an indication of the signal losses that may be encountered by inserting individual grid components into a PLC network. This may be calculated from the **ABCD** parameters of the component, using (7).

$$IL = -20 \log_{10} \left| \frac{Z_L + Z_S}{A.Z_L + B + Z_S(C.Z_L + D)} \right| \quad (7)$$

### 2.9.1 Traditional Modelling

The FRFs of power grid components may be used to obtain their equivalent time-domain models in differential equation or transfer function (TF) format, which can then be used in communication simulations [66-69]. The FRF conversion process primarily involves the determination of its inverse Fourier transform; therefore the accuracy of the final time-domain PLC channel model is dependent on the spectral resolution of the FRF, assuming the FRF itself is accurate at the measurement frequencies.

This means that the more the number of frequency points measured, the better the accuracy of the final model. However, the number of frequency measurement points is directly proportional to the complexity and duration of the experimental process. This means that a desire for accuracy may result in massive amounts of data and more post-processing time [70], therefore a balance needs to be struck between model accuracy and complexity.



Since PLC is inherently implemented on energized grids, this brings up fresh challenges for modelling power grid components, especially distribution transformers, for the purpose of accurate simulation of PLC under realistic operational conditions.

### 2.9.2 Hybrid Modelling

In the past, combining the merits of individual modelling methods, like the finite element method (FEM) and frequency response analysis (FRA) for increased accuracy when modelling complex systems such as transformers in high power, high frequency applications [71], required a lot of resources [72, 73]. Currently, with a wide selection of technical computing software and fast computers to run them, this approach, which is known as hybrid modelling, is increasingly being utilized for transformer modelling.

The basic hybrid modelling concept involves using continuous and/or discrete variables of a group of interlinked subsystems, to describe the behaviour of the larger system [74, 75]. In the electromagnetic domain, this offers the advantage of working with a multi-component transformer system's electric and magnetic variables, such as core complex permeability and winding current values, and coupling them via a set of discretized equations, to obtain solutions. An added advantage of this approach is that it may be numerically implemented and extended to computer programs [76]. This essentially means that hybrid models are simulation models.

With regards to transformers in particular, nonlinearities associated with the magnetic core can easily be considered as hysteresis elements in a feedback loop, according to [75]:

$$\dot{y} = H(y) + u \quad (8)$$

where  $H$  is the hysteresis (or scaling) function,  $u$  is the input to the hysteresis block at discrete time  $t$ ,  $\dot{y}$  is the output at discrete time  $t$ , and  $y$  is the output at discrete time  $t-1$ .

The cyclic variations of the PLC signals due to dielectric polarization described in Section 2.8.2, may be represented using a broad spectrum of hybrid modelling strategies, depending on the preference of the simulation model designer [77]. Two possible strategies are hereby described.

The first strategy involves the direct manipulation of the values of the distributed capacitances of the insulation shunt paths of a distribution transformer model [78], represented as lumped capacitances in its high frequency schematic representation shown in Figure 2.8.

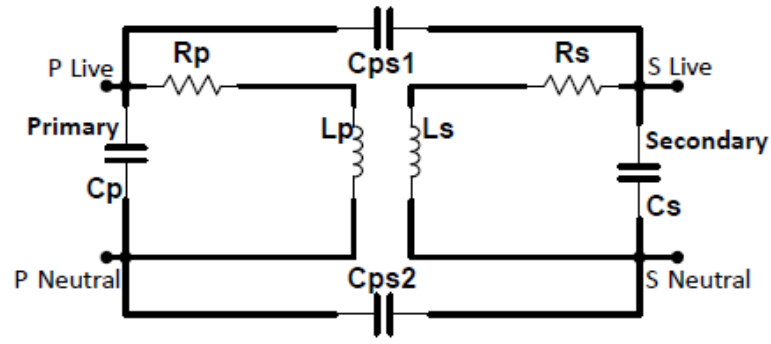


Figure 2.8 – High Frequency Schematic Diagram of Single Phase Distribution Transformer

Assuming favourable values of resistances  $R_p$  and  $R_s$  and inductive reactances due to  $L_p$  and  $L_s$ , the signal transfer between the primary and secondary terminals will occur only when  $C_p$  and  $C_s$  individually present a higher reactance than that of  $C_{ps1}$  and  $C_{ps2}$ . To reduce the complexity of the description of the capacitive mechanism,  $C_p$  and  $C_s$  can be assumed to have the maximum possible reactances, so that in effect they are absent.

By virtue of the typical core/winding arrangement of power transformers,  $C_{ps1}$  and  $C_{ps2}$  may not necessarily be equal. In the case of single phase transformers,  $C_{ps1}$  is the lumped representation of the capacitances between the region of the live end of the primary winding and its corresponding end of the secondary winding, while  $C_{ps2}$  is the lumped representation of the capacitances between the region of the neutral end of the primary winding and its corresponding end for the secondary winding. These regions are not the same, in terms of proximity [63, 79].

With the assumed absence of  $C_p$  and  $C_s$ , the live and neutral paths may be represented as high frequency inductor models [80]. Further simplification may be made by assuming that  $C_{ps1}$  and  $C_{ps2}$  are indeed equal, to enable a combination of the lumped circuit elements into a high frequency inductor model representation of the live path, with the applicable total inductances and resistances lumped into  $L$  and  $R_2$  respectively, as shown in Figure 2.9.  $R_1$  and part of  $R_2$  represent the lossy nature of the capacitance  $C_{ps}$  of the through-transformer path.

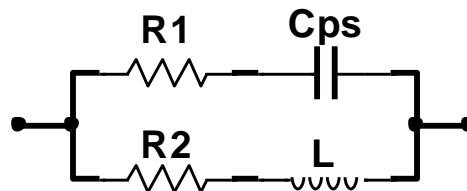


Figure 2.9 – High Frequency Inductor Model Representation of Through-transformer Live Path

The shunt capacitance  $C_{ps}$  provides an opportunity to model the signal variation mechanism of the through-transformer channel, by considering it to be a fractional

capacitor [81, 82]. The time variance may be effected by adjusting the order of  $Cps$  in accordance with established dielectric polarization characteristics of the transformer insulation [83]. In this way, the combination of  $Cps$  and  $RI$  may be considered as a block model entity and placed in parallel with the unenergized transformer TF, represented by  $R2$  and  $L$ , for simulation of the energized conditions. Alternatively, the entire transformer characteristics may be modelled as a high frequency inductor model similar to that shown in Figure 2.9.

The second strategy involves using the measured variation data to replicate the behaviour of the unenergized through-transformer PLC channels [84]. This strategy was used to develop a hybrid simulation model for the research, which was used in PLC simulations, to demonstrate the effects of cyclic transformer insulation dielectric polarization on through-transformer PLC data throughput. The model is fully described in Section 6.4.

## 2.10 Chapter Summary

In a global context, more benefits of the smart grid will be realized when a large number of independent power grids are able to share information, which will provide the opportunity for grid interoperability and cooperation, for the efficient and sustainable use of energy resources. Despite the problems associated with PLC, it is a cost-effective and practical means of achieving information transfer within distribution grids. Therefore, it is necessary to study the behaviour of grid components that may be used as PLC channels. Such studies will offer opportunities for improvements in general PLC reliability, in terms of macro and micro mitigation strategies.

Specifically, implementing PLC on SWER grids will make them smart grid compatible [85-87]. This has the potential of benefitting remote and sparsely populated rural communities with limited resources, especially if a through-transformer configuration is implemented as much as possible [88-92]. To carry out studies of through-transformer PLC channels and their associated MV and LV line PLC channels, it is necessary to characterize and model them accurately. Distribution transformers, in particular, need to be modelled in such a manner that their energized impedance characteristics are considered. This allows for power and PLC behaviour to be concurrently simulated [93, 94]. By implication, this increases the modelling and simulation complexity of distribution transformers for PLC applications, thereby requiring special considerations, such as utilizing hybrid approaches [95]. This thesis presents research findings that take account of the topics outlined in this chapter, in terms of PLC on SWER distribution grids.

# Chapter Three – Literature Review

## 3.1 Introduction

This Chapter provides a review of the literature on general and through-transformer PLC channel characterization, modelling and simulation in Sections 3.2 and 3.3 respectively. The influence of transformer insulation properties on transformer impedance is reviewed in Section 3.4, distribution transformer hybrid modelling and simulation is reviewed in Section 3.5, and PLC on SWER grids is reviewed in Section 3.6. The gaps identified from the reviewed literature are provided in Section 3.7, while the research design is given in Section 3.8.

## 3.2 General PLC Channel Characterization, Modelling and Simulation

Early PLC studies have involved the independent characterization of un-energized lines and transformers, using empirical methods at lower narrowband frequencies [28]. It was found that PLC signal loss on power lines increases exponentially with frequency, according to:

$$R = 0.765 \cdot e^{-\left(f/59000\right)+0.035} \quad (9)$$

where  $R$  is the ratio of received to transmitted current with the line terminated with its characteristic impedance, and  $f$  is the frequency in Hz. The studies also found that the transformer impedance exhibits resonance effects, which depend on its distributed capacitance. Losses of between 30% and 90% were recorded between 10 kHz and 160 kHz respectively, on approximately 160 km of a 110 kV transmission line. The studies further showed that multiple line branches and noise produced by energization, add significantly more attenuation to PLC signals, with increased probability of lower and irregular signal to noise ratio figures [96].

Results from analytical methods of characterizing power lines, transformers, and other grid components support empirical measurements by showing that multiple line branches present the most problems, and need to be avoided [97]. The use of line traps was also recommended, to keep the designated PLC channel's characteristics as homogeneous as possible and ensure reliable communication. Signal losses were found to depend on frequency, with up to 33% reflection loss for long lines.

Results of previous findings on line branches have been used in PLC simulations, and these found that the effect of line branches also relate to exponential loss, according to:

$$S = 0.985 \cdot e^{(-0.4001n)} \quad (10)$$

where  $S$  is the signal level and  $n$  is the integer number of line branches. However, the tools for properly modelling the lines were limited, necessitating the use of stochastic models with limited accuracy and validity [98].

Improvements in research methodology have also been made, with experiments being carried out on power lines up to 50 MHz using specialized instrumentation, to determine attenuation, radiation, and terminal load variables [99]. For lines under a transverse electromagnetic (TEM) mode of waveform propagation, powerline models were shown to have general transmission line characteristics, thereby placing them in the deterministic model class. These models indicated that most power lines have low pass characteristics as earlier established, with multiple resonance effects.

Multipath effects on powerline PLC channels have also been studied, showing that non-PLC portions of a power grid affect the PLC portions, due to their impedances at PLC frequencies. Studies were carried out with analytical transfer function models of LV grids that were improvised from equations for multipath effects on general communication media [100], and lossy transmission line models of MV grids with numerous line branches, in the narrowband region [101]. The frequency response of the multipath PLC channels in the latter case was found to be approximately -15 dB and -1 dB for the worst and best case scenarios respectively, for zero to 500 kHz and total line lengths of 5 km.

Improved simulations of MV grids, inclusive of distribution transformers, have shown that the primary terminal of some distribution transformers is capacitive at NB-PLC frequencies, resulting in variations in characteristics by resonance [102]. It was also found that the loading conditions on the secondary terminal of most distribution transformers have virtually no effect on the high frequency impedance of the primary terminal.

Research methodologies have evolved to include other stochastic and phenomenological-based PLC channel models, which include noise and other event-driven characterizations. Results from studies using these models further strengthen previous research results [103]. The physical characteristics of the PLC channels have also gained more importance, with emphasis on impedance determination for PLC channel characterization and interface design [104].

Empirical methods have also shown that line impedance values can be lower than  $10\ \Omega$  in many cases, with best to worst case attenuation and noise levels of 20 dB to 40 dB and 75 dB $\mu$ V to 100 dB $\mu$ V respectively, for the CENELEC-A band of 9 kHz to 95 kHz [105].

Non-traditional PLC applications have also been explored via simulations of data transfer over lines that supply power to equipment within industrial installations. A pulse width modulation (PWM) power supply line, feeding adjustable speed motors, was modelled as a PLC channel, between 1 MHz and 100 MHz. The line model was subsequently simulated for QPSK communication, resulting in a worst case bit error ratio (BER) of 0.5 at a signal to noise ratio of 3 dB, for a symbol period of 0.02 microseconds.

The transfer function representation of PLC channel models with the concurrent application of noise models were also found to be necessary for successful PLC simulation [106]. Such studies indicate that the same methodologies may be applied across various applications, as the issues of interest, namely the physical PLC channel's electrical characteristics and noise profile, have been consistently and universally important for PLC implementation over the years [107].

The advantages of hybrid and/or concurrent modelling and simulation of power grid components and noise profiles, for effective design and operation of broadband PLC networks, have also been articulated. Individual component models, developed through deterministic and stochastic methods, were coupled to form hybrid channel models based on the desired location of PLC modems, power grid components, and overall power grid topology. The results of some of these studies showed approximately linear attenuation variation from 2 to 40 dB in the narrowband region of 1 kHz to 30 kHz, and 10 to 60 dB between 100 kHz and 30 MHz [108, 109].

In summary, previous work shows that empirical methods based on two-port parameters have been favoured over analytical ones, in characterizing power grid components for the purpose of PLC implementation. This is because they involve a 'black-box' approach that provides more accurate results with the use of modern instrumentation such as Network Analysers. The literature also reveals that an important advantage of empirical methods over analytical ones is that the impedance characteristics of the power grid components change with time, and therefore periodic measurements offer the best strategy to account for these changes. However, analytical methods have the advantage of repeatability, thereby providing an opportunity for a hybrid of empirical and analytical methods for improved model performance. Previous work also shows that the signal to noise ratios of

MV and LV line PLC channels will reduce with increased frequency, with added branches increasing these losses further, through multipath fading.

### **3.3 Through-Transformer PLC Channel Characterization, Modelling and Simulation**

Key studies have revealed that, for simulation purposes, the analytical reduction of detailed winding models is accurate but computationally tasking, and therefore black-box models based on empirical measurements are considered to be most practical [110]. Some of these black-box transformer models perform well, with data rates of 8,640 bps with 1% error rate from the MV to LV side and 2,680 bps with 10% error rate from the LV to MV side; and maximum attenuation of 26dB and 30dB in the frequency bands of 10 kHz to 30 kHz and 40 kHz to 100 kHz respectively, for particular transformers [111, 112].

Transformer modelling methods for PLC applications, based on impedance/admittance measurements, have also been used to study through-transformer PLC with varying degrees of success [78]. While many measurements need to be carried out to obtain the required models using these methods, results from studies that used this method are accurate and reveal that distribution transformers act like impedance terminations at high frequency, with the conditions at the port opposite to the measurement port having very little influence on the measurements.

Results from similar transformer impedance/admittance studies have shown that distribution transformers exhibit multiple instances of resonance phenomena in the NB-PLC band, which depend solely on the impedance characteristics of the transformer [113, 114]. Best case attenuation for the transformers measured was 60 dB at approximately 18 kHz and 102 kHz for a 160 kVA 15/0.4 kV Dyn transformer, and 10 dB at 1 MHz for a 50 kVA 20/0.4 kV Dyn transformer.

Simulations of other empirical-based transformer models have provided results that show low losses at key high frequency regions. It was also mentioned that analytical modelling approaches are difficult to apply because transformer design details are usually proprietary and not available [115]. Also, other work revealed that the magnetic circuits of power transformers do not play any role in the signal propagation process through them, above certain frequencies which depend on the particular transformer. These two key points tilt the preference for transformer modelling towards empirical methods [116].

Replications of simulations in the field have also provided good results, which show that PLC based on modern digital communication methods can be implemented on a MV line to propagate over fairly long distances of up to 5 km through a distribution transformer [52, 117-121]. These simulations also show that PLC has an advantage over other power grid communication channels, due to the possibility of through-transformer signal transfer. Frequency response measurements of four unenergized transformers were also carried out. A maximum attenuation of 34 dB at 50 kHz, which reduced approximately linearly to 23 dB at 150 kHz was obtained for the 100 kVA transformer. For the 250 kVA and 400 kVA transformers, 29 dB to 19 dB attenuation was recorded between 50 kHz and 150 kHz, while 24 dB to 15 dB attenuation was recorded for the 630 kVA transformer, within the same bandwidth.

A detailed study found that the minimal attenuation that occurs at resonance between the winding inductances and stray capacitances offers a simple means of getting PLC signals through the transformer; especially if the resonant frequencies fall within the NB-PLC region of 3 kHz to 500 kHz, where noise and EMI are less likely to be an issue. The results of a Frequency Response Analysis (FRA) of a 20 kVA 20 kV/220V single-phase transformer, revealed a resonance region at approximately 490 kHz with a linear phase response, indicating that this frequency region is suitable for passing narrowband PLC signals with minimal phase distortion through the measured transformer [122]. This study also observed that bypassing the transformer is impractical for large-scale PLC implementation because this has to be done at each transformer, thereby making installation and running costs high.

Empirical measurements have also been carried out to indirectly obtain **ABCD** parameters of a 25 kVA single-phase transformer, MV line, and couplers, for the frequency band of 10 kHz to 490 kHz. These were subsequently modelled and simulated, with comparisons between the simulation and measurement results giving good agreement on the maximum attenuation figures of 35 dB between 5 kHz and 20 kHz and between 50 kHz and 150 kHz for very short line lengths. This study was the first to report the possibility of high frequency signals passing through energized distribution transformers experiencing variations, but no analysis or explanations were provided [123].

In summary, previous work shows that empirical methods based on two-port parameters are also favoured over analytical ones, in transformer modelling for PLC applications, with measurements carried out mostly on un-energized transformers. Previous work also shows that the focus for through-transformer PLC has shifted from a generalized through-



transformer PLC channel simulation model largely based on assumptions, to a bottom-up deterministic approach for accurately characterizing and modelling this PLC channel.

### **3.4 Influence of Transformer Insulation Properties on Transformer Impedance**

The effects of the dielectric polarization of transformer insulation, in relation to the impedance characteristics of through-transformer PLC channels, has not been previously studied. However, various studies on the direct and indirect influence of the insulation properties of transformers on inter-winding impedance have been carried out.

A fractional transmission line model of an oil-immersed power transformer winding was developed in [124]. This was done by considering the frequency-dependent properties of the oil-paper permittivity, amongst other parameters. The permittivity of oil-paper samples was measured and used to fit a model of the complex capacitance of the transformer winding, based on finite element methods. The work shows that transformer winding capacitance can be modelled by specifying fractional weights which correspond to the frequency-dependent properties of the oil-paper insulation.

A study of the mechanisms of dipole polarization, interfacial polarization, and space charge orientation in the presence of DC bias voltages was carried out on oil-paper samples in [125]. The results showed that dipole charge carrier peaks increased from approximately  $1.3\text{e}^{-7}$  to  $3.0\text{e}^{-7}$  Coulombs, while interfacial polarization was approximately constant at  $3.8\text{e}^{-6}$  Coulombs, with DC bias from -30 V to 50 V. Space charge orientation increased from -0.03 to 0.05 Coulombs from -30 V to 50 V, showing that it reverses with the polarity of the DC bias, as expected. Results from aged oil-paper tests also indicated significant increases in polarization with ageing, from  $1.21\text{e}^{-5}$  C/m<sup>2</sup> for zero hours, to  $3.25\text{e}^{-5}$  C.m<sup>2</sup> for 1,000 hours.

A summary of dielectric response behaviour in the frequency domain was provided in [83], together with a universal series resistor-capacitor model which is widely used to characterize dielectric materials. The frequency-dependent dielectric response of various mineral oil and natural ester samples was measured using frequency domain spectroscopy. Complex capacitance values of approximately 110 pF for the real part, and between 110 pF and 10 fF for the imaginary part, were obtained for measurements between 1 Hz and 1 kHz. Conductivity values ranged from 8 pS/m to 25 pS/m, between 1 Hz and 1 kHz. The results showed that while the capacitance values of the insulating liquids tested tend to reduce, the conductivity values tend to increase, with frequency.

A similar study to [83] with regards to moisture content of transformer oil-paper samples was carried out in [126], which showed that the complex relative permittivities of the samples increase with moisture content of between 0.5% and 4%, with the real part having values between 3 and 4, and the imaginary part having values between 0.01 and 0.1, for measurements between 1 kHz and 1 MHz. Conductivity was also found to increase with moisture content, with values of between 0.8 pS/m and 10  $\mu$ S/m, between 1 kHz and 1 MHz. The conclusions of increases of complex relative permittivity and conductivity with moisture content are also made in [127] and [128].

In summary, the literature on the properties of transformer insulation, such as relative permittivity and conductivity, shows that they are frequency-dependent. The literature also shows that these properties increase in value with moisture content. The dielectric polarization of the insulation, which is dictated by multiple mechanisms such as dipole allocation, interfacial polarization, and space charge orientation, was also found to be influenced by the presence of a DC bias field applied to the insulation space.

### **3.5 Distribution Transformer Hybrid Modelling and Simulation**

The hybrid modelling approach has been used to model transformers for a variety of applications [129]. An early use of this approach to model power systems is detailed in [130], where a surge arrester and a power source were modelled by analogue means, and the line was modelled by digital means, for a source capacity of 5800 A and line-surge impedance of 1.685  $\Omega$ . Another similar early study, using a hybrid of analogue and digital power system hard-wired models, is detailed in [95]. A 20 times faster than real-time simulation system for the nonlinear characteristics of a boiler and automatic gain control circuit were simulated by digital components, while the rest of the power system was represented by analogue components.

Processes such as numeric piecewise linearization of the nonlinear core characteristics, reduction of the transformer's detailed air-core winding model by Kron's method, and creation of quasi-static operating points at which the coupling of the core/winding characteristics occur, have been discretely controlled by time step iterations using equations similar to Equation (8) [131-133].

The duality principle has also been used to create a transformer core model, which was then hybrid coupled to a leakage inductance model, a capacitance model, and resistance (loss) models for the windings and core. The leakage inductance model was obtained by using the field theory method of images of conductors, the capacitance model was

obtained by using the charge simulation method, and the winding and core loss models were obtained by using Foster and Cauer circuits respectively [110, 134-136].

A hybrid modelling approach using black box measurements and grey box parameter estimation was used in a study, where a 525/18 kV 256 MVA single-phase transformer's terminal measurements were used in EMTP to obtain worst case transient conditions. These were then used in a grey box ladder network model to determine the internal winding response, with each rung representing a node. Various transfer functions obtained by taking FRA measurements for a given set of parameters were then fitted, using data from external dimensions and common design practices of transformers. Since only the high frequency response of the windings was of interest, the transformer core was not considered, however the simulation results compared favourably with actual transient data [137].

System modelling approaches based on non-numeric coupling without discrete variables, sometimes also referred to as hybrid approaches, have been used for transformer modelling. One example was provided in a study involving the development of a topologically correct transformer model for transient simulations up to 5 kHz. This model consists of a duality-based lumped-parameter saturable core, coupled to winding inductance, capacitance and resistance matrices determined by the use of appropriate formulae [138, 139].

In summary, hybrid transformer models have been successfully used to represent the various interactions between subsystems of power grids and their components, for the purpose of obtaining the operational characteristics of the entire system. Most of these hybrid transformer models were used for simulating power system phenomena such as fast transients, for transformer design optimization purposes. No PLC studies were carried out using transformer models based on these methods [140].

### **3.6 PLC on SWER Grids**

The literature on PLC for SWER distribution grids is limited. Analytical methods have been used to evaluate high frequency signal attenuation on SWER lines, indicating that data rates of up to 50 kbps were possible [141]. Similar approaches have been used to model a network of SWER transmission lines, based on hypothetical parameters. Carrier signal simulation results showed -3dB low-pass cut-off frequencies of 6,145 Hz and 187 Hz, for a 20 V 2 kHz square wave passing through the transmission line and transformers respectively [142].

The most detailed studies of PLC on SWER grids are given in [143-148]. The transfer function obtained from measurements on an 18 km SWER line with a single user at its end was compared with that obtained from simulations of an LC model of the line, in [143]. The results gave a constant value of approximately -10 dB from zero to 120 Hz, for the measured and simulated TFs. It was found that between 120 Hz and 100 kHz, both TFs dropped in value to -25 dB, with the simulated TF exhibiting resonance between these two frequencies and reaching its upper limit. Between 100 kHz and 160 kHz, the measured TF dropped to approximately -80 dB.

A similar study to [143] was repeated in [144], with similar results. It was however reported that the SWER line's earth return path losses depend on the impedance characteristics of the earthing system at both ends of the line, as well as on the soil properties which are frequency-dependent. It was also reported that powerline resistive losses could be analytically determined by using Carson's equation [43] for a single line above an imperfect earth.

The evaluation of MV/LV transformer bypass systems, based on SWER transformer models derived from off-line measurements, has also been carried out. A 3rd order high pass filter coupler that gave approximately 0.1 dB average insertion loss for the 35 kHz to 142 kHz frequency band was designed, resulting in worst case attenuation of -12 dB (MV - LV) and -38 dB (LV - MV). This is in contrast to -20 dB (MV - LV) and -40 dB (LV - MV), for signals passing through a 10 kVA SWER transformer. However, off-line measurements were carried out on the lines attached to the transformers, resulting in average impedances to ground of 260  $\Omega$  and 110  $\Omega$  for the MV and LV lines, respectively. It was found that, with different MV and LV line distances and transformer types, the coupler element values must be recalculated to maintain impedance matching [145].

Off-line impedance measurements were also taken to model 10 kVA and 25 kVA transformers on SWER grids, by using a bandpass-T matching network [146]. The TF of the 10 kVA model ranged from -60 dB to -30 dB between 30 kHz and 1 MHz, while its measured TF exhibited significant resonance between these frequencies, with an average of -40 dB. The modelling concept was again extended to the design of couplers [147], by making the transformer windings part of the coupling circuit. It was once more found that different coupler element values must be recalculated to maintain impedance matching.

A simulation of MV/LV PLC on a 10 km MV line model, though an improved 10 kVA transformer model, and then on a 10 km LV line model, gave a frequency response with a maximum value of between -40 and -60 dB from 30 kHz to 1 MHz, for the LV to MV

and MV to LV direction [148]. The inadequacy of distribution transformer modelling, based solely on un-energized (off-line) measurements, was also acknowledged in related studies [149].

Further studies on couplers and line branches on SWER grids revealed an attenuation of -8 dB for model simulation and actual measurement results on a 14 km line with branches, for frequencies up to 100 kHz. Between 100 kHz and 5 MHz, the attenuation characteristics of the line and its model exhibited significant resonance. It was mentioned that PLC is the only practical means of achieving data transfer on SWER grids. However, line branches must be properly terminated to reduce losses. It was emphasized that the necessary terminations were only possible with accurate SWER line models. It was concluded that G3-PLC communication on SWER lines of up to 2,000 km, with properly terminated branches and adequate repeaters, is feasible [150].

Previous work shows that black-box measurements are also favoured for developing transformer models for SWER grids, but to a lesser extent than for previously reviewed PLC studies [146-148]. Also, despite the acknowledgement that the earth return characteristics depend on the frequency-dependent soil properties and the earthing system, no indication was given that the SWER line models used in [143, 144, 150] were obtained with this consideration in mind.

The equations for inductance and capacitance of the single aerial conductor used in obtaining the SWER line model in [150] are based on transmission line parameter determination under TEM propagation with imperfect earth considered, as described in Section 2.6. The equations are provided in (11) to (13).

The per-unit length inductance of the conductor is obtained from (11).

$$L_{Cpul} = \frac{\mu_0 \mu_r}{2\pi} \ln \left[ \frac{2h}{r} \right] + L_{C(INT)pul} \quad \text{H/m} \quad (11)$$

where  $r$  is the conductor radius, and  $h$  is the conductor height above ground in meters, and  $L_{C(INT)pul}$  is the per-unit length internal inductance of the cable, given by:

$$L_{C(INT)pul} = \mu_0 \mu_r / \sqrt{\left[ \left( \frac{r^2}{4\delta^2} \right) + 1 \right]} \quad \text{H/m} \quad (12)$$

where  $\delta$  is the conductor skin depth.

The per-unit length line-to-earth capacitance of a single conductor is obtained from (13).

$$C_{(C-e)pul} = 2\pi\epsilon_0\epsilon_r / \ln \left[ \frac{2h}{r} \right] \quad \text{F/m} \quad (13)$$

The per-unit length resistance of the single aerial conductor of a SWER line may be obtained by using equation (2). The conductance of SWER lines is usually not included because it is negligible for a single powerline conductor suspended in the air [151, 152], especially at the minimum height of 7 meters specified for SWER lines.

The equations for determining the contribution of the imperfect earth path to the total line impedance, which belong together with (11) to (13) [153], were not used in [150]. These are provided in equations (14) and (15).

The per-unit length earth path impedance contribution is given by:

$$Z_{epul} = jf\mu_0 \ln\left(\frac{1+h\gamma_e}{h\gamma_e}\right) \Omega \quad (14)$$

where  $j$  is the complex operator,  $f$  is the frequency in Hertz,  $\mu_0$  is permeability of free space,  $h$  is the height of the specified aerial conductor above ground level, and  $\gamma_e$  is the earth propagation constant, given by:

$$\gamma_e = \sqrt{j2\pi f\mu_0(\{1/\rho_e\} + j2\pi f\varepsilon_e)} \quad (15)$$

where  $\rho_e$  is the soil resistivity and  $\varepsilon_e$  is the soil permittivity.

Also, the per-unit length earth path admittance contribution is given by:

$$Y_{epul} = \frac{\gamma_e^2}{Z_{epul}} \quad (16)$$

The field depth of penetration (earth path skin effect) is given by:

$$\delta_e = \left\{ 2\pi f \sqrt{\frac{\mu_0 \varepsilon_e}{2}} \left[ \sqrt{1 + \left( \frac{1}{2\pi \rho_e \varepsilon_e} \right)^2} - 1 \right] \right\}^{-1} \quad (17)$$

And, the depth of the mirror image conductor within the earth is given by:

$$P_e = h + 2\delta_e \quad (18)$$

The per-unit length transmission line representation of the analytical model of a SWER line, based on equations (2) and (11) to (14), is shown in Figure 3.1.

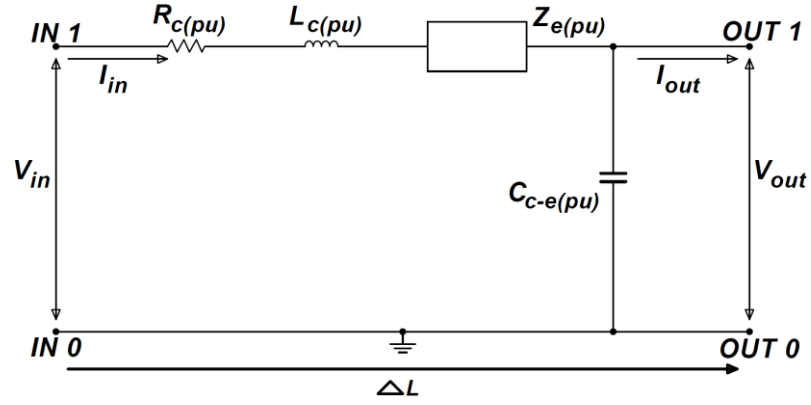


Figure 3.1 – Analytical per-unit length Transmission Line Model Representation of a SWER Line

Equations (11) to (18) are derived from the theory of images of conductors, which is a part of electromagnetic field theory [43]. As such, they are mainly for determining the influence of the imperfect earth plane on the overall transmission line parameters. In this situation, the earth path exists, not as an actual signal routing path, but rather as a fundamental component of the earthing system of the transmission line through which fault and phase sequence currents may be safely drained away, due to the role of the literal earth as the reference zero potential of the power grid [153]. Therefore, it may not be sufficient to use these equations for characterizing earth return paths for use in line-to-earth or SWER PLC applications, as has been done in a previous study which used a per-unit length transmission line model of a SWER line similar to that of Figure 3.1 [154].

Even if (14) and (15) were used in [150], no indication was given that the impedance of the earth path itself was considered, thereby creating reservations for the accuracy of the SWER line model derived in this study.

The earth's electrical characteristics are resistive and capacitive in nature, as earlier mentioned in Section 2.6 [44, 45]. Equations (14) and (15) show that the imaginary part of  $Z_{epu}$  cannot be negative, to equate to a capacitive value. This implies that the equations do not represent the earth return path impedance.

The per-unit length admittance of the earth path  $Y_{epu}$ , which may be determined using (16), has been claimed to contain the capacitive element [153]. However, this also doesn't apply to the conduction path because the inductive term of  $Z_{epu}$  refers to the loop inductance between the aerial conductor and its earth mirror image path, therefore  $Y_{epu}$  refers to the additional element of the aerial conductor to earth capacitance, as shown in Figure 3.2.

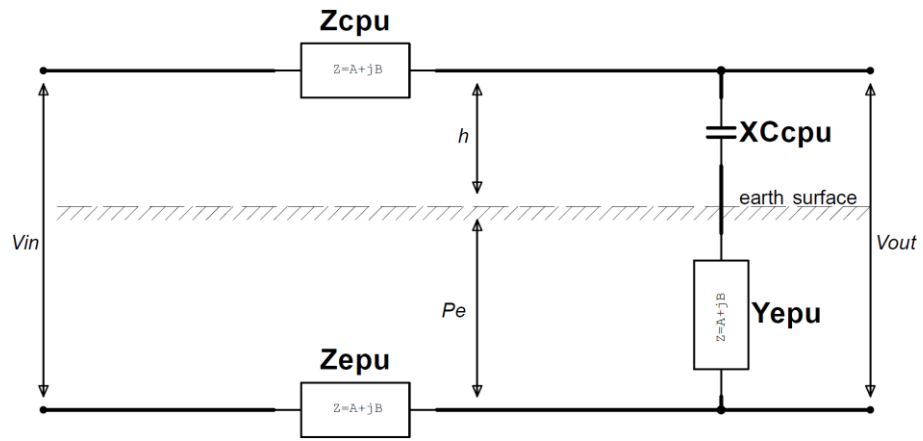


Figure 3.2 – Depiction of Power Transmission Line Elements, According to Field Theory of Images [153]

Also, the characteristics of the earthing system are not taken into account in any of the equations (11) to (18), thereby limiting their accuracy for the determination of signal routing impedance through the earth path. The earthing system is known to have an influence on the impedance characteristics of the soil/electrical conductor interface [155, 156], and therefore this ought to be factored into calculations or measurements. A number of sources [45, 157, 158] indicate that this impedance is also capacitive, thereby leading to the conclusion that increased accuracy will be obtained when the influence of the earthing system is properly taken into account.

### 3.7 Gaps Identified from Literature

The body of reviewed information from the literature reveals the following gaps:

1. NB-PLC channel characterization for distribution grid components has been mostly carried out on unenergized components. Taking measurements on grid components while energized allows phenomena peculiar to their operational state to be observed, captured and used in PLC channel analysis. This is particularly important for through-transformer channels of distribution transformers, on account of their potential for high frequency signal variation due to insulation dielectric polarization, under energization.
2. Although the majority of power grid components are modelled using black-box methods, there is no benchmark approach for doing so, especially for energized transformers. The vast majority of spectral measurements at NB-PLC frequencies were made using *s*-parameters, which is unnecessary because they are more suited for conditions where frequencies above narrowband and small physical dimensions combine to make it difficult to measure voltages and currents accurately. *ABCD* parameters, which are already routinely used in power system



analysis and are valid for NB-PLC frequencies, may be a suitable alternative. The process of estimating the time-domain representations of the grid components from the FRFs are also not streamlined, leading to inconsistencies which make model comparison difficult.

3. Studies on PLC on SWER grids mostly rely on assumptions of the earth path's resistivity, which is required for using analytical equations. Also, no consideration is given to the earthing system in relation to the total earth path characteristics, when it is determined analytically. Due to the inhomogeneous and anisotropic nature of the earth path, variations of its impedance characteristics with seasonal, geographical, and non-natural changes may occur. Therefore, it may be better to carry out regular characterization and modelling of the earth path using empirical or hybrid empirical/analytical approaches, to reduce errors.

### **3.8 Research Design**

This section provides details of the research design. The research scope is given in Section 3.8.1, the research plan is given in Section 3.8.2, and the methodological approach is given in Section 3.8.3.

#### **3.8.1 Research Scope**

The research was limited to, and focused on the following:

1. Single Phase Platform: As many rural grids, such as SWER grids, are single phase, the complex transformer dynamics to be investigated can be carried out on a single phase basis.
2. Bandwidth: Only the frequency band of 30 kHz to 150 kHz was considered because the European NB-PLC Standard CENELEC 50065-1 and the G3-PLC protocol [39] prescribe operational frequency bands of 3 kHz to 148.5 kHz, and 35.9 kHz to 90.6/480 kHz, respectively. The working frequency band for the research will be from 30 kHz to 150 kHz, which will include the upper portion of the band specified by CENELEC A, all the bands specified by CENELEC B, C, and D, as well as part of the G3-PLC band.
3. Modelling: All grid and PLC interface components were characterized and modelled separately and combined to form the PLC channels as required. This was necessary to identify variables specific to each component separately. Also,

distribution transformer models were estimated empirically and modified analytically for simulation purposes.

4. PLC Simulation: Only basic communication system implementations were considered, no error correction or encoding was performed.

### **3.8.2 Research Plan**

The physical characteristics of the individual grid components within the desired frequency range have to be determined first, to achieve PLC through MV/LV grids. It is preferable to use empirical methods for the required characterization, because a number of power grid components, such as earth return paths and distribution transformers, have characteristics that vary with time. The impedance of the earth return path is dependent on the soil ionic and moisture content, which is a seasonal variable, while the capacitive shunt paths of distribution transformers depend on the permittivity of the insulation system, which tends to increase with age and deformation [71, 159, 160].

It is necessary to carry out simulations of data transfer through the characterized grid components. This requires that the components have to be modelled as PLC channels. There is an advantage to using hybrid approaches to carry out the desired modelling, which entails applying analytical methods to process the data obtained from the empirical measurements.

### **3.8.3 Methodological Approach**

The research methodology was quantitative, leaning on empirical methods, and supported by analytical and correlational components [161]. The bulk of the work involved hybrid characterization, modelling, and simulation through the use of various computational tools. Therefore, the research may be classified under the Constructive Research paradigm [162]. This incorporates systems development as the focus, with three basic research elements of Observation, Theory Building, and Experimentation, as shown in Figure 3.3.

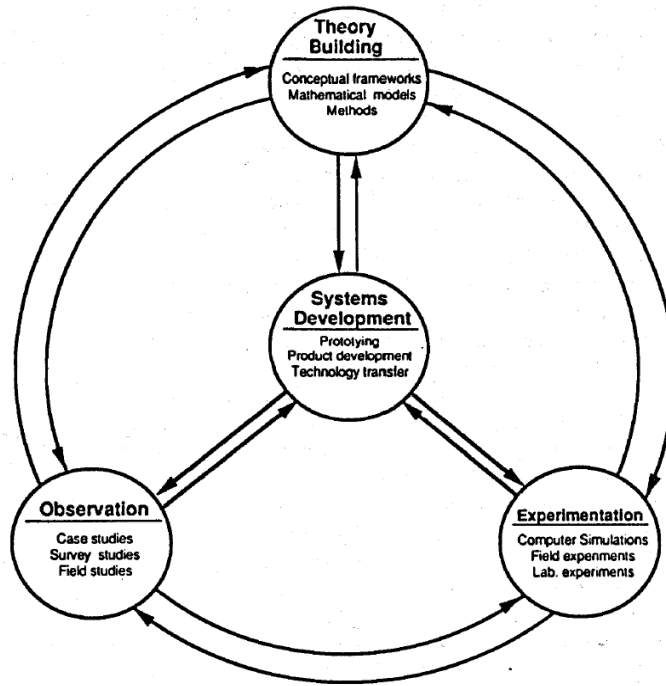


Figure 3.3 - Multi-Methodological Approach for Constructive Research [162]

Experimentation was carried out through physical tests and simulations, which produced results that were observed in order to build on established theories. These results were then applied to the model modification process, and the cycle was repeated till the results were satisfactory.

There were two categories of PLC channels of interest for experimentation, one was the MV line PLC channels, and the other was the through-transformer PLC channels. All the experiments conducted in the course of this research were focused on the interactions between these power system components and the high frequency signals that propagate through them.

# **Chapter Four – Methods**

## **4.1 Introduction**

This chapter describes the methods that were used in carrying out the experimental and analytical tasks used in the research. The methods used for obtaining the characteristics of the SWER MV line in the lower NB-PLC frequency region are described in Section 4.2, the methods used in obtaining the through-transformer characteristics of the 0.5 kVA transformers in the lower NB-PLC frequency region are described in Section 4.3, and the methods used in obtaining the through-transformer characteristics of the 1 kVA and 15 kVA transformers in the lower NB-PLC frequency region are described in Section 4.4.

The methods used in estimating the PLC models of the SWER and Two-wire MV line and through-transformer channels of the 1 kVA and 15 kVA transformers are described in Section 4.5, the methods used in carrying out PLC simulations of the PLC models of the SWER MV line and through-transformer channels of the 1 kVA and 15 kVA transformers are described in Section 4.6, and the conclusion is given in Section 4.7.

## **4.2 SWER MV Line NB-PLC Characteristics**

This section describes the methods used in obtaining the lower NB-PLC characteristics of the SWER line, including details of the developed earth path characterization method. A description of the method is given in Section 4.2.1, the experimental procedure for the method is described in Section 4.2.2, and the experimental procedure for the characterization of the SWER MV line is given in Section 4.2.3.

### **4.2.1 Description of Earth Path Characterization Method**

The main consideration for the method is that the earthing system used for the experiments should be very similar to that which is to be used for the planned line-to-earth path PLC channel. This is to ensure consistency of the derived earth path impedance characteristics.

The experimental platform for the earth path impedance determination is shown in Figure 4.1.

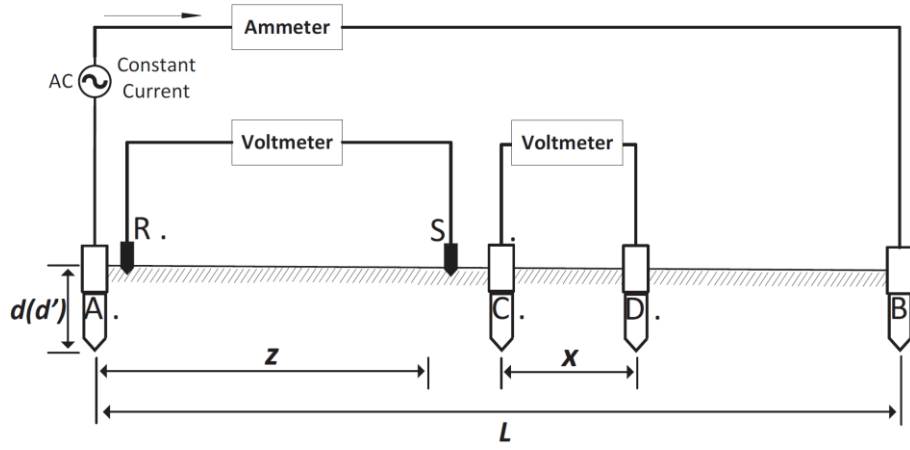


Figure 4.1 – Earth Path Impedance Experimental Platform

$A$  and  $B$  represent the injection rods,  $C$  and  $D$  represent the measurement rods identical to the injection rods, while  $R$  and  $S$  represent identical earth probes. The variables  $d'$ ,  $d$ ,  $z$ ,  $x$ , and  $L$  are measurement rod depth, injection rod depth, probe separation, measurement rod separation and injection rod separation respectively, in meters.

The earth path, which henceforth is used to denote everything between the cable connections, is modelled as a lossy capacitor based on its inherent permeability. If the current is passed through the earth path via rods  $A$  and  $B$  using an insulated cable at an arbitrary height above the earth surface, the experimental platform may be described electrically by the schematic diagram of Figure 4.2, consisting of lumped versions of distributed elements.

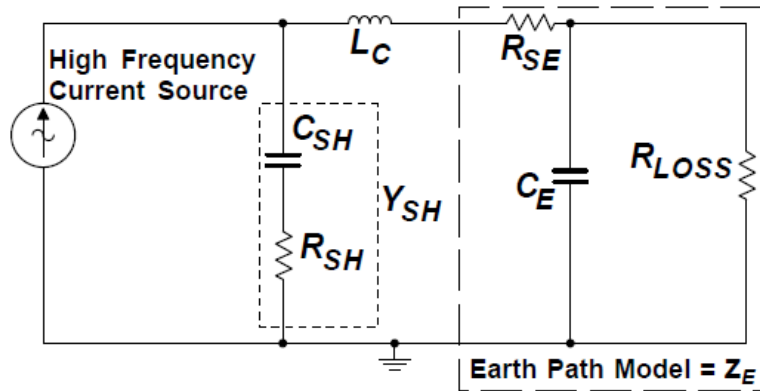


Figure 4.2 – Earth Path Impedance Measurement Schematic Diagram

The resistance of the cable, earth rods and series component of the lossy capacitor are represented by the series resistance  $R_{SE}$ , the earth path capacitance is represented by  $C_E$  in parallel with its associated shunt resistance  $R_{LOSS}$ , the loop inductance is represented by  $L_C$ , and the shunt admittance  $Y_{SH}$  of the cable and all other stray paths to an imperfect earth plane are represented by  $C_{SH}$  and  $R_{SH}$ . The elements  $R_{SE}$ ,  $C_E$ , and  $R_{LOSS}$  collectively

make up  $Z_E$ . This is the earth path impedance with earth rods and superfluous material inclusive, which is the variable of interest.

A range of physical phenomena influencing the experimental platform can be accounted for, using Figure 4.2. For example, a small  $d$  suggests that only the topmost layer of soil, which usually has low moisture content, is in contact with the rod surfaces; therefore the impedance of the earth path  $Z_E$  will be high. This translates to a low  $C_E$  and a high  $R_{LOSS}$ . Also, the rod hemispherical zones of influence (ZOI) will cover a small radius [155].

If the cable remains at a fixed height and the injection rod depth  $d$  is increased, the contact area between the rods and soil increases. More importantly, in addition to the topmost layer, the rods now make contact with the deeper soil layer, which usually has higher moisture content, and by extension less impedance. This translates to a higher  $C_E$  and a lower  $R_{LOSS}$  than previously. Also, the rod ZOI will be larger than previously [163, 164].

These larger ZOI will reduce the voltage gradient and make more low impedance paths in the deeper layer available for current flow. Assuming all other shunt paths remain the same, this situation will translate to a lower  $C_{SH}$ . Although the loop inductance will increase with increased rod depth [163], there will be a net inductance reduction up to the maximum rod depth. This may be due to the earth rod being of standard copper-cladding steel type with the dominant material of the rod being steel, which has a high relative permeability value. Consequently, a reduction of the length of the rod above ground reduces the effective series inductance of the line-to-earth path capacitance [165]. This translates to a lower  $L_C$ . There will also be a net reduction in shunt resistance  $R_{SH}$ , up to a certain rod depth, which is probably due to the same influence of the exposed earth rods.

For a short path length  $L$  with the height unchanged, a shorter cable will be used, and therefore it is expected that  $L_C$  and  $Y_{SH}$  will reduce by an approximately equal proportion. This serves as an important experimental control for more accurate separation of the cable and earth path influences. Also, with current flowing through the main circuit, if voltage drop measurements  $V_{drop}$  are carried out between rods  $C$  and  $D$  using an insulated cable on the earth's surface, it is expected that  $L_C$  and  $Y_{SH}$  will reduce and increase respectively.

The earth path impedance  $Z_E$  can be heuristically estimated by the correlation of the voltage and current measurements obtained from the experimental platform to the lumped elements of Figure 4.2, using the procedure described in Section 4.2.2. However,  $V_{drop}$  measured between rods  $C$  and  $D$  will represent only a proportion of the actual impedance

magnitude of the earth section,  $|Z_{Section}|$ , due to multipath characteristics of the earth path [158].

With total platform current  $I$ ,  $|Z_E|$  is:

$$|Z_E| = \frac{V_{A-B}}{I} \quad (19)$$

Assuming there are no multipath effects,

$$|Z_{Section}| = \frac{V_{drop}}{I} \quad (20)$$

Equating currents in (19) and (20),

$$\frac{V_{A-B}}{|Z_E|} = \frac{V_{drop}}{|Z_{Section}|} \quad (21)$$

However, with multipath effects, the current flowing through a particular measured path within the section will be a fraction of the total current flowing through the section. Therefore,

$$\frac{V_{A-B}}{|Z_E|} = \frac{V_{drop}}{K \cdot |Z_{Path}|} \quad (22)$$

where  $K$  contains the factors of the variables  $x$ ,  $L$ ,  $d'$  and  $d$ , which influence the number and location of the paths.

Solving for the magnitude of  $Z_{Path}$ ,

$$|Z_{Path}| = \frac{1}{K} \cdot V_{drop} \cdot \frac{|Z_E|}{V_{A-B}} = \frac{1}{KI} \cdot V_{drop} \quad (23)$$

The path/section impedance phase angle may be obtained from the values of the parallel elements of the estimated  $Z_E$  by:

$$Z_{Path} \angle \theta = \tan^{-1} \left[ \frac{R_{LOSS}}{XC_E} \right] \quad (24)$$

Rearranging (22) to obtain a ratio of  $V_{drop}$  to  $V_{A-B}$  yields:

$$\frac{V_{drop}}{V_{A-B}} = \frac{|Z_{Path}|}{|Z_E|} \cdot K = F \quad (25)$$

Equation (25) allows the simulated values of  $V_{A-B}$  to be compared with the measured voltage drop values  $V_{drop}$ , for each frequency of interest. A constant value of  $F$  throughout the bandwidth of interest suggests a correlation between measured and simulated quantities, with the mean and variance of  $F$  serving as a measure of the accuracy of the method in deriving the earth path impedance  $Z_E$  with earth rods inclusive.

### 4.2.2 Procedure for Earth Path Characterization

An open flat field with approximately 88 meters of diagonal length, with a building at one end and a structured playground at the other, was identified and used. A decision for total earth path length  $L$  of 85.5 meters between rods  $A$  and  $B$  was made, to provide sufficient length for upward scaling. A decision for an initial value of 0.5 m for current injection depth  $d$  was also made [164]. For these experiments,  $d$  was a variable. However, the earth rod's maximum depth of 1.8 meters was used as the fixed value of  $d$ , for the SWER line characterization experiment described in Section 4.2.3. Standard earth rods that are used in regular low voltage (LV) electrical installations were used.

The earth path characterization experiment was carried out in four parts. The first part of the experiment involved passing constant current sinusoidal waveforms through the entire length of the earth path via injection rods  $A$  and  $B$  at each frequency of interest  $f$ , while the voltage and current waveform data were captured.

The second part of the experiment involved the determination of each rod's ZOI radius by driving a small earth probe  $S$  into the ground at approximately the halfway point of  $L$ , and driving a similar probe  $R$  into the ground at varying distances  $z$  between earth rods  $A$  and  $B$ ; each time measuring the voltage drop between the two probes. After the ZOI radii had been determined for all frequencies, the largest radius value was taken as the global ZOI radius value for all the earth rods.

The third part of the experiment involved carrying out a control experiment. This was set up by driving rod  $C$  into the earth at a point that is slightly greater than twice the zone radius from rod  $A$ . Current was then passed through the short earth section, with voltage and current data captured at each frequency of interest, as was done in the first part. The first three parts of the experiment were then repeated for varying  $d$ . A 1:2 ratio high frequency transformer was used to reduce output voltage and increase output current, from the constant current source, for  $d = 1.8\text{m}$ .

The fourth part of the experiment involved taking voltage drop measurements between two points along the earth path. Rods  $C$  and  $D$  were sunk into the earth in the vicinity of the midpoint of  $L$ . Length  $x$  was chosen with the global zone radius considered as the lower limit; an upper limit for  $x$  of about three times the global zone radius allows for an assumption of homogeneous earth, whereby any differences in voltage drop with frequency may be considered as being due to impedance changes only [166]. The voltage drop  $V_{drop}$  between  $C$  and  $D$  was then measured for frequencies between 30 Hz to 1 MHz



inclusive. This final part of the experiment was repeated for varying  $d$  and  $d'$  ranging from 0.5 to 1.8 meters. A flowchart of the experimental procedure is provided in Appendix D.

By considering the experimental platform's total impedance magnitude and phase values obtained from the voltage and current data, iterative calculations were carried out using a MATLAB script, to heuristically estimate the lumped element values of Figure 4.2. This process began by assuming initial values for  $C_E$  and  $R_{LOSS}$  at the starting frequency  $f$  of 30 Hz, followed by  $R_{SE}$ ,  $L_C$ ,  $C_{SH}$ , and  $R_{SH}$ , in that order. Then, the frequency was increased to the next step, and the order of estimations was repeated again. For each iteration, the calculated magnitude and phase values were compared with the measured values and increased or decreased accordingly to achieve the closest fit possible.

The same iterative process is repeated with data from the control experiment, to determine if the results can be scaled with length. If the control results do not give an impedance value which is in scale with the control length, this suggests the presence of superfluous material within the soil. The previously obtained values of  $R_{SE}$ ,  $C_E$ , and  $R_{LOSS}$  are kept fixed, and other values associated with a short cable span are estimated via the iterations. If the simulated and measured values don't agree, adjustments are made to the initially assumed values of  $C_E$  and  $R_{LOSS}$ , and the iteration is repeated. If there is a good agreement, then the hybrid empirical/analytical characterization method based on a lossy capacitor earth path model can be considered to be verified. The same iterative process is again repeated for the  $V_{drop}$  data, with equation (25) being used to verify the earth path model of Figure 4.2 partially.

### 4.2.3 Description and Procedure for SWER MV line Characterization

The determined earth path impedance was fully verified by setting up a SWER MV line characterization experiment, as a basis for the use of the earth path characterization method for line-to-earth path NB-PLC channel modelling. The verification was achieved by comparing results of simulations of the calculated line parameters with those obtained from measurements incorporating an industry-standard bare aerial conductor, which were carried out on the same site as the earth path impedance experiments. The experimental platform for the SWER MV line characterization is shown in Figure 4.3.

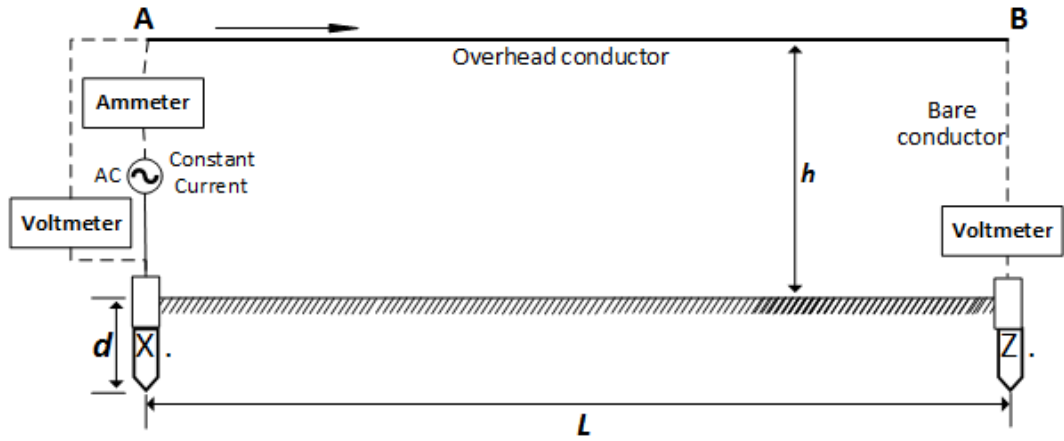


Figure 4.3 – SWER Transmission Line Impedance Experimental Platform

The aerial conductor was mounted on existing structures at ends *A* and *B* of the field, at height *h* of 3.74 and 3.10 meters above ground respectively, for an average height *h* of 3.5 meters and total length *L* of 86 meters. The two-port ***ABCD*** parameters of the experimental SWER line were then measured, for frequencies between 30 Hz to 1 MHz inclusive, in variable frequency steps for a total of 52 frequency points.

Two types of aerial conductors of similar size were used in turn, for the SWER line characterization experiment. One was a traditional ACSR (Aluminium Conductor Steel Reinforced) twisted strand type, commonly referred to as Squirrel, and the other was a specialized smooth body ACSR, commonly referred to as Flounder. The Flounder conductor is primarily designed as a low-loss option for use on rural distribution lines, where significant line lengths are common [167]. The objective for also using this conductor for the experiment was to investigate if its low-loss rating has any corresponding advantage for high frequency signals, which could translate to improved PLC performance.

The calculation of the impedance parameters of the SWER line for Squirrel and Flounder conductors was done using equations (2) and (11) to (15), along with the required conductor specifications obtained from their respective data sheets, given in Appendix E. The value of relative permeability for the conductors was adjusted from 1.0 for pure aluminium to 1.3, to account for the presence of the steel cores of the aerial conductors.

Also, constant values of soil resistivity of 10  $\Omega\cdot\text{m}$  and 100  $\Omega\cdot\text{m}$  were assumed, based on typical published values [157, 168]. A fixed value 10 for soil relative permittivity was also assumed, based on results which state that the electrical characteristics of average soil types do not drastically change with changes in its average permittivity, under TEM wave propagation [169]. The values obtained were fitted into the per-unit length

transmission line representation of the analytical SWER line model, for simulation purposes.

The per-unit length lossy capacitor model of the earth path was merged with the per-unit length transmission line representation of the analytical SWER line model, to form a hybrid empirical/analytical per-unit length transmission line representation of a SWER line model. This is shown in Figure 4.4.

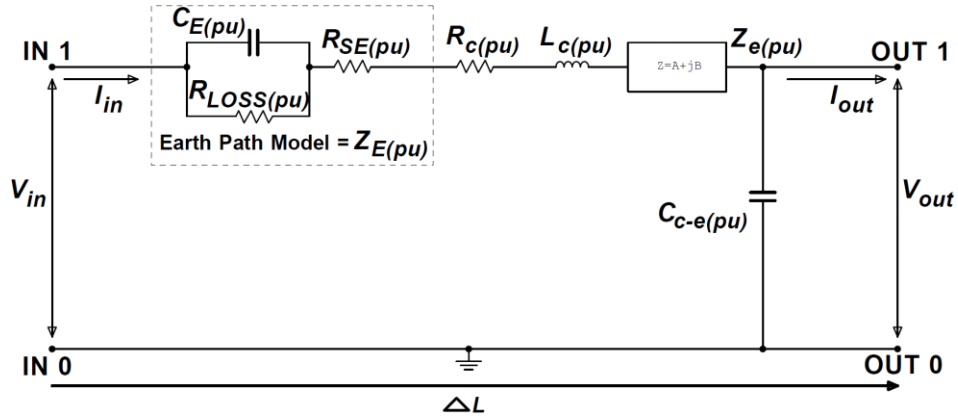


Figure 4.4 – Hybrid per-unit length Transmission Line Model Representation of a SWER Line

The values of the earth path lossy capacitor model, which were determined by the application of the earth path characterization method, were fitted into the per-unit length transmission line representation of the hybrid SWER line model, along with the previous analytically determined line parameters, for simulation purposes.

### 4.3 0.5 kVA Transformer NB-PLC Characteristics

This section describes the methods used in obtaining the through-transformer NB-PLC characteristics of the 0.5 kVA, 11 kV/230 V transformers. A description of the experimental method is given in Section 4.3.1, and the procedure is given in Section 4.3.2.

#### 4.3.1 Description

The block diagram of the experimental platform that was used to study the effects that energized 0.5 kVA, 11 kV/230 V transformers have on high frequency signals passing through their terminals bi-directionally is shown in Figure 4.5.

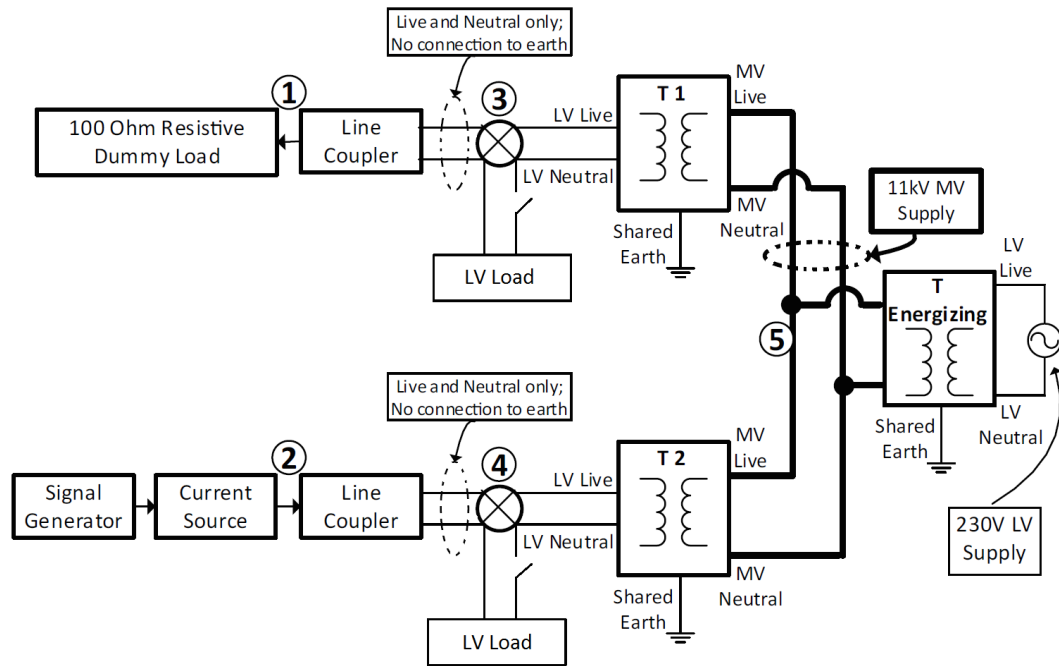


Figure 4.5 – Block Diagram of 0.5 kVA Energized Through-transformer Experimental Platform

Transformers  $T1$ ,  $T2$ , and  $T$  were identical single phase 0.5 kVA transformers. Transformer  $T$ , termed the energizing transformer, was connected to supply 11 kV from a standard 230 V RCD-protected wall socket via a 0 – 270 V variac. LV PLC coupling units were set up on the secondary sides of  $T1$  and  $T2$  for through-transformer signal transfer. The signal generator was used to provide high frequency sinusoidal waveforms from 30 kHz to 150 kHz, in 10 kHz steps, to the voltage-controlled current source. The current source provided high frequency constant current waveforms in accordance with the input waveforms, up to a maximum of 48 V peak-to-peak.

#### 4.3.2 Procedure

The high frequency constant current was injected into the platform at point 2 and measured at point 1 and 2 with an oscilloscope. At each frequency, the high frequency measurements were taken at the coupling points 3 and 4 with no LV load connected. Each measurement was taken with the platform energized with 50 Hz voltage at 110 V, 190 V, 230 V and 270 V. The measurements were repeated with the coupling points 3 and 4 connected to resistive, capacitive and inductive LV loads, in turn.

#### 4.4 1 kVA and 15 kVA Transformer NB-PLC Characteristics

This section describes the methods used in obtaining the through-transformer NB-PLC channel characteristics of brand-new 1 kVA and 15 kVA, 11 kV/230 V transformers. A description of the process of designing and implementing the PLC interfaces required for

the experiments is given in Section 4.4.1, the experimental method is given in Section 4.4.2, and the procedure is given in Section 4.4.3.

#### 4.4.1 MV and LV PLC Interface Design and Implementation

MV and LV PLC interfaces needed to carry out the 1 kVA and 15 kVA energized transformer experiments were designed based on the procedures described in Appendices A and B, and then physically implemented. The main objective of the design and implementation process was to produce simple PLC interfaces that provided satisfactory performance in preventing virtually all the 50 Hz 11 kV and 230 V signals from getting to the signal injection and measurement nodes, in order to ensure a safe experimental platform, while also keeping the high frequency signal losses to a minimum.

##### 4.4.1.1 MV PLC Interface

The schematic diagram of the MV PLC interface design used on the through-transformer channel experimental platform is shown in Figure 4.6.  $Z_0$  represents the MV line impedance.

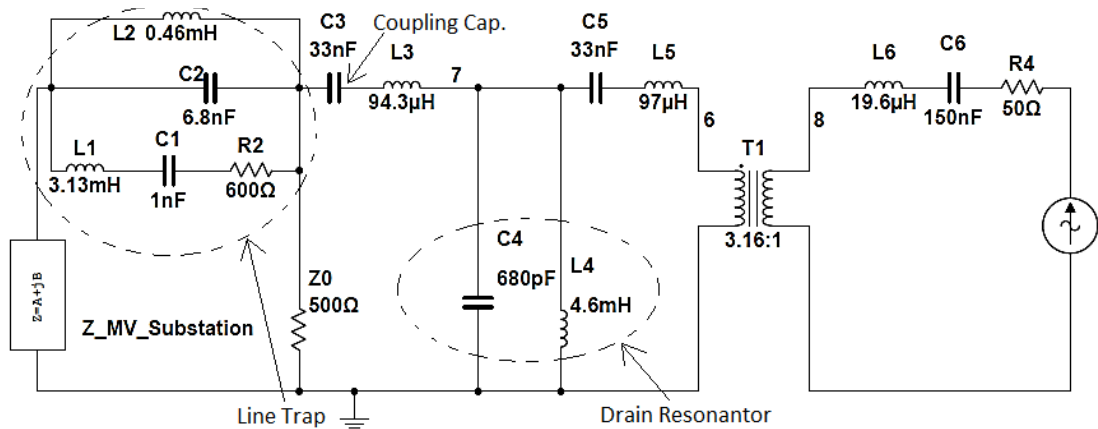


Figure 4.6 – Medium Voltage PLC Interface

The MV PLC interface design was physically implemented using polypropylene film capacitors suitable for high power, high frequency signals, and triple-insulated winding wire for creating MV inductors at elevated voltages.

The impedances of the implemented MV line trap and drain resonator were measured, to establish that they have the desired characteristics. The measured and simulated MV line trap impedance plots are shown in Figure 4.7.

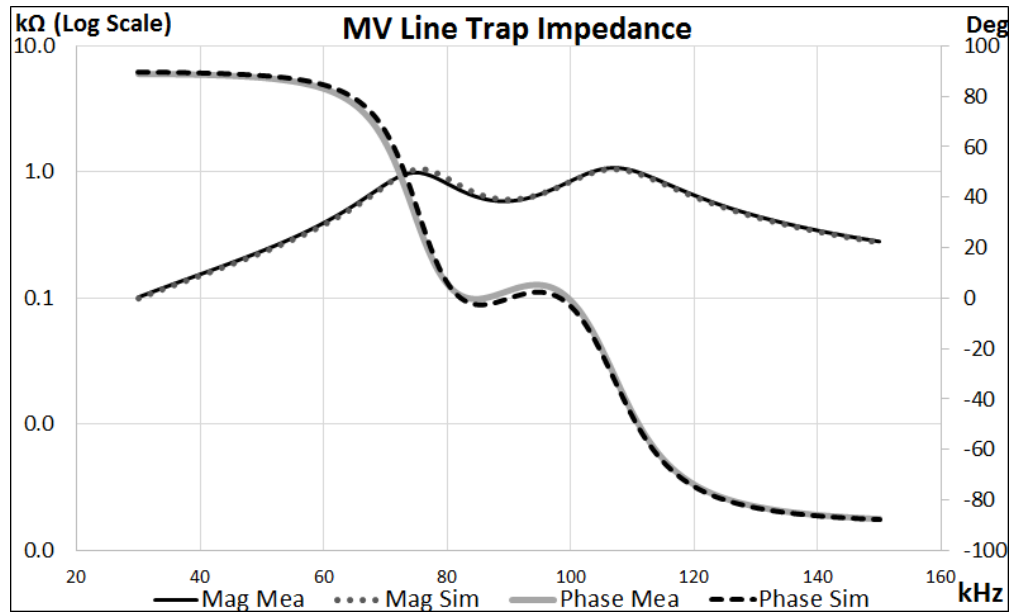


Figure 4.7 – Measured and Simulated Medium Voltage Line Trap Impedance

The measured phase plot of the MV line trap shown in Figure 4.7 reveals that resonance occurs at approximately 85 kHz. However, the resonance trough is at 90 kHz, with a resistive value of 600  $\Omega$  as expected. The measured magnitudes are approximately 100  $\Omega$  at 30 kHz, 1 k $\Omega$  at the 75 kHz pre-resonance peak, 1.1 k $\Omega$  at the 108 kHz post-resonance peak, and 300  $\Omega$  at 150 kHz. In comparison with the simulated impedance values, the measured values were determined to have fulfilled the design objective for creating a low impedance path for the 50 Hz current, while preventing most of the high frequency signals from being lost through the MV substation path, which is represented by the energizing transformer primary terminal. The MV line trap was therefore considered satisfactory for use in the transformer experiments.

The measured and simulated MV drain resonator impedance plots are shown in Figure 4.8.

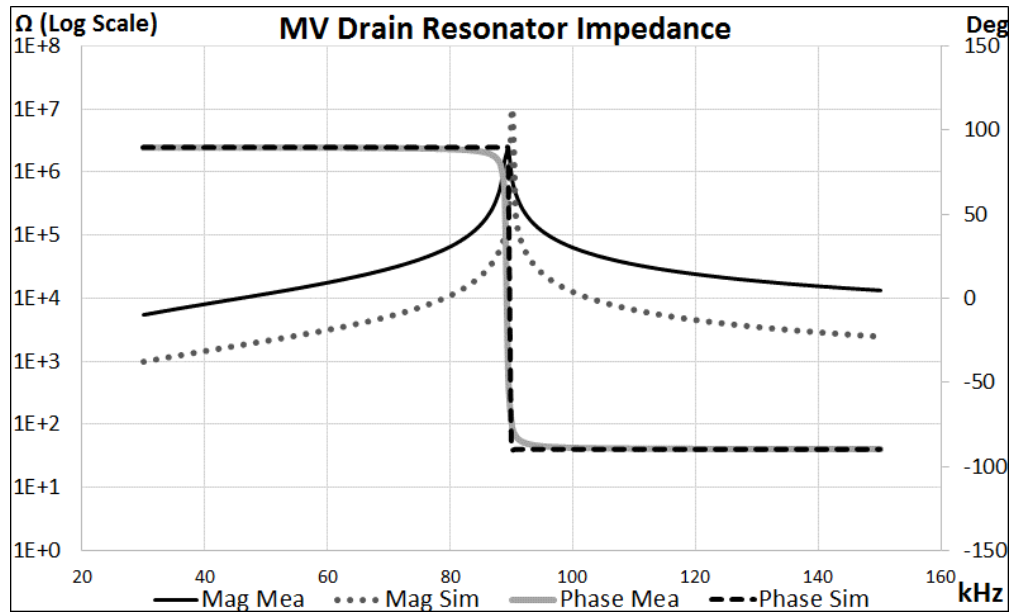


Figure 4.8 – Measured and Simulated Medium Voltage Drain Resonator Impedance

The measured magnitude plot of the MV drain resonator shown in Figure 4.8 reveals an impedance of approximately 2.2 MΩ at 90 kHz. However, this value sharply rolls off to much lower values, on either side of this frequency. The measured impedance is approximately 5 kΩ at 30 kHz and 15 kΩ at 150 kHz. In comparison with the simulated impedance values which have equal phase but lower magnitude values outside the resonance point, the measured values were determined to have fulfilled the design objective for creating a low impedance path for residual 50 Hz current that gets through the MV coupling capacitor, while preventing most of the high frequency signals from being lost through the shunt path.

#### 4.4.1.2 LV PLC Interface

The schematic diagram of the LV PLC interface design used on the through-transformer channel experimental platform is shown in Figure 4.9.  $Z_{Sec}$  represents the secondary impedance of the analysis transformer described in Section 4.4.2.

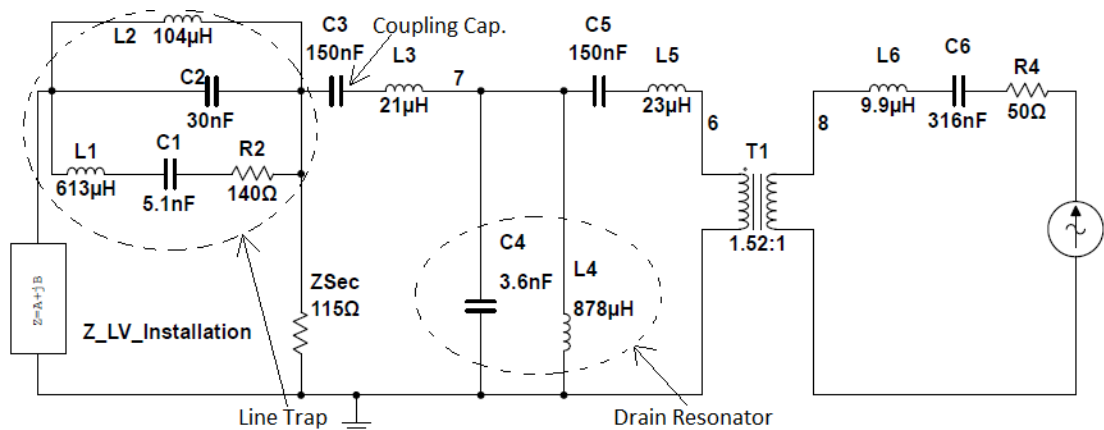


Figure 4.9 – Low Voltage PLC Interface

The LV PLC interface design was physically implemented, using low loss copper winding wire for creating the LV inductors at elevated currents of up to 5A.

The impedances of the implemented LV line trap and drain resonator were also measured, to establish that they have the desired characteristics.

The measured and simulated LV line trap impedance plots are shown in Figure 4.10.

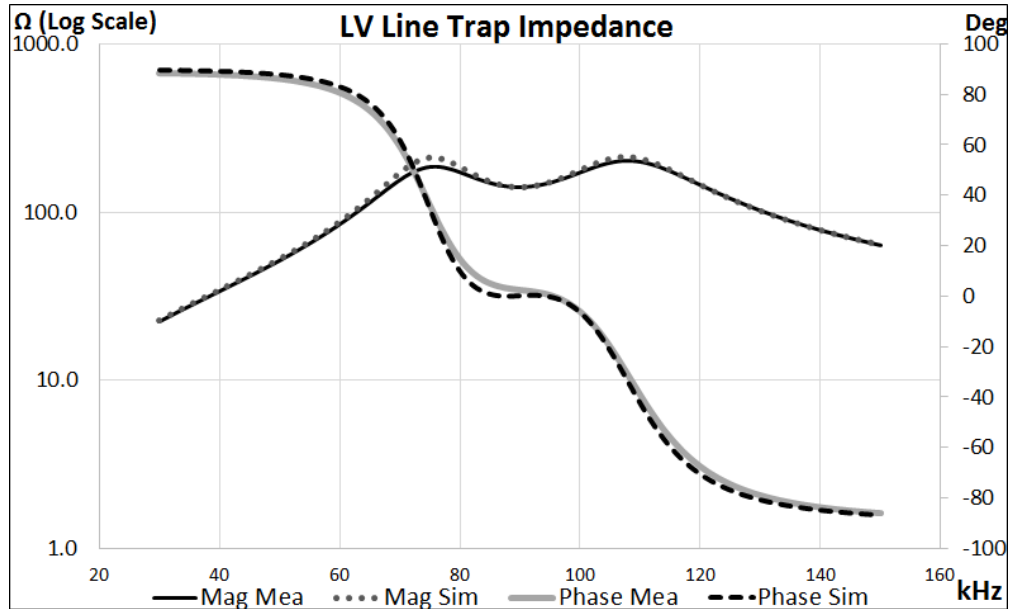


Figure 4.10 – Measured and Simulated Low Voltage Line Trap Impedance

The measured magnitude and phase plots of the LV line trap shown in Figure 4.10 reveal that resonance occurs at approximately 90 kHz with an impedance value of 140  $\Omega$  resistive, as expected. The measured impedance is approximately 50  $\Omega$  at 30 kHz, 170  $\Omega$  at the pre-resonance peak at 75 kHz, 200  $\Omega$  at the post-resonance peak at approximately 108 kHz, and 65  $\Omega$  at 150 kHz. In comparison with the simulated impedance values, the measured values were determined to have fulfilled the design objective for creating a low impedance path for the 50 Hz current, while preventing most of the high frequency signals from being lost through the LV energizing source for the transformer bypass control experiment described in Section 4.4.2, which is represented by the variac. The LV line trap was therefore considered satisfactory for use in the transformer experiments.

The measured and simulated LV drain resonator impedance plots are shown in Figure 4.11.



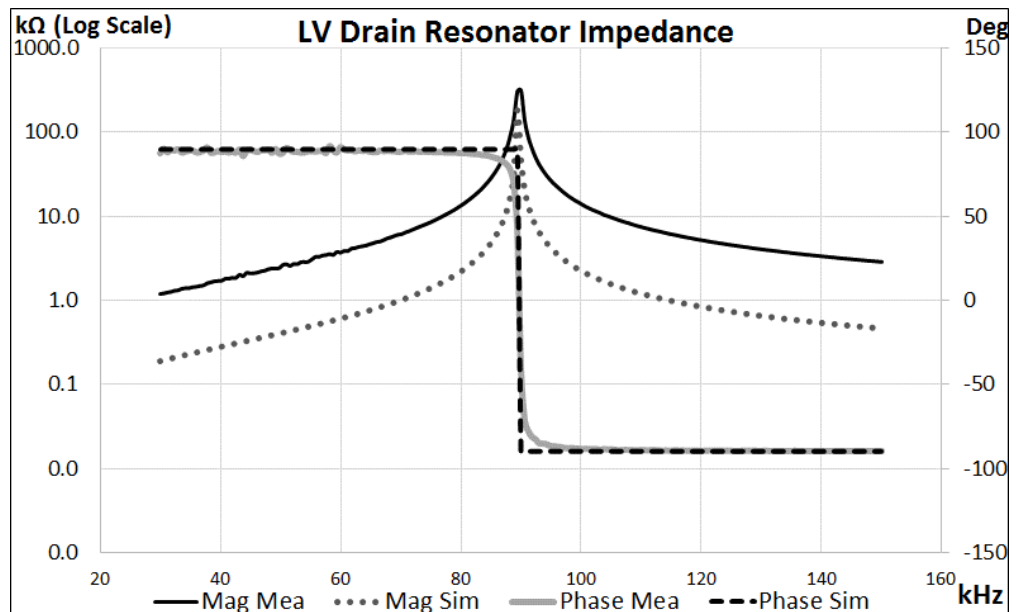


Figure 4.11 – Measured and Simulated Low Voltage Drain Resonator Impedance

The measured magnitude plot of the LV drain resonator shown in Figure 4.11 reveals an impedance of approximately 320 kΩ at 90 kHz, however, this value also sharply rolls off to much lower values, either side of this frequency. The measured impedance is approximately 1.2 kΩ at 30 kHz and 3 kΩ at 150 kHz. In comparison with the simulated impedance values which have equal phase but lower magnitude values outside the resonance point, the measured values were determined to have fulfilled the design objective for creating a low impedance path for residual 50 Hz current that gets through the MV coupling capacitor, while preventing most of the high frequency signals from being lost through the shunt path.

Figure 4.12 shows an overhead view of the fully tested MV and LV PLC interfaces connected to the transformers and instrumentation, with the exception of the LV line trap. These formed the platform for the 1 kVA and 15 kVA energized through-transformer experiments, located within a safety enclosure, as shown in the figure. The enclosure was caged off and interlock-protected to ensure energization only from outside with its entrance door fully closed, for health and safety compliance. Figure 4.13 shows the control and measurement station for the experimental platform, with all necessary cables connections made between this point and others within the enclosure.

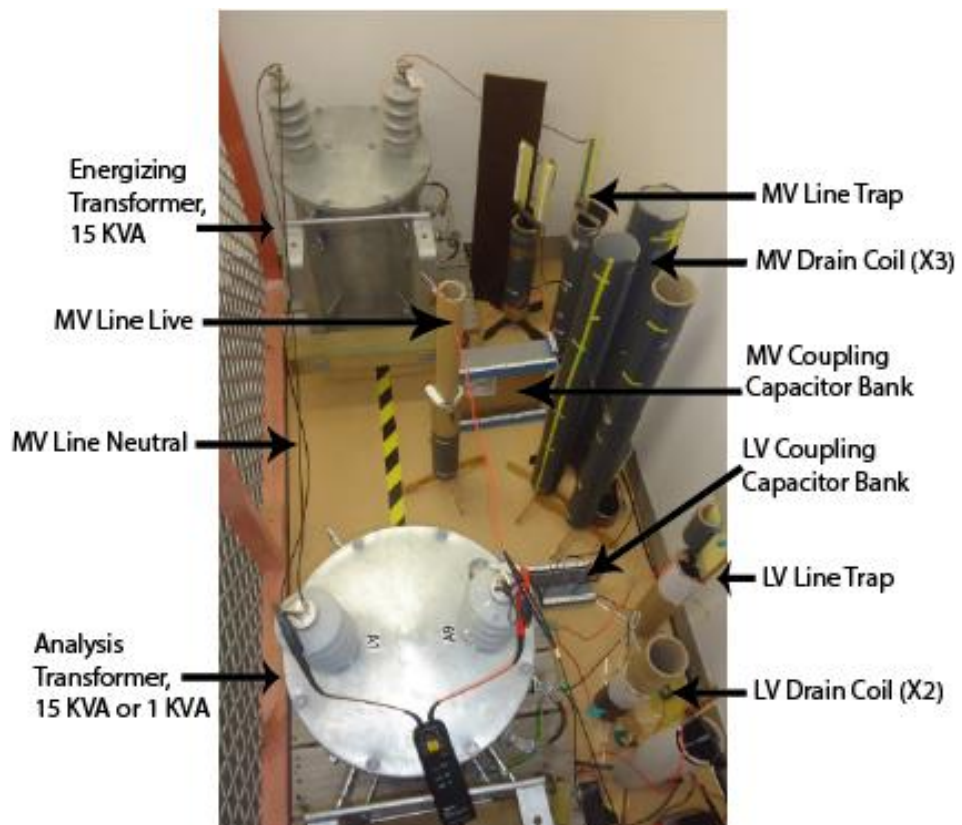


Figure 4.12 – Overhead View of the Assembled 1 kVA and 15 kVA Transformer Experimental Platform

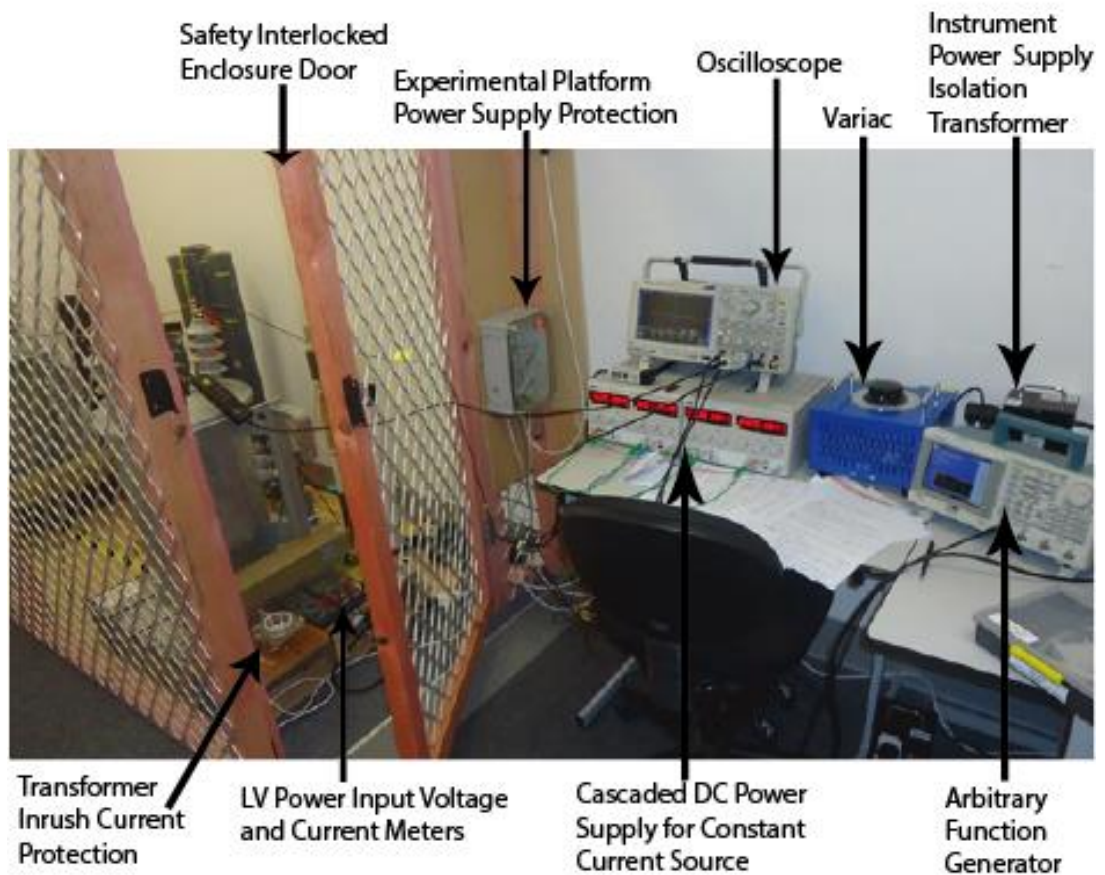


Figure 4.13 – Control and Measurement Station for the 1 kVA and 15 kVA Transformer Experimental Platform

#### 4.4.2 Experimental Description and Procedure

The 1 kVA and 15 kVA energized through-transformer experimental platform was a laboratory replication of a PLC-enabled single-phase MV to LV grid boundary section. Its block diagram representation is shown in Figure 4.14, while its actual implementation is shown in Figures 4.12 and 4.13.

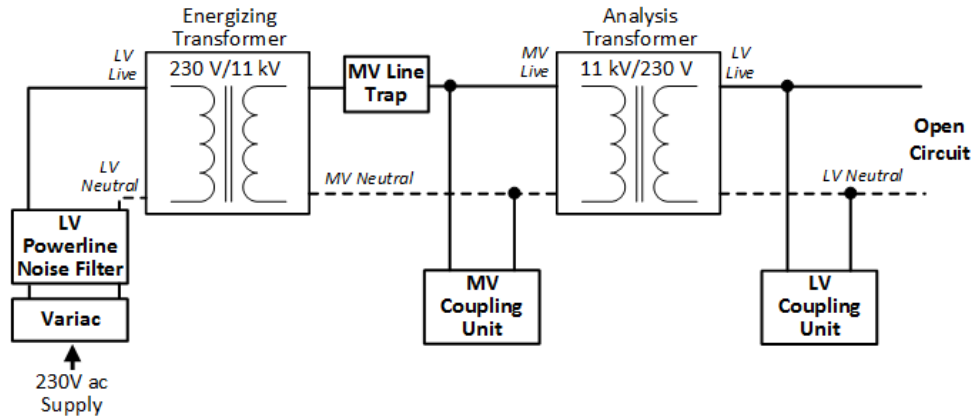


Figure 4.14 – Block Diagram of 1 kVA and 15 kVA Energized Through-transformer Experimental Platform

The MV and LV PLC interfaces, depicted in the schematic diagrams of Figures 4.6 and 4.9 respectively, were set up on the primary and secondary sides of a 15 kVA (and 1 kVA) 11 kV/230 V single phase transformer, with the exception of the LV line trap, to achieve through-transformer signal transfer. This transformer is termed the analysis transformer. Each interface consisted of a line trap and a coupling unit made up of a coupling capacitor, bandpass filter, and impedance matching/isolation transformer. The coupling units and line traps had similar bandpass and bandstop filtering characteristics respectively, as shown in Section 4.4.1.

The analysis transformer was energized by another similar transformer, termed the energizing transformer. This transformer was connected to supply 11 kV from a standard 230 V RCD-protected wall socket, via a 0 – 255 V variac and LV powerline noise filter. No LV load was connected.

The signal flow direction and measurement points for the LV to MV and MV to LV signal transfer through the analysis transformer are shown in Figures 4.15 and 4.16 respectively.

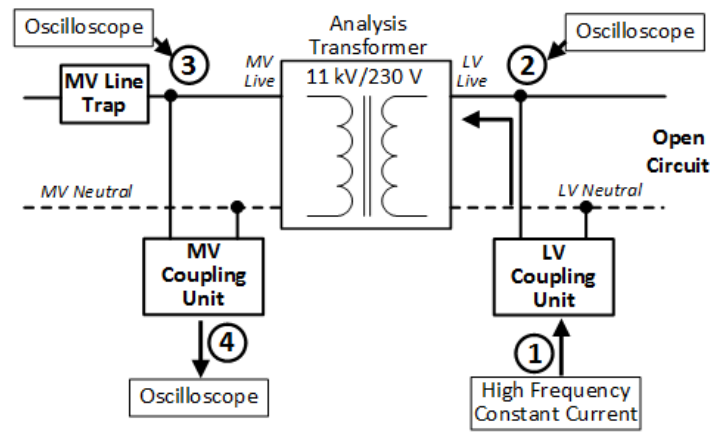


Figure 4.15 – Flow Direction and Measurement Points for LV to MV Signal Transfer through Analysis

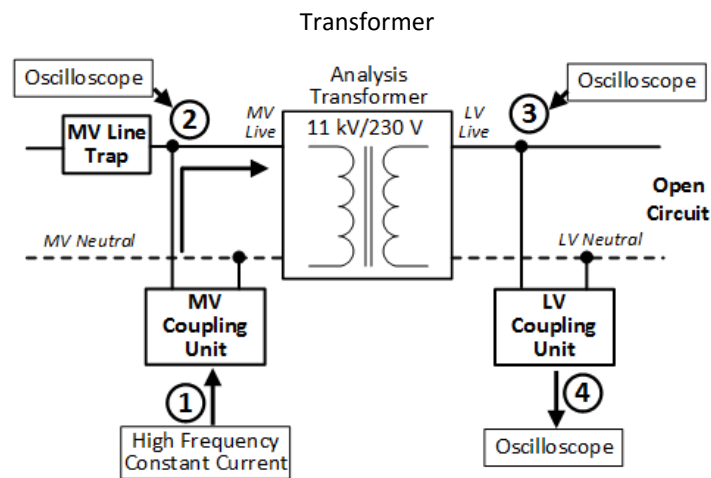


Figure 4.16 – Flow Direction and Measurement Points for MV to LV Signal Transfer through Analysis

Transformer

A periodic constant current source supplied the sinusoidal test waveforms at point **1** via a signal generator. The frequencies ranged from 30 to 150 kHz, in 5 kHz intervals, for a total of 25 frequency points. The waveforms were measured at the line coupling points **2** and **3**, and the final output at point **4**, using an oscilloscope.

The experimental procedure involved energizing the analysis transformer at five 50 Hz voltage levels, 0 V, 110 V, 190 V, 230 V and 255 V. At each designated energization level and frequency, the test signal was injected through the platform in the LV to MV and MV to LV direction. The dependent variables were the test signal voltage and current waveforms at point **4**. Additional dependent variables were the test signal frequency, and test signal total power input and output at points **2** and **3**. Measurements on the MV side of the analysis transformer were taken only while the platform was un-energized.

To establish causality between the observed dependent variables and the transformer energization, its 50 Hz energization voltage was taken as the independent variable. The value of this variable was manipulated using the variac. An experimental control, in the

form of a bypass of the energizing and analysis transformers, was used. This is shown in Figure 4.17. The experimental procedure was repeated for the control experiment, with current injection at point *I*, and measurements taken at point *2* and *3*.

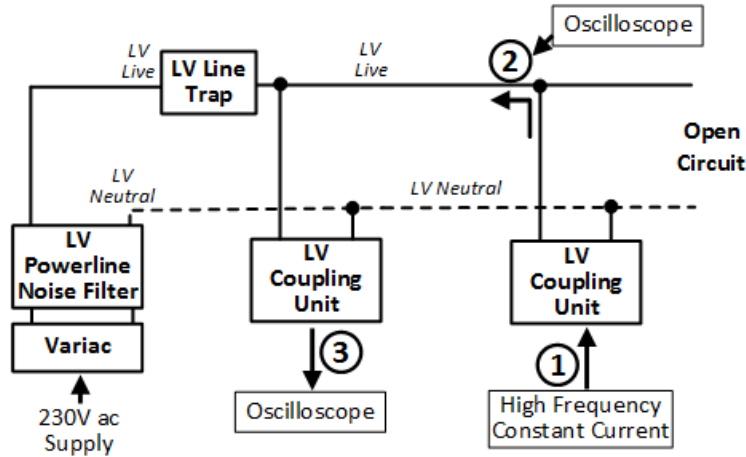


Figure 4.17 – Block Diagram of Experimental Platform with Transformers Bypassed

## 4.5 MV Line and Through-transformer NB-PLC Channel Model Estimation

This section describes the methods used in estimating the MV line and through-transformer NB-PLC channel models. The method used in determining the FRFs of the SWER and Two-wire MV lines is described in Section 4.5.1, the method used in determining the FRFs of the 1 kVA and 15 kVA through-transformer channels in the LV to MV and MV to LV directions is described in Section 4.5.2, and the method used in estimating the PLC channel models of the MV lines and unenergized through-transformer channels from their FRFs, using MATLAB, is described in Section 4.5.3.

### 4.5.1 Determination of SWER and Two-wire MV Line FRFs and ILs

The *ABCD* parameters for a 100 m and 1 km SWER MV line, made up of a Squirrel conductor, were determined from simulations of the hybrid model, for frequencies from 30 kHz to 250 kHz. A value of 10  $\Omega$ .m was used for soil resistivity and 10 for relative permittivity in the simulations. Equation (6) was then used to calculate the FRFs for the two SWER line lengths at the frequencies of interest, with equal source ( $Z_S$ ) and load ( $Z_L$ ) resistances of 50  $\Omega$ .

There are more Two-wire MV line PLC models available in literature, compared with SWER MV line models. Therefore, to provide a basis for the evaluation of the

performance of the SWER MV line model in PLC simulations, it was compared with an analytical model of a single-phase Two-wire MV line.

Equations (2) to (4) were used to calculate the resistance, loop inductance and line-to-line capacitance of a Two-wire line of equal lengths with the two SWER lines, made up of Squirrel conductors. A minimum clearance of 500 mm is required for power lines of less than 245 kV nominal voltage in New Zealand [170], and so this value was used for  $D$  in the calculations.

The **ABCD** parameters and FRFs for the Two-wire MV line were then determined from simulations of the line parameters, for frequencies from 30 kHz to 250 kHz, with equal source ( $Z_S$ ) and load ( $Z_L$ ) resistances of 50  $\Omega$ .

The insertion loss of the SWER and Two-wire line were also evaluated using equation (7), for 30 kHz to 250 kHz and 100 m length, with equal source ( $Z_S$ ) and load ( $Z_L$ ) resistances of 50  $\Omega$ .

#### **4.5.2 Determination of 1 kVA and 15 kVA Through-transformer Channel FRFs and ILs**

A periodic constant current source was used to empirically determine the **ABCD** parameters of the 15 and 1 kVA transformers in the lower NB frequency region, with the primary and secondary terminal pairs designated as ports [171]. Measurements were carried out between 30 kHz and 150 kHz inclusive, in steps of 5 kHz, with and without the transformer tank being electrically bonded to the LV neutral terminal.

The interpolation tool available in MATLAB was used to obtain a higher spectral content with fixed frequency steps from the original FRFs. The Piecewise Cubic Hermite Interpolating Polynomial (pchip) method was specified, due to its piecewise linear approximation routine, which gives good results depending on the length of the desired independent variable vector. The independent variable vector, in this case, was frequency, which was specified in equal steps of 1 Hz for the interpolated version.

#### **4.5.3 Estimation of MV Line and Unenergized Through-transformer PLC Channel Models**

The MATLAB System Identification Toolbox offers the option of identifying linear time invariant (LTI) systems directly from frequency domain data, which includes FRFs. Amongst a number of options, the FRFs may be initially specified as complex arrays, which are then imported into the toolbox for identification. Transfer function (TF)

representations were chosen for the final identified LTI transformer PLC channel models; the reason for this choice is explained in Section 6.4. The SWER and Two-wire MV line channel models of length 100 m and 1 km were obtained by using this process, giving a total of four MV line channel models for PLC simulations.

The measured transformer FRFs exhibit resonance phenomena as expected, therefore the process of estimating time-domain equivalent models involved a heuristic technique of predicting the number of poles and zeros of the desired transfer functions, within the desired bandwidth of 30 kHz to 150 kHz. This resulted in a higher number of poles and zeros for the estimated models of the through-transformer channels, in comparison with those of the MV lines. The 1 kVA and 15 kVA through-transformer channel models in the LV to MV and MV to LV directions were obtained by using this process, giving a total of four through-transformer channel models for PLC simulations.

## **4.6 MV Line and Through-transformer Channel NB-PLC Simulation**

The methods used in the simulation of the MV line and through-transformer PLC channel models, using various digital modulation methods contained in standard Simulink function blocks, are described in this section. The set-up for the MV line PLC simulation is described in Section 4.6.1, the set-up for the unenergized through-transformer channel PLC simulation is described in Section 4.6.2, and the set-up for the energized through-transformer channel PLC simulation is described in Section 4.6.3.

### **4.6.1 MV Line PLC Simulation Set-up**

The method set-up used for PLC simulation through the MV line NB-PLC models in Simulink is shown in Figure 4.18.



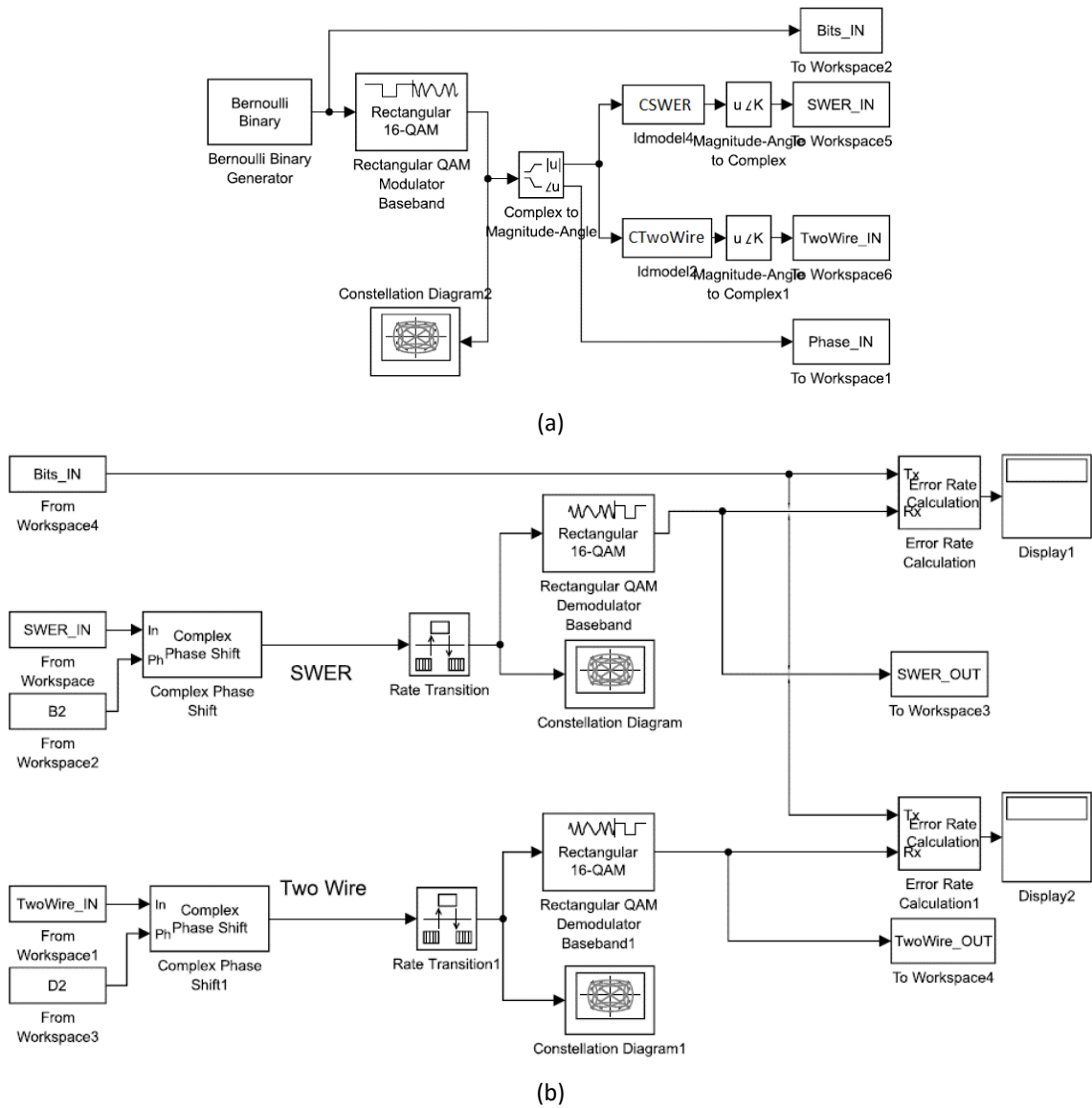


Figure 4.18 – Simulink Block Diagram for Medium Voltage Line PLC Simulation

In Figure 4.18 (a), the Bernoulli Binary Generator produced binary bit streams with equal probability for either bit. It required a sample time to be specified, which is directly related to the bit rate and carrier frequency. The Modulator block received the bit stream and executed the specified modulation at an average channel input power of 1 Watt, as measured at the input constellation map block connected to the modulator block. The complex modulated signal was then split into its magnitude and phase components.

The phase components of the complex modulated signals were sent to the MATLAB workspace to be stored as a vector of variables. The magnitude components were passed through the SWER and Two-wire channel models, reconstructed into their original complex number representations, and then sent to the MATLAB workspace as a vector of variables. The original bit stream was also sent to the MATLAB workspace as a vector of variables. Within the MATLAB workspace, the SWER and Two-wire channel phase



shifts due to a sinusoidal waveform at the simulation frequency were determined. These values were then placed into all the cells of vectors of the same size as those containing the modulated magnitude and phase variables. These vectors were then sent into the simulation space via blocks B2 and D2, shown in Figure 4.18 (b).

In figure 4.18 (b), phase angle offsets were applied to the modulated magnitude variables by the Complex Phase Shift block. Rate Transition blocks were also required to specify sample times for signals coming out of the PLC channels, which were continuous-time entities and hence had default sample times which would not correspond with those applicable to the simulation frequencies. After rate transition, simultaneous demodulation and constellation mapping was performed. The demodulated bits were connected to an error rate calculator that compared the original bit stream with the modulated versions and displayed the results.

The demodulated bits from the SWER and Two-wire channels were also sent to the MATLAB workspace, for further BER calculation and storage. The simulation model was therefore integrated with a MATLAB script for the purpose of implementing iterative simulation runs at various frequencies and processing the results. Hard decision decoding was selected for the demodulation blocks.

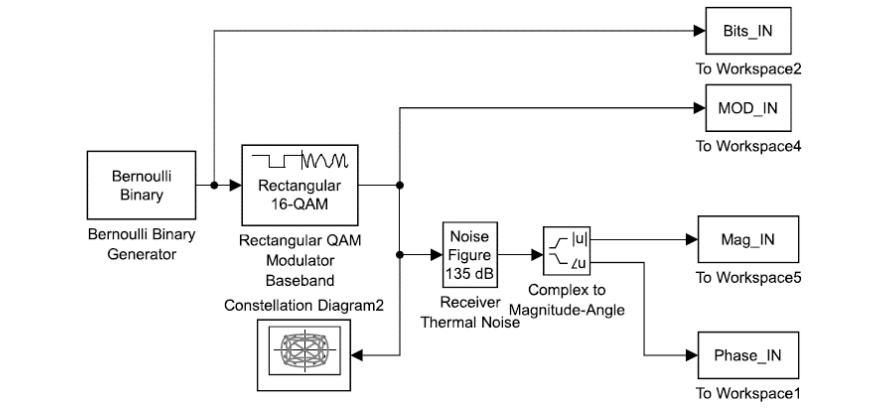
The simulation was set up primarily to compare the estimated MV line PLC channels of 100 m and 1 km length and therefore was not primed to consider real-life conditions such as noise and bit synchronization. The modulation/demodulation blocks shown in Figure 4.18 are for Quadrature Amplitude Modulation of 16 symbols (16QAM). Phase Shift Keying modulation of two symbols (BPSK), four symbols (QPSK) and eight symbols (8PSK) were also simulated.

#### **4.6.2 Unenergized Through-transformer Channel PLC Simulation Set-up**

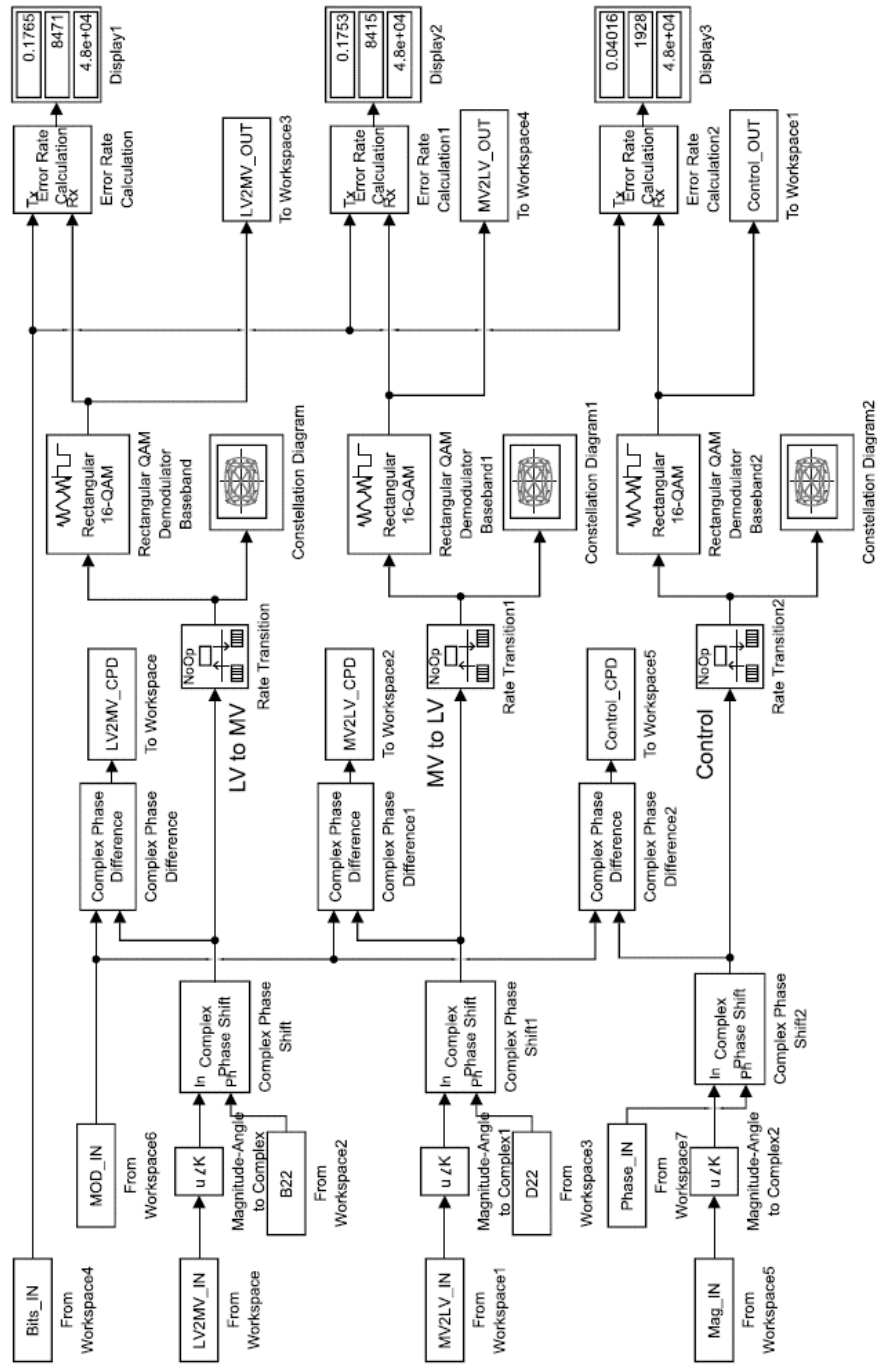
The method set-up for the simulation of unenergized through-transformer PLC channel models using Simulink is identical to that for the simulation of the MV line PLC channel models shown in Figure 4.18. The LV to MV model for the 1 kVA through-transformer channel was placed in idmodel 4, while the MV to LV model for the 1 kVA through-transformer channel was placed in idmodel 2. The simulations were repeated for the corresponding models of the 15 kVA transformer.

#### **4.6.3 Energized Through-transformer Channel PLC Simulation Set-up**

The method set-up for the simulation of the magnitude and phase angle variations of the 1 kVA energized through-transformer channels is shown in Figure 4.19.



(a)



(b)

Figure 4.19 – Simulink Block Diagram for Energized Through-transformer PLC Simulation

Differences exist between the set-up for the simulation of the energized through-transformer PLC channels and those for the MV line and unenergized through-transformer PLC simulations. The objective of the simulation of the energized through-transformer channels was to observe the effects of the magnitude and phase angle variations on PLC signal integrity. Therefore, the magnitude and phase angle variation values themselves represented the energized through-transformer channel characteristics in the simulations.

The presumption was that the simulation of the unenergized through-transformer channel transfer functions results in zero BER. This allowed the results obtained from the simulation of the magnitude and phase angle variations to be regarded as incremental values of the BER results of the unenergized through-transformer channels. The determination of the discrete magnitude and phase angle variations depends on the measured variations of the through-transformer channel and therefore are described in detail in Section 6.4.

The Receiver Thermal Noise block, which is shown in Figure 4.19 (a), injected just enough noise to reduce the  $E_b/N_0$  ratio to the level where a minimal BER for a 30 kHz BPSK modulated signal was produced. The noise figures used were 148 dB for BPSK, 145 dB for QPSK, 140 dB for 8PSK, and 136 dB for 16QAM. Directly after this operation, the complex modulated signal was then split into its magnitude and phase components, which were sent to the MATLAB workspace. In addition to the original bit stream, the complex modulated signal was also sent to the MATLAB workspace.

Within the MATLAB workspace, the discrete phase angle values of the energized through-transformer channels were processed and then placed into vectors of the same size as those containing the modulated phase variables. These vectors were then sent into the simulation space via blocks B22 and D22 shown in Figure 4.19 (b). Likewise, the magnitude ratios of the energized through-transformer channels were processed and then placed into vectors of the same size as those containing the modulated magnitude variables. These vectors were then sent into the simulation space via blocks LV2MV\_IN and MV2LV\_IN.

The Complex Phase Difference blocks, which are shown in Figure 4.19 (b), were used to determine the applicable complex phase differences between the original complex modulated waveform and the waveform coming through the energized through-transformer channel. These complex phase difference values were sent to the MATLAB

workspace for further calculation and storage, together with the results obtained from the previously described blocks.

A control channel was also included in this set-up to provide a basis for comparison, which takes the effect of the introduced channel noise into consideration, for BER comparison. As such, the BER figures obtained were termed as incremental BERs.

The complex phase differences of the energized through-transformer PLC channels in the LV to MV and MV to LV direction were compared with those from the control channel, whereby values falling within a tolerance of  $\pm 0.0156$  were correlated as being equal and allocated a value of one. These correlated values, termed incremental complex phase difference correlation coefficients, provided a measure of the effects of the applied phase variations due to energization.

A minimum simulation time of 0.02 seconds was used, to ensure that the entire energization variation values were fully applied to the PLC waveforms.

#### **4.7 Conclusion**

This chapter provided a description of the methods that were used in carrying out the various experimental and analytical tasks for the research. Descriptions of the empirical and analytical methods used for obtaining the characteristics of the SWER MV line in the lower NB-PLC frequency region were provided. In particular, details of the procedures for the developed method for earth path characterization were provided. Descriptions of the methods used in obtaining the through-transformer characteristics of the 0.5 kVA, 1 kVA and 15 kVA transformers in the lower NB-PLC frequency region were also provided.

As the research included questions involving PLC, descriptions of the methods used in estimating the NB-PLC models of the SWER MV line and through-transformer channels of the 1 kVA and 15 kVA transformers, as well as the methods used in carrying out PLC simulations of the estimated models, were also provided.

# Chapter Five – SWER Medium Voltage Line NB-PLC Characterization Results

## 5.1 Introduction

Power lines are the principal grid components for PLC implementation, and therefore, it is important to determine the impedances of the conductors that make up such power lines, within the desired frequency range. The analytical determination of the impedance of regular power conductors is straightforward, but this is not the case for the earth path, which constitutes the return conductor for SWER MV lines.

The results of the SWER MV line characterization experiment, which include the experiments for earth return path characterization, are provided in this chapter. These results form the foundation for the first thesis contribution, namely the development of a hybrid empirical/analytical method for earth path characterization, inclusive of the earthing system and additional impedances due to superfluous material.

The results of the earth rod ZOI determination are provided in Section 5.2, the results for the iterative determination of the measured platform impedance are given in Section 5.3, the results of the derivation of the earth path impedance are detailed in Section 5.4, and the results of the voltage drop measurements, and the subsequent derivation of the earth path impedance scaling factor, are given in Section 5.5.

The results of the analytical and hybrid SWER MV line characterization are detailed in Sections 5.6 and 5.7 for constant and frequency-dependent soil parameters respectively, the result of the comparison of Squirrel and Flounder aerial conductors is given in Section 5.8, and the conclusion is given in Section 5.9.

## 5.2 Determination of Rod ZOI

The results for the second part of the experiment outlined in Section 4.2.2, i.e. determination of rod ZOI, are summarized in Figure 5.1 for  $d = 1.8$  meters.

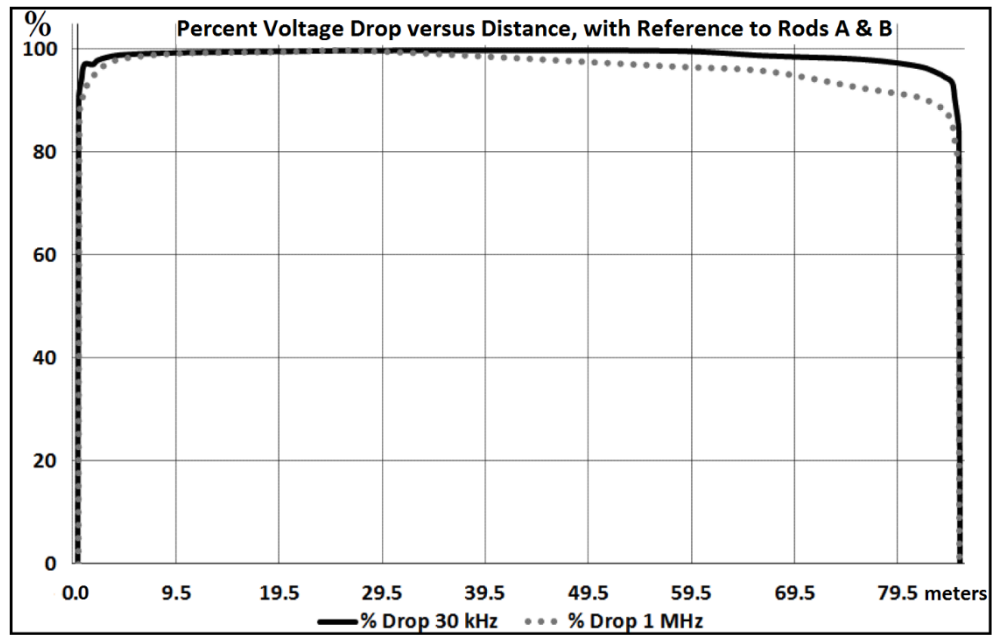


Figure 5.1 – Percent Voltage Drop versus Distance  $z$ , with Reference to Rods A and B, for  $d = 1.8$  m

The voltage drop plots of Figure 5.1 show that between 30 kHz and 1 MHz, the ZOI for each rod is within 3 m radius. The plots also show a higher voltage drop per unit length towards location A than location B. This can be attributed to a building located at this end, which indicates the presence of artificial building material within the soil that is not favourable to current flow of frequency between 30 kHz and 1 MHz. The voltage drops are also inversely proportional to signal frequency, indicating the presence of a capacitive reactance, as expected [158].

### 5.3 Correlation of Measured Platform Impedances

The results obtained from the first and third part of the earth path experiment, i.e. the determination of total impedance of the full and control length of the earth path respectively, are summarized in Figures 5.2 and 5.3.

The measured impedance magnitude plots for the total length  $L_T$  of the earth path for injection rod depth  $d$  of 0.5m (Mag 0.5d Mea), 1.0m (Mag 1.0d Mea) and 1.8m (Mag 1.8d Mea) are shown in Figure 5.2. The measured impedance magnitude plots for the control length  $L_C$  of the earth path are also shown in Figure 5.2, for injection rod depth  $d$  of 1.0m (Mag 1.0d Mea Control). The frequencies ranged from 30 Hz to 1 MHz.

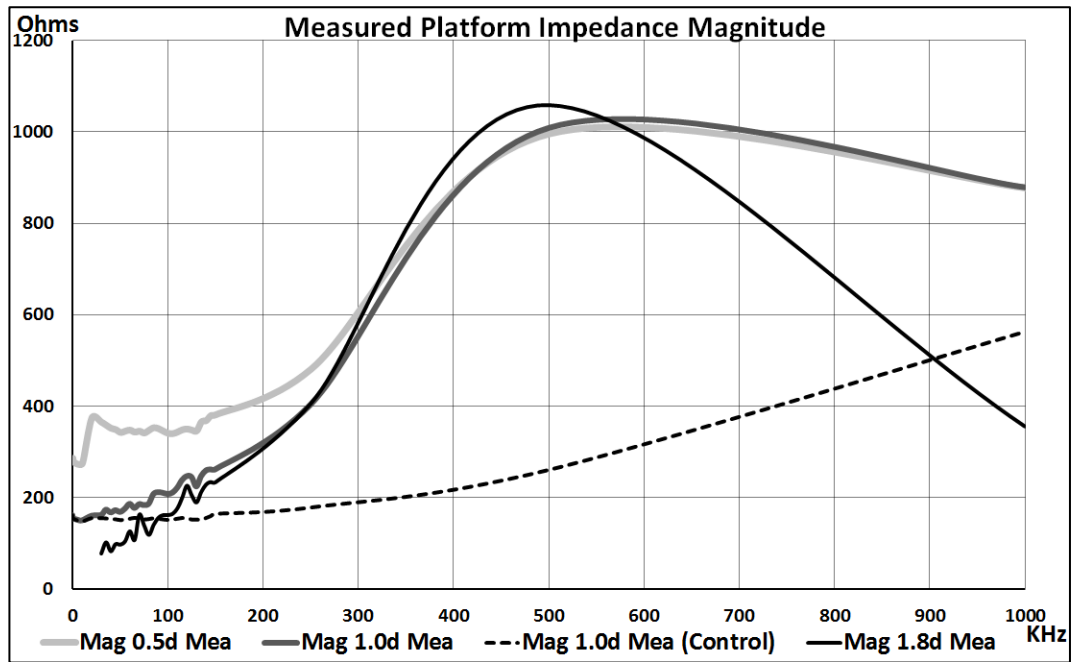


Figure 5.2 – Magnitude (Mag) Plots of Measured (Mea) Platform Impedance for  $d=0.5\text{m}$ ,  $1.0\text{m}$  and  $1.8\text{m}$

The measured impedance phase plots for the total length  $L_T$  of the earth path for injection rod depth  $d$  of  $0.5\text{m}$  (Ph 0.5d Mea),  $1.0\text{m}$  (Ph 1.0d Mea), and  $1.8\text{m}$  (Ph 1.8d Mea), are shown in Figure 5.3. The measured impedance phase plots for the control length  $L_C$  of the earth path are also shown in Figure 5.3, for injection rod depth  $d$  of  $1.0\text{m}$  (Ph 1.0d Mea Control). The frequencies ranged from  $30\text{ Hz}$  to  $1\text{ MHz}$ .

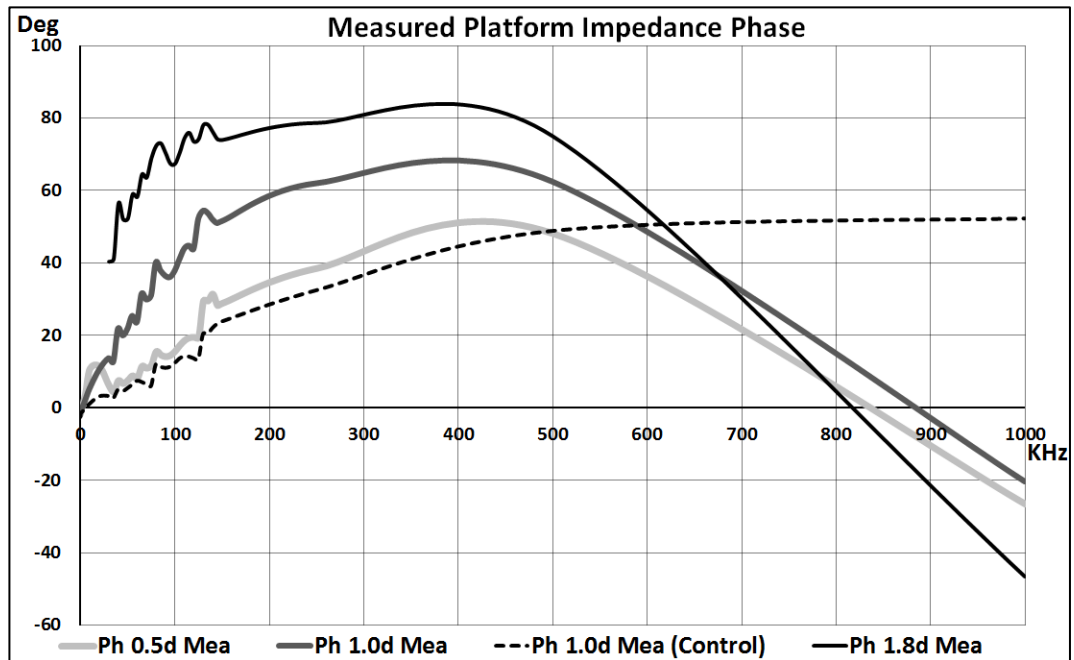


Figure 5.3 – Phase (Ph) Plots of Measured (Mea) Platform Impedance for  $d=0.5\text{m}$ ,  $1.0\text{m}$  and  $1.8\text{m}$

The results for rod depth  $d$  of  $0.5\text{ meters}$  show an impedance magnitude (Mag 0.5d Mea) of approximately  $280\ \Omega$  at  $30\text{ Hz}$ , which slowly reduces with frequency up to  $10\text{ kHz}$  but

increases rapidly between approximately 10 kHz and 20 kHz to 380  $\Omega$ . Between 20 kHz and 100 kHz, it further reduces to approximately 250  $\Omega$ , after which it increases to approximately 1 k $\Omega$  at 560 kHz. After this point, the magnitude decreases approximately linearly to 890  $\Omega$  at 1 MHz. The magnitude characteristics between 10 kHz and 100 kHz are inconsistent, which may be attributed to the poor rod contact with the soil because the magnitude ought to steadily increase up to a certain point, which depends on the total platform capacitance. This assertion is supported by the large peak in the phase plot (Ph 0.5d Mea) between approximately 30 Hz and 30 kHz, with centre at approximately 10 kHz, which indicates frequency-dependent behaviour.

The results for  $d = 1.0$  meters show an impedance magnitude (Mag 1.0d Mea) of approximately 160  $\Omega$  at 30 Hz, which also slowly reduces with frequency up to approximately 10 kHz. Beyond this point, it increases to approximately 1.03 k $\Omega$  at 560 kHz. After this point, the magnitude also decreases approximately linearly to 890  $\Omega$  at 1 MHz. The trend of the phase plot (Ph 1.0d Mea) remains consistent, without any indications of resonance behaviour. These results show less earth path impedance, which may be directly attributed to the increased rod depth which gives improved contact between the rod and soil.

The results for  $d = 1.8$  meters and frequency ranging from 30 kHz to 1 MHz show an impedance magnitude (Mag 1.8d Mea) of approximately 100  $\Omega$  at 30 kHz, which increases to approximately 1.07 k $\Omega$  at 500 kHz. After this point, the magnitude decreases approximately linearly to 360  $\Omega$  at 1 MHz. The trend of the phase plot (Ph 1.8d Mea) also remains consistent, without any indications of resonance behaviour. However, it shows a marked increase in inductive reactance at the lower frequency region and a marked increase in capacitive reactance at the higher frequency region. This may be attributed to the use of the 1:2 ratio high frequency transformer, to reduce output voltage and increase output current from the constant current source. These results show even less earth path impedance, which may again be directly attributed to improved contact between the earth rods and soil at greater rod depth.

The control experiment results are for a short length  $L$  of 20 meters from point A, which gives enough clearance for avoiding the ZOI of both rods. While it will be expected that the impedance magnitude for this short section will be approximately a quarter of the value for the full path length of 85.5 meters, between 30 Hz and 20 kHz the Mag 1.0d Mea (Control) plot and the Mag 1.0d Mea plot are approximately equal. This may be attributed to the disproportionate earth impedances within the soil at the locations of the



rods, as indicated from the results of ZOI determination shown in Figure 5.1. This confirms the presence of superfluous material which increases the impedance at the region of rod A.

Also, judging from the differences in the phase plots of Ph 1.0d Mea (Control) and Ph 1.0d Mea, the inductance is less than that for the full length at the same depth, but still significant. However, the shunt capacitive reactance values are much less, preventing resonance prior to 1 MHz, unlike the full-length cases. The reduced earth path and supply cable lengths also result in reduced resistance. These reduced capacitive reactance and resistance values are responsible for the gradual increase in magnitude as shown by Mag 1.0d Mea (Control), which is largely attributed to inductance.

## 5.4 Derivation of Earth Path Impedance

The results obtained from the iteration process for estimating the values of the earth path impedance, in accordance with the earth path impedance measurement schematic diagram shown in Figure 4.2, are given in Table 5.1.

Table 5.1 – Results of Iterations for Deriving Circuit Element Values

$d$ (m)	$L_C$	$R_{SE}$	$C_{SH}$	$R_{SH}$	$C_E$	$R_{LOSS}$
0.5	$300 \mu H$	$170 \Omega$	$450 pF$	$850 \Omega$	$3.75 nF$	$180 \Omega$
1.0	$143 \mu H$	$2 \Omega$	$300 pF$	$700 \Omega$	$4.91 nF$	$70 \Omega$
1.8	$135 \mu H$	$2 \Omega$	$300 pF$	$700 \Omega$	$22.3 nF$	$28 \Omega$

From Table 5.1, it can be seen that virtually all the  $L_C$  and  $Y_{SH}$  i.e.  $C_{SH}$  and  $R_{SH}$ , may be attributed to the supply cable. From 0.5 to 1.0 m depth, the earth path is deeper and therefore  $Y_{SH}$ , and  $L_C$  reduce with depth, as expected.  $R_{SE}$ ,  $C_E$  and  $R_{LOSS}$  also behave as expected, reducing with depth. The control experiment required less cable length than for the main experiments, as it covered a smaller distance of 20 meters. Also, the impedance plots which are given in Figures 5.2 and 5.3 further support the observation that  $Y_{SH}$  and  $L_C$  are largely due to the cable.

Figures 5.4 and 5.5 summarize the comparisons between the measured impedance plots and those obtained from simulations of the earth path impedance measurement schematic diagram shown in Figure 4.2, for frequencies from 30 kHz to 250 kHz. The estimated values of Table 5.1 were used for the designated rod depths.

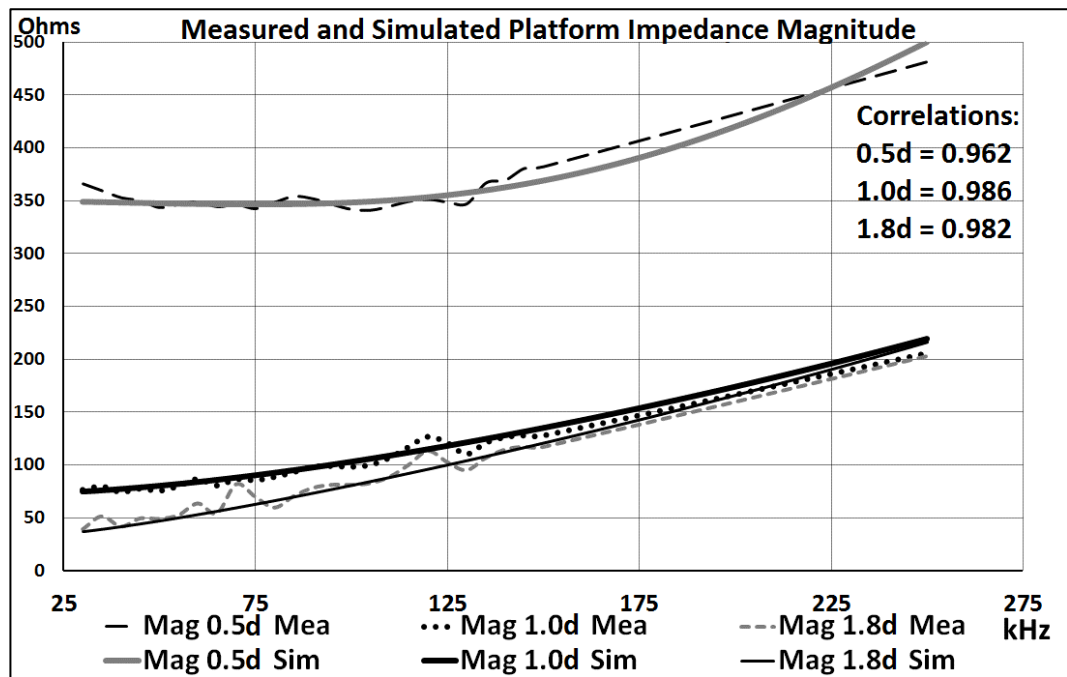


Figure 5.4 – Magnitude Plots of Measured (Mea) and Simulated (Sim) Platform Impedance for  $d = 0.5\text{m}$ ,  $1.0\text{m}$  and  $1.8\text{m}$ ; 30 kHz - 250 kHz

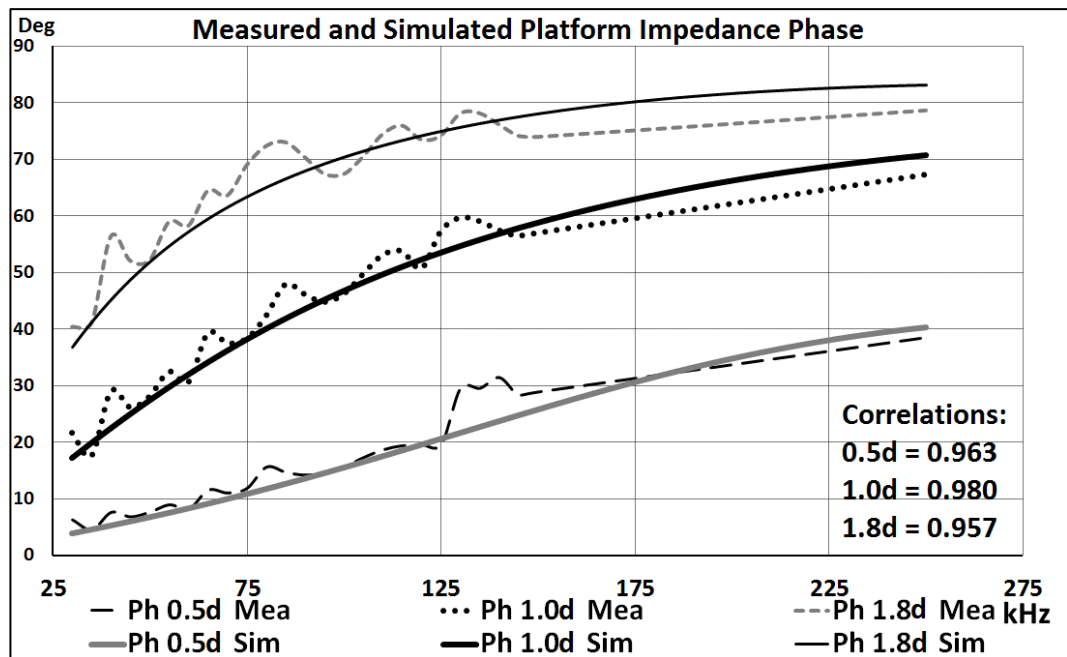


Figure 5.5 – Phase Plots of Measured (Mea) and Simulated (Sim) Platform Impedance for  $d = 0.5\text{m}$ ,  $1.0\text{m}$  and  $1.8\text{m}$ ; 30 kHz - 250 kHz

There is good agreement between the simulated and measured results, as quantified by the given correlation coefficients. However, as can be seen from the plots, the measured and simulated impedance values correspond less as  $f$  increases, especially for the cases of shallow current injection depth. This is mainly due to shunt capacitive effects, which are distributed in nature and difficult to represent as lumped elements with increased

frequency. However, the minimum correlation coefficient values of 0.982 and 0.957 for the magnitude and phase plots respectively confirm that the earth path impedance values of Table 5.1 accurately represent the earth path impedances at the various rod depths, between 30 kHz and 250 kHz.

## 5.5 Derivation of Earth Path Impedance Scaling Factor from $V_{drop}$ Results

The results for the fourth part of the experiment, i.e. voltage drop ( $V_{drop}$ ) measurement, are summarized in Figures 5.6 and 5.7, for frequencies from 30 kHz to 1 MHz.

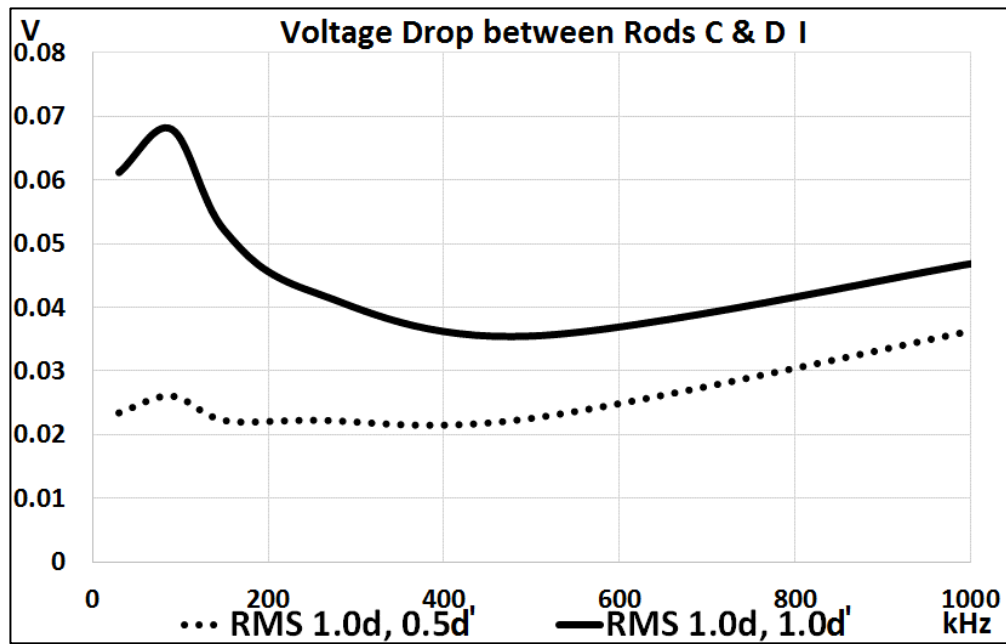


Figure 5.6 – RMS  $V_{drop}$  versus  $f$  for 9.5 meter Earth Section for  $d = 1.0$  m; 30 kHz to 1 MHz

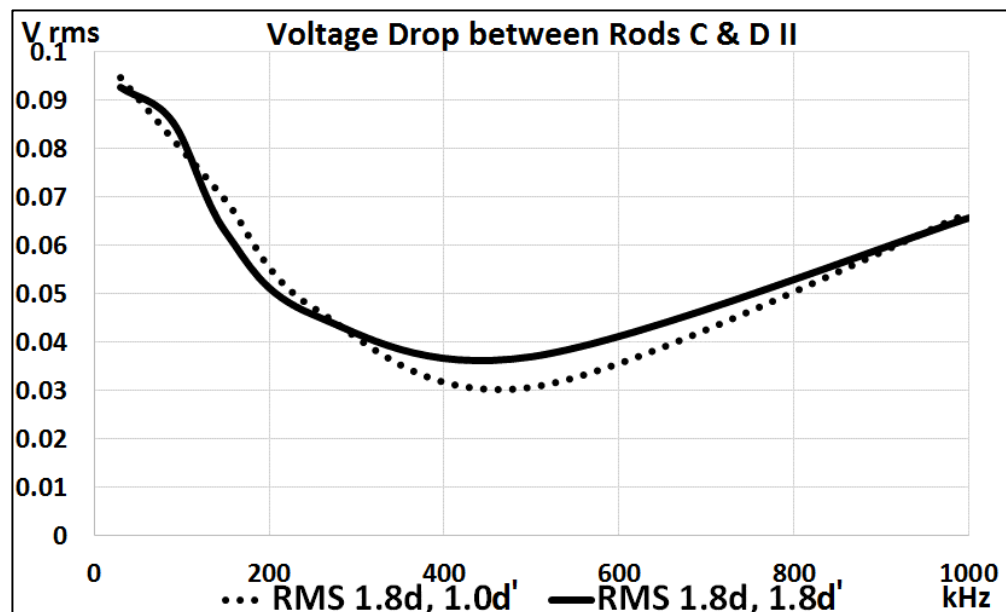


Figure 5.7 – RMS  $V_{drop}$  versus  $f$  for 9.5 meter Earth Section for  $d = 1.8$  m; 30 kHz to 1 MHz

The plots are for  $x = 9.5\text{m}$ , between rods  $C$  and  $D$  at 38m and 47.5m from rod  $A$  respectively, for  $d' = 0.5, 1.0$  and  $1.8\text{m}$ , and  $d = 1.0$  and  $1.8\text{m}$ , as shown in the diagram of the experimental platform given in Figure 4.1. The plots for equal injection and measurement rod depths (RMS  $1.0d, 1.0d'$  and RMS  $1.8d, 1.8d'$ ) reveal changes in trend at approximately 80 kHz, with the  $d' = 1.8\text{m}$  plot showing fewer changes. The RMS  $1.0d, 0.5d'$  plot also shows this effect, but the RMS  $1.8d, 1.0d'$  does not. These differences confirm that a relationship exists between injection and measurement rod depths for earth current flow measurement [172]. The plots also show that the earth path impedance remains either fairly consistent or reduces with frequency up to a certain point, after which it increases with frequency.

The difference in the shape of the plots of Figure 5.6 compared with those of Figure 5.7 reveal that the deeper the earth rods, the better the current flow is confined to a defined path within the earth [163], resulting in plots with predictable trends. This is supported by the close similarities of the plots of Figure 5.7, which confirm that the injection rod depth dictates the current flow path depth and by extension, the effective earth path impedance, to a large extent.

The values of  $Z_E$  for  $d = 1.8\text{ m}$  in Table 5.1 were simulated with  $L_C = 5\text{ }\mu\text{H}$ ,  $R_{SH} = 2\text{ }\Omega$  and  $C_{SH} = 14\text{ nF}$ , which were obtained from iterations with initial values that are consistent with those of an insulated cable on the earth's surface, to obtain  $V_{A-B}$  from 30 kHz to 250 kHz. These values of  $V_{A-B}$  were then directly compared with the measured  $V_{drop}$  values for  $d' = 1.0\text{m}$  and  $1.8\text{m}$  summarized in Figure 5.7. The simulation results for  $V_{A-B}$  correlate strongly with the measured  $V_{drop}$  values. A comparison of the two measured quantities with the simulated values gave a correlation coefficient of 0.96 and 0.94 for  $d' = 1.0\text{m}$  and  $1.8\text{m}$  respectively, as shown in Figure 5.8.

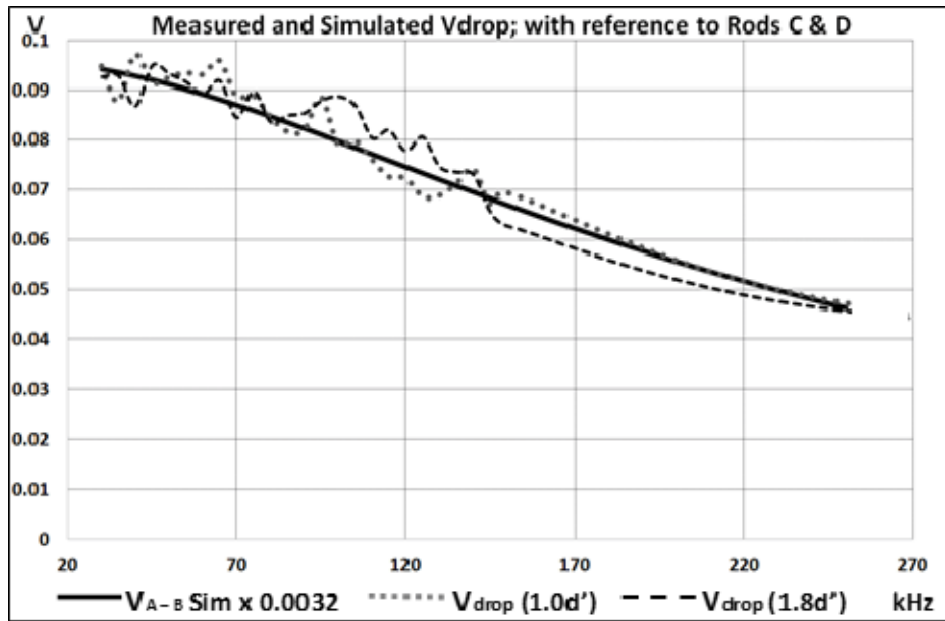


Figure 5.8 – Measured and Simulated  $V_{drop}$  versus  $f$ ; Simulated Value Scaled by 0.0032; 30 kHz to 250 kHz

These results help in the verification of the earth path characterization method and indicate that indeed the total earth path impedance  $Z_E$  can be represented by the values of  $R_{SE}$ ,  $C_E$ , and  $R_{LOSS}$  for  $d = 1.8$  in Table 5.1. In accordance with equation (25), the proportionality is represented by the scaling factor  $F$  of 0.0032, which is applied to the simulated  $V_{A-B}$  plot to line it up with the  $V_{drop}$  plots of Figure 5.8. The scaling factor, therefore, provides a means of using the voltage drop measurements to determine the earth path impedance, for similar measurement platforms.

## 5.6 Analytical and Hybrid SWER MV Line Characterization with Constant Soil Parameters

Table 5.2 gives the calculated element values for Squirrel and Flounder conductors, as well as the calculated contribution of the earth return path  $Z_{epul}$ , at 90 kHz centre frequency.

Table 5.2 – Calculated per-unit length (meters) SWER Line Parameters

Aerial Conductor						Earth Path @ 90 kHz		
Squirrel			Flounder			for $\rho_e =$	$\gamma_e$	$Z_e (\Omega)$
$R_c$	$L_c$	$Cc-e$	$R_c$	$L_c$	$Cc-e$	10	$0.626 + j0.63$	$0.231 + j0.278$
91.44 m $\Omega$	2.365 $\mu$ H	7.032 pF	103.6 m $\Omega$	2.375 $\mu$ H	7.017 pF	100	$0.193 + j0.204$	$0.515 + j0.774$

The values given in Table 5.2 for the Squirrel conductor were simulated in NI Multisim using the analytical per-unit length SWER transmission line model representation of a

SWER line given in Figure 3.1, for a short-circuit condition applied across OUT 1 – OUT 0, to obtain the short-circuit impedance of the line [173].

Figures 5.9 and 5.10 compare the magnitude and phase plots obtained from the simulation with those from the *B* and *D* measurement on the experimental line with the Squirrel conductor, for  $f = 30$  kHz to 250 kHz and  $L = 85.5$  m.

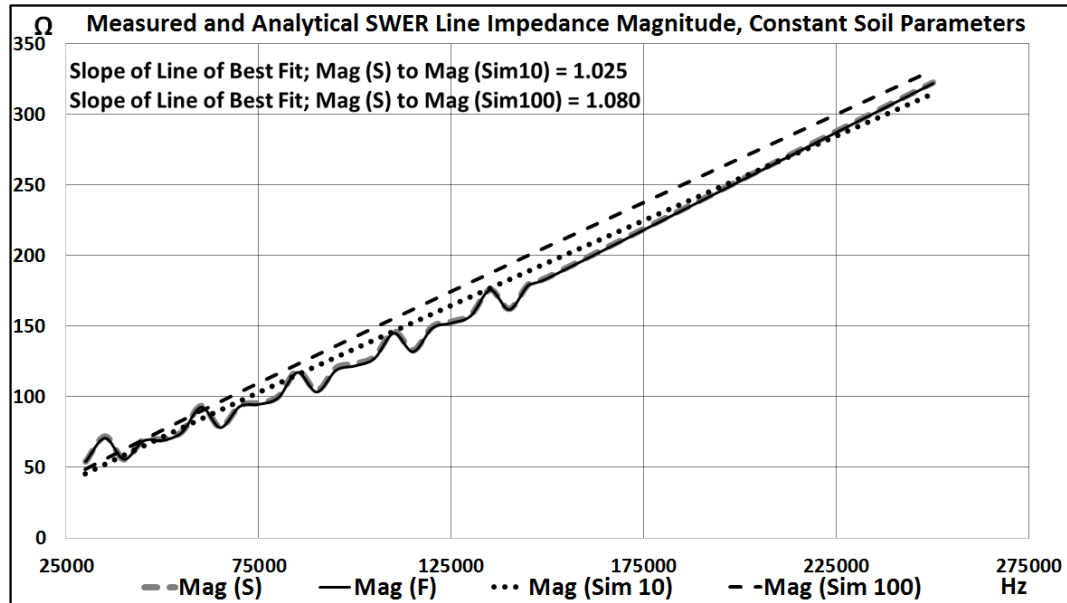


Figure 5.9 – SWER Line  $Z_{in}$  (Mag) vs.  $f$ ; Measured with Squirrel (S) and Flounder (F); Simulated with Analytical Model for  $\rho = 10$  (Sim 10) and 100 (Sim 100)

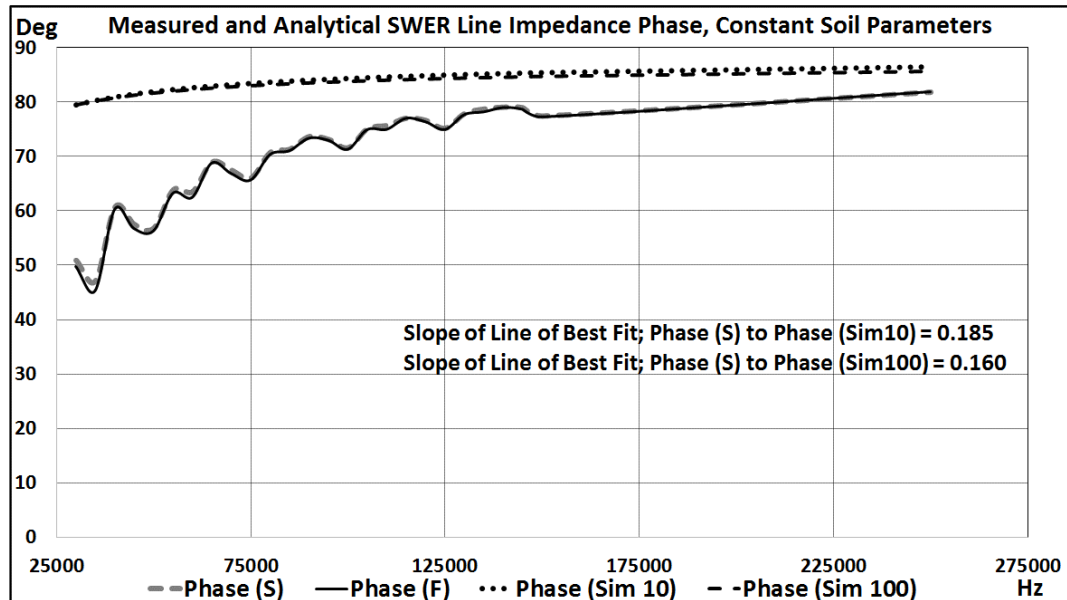


Figure 5.10 – SWER Line  $Z_{in}$  (Phase) vs.  $f$ ; Measured with Squirrel (S) and Flounder (F); Simulated with Analytical Model for  $\rho = 10$  (Sim 10) and 100 (Sim 100)

The plots show that, although the magnitude of the analytical model's impedance corresponds with that of the measured results, the phase plots do not. As the impedance

characteristics of the Squirrel conductor are essentially the same as those of the Flounder conductor, as shown in Section 5.8, the slope of the line of best fit between the measured results of the SWER line with the Squirrel conductor connected, and the simulation results, were determined. The slope for the measured versus simulated impedance magnitude is 1.025 and 1.08 for soil resistivity of 10 and 100 respectively, while that for the impedance phase is 0.185 and 0.16 for soil resistivity of 10 and 100 respectively.

The simulation was repeated using the hybrid per-unit length SWER transmission line model representation of a SWER line shown in Figure 4.4, with the element values for the earth path model corresponding to those for  $d = 1.8$  m in Table 5.1. Figures 5.11 and 5.12 compare the magnitude and phase plots obtained from this hybrid model simulation with those from the *B* and *D* measurement on the experimental line with the Squirrel conductor.

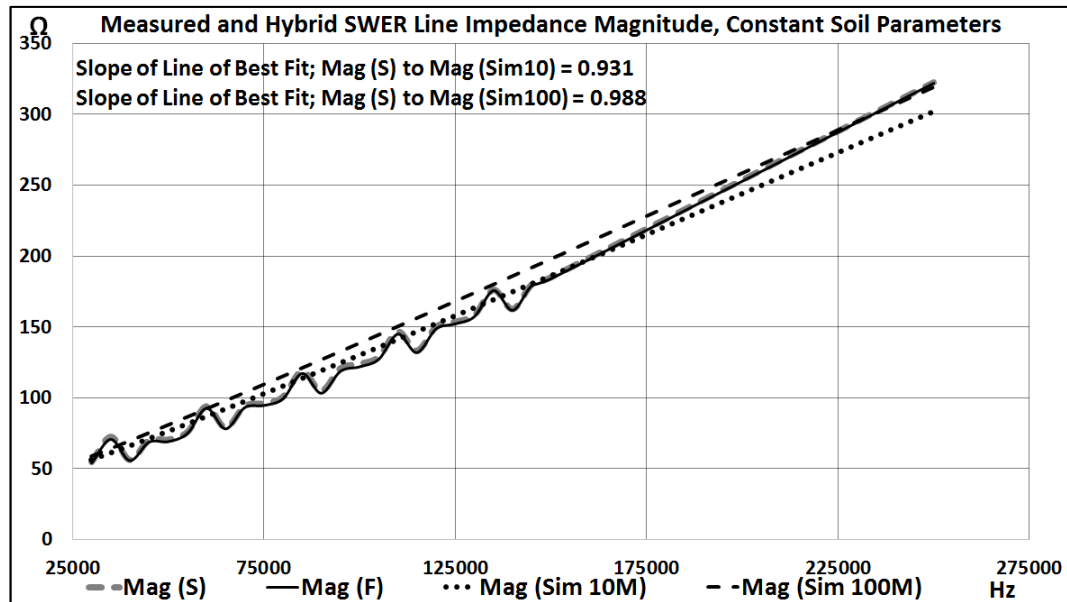


Figure 5.11 – SWER Line  $Z_{in}$  (Mag) vs.  $f$ ; Measured with Squirrel (S) and Flounder (F); Simulated with Hybrid Model for  $p = 10$  (Sim 10M) and 100 (Sim 100M)

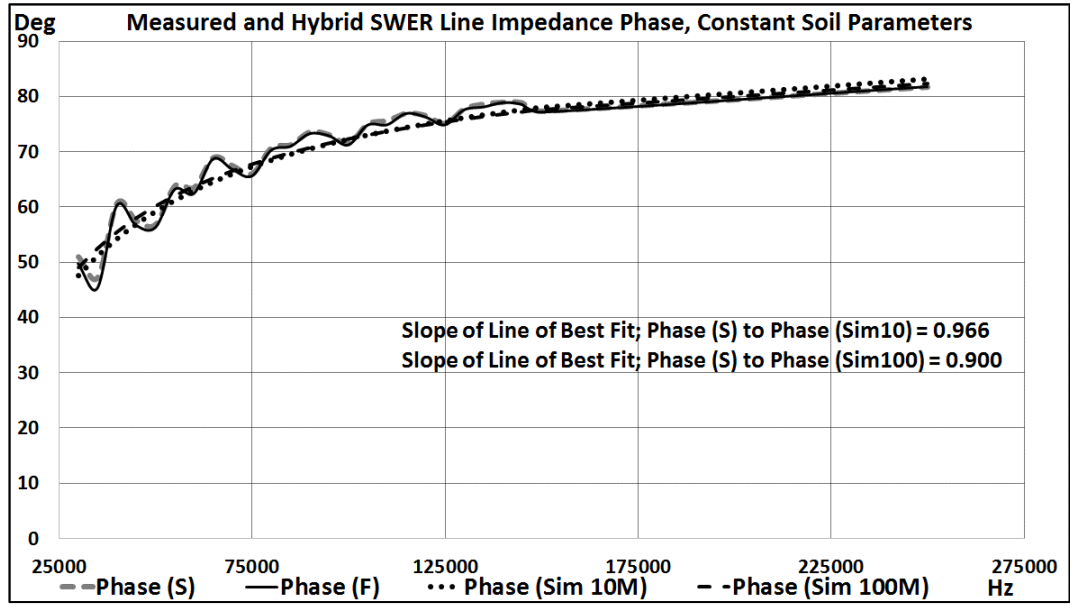


Figure 5.12 – SWER Line  $Z_{in}$  (Phase) vs.  $f$ ; Measured with Squirrel (S) and Flounder (F); Simulated with Hybrid Model for  $p = 10$  (Sim 10M) and 100 (Sim 100M)

Both the magnitude and phase plots correspond to a high degree. The slope of the line of best fit between the measured and simulated impedance magnitude is 0.931 and 0.988 for soil resistivity of 10 and 100 respectively, while that for the impedance phase is 0.966 and 0.9 for soil resistivity of 10 and 100 respectively. A comparison between the slopes of the results for the analytical and hybrid models reveals that the magnitude plots closely agree while the phase plots do not. This establishes that the analytical model based on equations for determining transmission line parameters with earth return paths does not closely represent the characteristics of this SWER line as accurately as the hybrid model does, for the frequency range  $f = 30$  kHz to 250 kHz.

## 5.7 Analytical and Hybrid SWER MV Line Characterization with Frequency-dependent Soil Parameters

The previous simulation of the analytical SWER line model was done with a constant value of relative permittivity of 10 and soil resistivity of 10  $\Omega \cdot m$  and 100  $\Omega \cdot m$ . The use of models to include the frequency-dependent nature of soils in the calculation of earth path impedance characteristics at high frequencies was also investigated. Six of such models described in detail in [174], namely the Scott (S), Smith and Longmire (SL), Messier (M), Visacro and Portela (VP), Portela (P) and Visacro and Alipio (VA) models, were applied to the simulation of the analytical SWER line model for total impedance. The results for frequencies of 30 Hz to 250 kHz are summarized in Figures 5.13 and 5.14.



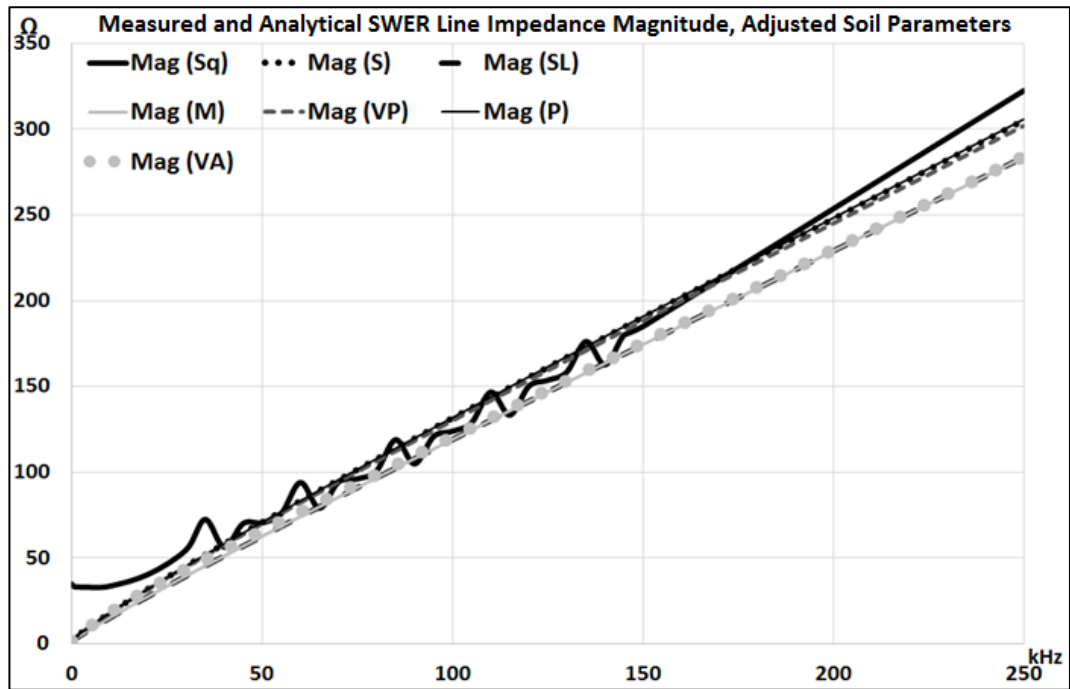


Figure 5.13 – SWER Line  $Z_{in}$  (Mag) vs.  $f$ ; Measured with Squirrel (Sq); Simulated with Analytical Model Adjusted for Frequency-Dependency with Models S, SL, M, VP, P, and VA

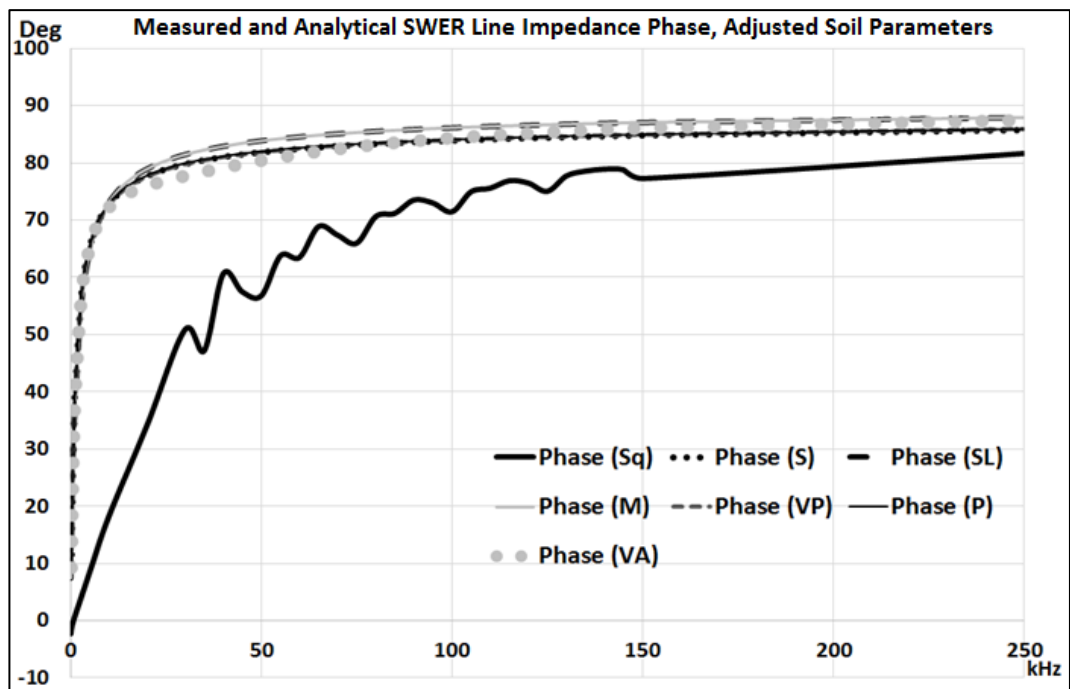


Figure 5.14 – SWER Line  $Z_{in}$  (Phase) vs.  $f$ ; Measured with Squirrel (Sq); Simulated with Analytical Model Adjusted for Frequency-Dependency with Models S, SL, M, VP, P and VA

As was previously found for the constant permittivity and resistivity cases shown in Figures 5.9 and 5.10, the simulated impedance magnitude plots correspond to varying degrees with the measured plot, in the lower NB-PLC frequency region. However, the simulated phase plots still do not agree. This further proves that the existing analytical

methods of determining earth path impedance characteristics are not sufficiently accurate to produce PLC channel models of SWER lines, due to the influences of the earthing system and superfluous components within the soil.

The phase plots of Figure 5.14 show that the Visacro and Alipio (VA), Scott (S) and Portela (P) models are marginally closer to the measured phase values. However, the magnitude plots of Figure 5.13 show that the Portela (P) model offers the closest fit overall. Therefore, this model was applied to the simulation of the hybrid SWER line model for total impedance. The results for 30 Hz to 250 kHz are summarized in Figures 5.15 and 5.16.

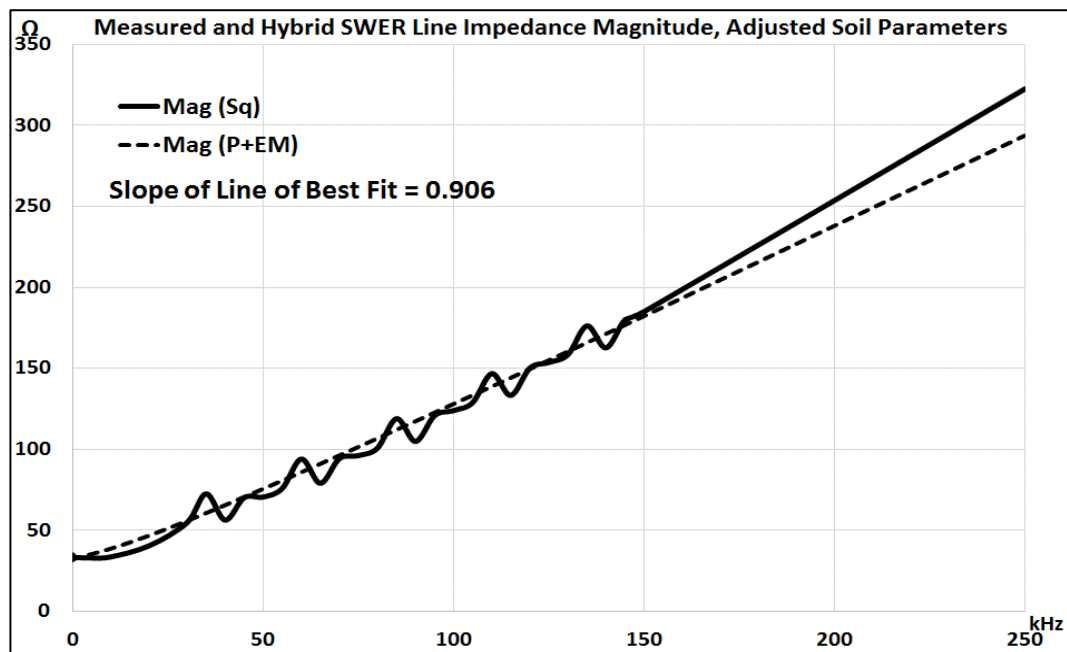


Figure 5.15– SWER Line  $Z_{in}$  (Mag) vs.  $f$ ; Measured with Squirrel (Sq); Simulated with Hybrid Model Adjusted for Frequency-Dependency with Model (P+EM)

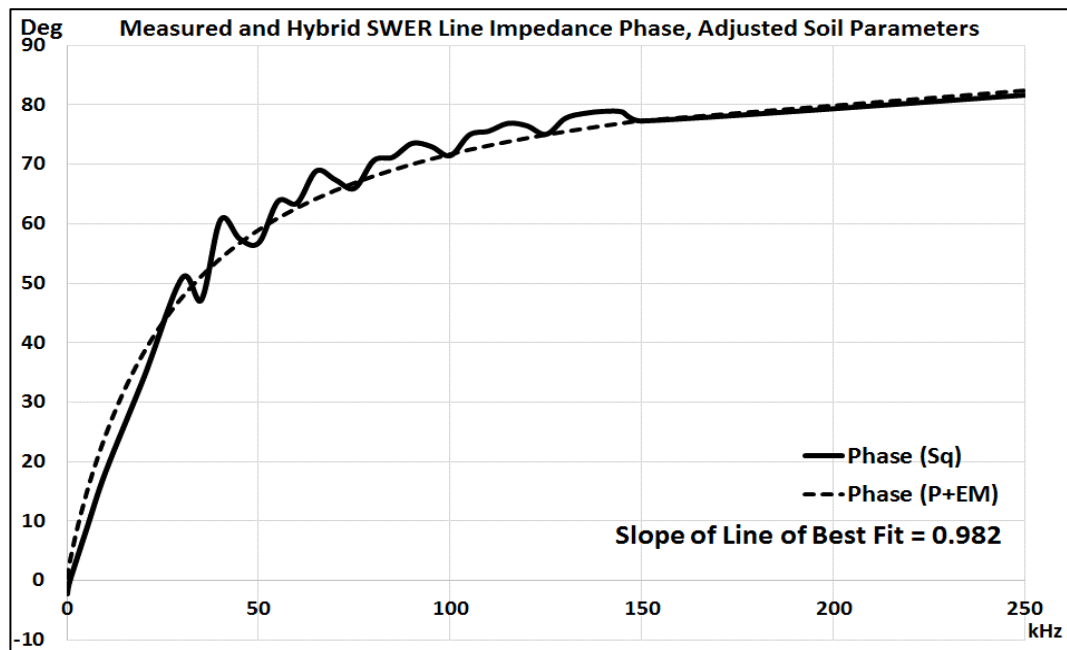


Figure 5.16 – SWER Line  $Z_{in}$  (Phase) vs.  $f$ ; Measured with Squirrel (Sq); Simulated with Hybrid Model Adjusted for Frequency-Dependency with Model (P+EM)

Table 5.3 summarizes the slope of the line of best-fit values for the simulation results in comparison with the measured results, with constant and frequency-dependent permittivity and resistivity.

Table 5.3 – Slope of Line of Best Fit Values for SWER Model Simulation Results

		<b>Analytical Model</b> Constant Parameters, $\epsilon_r = 10$	<b>Hybrid Model</b> Constant Parameters, $\epsilon_r = 10$	<b>Hybrid Model</b> Frequency-dependent Parameters, starting $\epsilon_r = 10, \rho = 10$
Magnitude Plots	$\rho=10$	1.03	0.93	0.91
	$\rho=100$	1.08	0.99	
Phase Plots	$\rho=10$	0.19	0.97	0.98
	$\rho=100$	0.16	0.90	

The slopes of the line of best fit for the hybrid results with constant resistivity and permittivity shown in Figures 5.11 and 5.12 are closer to those for the hybrid results with frequency-dependent resistivity and permittivity shown in Figures 5.15 and 5.16, compared with those for the analytical results shown in Figures 5.9 and 5.10.

The magnitude plots of Figures 5.15 and 5.11 for resistivity of  $10 \Omega.m$  are virtually identical, as evidenced by their approximately equal slope values of 0.93 and 0.91 respectively. The phase plots of Figures 5.16 and 5.12 for resistivity of  $10 \Omega.m$  are also virtually identical, as evidenced by their approximately equal slope values of 0.98 and 0.97 respectively. Therefore, it can be concluded that the application of frequency-

dependent models for permittivity and resistivity does not significantly improve the performance of the analytical model, and also does not improve the accuracy of the hybrid model. The hybrid model has therefore been shown to be able to stand on its own.

However, beyond 250 kHz, all the plots for the hybrid model agree less with those measured, thereby limiting the accuracy of the hybrid model to approximately 250 kHz. This is mostly due to stray capacitive effects. The essentials of the characterization process have nonetheless been achieved, as have been shown through the results provided. The developed earth path characterization method can, therefore, be considered to be fully verified.

## 5.8 Comparison of Squirrel and Flounder Conductors

The impedance characteristics of the Flounder conductor are compared with those of the Squirrel conductor in Figure 5.17.

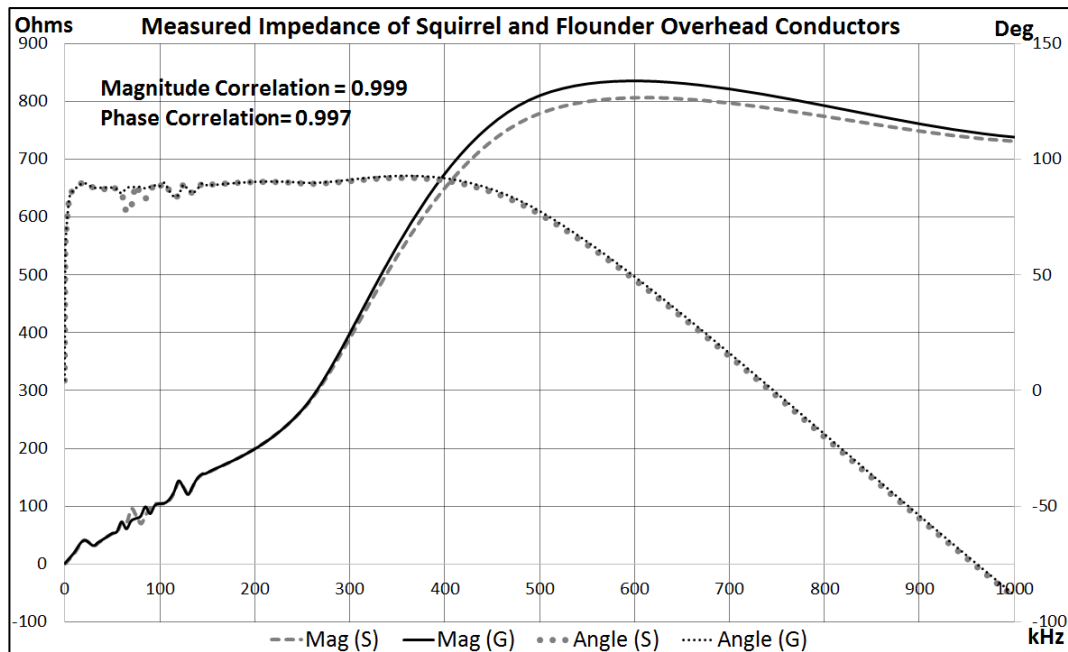


Figure 5.17 – Measured Line Impedance of Squirrel (S) and Flounder (F) Conductors; Zero – 1 MHz

The plots reveal that the differences in the characteristics of the conductors are not significant, especially in the lower NB region. Correlations between the magnitude and phase plots were found to be 0.999 and 0.997 respectively. This indicates that conductor spiralling methods may have no significant bearing on their high frequency performance. However, these results do not represent an extensive study on the subject-matter, and therefore additional experimentation may be required to reach definite conclusions.

## **5.9 Conclusion**

This chapter presented results of the characterization of a SWER MV line. This required a hybrid process of independent characterization of the earth return path of the SWER line using a method developed in the course of the research, and therefore results of this process were also presented.

An extensive comparison of the results showed a marked difference between the sole use of analytical methods to characterise SWER MV lines, and the use of hybrid empirical/analytical methods. Therefore, the developed hybrid characterization method forms the first original and significant contribution to knowledge, through the research outlined in this thesis.

A brief comparison of a standard and low-loss aerial conductor of similar ratings but different spiral construction was also carried out, with results showing negligible differences in characteristics in the NB-PLC frequency range.

# Chapter Six – Through-transformer NB-PLC Characterization Results

## 6.1 Introduction

Transformers are necessary and prominent fixtures of distribution grids, especially SWER grids. The high frequency characteristics of distribution transformers have been known to affect PLC, due to their influence on the overall grid impedance. These characteristics have been studied mostly under un-energized conditions, as revealed by the literature review. This limits the observation of the effects that transformers have on the integrity of PLC signals passing through them.

The results of the experiments for high frequency signal injection through energized 11 kV/230 V 0.5 kVA, 1 kVA and 15 kVA transformers are provided in this chapter. Through the processing of the results, it was observed that significant amounts of high frequency signals do not flow through the transformer windings, due to the high inductive reactance of these paths. Relevant paths are therefore taken to be through the distributed shunt capacitances, in accordance with reviewed literature. This includes paths between the live and neutral terminals, the MV and LV terminals, and the tank, of the transformers.

The results form the basis for the second thesis contribution, namely that the cyclic polarization of the insulation system of distribution transformers causes cyclic variations of high frequency signals passing through its terminals, which negatively affects through-transformer PLC data throughput.

The results of the 0.5 kVA transformer experiments are provided in Section 6.2, the results of the 1 kVA and 15 kVA transformer experiments are provided in Section 6.3, the development of a simulation model for energized through-transformer PLC channels from the analysed results is described in Section 6.4, and the conclusion is given in Section 6.5.

## 6.2 0.5 kVA Transformer Results

The plots of a 50 Hz 270 V RMS energizing voltage waveform and a 110 kHz sinusoidal waveform measured at point *I*, with no LV load connected, are shown in Figure 6.1.

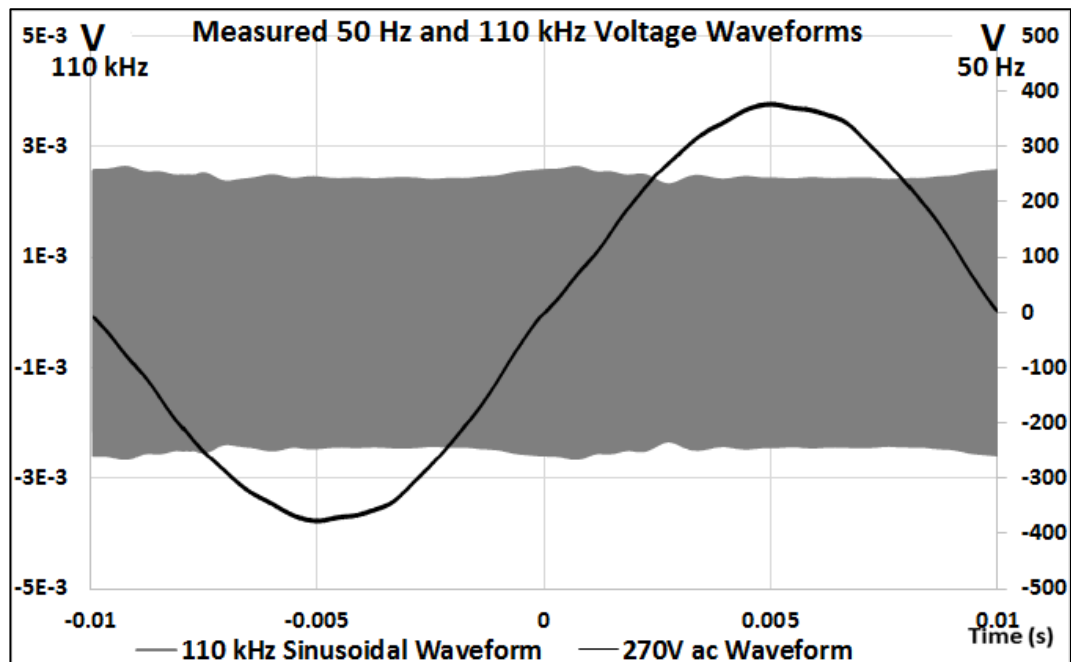


Figure 6.1 – Measured 110 kHz Sinusoidal Waveform, plotted with One Cycle of 270 V 50 Hz Waveform

The plots show variation in the magnitude of the 110 kHz waveform, in accordance with the instantaneous 50 Hz voltage.

The envelope and single cycle RMS values of the 110 kHz waveform, for the single 50 Hz cycle, were calculated. The plots of the calculated upper envelope and cycle RMS are shown in Figure 6.2.

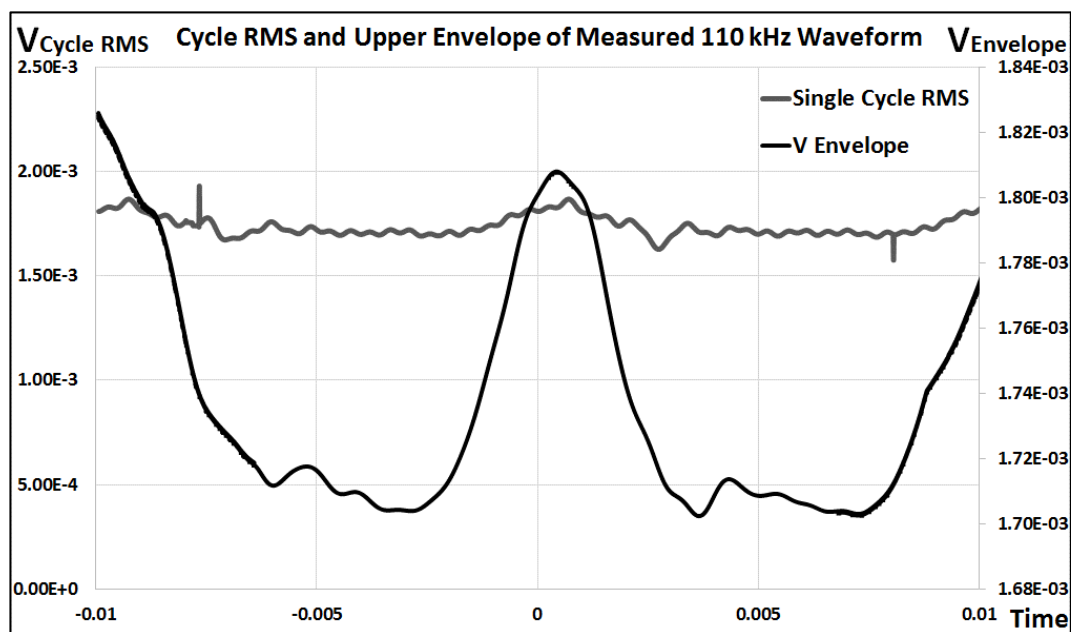


Figure 6.2 – Plots of Cycle RMS Values and Upper Envelope for Measured 110 kHz Waveform

The envelope was calculated by filtering the 110 kHz waveform data with a Hilbert FIR filter of length 2.5 ms, which corresponds to  $1/8^{\text{th}}$  of the 50 Hz cycle length. A single period of a 110 kHz sinusoidal waveform is approximately  $9.09 \mu\text{s}$ , giving approximately

275 complete periods of the 110 kHz waveform within the applied Hilbert FIR filter. The average difference between the minimum and maximum value of the 110 kHz upper envelope is approximately 0.11 mV. The zero-to-peak voltage value of the 110 kHz waveform at the output of the unenergized experimental platform is approximately 2.5 mV, which places its maximum peak voltage variation at approximately 4.4%.

The RMS voltage value of the 110 kHz signal at the output of the unenergized experimental platform is 1.7 mV. The cycle RMS plot of Figure 6.2 shows that the RMS value varies between 1.65 mV and 1.8 mV, as the 270 V 50 Hz waveform goes through its cycle.

The plots of Figures 6.1 and 6.2 are given as an illustration of the variations that high frequency signals encounter while passing through energized transformers. In this case, the plots reveal that the maximum voltage magnitude of the 110 kHz waveform occurs at just beyond the zero crossing points of the 50 Hz voltage waveform.

Figure 6.3 summarizes the results obtained for all the frequencies and 50 Hz voltage energization levels of interest, with no LV load connected.

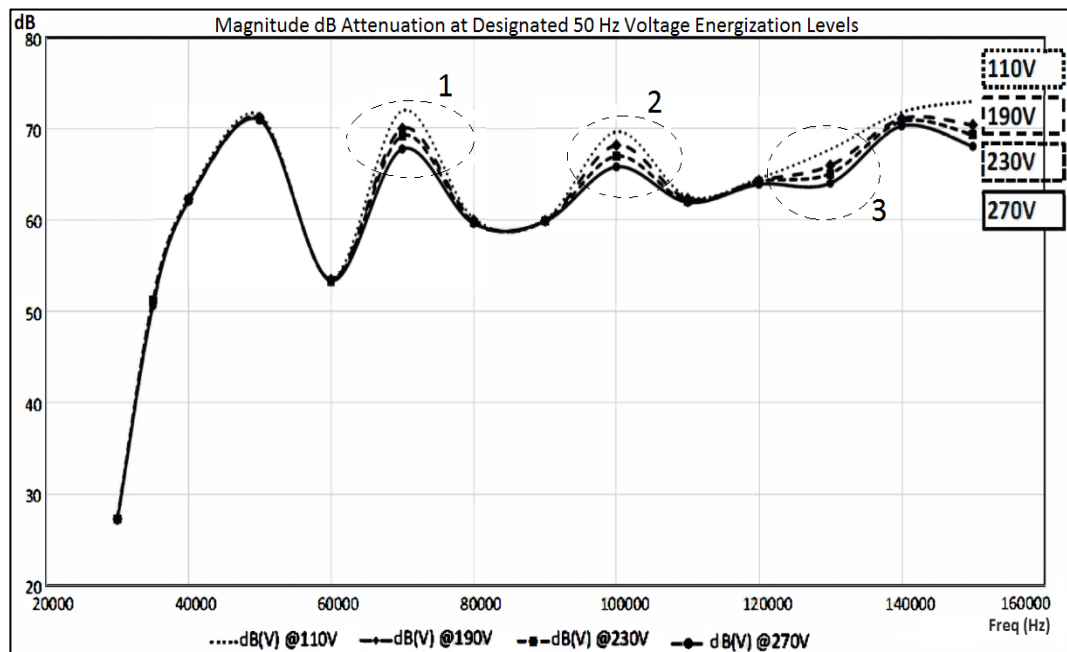


Figure 6.3 – High Frequency Signal Magnitude dB Attenuation at Designated 50 Hz Voltage Energizations

Figure 6.3 shows the dB attenuation of the high frequency signals going through the platform, throughout the specified bandwidth, under various transformer energization levels. The attenuation values were inverted to create the given plot, whereby the maximum attenuation is higher on the y axis, for better visual representation. The plots show the expected resonance effects of the through-transformer channel [123], but this is not of paramount importance to the analysis to be performed. The differences in



attenuation with transformer energization levels, as marked on the plots by the dotted circles in Figure 6.3, are of interest.

Each plotted point of Figure 6.3 is a representation of the dB ratio of the RMS value of the output versus input high frequency voltage waveform of length 20 ms, for each energization level. Differences exist in the four plots between 40 and 150 kHz, with a distinct pattern observable between 60 and 120 kHz at regions of peak attenuation. In this latter frequency range, it can be seen that transformer energization significantly influences the peak attenuation level. Beyond 140 kHz, the 110 V plot is trending towards a different direction from the other three plots.

The plots show that higher transformer energization is associated with less high frequency signal attenuation, at certain frequencies. Also, these attenuation patterns seem to occur in tandem with resonance effects. This is supported by the fact that the minimas of the plots correspond regardless of energization levels, while the maximas exhibit the most attenuation variation, as shown by circles 1 and 2. However, there is a reversal of this particular effect between 130 kHz and 150 kHz inclusive, whereby the minimas exhibit the most attenuation variation while the maximas exhibits the least, with the maxima values at 140 kHz being approximately equal with energization, as shown by circle 3.

The plots of Figure 6.3 show that there are distinct effects occurring within the through-transformer channel, due to the transformer energization levels. A calculation of the variations in high frequency RMS voltage magnitude was carried out, by comparing the percentage attenuation of the signals at 110 V, 190 V, and 270 V to the values at nominal 50 Hz energization of 230 V. The results are summarized in Table 6.1.

Table 6.1 - Variation of Test Signal Output Voltage with Energization

Freq. (kHz)	Signal RMS Value at Nominal 230 V (mV)	Variation from Value at Nominal 50 Hz 230 V Energization					
		110 V		190 V		270 V	
		Value	%	Value	%	Value	%
30	81.1	-1.47	1.81	0.64	0.79	-1.5	1.88
40	2.7	0.05	1.67	0.08	2.88	-0.08	2.93
50	1.3	0.05	3.64	0.04	3.27	-0.01	0.82
60	10.3	0.16	1.60	0.07	0.65	0.2	1.98
70	1.4	0.4	28.24	0.11	7.90	-0.26	18.16
80	3.5	0.08	2.21	-0.02	0.54	-0.09	2.46
90	3.0	-0.04	1.28	-0.02	0.68	0.004	0.13
100	1.1	0.27	23.39	0.12	10.18	-0.18	15.84
110	1.8	0.05	2.77	0.01	0.53	-0.06	3.24
120	1.3	0.06	4.92	0.06	4.99	-0.04	3.35
130	1.1	0.3	28.04	0.11	10.37	-0.13	12.61
140	0.49	0.06	11.86	0.01	2.32	-0.04	7.12
150	0.55	0.19	34.95	0.06	11.38	-0.08	14.27

Table 6.1 shows that the changes in attenuation can be high, reaching 35% at 150 kHz, followed by 28.2% at 70 kHz, for 110 V energization.

### 6.3 1 kVA and 15 kVA Transformer Results

The results from the 1 kVA and 15 kVA through-transformer paths are presented in this section. A general description of the pre-processing carried out on the results is given in Section 6.3.1, the results of the determination of the modal occurrence of minimum and maximum signal variations within a single 50 Hz voltage waveform are provided in Section 6.3.2, and the results of the calculation of the minimum and maximum variation values are provided in Section 6.3.3.

#### 6.3.1 Pre-processing of Results

The plots of a single 50 Hz cycle of the platform energizing voltage waveform of 255 V RMS, and a 35 kHz sinusoidal waveform that was passed through the 1 kVA analysis transformer in the LV to MV direction are shown in Figure 6.4. No LV loads were used.

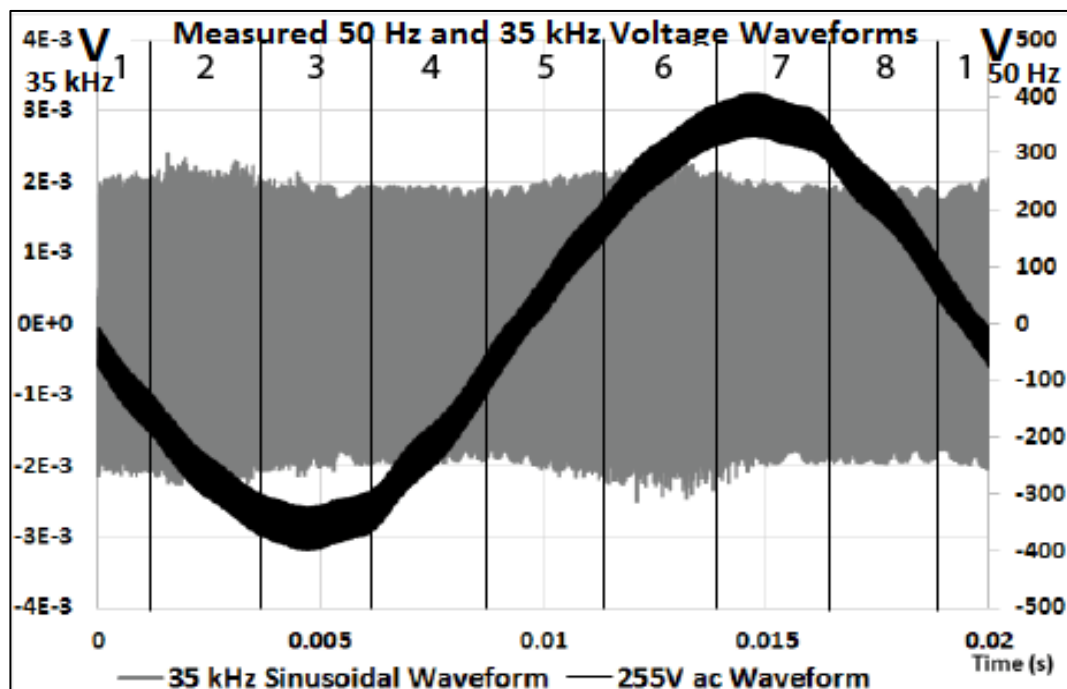


Figure 6.4 – Measured 35 kHz Sinusoidal Waveform, plotted with One 50 Hz Cycle of 255 V Waveform

These plots again show that the high frequency voltage magnitude varies in accordance with the instantaneous 50 Hz voltage energization. This variation was not observed when the transformers were bypassed, thereby indicating that this effect is due to phenomena associated with the transformer energization.

The envelope and 10-cycle RMS values of the 35 kHz waveform, for the single 50 Hz cycle, were calculated. The plots of the calculated upper envelope and 10-cycle RMS are shown in Figure 6.5.

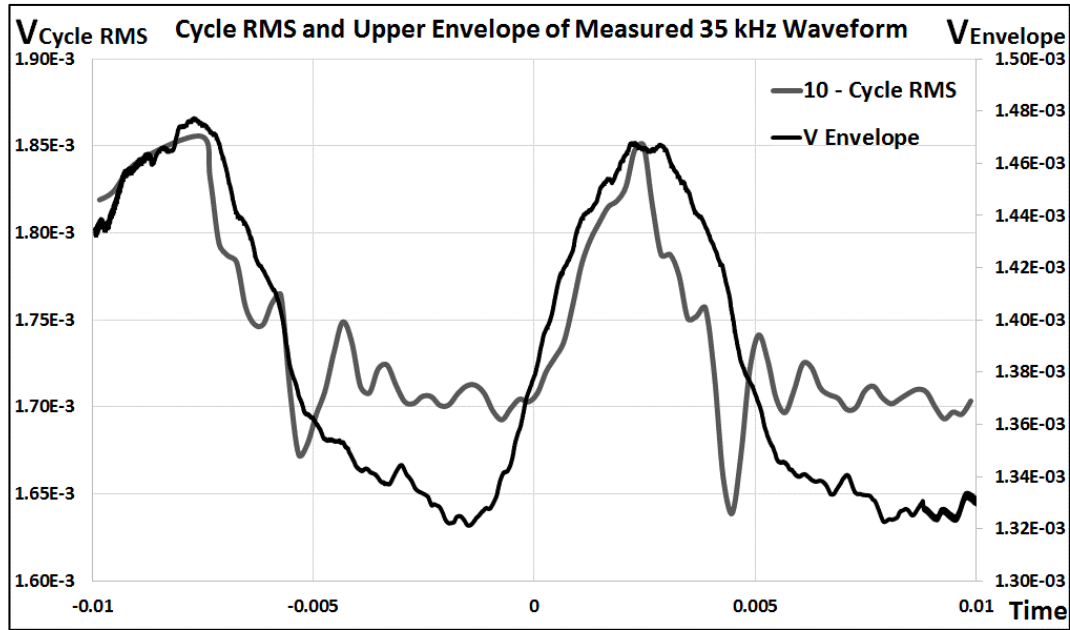


Figure 6.5 – Plots of 10-Cycle RMS Values and Upper Envelope for Measured 35 kHz Waveform

The envelope was calculated by also filtering the 35 kHz waveform data with a Hilbert FIR filter of length 2.5 ms, corresponding to  $1/8^{\text{th}}$  of the 50 Hz cycle length. A single period of a 35 kHz sinusoidal waveform is approximately  $28.57\text{ }\mu\text{s}$ , giving approximately 87.5 complete periods of the 35 kHz waveform, within the applied Hilbert FIR filter. The average difference between the minimum and maximum value of the 35 kHz upper envelope is approximately 0.16 mV. The zero-to-peak voltage value of the 35 kHz waveform at the output of the unenergized experimental platform is 6 mV, which places its maximum peak voltage variation at 2.6%.

The RMS voltage value of the 35 kHz waveform at the output of the unenergized experimental platform is 1.8 mV. The 10-cycle RMS plot of Figure 6.5 shows that the RMS value varies between approximately 1.7 mV and 1.85 mV, as the 255 V 50 Hz waveform goes through its cycle.

The plots of Figure 6.5 reveal that the maximum magnitude of the 35 kHz waveform occurs at approximately halfway between the zero crossing points and the peaks of the 50 Hz voltage waveform, i.e. at the  $45^\circ$  and  $225^\circ$  points of the  $360^\circ$  cycle.

The high frequency waveforms measured at each 50 Hz energization level was stored as waveform data, which was subsequently split into eight equal segments of 2.5 ms length,

as shown in Figure 6.4. The choice of eight segments was to provide a basis for observing the influence of the instantaneous 50 Hz voltage energization on the high frequency waveform variation, averaged over the stated duration.

For eight segments, the 50 Hz voltage waveform advances by 45° after each segment, corresponding to a point halfway to a peak, at a peak, or at a zero crossing. Less than eight segments may not properly capture the effects of instantaneous transformer energization, while more segments may result in too much data that may not be particularly useful.

A MATLAB script was written to determine the values, and locations of occurrence, of minimum and maximum high frequency waveform magnitude and phase angle variations within the 50 Hz energizing voltage segments.

The high frequency input and output waveforms were paired up and then grouped according to the 50 Hz voltage energization levels they were measured at, resulting in one input-output waveform pair per 50 Hz energization level group. Then, each input-output waveform pair was analysed within each segment.

For each segment, the minimum and maximum RMS voltage values of the high frequency input-output waveform pairs were determined. The high frequency waveform magnitude variation at 110 V 50 Hz energization is the ratio of the high frequency RMS waveform magnitude at 110 V 50 Hz energization, to the high frequency waveform magnitude at 0 V 50 Hz energization, i.e.:

$$\text{Magnitude Variation} = \frac{V_{HF @ 110V}}{V_{HF @ 0V}} \quad (26)$$

where  $V_{HF}$  is the RMS voltage of the high frequency waveform within each segment.

Equation (26) was used for calculating input and output waveform magnitude variation. This magnitude variation calculation was repeated for the high frequency waveforms measured at 190 V, 230 V, and 255 V energization.

For each segment, the minimum and maximum phase angle variation between each high frequency input-output waveform pair was also determined. The high frequency waveform phase angle variation at 110 V 50 Hz energization is the phase angle difference for the input-output waveform pair at 0 V energization subtracted from the phase angle difference for the input-output voltage pair at 110 V 50 Hz energization, i.e.:

$$\text{Phase Variation} = (V_{HF IN} \theta - V_{HF OUT} \phi)_{@110V} - (V_{HF IN} \theta - V_{HF OUT} \phi)_{@0V} \quad (27)$$

where  $\theta$  is the phase angle of the input waveform, and  $\phi$  is the phase angle of the output waveform, within each segment.

This phase variation calculation was repeated for the input-output high frequency waveform pairs measured at 190 V, 230 V, and 255 V energization.

This process of calculating the magnitude and phase variations at various 50 Hz voltage energization levels and cycle segments was performed for the data from the 25 frequency points measured.

### 6.3.2 Modal Occurrence of Minimum and Maximum Variations within the 50 Hz Voltage Segments

Tables 6.2 and 6.3 summarize the results for the modal occurrence of the minimum and maximum high frequency RMS voltage magnitude variations within the 50 Hz voltage segments, for the 25 frequency points measured.

Table 6.2 – Modal Occurrence of Minimum and Maximum Input Voltage Magnitude Variations within the 50 Hz Voltage Segments; 30 kHz - 150 kHz

Energization Level		Minimum Input Voltage								Av. Pos.	Maximum Input Voltage								Av. Pos.
		1	2	3	4	5	6	7	8		1	2	3	4	5	6	7	8	
1 kVA, LV to MV	110V	3	11	2	--	2	2	--	5	2	1	2	1	1	17	3	--	--	5
	190V	1	12	1	--	3	2	1	5	2	1	--	--	1	17	2	--	4	5
	230V	1	16	1	--	3	--	--	4	2	2	1	1	--	19	--	1	1	5
	255V	--	16	1	--	5	--	--	3	2	--	--	1	--	20	--	2	2	5
1 kVA, MV to LV	110V	5	1	1	--	9	4	5	--	5	5	4	5	2	3	1	2	3	3
	190V	7	5	--	--	--	6	7	--	1	7	--	3	7	7	--	--	1	4
	230V	6	7	--	--	--	6	6	--	2	9	--	--	9	6	--	--	1	4
	255V	4	5	--	--	--	10	6	--	6	11	--	--	10	2	--	--	2	4
15 kVA, LV to MV	110V	13	4	8	--	--	--	--	--	1	2	--	5	--	5	4	6	3	7
	190V	14	11	--	--	--	--	--	--	1	1	--	1	--	9	--	14	--	7
	230V	1	11	--	--	13	--	--	--	5	--	--	--	--	11	--	14	--	7
	255V	1	11	--	--	13	--	--	--	5	--	--	--	--	11	--	13	1	7
15 kVA, MV to LV	110V	1	--	1	2	2	5	10	4	7	6	8	5	4	--	1	--	1	2
	190V	--	--	--	--	1	7	10	7	7	2	12	7	4	--	--	--	--	2
	230V	--	--	--	--	--	1	19	5	7	--	13	10	2	--	--	--	--	2
	255V	--	--	--	--	--	3	12	10	7	1	7	15	2	--	--	--	--	3

Table 6.3 – Modal Occurrence of Minimum and Maximum Output Voltage Magnitude  
Variations within the 50 Hz Voltage Segments; 30 kHz - 150 kHz

Energization Level		Minimum Output Voltage								Av. Pos.	Maximum Output Voltage								Av. Pos.
		1	2	3	4	5	6	7	8		1	2	3	4	5	6	7	8	
1 kVA, LV to MV	110V	<b>19</b>	--	--	--	5	--	1	--	<b>1</b>	--	1	--	--	1	--	--	<b>23</b>	<b>8</b>
	190V	<b>11</b>	--	--	4	7	--	3	--	<b>1</b>	--	2	--	--	1	7	--	<b>15</b>	<b>8</b>
	230V	<b>15</b>	5	1	--	--	--	1	3	<b>1</b>	3	2	--	1	1	<b>14</b>	--	4	<b>6</b>
	255V	<b>12</b>	3	2	4	1	--	3	--	<b>1</b>	<b>15</b>	--	1	--	2	4	--	3	<b>1</b>
1 kVA, MV to LV	110V	2	--	--	--	<b>12</b>	2	9	--	<b>5</b>	--	--	--	4	--	--	--	<b>21</b>	<b>8</b>
	190V	8	1	--	--	5	1	<b>10</b>	--	<b>7</b>	--	1	--	10	2	1	1	<b>10</b>	<b>8</b>
	230V	4	--	--	2	<b>12</b>	6	1	--	<b>5</b>	4	4	7	--	--	4	<b>6</b>	--	<b>7</b>
	255V	--	7	--	--	2	--	<b>16</b>	--	<b>7</b>	10	--	--	1	--	<b>14</b>	--	--	<b>6</b>
15 kVA, LV to MV	110V	<b>20</b>	--	1	2	--	2	--	--	<b>1</b>	2	--	4	1	1	--	<b>14</b>	3	<b>7</b>
	190V	<b>22</b>	--	--	2	--	1	--	--	<b>1</b>	1	--	2	--	4	--	<b>16</b>	2	<b>7</b>
	230V	<b>9</b>	1	--	5	7	3	--	--	<b>1</b>	1	--	2	1	6	--	<b>9</b>	6	<b>7</b>
	255V	<b>13</b>	1	2	7	2	--	--	--	<b>1</b>	--	3	--	--	7	2	<b>12</b>	1	<b>7</b>
15 kVA, MV to LV	110V	3	--	<b>8</b>	1	--	--	3	10	<b>3</b>	7	1	--	1	2	<b>14</b>	--	--	<b>6</b>
	190V	--	--	4	--	--	--	<b>17</b>	4	<b>7</b>	8	--	--	5	<b>12</b>	--	--	--	<b>5</b>
	230V	--	3	1	--	--	--	<b>19</b>	2	<b>7</b>	<b>22</b>	--	2	--	1	--	--	--	<b>1</b>
	255V	--	--	2	--	--	--	<b>21</b>	2	<b>7</b>	<b>23</b>	--	--	2	--	--	--	--	<b>1</b>

Table 6.4 summarizes the results for the modal occurrence of the minimum and maximum phase angle variations within the segments, for the 25 frequency points measured.

Table 6.4 – Modal Occurrence of Minimum and Maximum Phase Angle Variations within the 50 Hz Voltage Segments; 30 kHz - 150 kHz

Energization Level		Minimum Phase Angle								Av. Pos.	Maximum Phase Angle								Av. Pos.
		1	2	3	4	5	6	7	8		1	2	3	4	5	6	7	8	
1 kVA, LV to MV	110V	3	--	--	3	5	1	--	<b>13</b>	<b>8</b>	--	11	--	--	--	--	<b>14</b>	--	<b>7</b>
	190V	11	--	--	<b>13</b>	1	--	--	--	<b>4</b>	1	<b>18</b>	--	--	--	4	2	--	<b>2</b>
	230V	<b>14</b>	--	--	11	--	--	--	--	<b>1</b>	2	<b>15</b>	--	--	--	7	1	--	<b>2</b>
	255V	6	--	--	<b>17</b>	2	--	--	--	<b>4</b>	4	3	--	--	--	<b>17</b>	1	--	<b>6</b>
1 kVA, MV to LV	110V	6	--	2	5	3	1	--	<b>8</b>	<b>8</b>	1	2	3	<b>8</b>	6	--	3	2	<b>4</b>
	190V	5	4	<b>6</b>	3	3	2	1	1	<b>3</b>	--	7	--	<b>6</b>	3	1	5	3	<b>4</b>
	230V	7	<b>5</b>	4	2	2	--	3	2	<b>2</b>	6	4	1	<b>4</b>	1	3	3	3	<b>4</b>
	255V	4	3	<b>5</b>	5	2	2	4	--	<b>3</b>	6	2	2	<b>8</b>	--	3	3	1	<b>4</b>
15 kVA, LV to MV	110V	5	1	4	1	2	1	4	<b>7</b>	<b>8</b>	<b>9</b>	--	2	--	6	--	8	--	<b>1</b>
	190V	4	--	6	4	2	--	--	<b>9</b>	<b>8</b>	<b>9</b>	6	--	2	1	2	5	--	<b>1</b>
	230V	1	1	7	1	3	2	1	<b>9</b>	<b>8</b>	1	<b>11</b>	--	1	7	1	4	--	<b>2</b>
	255V	3	--	<b>12</b>	--	4	--	2	4	<b>3</b>	7	6	--	--	<b>8</b>	2	2	--	<b>5</b>
15 kVA, MV to LV	110V	--	--	<b>7</b>	--	4	6	1	7	<b>3</b>	--	--	4	1	7	<b>11</b>	--	2	<b>6</b>
	190V	2	1	<b>11</b>	--	5	2	--	4	<b>3</b>	1	--	2	1	6	<b>10</b>	1	4	<b>6</b>
	230V	9	--	3	--	1	1	--	<b>11</b>	<b>8</b>	<b>11</b>	--	4	--	7	--	3	--	<b>1</b>
	255V	4	2	<b>8</b>	--	2	2	4	3	<b>3</b>	<b>14</b>	--	4	--	3	1	2	1	<b>1</b>

Tables 6.2 to 6.4 show that the minimum and maximum high frequency waveform magnitude and phase angle variations occurred within different segments for each 50 Hz energization level, with moderate patterns of repetition.

The tables show that the 1 kVA transformer influenced the minimum and maximum input voltage magnitude variation in the LV to MV direction to consistently occur within segments 2 and 5 respectively, with increased energization. Out of 25 occurrences, between 11 and 16 were in segment 2, and between 17 and 20 were in segment 5, for all energization levels.

Similar consistent occurrences were observed for the minimum output voltage magnitude variation in the LV to MV direction, with segment 1 recording between 11 and 19 occurrences, and for the maximum phase angle variation in the MV to LV direction, with segment 4 recording between 4 and 8 occurrences. The 15 kVA transformer also produced similar occurrences.

These differences in the modal occurrences of the maximum and minimum voltage values given in Tables 6.2 and 6.3 indicate phase shifting effects, which is supported by the minimum and maximum phase angle locations of Table 6.4. The segments where the changes occurred were more consistent for the 15 kVA transformer, compared with the 1 kVA transformer. This suggests that the 1 kVA transformer exhibits much more phase angle variation than the 15 kVA transformer, especially if the number of occurrences for each segment in Table 6.4 is considered. The number of occurrences per segment was highest for the 1 kVA transformer, in the LV to MV direction.

### **6.3.3 Minimum and Maximum Waveform Variation Values**

The results of the magnitude and phase angle variation calculations, using equations (26) and (27) respectively, revealed that the 1 kVA transformer exhibits more signal variation than the 15 kVA transformer. The calculations also revealed that the variations are generally higher going from the LV to MV direction, compared with the MV to LV direction. Therefore, the plots of all the MV to LV results for the 1 kVA transformer, with the exception of the minimum and maximum input voltage magnitude variation plots, are provided in Appendix F. The plots of the LV to MV output voltage magnitude variation for the 15 kVA transformer are also provided in Appendix F.

The 1 kVA transformer MV to LV minimum and maximum input voltage magnitude variation plots were not significant, showing variations within only 0.5 %. The rest of the results for the 15 kVA transformer were also not significant. These showed variations

within only 2.5 % for the minimum and maximum LV to MV input voltage magnitude,  $\pm 1.4^\circ$  for the minimum and maximum LV to MV phase angle, 0.5 % for the minimum and maximum MV to LV input voltage magnitude, 1.5 % for the minimum and maximum MV to LV output voltage magnitude, and  $\pm 0.5^\circ$  for the minimum and maximum MV to LV phase angle. These plots were therefore not provided.

### 6.3.3.1 Magnitude Variation Values

The plots of Figures 6.6 to 6.9 summarize the magnitude variation results for the 1 kVA transformer, in the LV to MV direction. The LV to MV minimum input RMS voltage magnitude variation values for the various energization levels of the 1 kVA transformer (110 V to 255 V), expressed as percentages, are summarized in Figure 6.6.

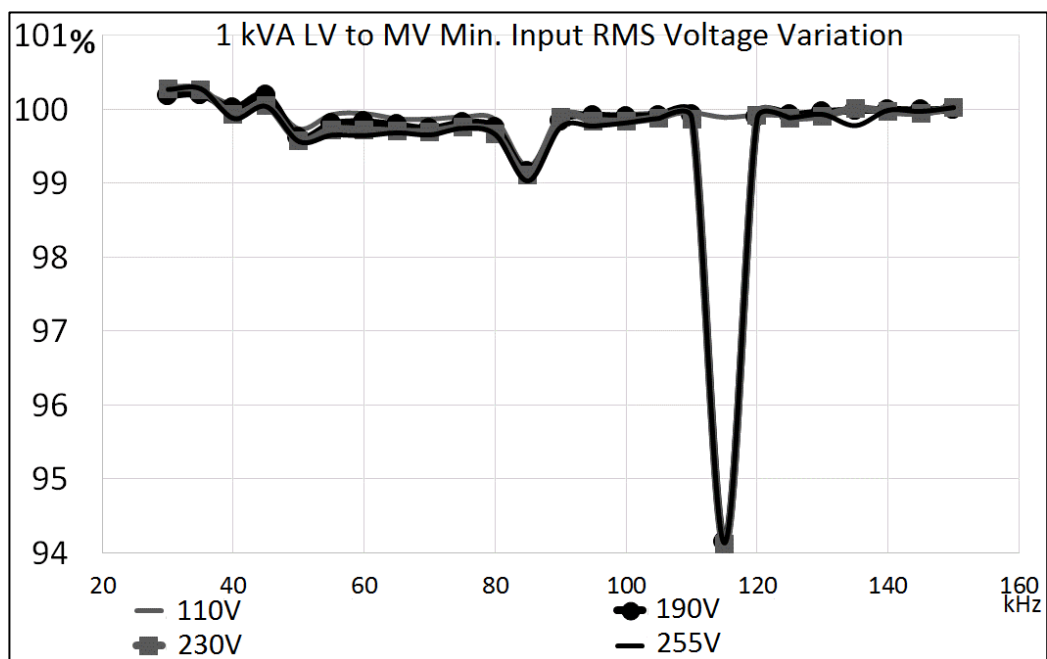


Figure 6.6 – 1 kVA LV to MV Minimum Input RMS Voltage Magnitude Variation

The plots show very little change in voltage magnitude with energization across the entire spectrum, with the exception of the values for 190, 230 and 255V at approximately 115 kHz. These show a marked and approximately equal reduction in the minimum input voltage at this frequency of 6%, indicating a corresponding decrease in impedance.

The LV to MV maximum input RMS voltage magnitude variation values for the various energization levels of the 1 kVA transformer, expressed as percentages, are summarized in Figure 6.7.



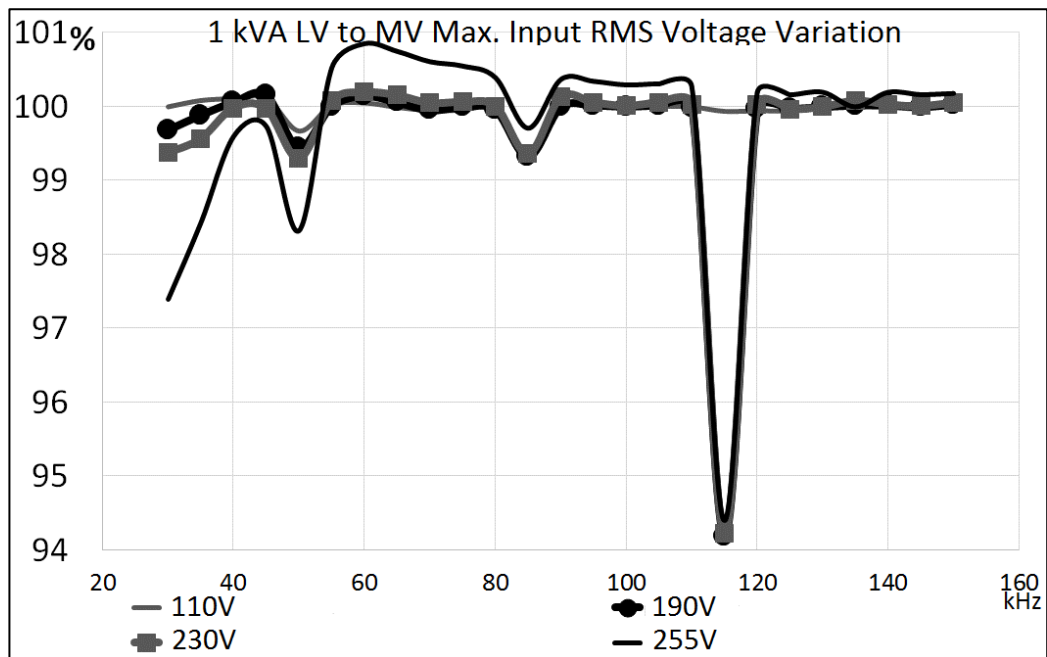


Figure 6.7 – 1 kVA LV to MV Maximum Input RMS Voltage Magnitude Variation

These plots also show very little change in voltage magnitude with energization for the 110, 190 and 230 V values across the entire spectrum. However, the 255 V plot shows approximately 2.5% and 1.5% reduction at 30 kHz and 50 kHz respectively, in addition to the previous significant reductions in the 190 V, 230 V and 255 V values of approximately 5.8% at 115 kHz. The 255 V plot also shows a slight increase in value between 55 and 110 kHz. These reductions in input voltage all indicate impedance decrease.

The 1 kVA LV to MV input voltage variations of Figures 6.6 and 6.7 are relatively insignificant compared with the rest of the LV to MV magnitude results for the 1 kVA transformer summarized in Figures 6.8 and 6.9. However, they were provided to show the relationship between the transformer input and output high frequency waveform variations. The input variations are mainly due to the shunt path between the live and neutral terminals of the LV side of the transformer, as expected [123].

The LV to MV minimum output RMS voltage magnitude variation values for the various energization levels of the 1 kVA transformer, expressed as percentages, are summarized in Figure 6.8.

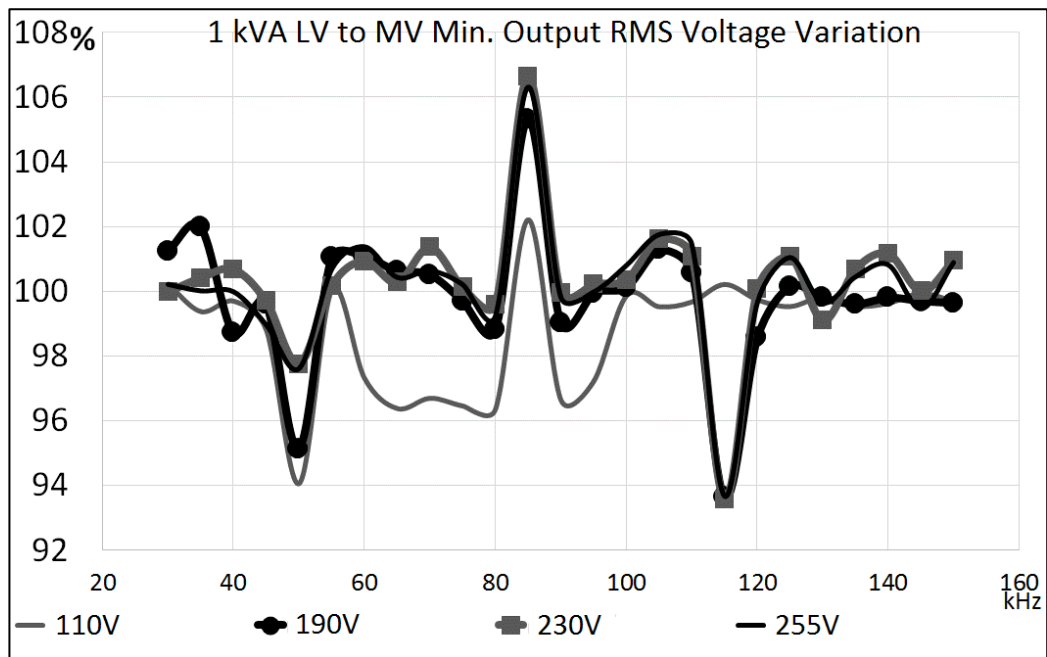


Figure 6.8 – 1 kVA LV to MV Minimum Output RMS Voltage Magnitude Variation

The plots show that there is a corresponding signal reduction of approximately the same value of 94% at 115 kHz for the minimum output variation as was observed for the minimum and maximum input variation, at all but the 110 V energization levels. Also, there are now significant decreases and increases of up to 6% at 50 kHz and 85 kHz respectively, especially for the 190 V, 230 V, and 255 V values. These decreases and increases were trending in both of the 1 kVA minimum and maximum input voltage plots of Figures 6.6 and 6.7, showing that a relationship exists between the transformer input and output variations.

The 110 V values also show marked decreases between 60 kHz and 80 kHz, and at 90 kHz, of approximately 4%.

The LV to MV maximum output RMS voltage magnitude variation values for the various energization levels of the 1 kVA transformer, expressed as percentages, are summarized in Figure 6.9.

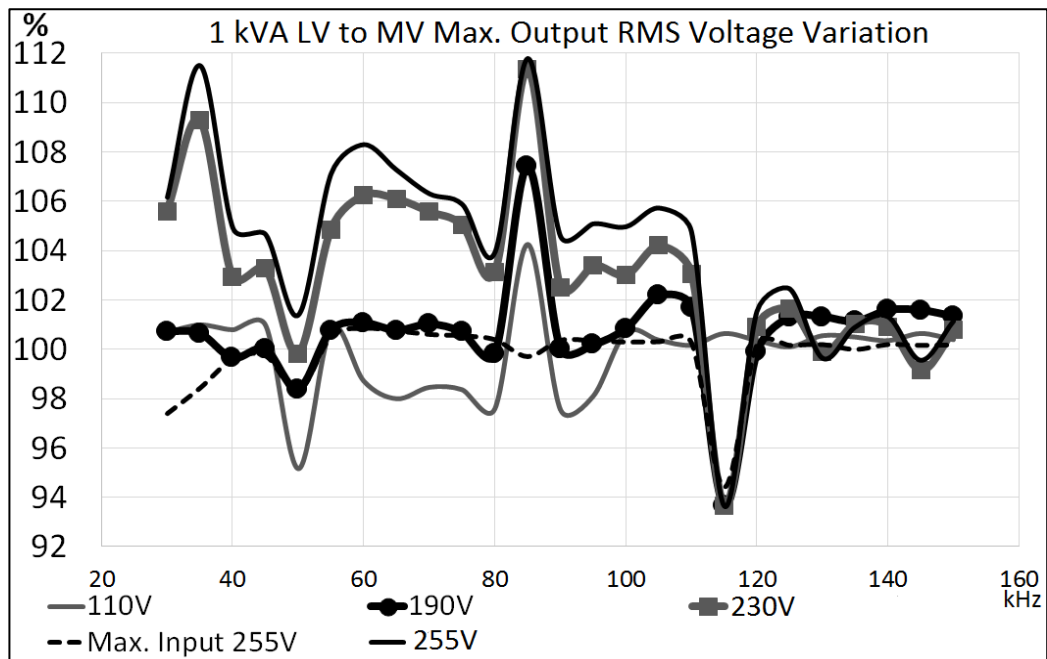


Figure 6.9 – 1 kVA LV to MV Maximum Output RMS Voltage Magnitude Variation (Maximum Input Voltage Variation at 255 V Included for Comparison)

The plots once more show that there is a signal reduction of approximately the same value of 94% at 115 kHz for the maximum output variation as was observed for the minimum and maximum input variation, at all but the 110 V energization levels. Also, there are now much more significant signal variation increases than decreases. The plot of maximum input magnitude variation at 255 V was added for comparison with these plots, showing that the maximum output variations are much higher than those for the maximum input variations, for the 1 kVA transformer in the LV to MV direction.

The plots of maximum output magnitude variation at 230 V and 255 V now show a significant increase compared with those for 110 and 190 V energization between 30 kHz and 110 kHz, with up to approximately 10, 8, 11 and 6% at 35 kHz, 60 kHz, 85 kHz and 105 kHz respectively. The 190 V plot is comparable with the maximum input magnitude variation at 255 V plot for much of the bandwidth between 40 kHz and 100 kHz, at approximately 100%. However, the 110 V values still show marked decreases, with values of approximately 5% at 50 kHz, and 4% between 60 kHz and 80 kHz, and at 90 kHz.

### 6.3.3.2 Phase Angle Variation Values

The LV to MV minimum phase angle variation values for the various energization levels of the 1 kVA transformer (110 V to 255 V), expressed in angle degrees, are summarized in Figure 6.10.

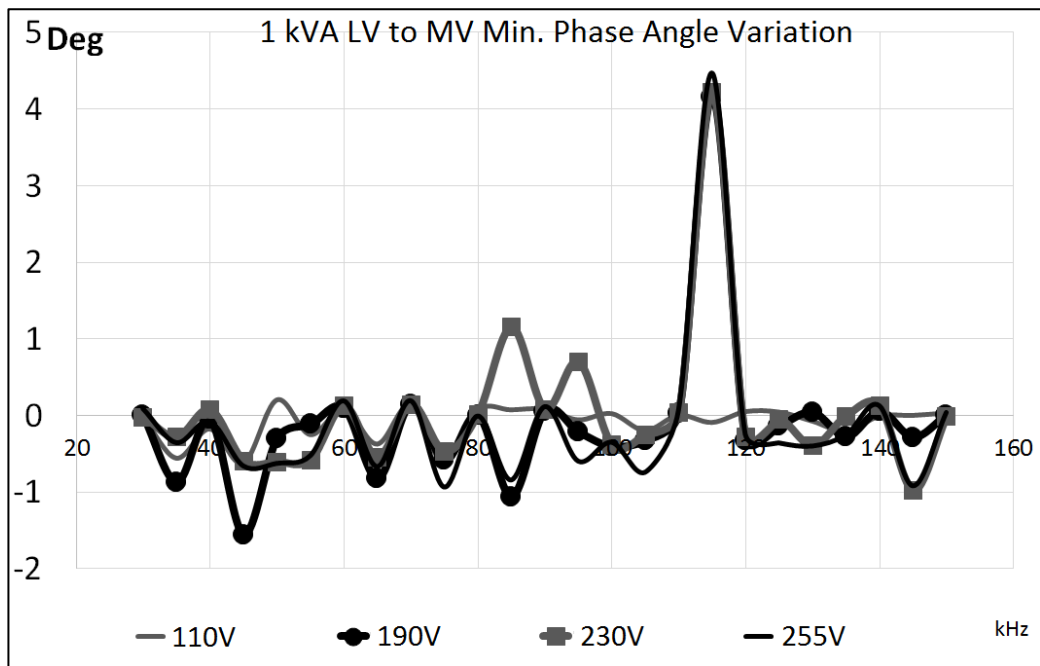


Figure 6.10 – 1 kVA LV to MV Minimum Phase Angle Variation

The plots show that the minimum phase angle changes are relatively insignificant at a modal average of  $\pm 1^\circ$  throughout the bandwidth. However, there is a significant phase angle change at 115 kHz, which is the frequency that has consistently produced magnitude reductions, even in the case of the maximum output magnitude variation plots where the increases were markedly higher. The phase angle increases to approximately  $4.5^\circ$  at this frequency.

The LV to MV maximum phase angle variation values for the various energization levels of the 1 kVA transformer, expressed in angle degrees, are summarized in Figure 6.11.

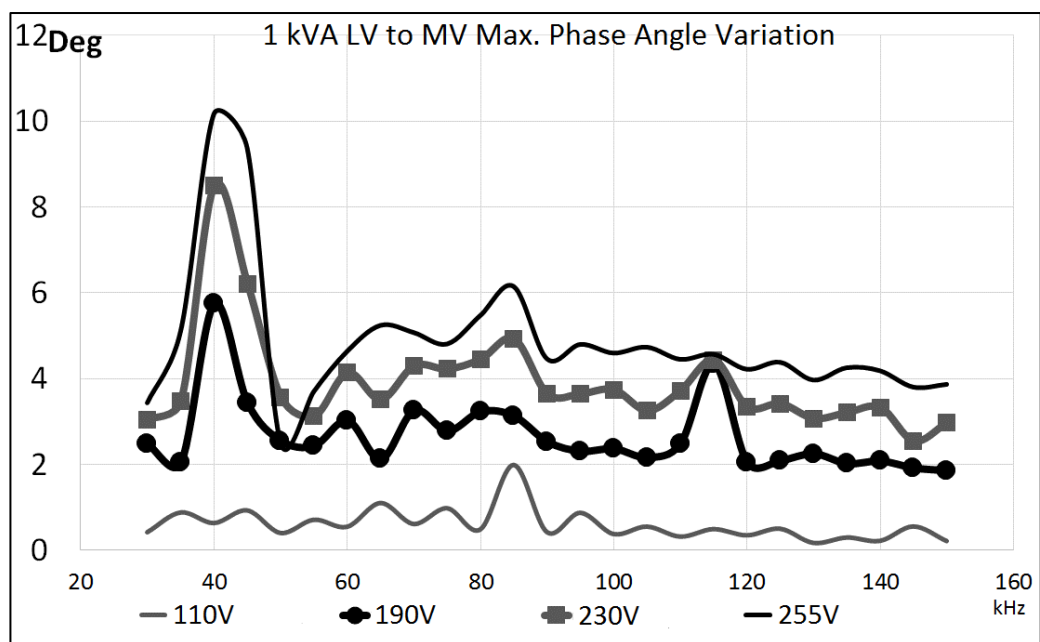


Figure 6.11 – 1 kVA LV to MV Maximum Phase Angle Variation

The plots show that the maximum phase angles significantly vary from one energization level to the next throughout the bandwidth, with distinct variations for the 190 V and 230 V values of up to approximately  $4.5^\circ$  for all but the 110 V value at 115 kHz yet again. Other values are up to  $6^\circ$ ,  $5^\circ$ ,  $3^\circ$  and  $2^\circ$  for the 255 V, 230 V, 190 V and 110 V levels respectively, at 85 kHz. A new peak cluster exists at 40 kHz, with up to  $10^\circ$ ,  $8.5^\circ$  and  $6^\circ$  for the 255 V, 230 V and 190 V levels respectively.

## **6.4 Development of Energized Through-transformer PLC Channel Simulation Model from Variation Data**

Sections 6.2 and 6.3 provide results which show that high frequency signals passing through energized distribution transformers exhibit magnitude and phase variations, depending on the instantaneous value of the energizing voltage. Since PLC is inherently implemented on energized grids, this brings up challenges for modelling distribution transformers for the purpose of accurate simulation of through-transformer PLC.

The differences between the characteristics of the unenergized and energized through-transformer paths reveal a cyclic time-variance of the magnitude and phase values. However, the energized characteristics may still be considered as linear time-invariant (LTI), because the signal variation occurs slowly, with respect to the signal frequency itself [75, 175]. The variations occur twice every 50 Hz voltage cycle, once for each negative and positive half-cycle, thereby placing the variance frequency at 100 Hz; this is slow compared with the lowest frequency of 30 kHz being considered for the PLC signals. Therefore, the unenergized transformer characteristics may still be considered valid for the energized cases, allowing for the universal use of the unenergized TFs, with adjustments for the cyclic variations made by applying time-varying magnitude and phase angle value vectors to the TF outputs [78].

### **6.4.1 Procedure**

The maximum magnitude and phase angle variation values calculated using equations (26) and (27) were more appropriate for creating the magnitude and phase angle value vectors because the minimum values were still generally higher than those for 0 V 50 Hz energization. Also, as stated in Section 6.3.3, the variation data for the 15 kVA transformer were insignificant and so were not considered for demonstrating the energized through-transformer PLC channel simulation model.

Variable files were created in MATLAB to store the 1 kVA through-transformer channel maximum variation values plotted in Figures 6.8 to 6.11, namely the 1 kVA LV to MV maximum output RMS voltage variation, the 1 kVA LV to MV maximum phase angle variation, the 1 kVA MV to LV maximum output RMS voltage variation, and the 1 kVA MV to LV maximum phase angle variation, for the 25 frequency points measured.

The information for the segments where the applicable maximum variation values were to be applied within the single 50 Hz energization waveform period, was provided by Tables 6.3 and 6.4. For example, if the 1 kVA transformer is being energized at a value of 255 V 50 Hz RMS, and an 85 kHz sinusoidal waveform is propagating through it from the LV to the MV direction, magnitude values will be linearly ramped up from a starting value of 1.00 at 6.25ms (segments 3) and 16.25ms (segment 7), to the maximum value of approximately 1.12 at 1.25ms (segment 1) and 11.25ms (segment 5), of the 50 Hz energization cycle, and then linearly ramped down by the same process. These linearly ramped magnitude values may either be used to scale the transfer function coefficients of the unenergized transformer model or be independently applied to scale the output of the transfer function of the unenergized transformer model. The latter option was used in developing the PLC simulation model of the energized through-transformer channel.

A magnitude and phase angle variation value was required to be applied to each discrete sample of the PLC waveform propagating through the energized through-transformer channel model. This required the total number of discrete samples of the PLC waveform for a single 50 Hz period, i.e. 0.02 seconds, to be determined, in order to create appropriate magnitude and phase angle ramp value vectors of appropriate size. The size of these vectors, therefore, depended on the carrier frequency and modulation method.

The total number of discrete PLC waveform samples  $T$  in 0.02 seconds was determined by:

$$T = \left( \frac{f}{50} * L * a \right) + 1, \text{ rounded down to the nearest integer} \quad (28)$$

where  $f$  is PLC carrier frequency in Hertz,  $L$  is the modulation length, or bits per symbol, and  $a$  is a compensation factor for the inclusion of 8PSK modulation. For BPSK,  $L = 1$ ,  $a = 2$ . For QPSK,  $L = 2$ ,  $a = 1$ . For 8PSK,  $L = 3$ ,  $a = 0.88889$ . For 16QAM,  $L = 4$ ,  $a = 1$ .

The slope of the linear ramp for the magnitude and phase angle values was determined by:

$$S = \frac{1}{(seg-1)} \quad (29)$$

where  $seg$  is the number of samples for the slope, given by  $\frac{T}{4}$  rounded down to the nearest integer.

A single magnitude variation ramp vector value was calculated by using:

$$M = \{(MaxMag - 1) * S * (k - 1) * G(k) + 1\} \quad (30)$$

where  $k$  = the index value for the number of samples for the slope, i.e.  $seg$ ,  $G$  = half-Gaussian distribution vector with  $\sigma = 0.33*seg$  and length =  $seg$ , and  $MaxMag$  = maximum magnitude variation value for the applicable through-transformer channel direction and frequency.

Likewise, a single phase variation ramp vector value was calculated by using:

$$P = MaxPhase * S * (k - 1) \quad (31)$$

where  $MaxPhase$  = maximum phase variation value for the applicable through-transformer channel direction and frequency.

Equations (30) and (31) were used in iterations for  $k = 1$  to  $seg$ , each time storing the value obtained into the magnitude and phase variation ramp vectors. These ramp vectors were then manipulated by dissection, splicing and/or inversion, to recreate larger vectors of the measured variations, based on the determined modal segments of occurrence of maximum variation detailed in Tables 6.3 and 6.4.

The recreated variation value vectors were of equal length with the total number of bits, and therefore were directly applied to the modulated magnitude and phase vectors, according to the energized through-transformer channel simulation method described in Section 4.6.3. The results of the Simulation are provided in Section 7.4. A flowchart of the energized through-transformer PLC simulation process is provided in Appendix G, while an abridged profile report for the program's timing performance is provided in Appendix H.

## 6.5 Conclusion

This chapter presented results of the characterization of 0.5 kVA, 1 kVA, and 15 kVA single phase transformers, at the unenergized state as well as under various 50 Hz voltage energization levels, for frequencies between 30 kHz and 150 kHz inclusive. The characterization process involved passing high frequency signals through the transformers, in the LV to MV and MV to LV directions.

Pre-processing of the results showed that cyclic variations of high frequency signals impinging on the terminals, or passing through energized distribution transformers, experience variations that are in accordance with the 50 Hz energizing voltage. This cyclic variation was found to be due to the dielectric polarization process of the transformer insulation. These cyclic variations have not been explicitly identified and demonstrated in relation to PLC previously, and therefore form the basis of the second original and significant contribution to knowledge, through the research outlined in this thesis.

Through the assumption that significant amounts of the high frequency signals do not pass through the inductive paths represented by the windings, the impedance characteristics of the through-transformer paths are simplified to some extent. However, the specific number and location of paths through which the high frequency signals can propagate are still numerous, complex, and dependent on the design of the transformer. Therefore, generalisations related to the magnitude and phase of the signal passing through the transformer are difficult to make. However, as apparent from the experimental evidence, variations do exist. These are important because they can affect through-transformer PLC data throughput.

The variation results were also used as a basis for the development of a simulation model of an energized through-transformer PLC channel.



# Chapter Seven – NB-PLC Modelling and Simulation Results

## 7.1 Introduction

The priority for PLC implementation is the determination of the transmission line characteristics of power lines, within the desired frequency range. The common characteristics of interest are frequency response function (FRF) and insertion loss (IL) [21-23, 176]. The former is required to develop a PLC channel model of the line, while the latter defines the total signal power loss due to the insertion of the line into a communication channel. The results of MV line and transformer path FRF and IL determination, and NB-PLC simulation of the estimated models using standard function blocks in Simulink, are provided in this chapter.

The results of the SWER and Two-wire MV line FRF and IL determination are provided in Section 7.2, the results of the 1 kVA and 15 kVA through-transformer FRF and IL determination are provided in Section 7.3, and the results of a simulation of the energized through-transformer simulation model are provided in Section 7.4.

The results of the NB-PLC simulation of the MV line and transformer channels are given in Section 7.5 and 7.6 respectively, while those of the simulation of the 1 kVA transformer under energization at the voltages of interest are given in Section 7.7, and the conclusion is given in Section 7.8.

## 7.2 Unenergized Through-transformer Channel FRFs and ILs

The results for the determination of unenergized through-transformer channel FRFs are provided in Section 7.2.1, while the results for the determination of unenergized through-transformer channel IL are provided in Section 7.2.2.

### 7.2.1 Unenergized Through-transformer Channel FRFs

The FRF magnitude and phase plots of the through-transformer channels of the 15 kVA transformer are shown in Figures 7.1 and 7.2, while those for the 1 kVA transformer are shown in Figures 7.3 and 7.4, evaluated for an equal source and load resistance of 50  $\Omega$ .

The FRF magnitude plots for the 15 kVA through-transformer channels are shown in Figure 7.1.

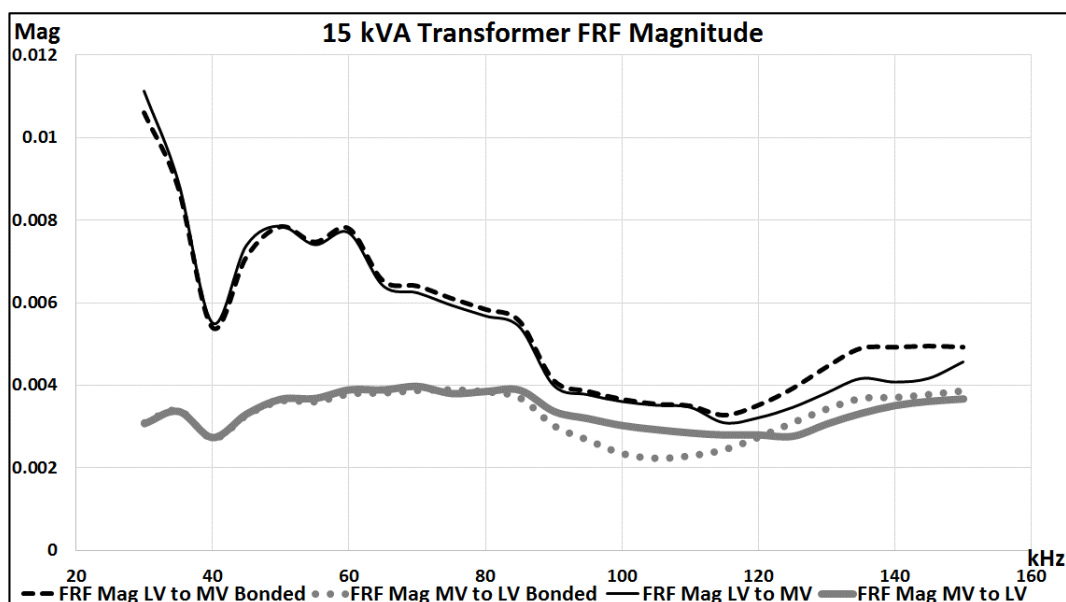


Figure 7.1 – FRF (Magnitude) of 15 kVA Through-transformer Channels

The magnitude plots for the LV neutral terminal not bonded to the transformer tank (FRF Mag LV to MV and FRF Mag MV to LV) are very similar to those for the LV neutral terminal bonded to the transformer tank (FRF Mag LV to MV Bonded and FRF Mag MV to LV Bonded), up to 110 kHz in the LV to MV direction, and 85 kHz in the MV to LV direction. The LV to MV FRFs exhibit a decaying trend from approximately 0.011 to 0.005 across the bandwidth. Distinct resonance troughs occur at 40 kHz, 55 kHz, 65 kHz, 90 kHz and 115 kHz, and resonant peaks at 50 kHz, 60 kHz, 70 kHz and 85 kHz.

The MV to LV FRFs are approximately linear from 0.003 at 30 kHz, to 0.004 at 85 kHz, and then to 0.0025 at 125 kHz for the unbonded plot, and 0.002 at 105 kHz for the bonded plot. Both plots finally end at approximately 0.004, at 150 kHz. These plots show that the PLC channel characteristics of the 15 kVA transformer will exhibit more PLC signal magnitude attenuation in the LV to MV direction than in the MV to LV direction, with the bonding of the LV neutral terminal to the transformer tank resulting in slight improvements from 110 kHz to 150 kHz in the LV to MV direction, and 85 kHz to 150 kHz in the MV to LV direction.

The FRF phase plots for the 15 kVA through-transformer channels are shown in Figure 7.2.

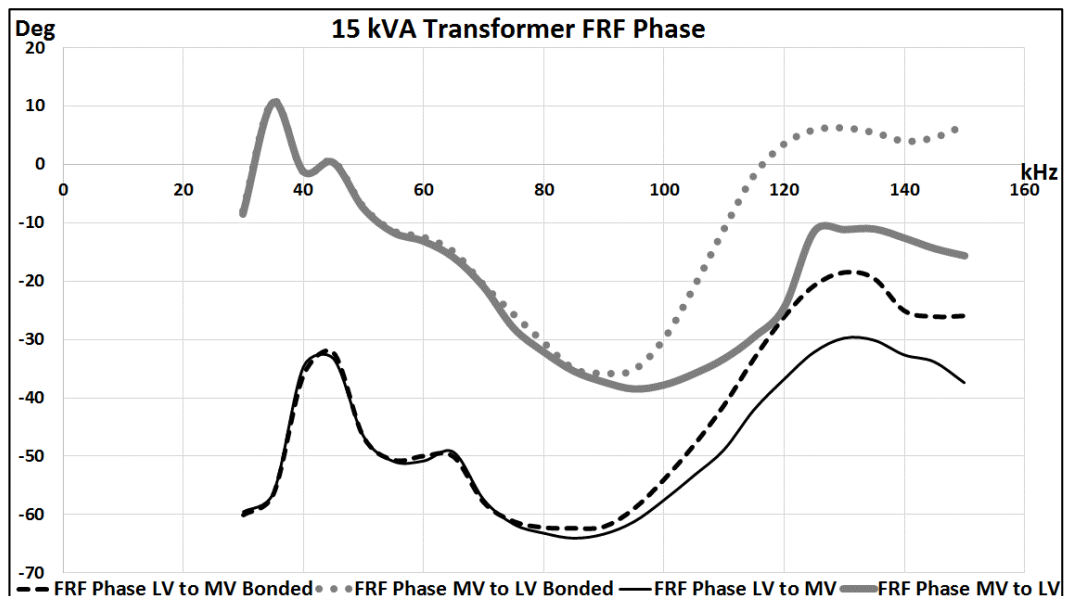


Figure 7.2 – FRF (Phase) of 15 kVA Through-transformer Channels

The phase plots for the LV neutral terminal not bonded to the transformer tank (FRF Phase LV to MV and FRF Phase MV to LV) are similar to those for the LV neutral terminal bonded to the transformer tank (FRF Phase LV to MV Bonded, FRF Phase MV to LV Bonded), up to approximately 75 kHz in the LV to MV direction, and 55 kHz in the MV to LV direction. Beyond these frequencies, the phase angle increases for the bonded plots, signifying a decrease in capacitive reactance, which translates to a reduction in impedance, with increased frequency. This indicates that the transformer tank forms part of the through-transformer channel, due to the bonded LV neutral terminal.

The FRF magnitude plots for the 1 kVA through-transformer channels are shown in Figure 7.3.

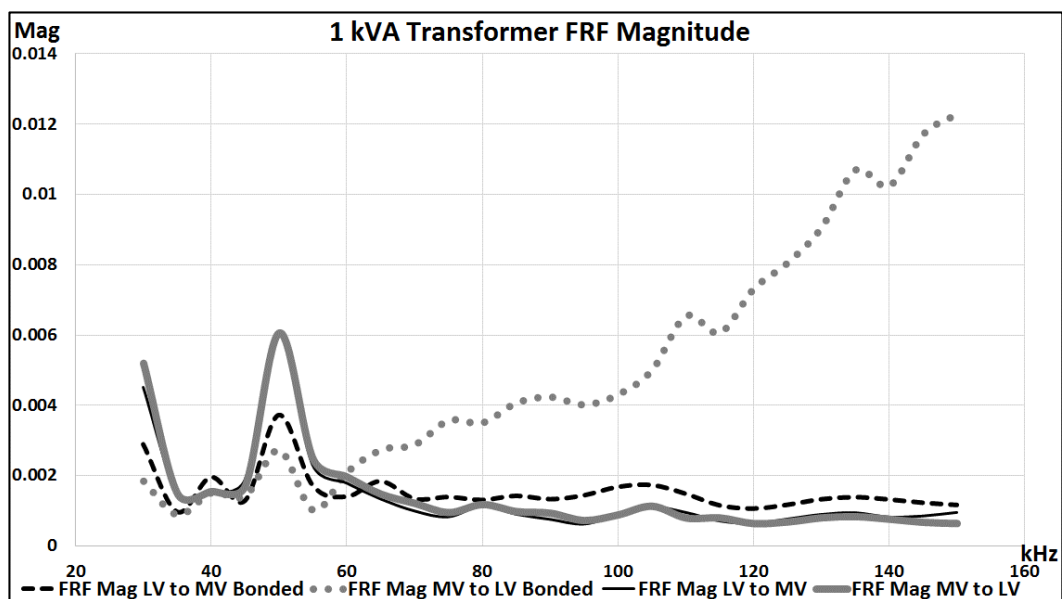


Figure 7.3 – FRF (Magnitude) of 1 kVA Through-transformer Channels

A distinct difference exists between the magnitude plots of the 15 kVA and 1 kVA plots. The plots for the LV neutral terminal not bonded to the transformer tank (FRF Mag LV to MV and FRF Mag MV to LV) are approximately equal throughout the bandwidth. With a value of approximately 0.005 at 30 kHz, the plots show a rapid reduction to approximately 0.0016 at 35 kHz. Beyond this point, the plots gradually reduce with frequency to approximately 0.001 at 150 kHz, with the exception of a peak value of 0.006 at 50 kHz. This shows that the PLC channel characteristics of the 1 kVA transformer will exhibit approximately the same PLC signal magnitude attenuation in either direction if the LV neutral terminal is not bonded to the transformer tank.

The magnitude plot for the 1 kVA transformer in the LV to MV direction, with the LV neutral terminal bonded to the transformer tank (FRF Mag LV to MV Bonded), is similar to the unbonded plots throughout the bandwidth. However, it starts with a lower value of 0.003 at 30 kHz, reducing to 0.001 at 35 kHz and gradually increasing with frequency to approximately 0.0015 at 150 kHz, with the exception of a peak value of 0.0038 at 50 kHz. This shows that the PLC channel characteristics of the 1 kVA transformer, in the LV to MV direction with the LV neutral terminal bonded to the transformer tank, will exhibit slightly less PLC signal magnitude attenuation compared with when the LV neutral terminal is not bonded to the transformer tank.

The magnitude plot for the 1 kVA transformer in the MV to LV direction, with the LV neutral terminal bonded to the transformer tank (FRF Mag MV to LV Bonded), shows a remarkable difference to all the other plots. Between 30 kHz and 55 kHz it is very similar to the FRF Mag LV to MV bonded plot, but beyond this frequency, it increases approximately linearly to 0.012 at 150 kHz. This shows that the PLC channel characteristics of the 1 kVA transformer, in the MV to LV direction with the LV neutral terminal bonded to the transformer tank, will exhibit the least PLC signal magnitude attenuation between 55 kHz and 150 kHz, compared with all the other directions and bonding conditions.

The FRF phase plots for the 1 kVA through-transformer channels are shown in Figure 7.4.

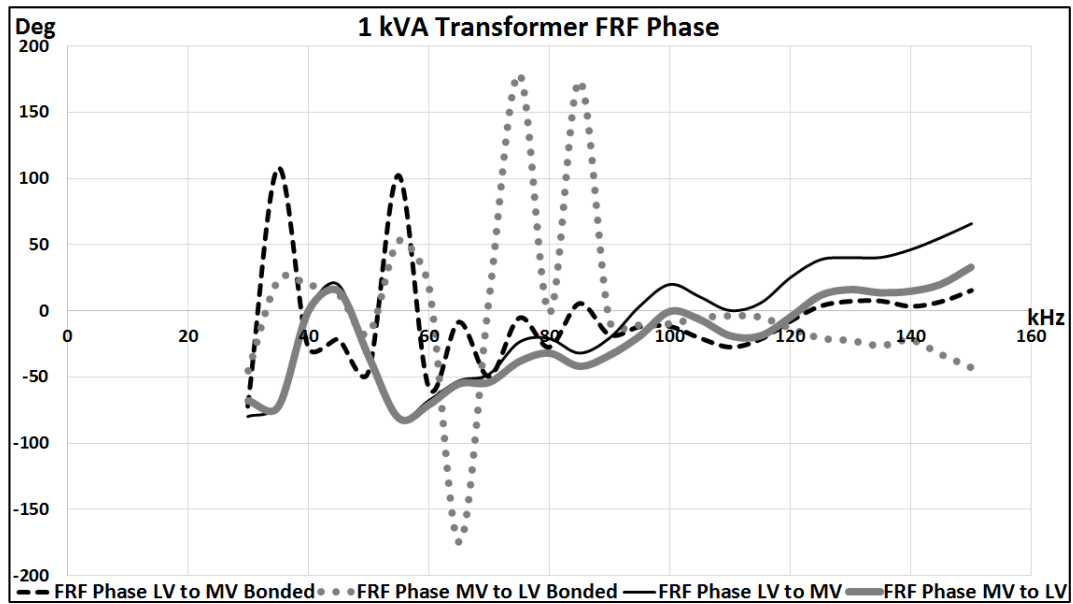


Figure 7.4 – FRF (Phase) of 1 kVA Through-transformer Channels

The phase plots for the LV neutral terminal not bonded to the transformer tank (FRF Phase LV to MV and FRF Phase MV to LV) are approximately equal up to 70 kHz, after which the LV to MV plot shows a progressive increase in phase angle, with a similar resonance pattern to the MV to LV plot. This shows a slight decrease in capacitive reactance in the LV to MV direction, compared with the MV to LV direction, from 70 kHz to 150 kHz.

The phase plots for the LV neutral terminal bonded to the transformer tank (FRF Phase LV to MV Bonded and FRF Phase MV to LV Bonded) show a lot of resonance between 30 kHz and 90 kHz, with up to approximately  $110^\circ$  shifts in the LV to MV direction, and  $180^\circ$  shifts in the MV to LV direction. This shows that some amount of instability may be encountered in the PLC channel characteristics at these frequencies. Between 90 kHz and 150 kHz, the phase angles average to approximately  $-10^\circ$ , which indicates good signal stability characteristics for PLC channels.

### 7.2.2 Unenergized Through-transformer Channel ILs

The insertion losses for the through-transformer channels are given in the plots of Figures 7.5 and 7.6, to provide an indication of the losses that may be encountered for signals propagating through the transformers when they are placed in a lossless PLC channel, for the given source and load resistance of  $50\ \Omega$ .

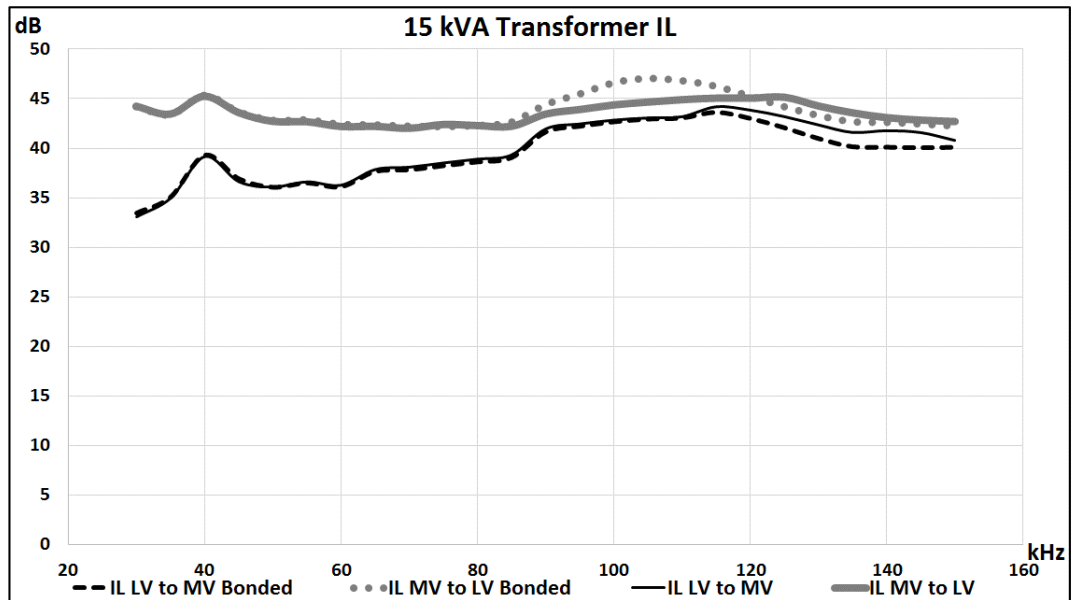


Figure 7.5 – IL of 15 kVA Through-transformer Channels

The 15 kVA transformer will impose between 33 and 44 dB, and approximately 44 dB loss, in the LV to MV and MV to LV direction respectively, with source and load resistance of 50  $\Omega$ . This is largely irrespective of LV bonding condition.

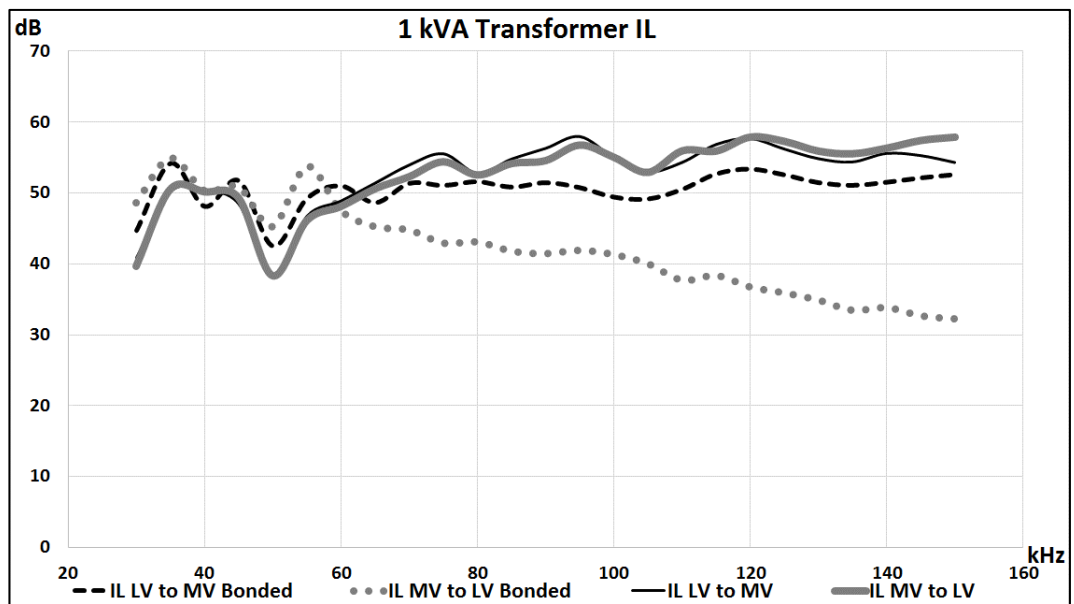


Figure 7.6 – IL of 1 kVA Through-transformer Channels

The 1 kVA transformer will impose between 40 and 55 dB loss for all directions and bonding conditions, with the exception of a reduction in loss from 45 to approximately 30 dB, between 60 kHz and 150 kHz in the MV to LV direction, with the LV terminal bonded to the tank.

The final through-transformer NB-PLC models obtained have bandwidth specifications in accordance with the original FRFs, which is between 30 kHz and 150 kHz.

### 7.3 Energized Through-transformer Channel Simulation Model

The 1 kVA transformer LV to MV discrete magnitude and phase angle variation values for 35 kHz and 255 V 50 Hz energization were calculated using the procedure outlined in Section 6.4.1. The values obtained were applied to a 35 kHz sinusoidal waveform for 0.02 seconds, using the energized through-transformer PLC simulation model described in Section 4.6.3. The waveform obtained is shown in Figure 7.7.

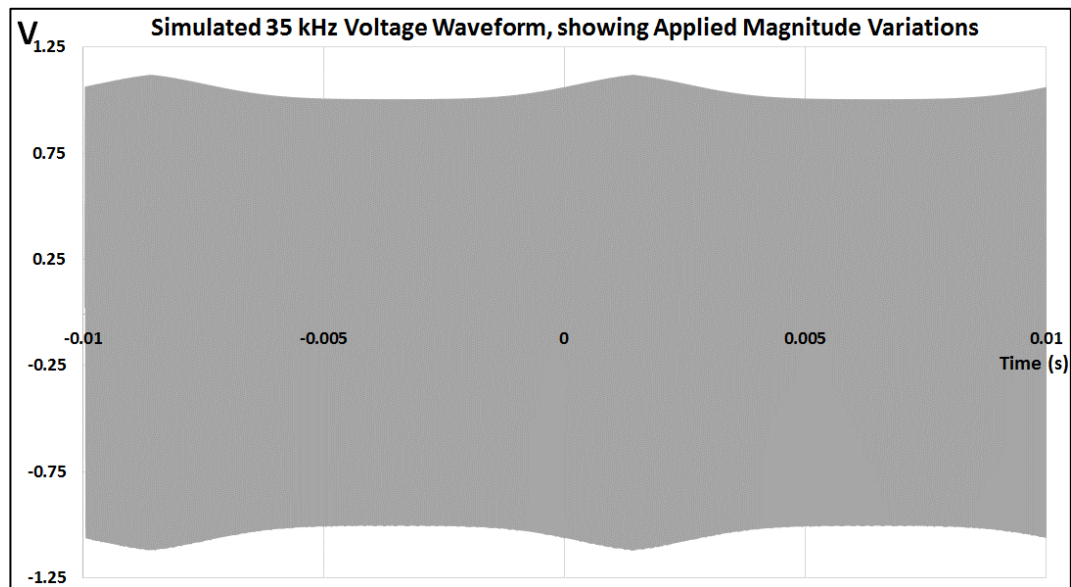


Figure 7.7 – Plot of 1 kVA Transformer LV to MV Voltage Magnitude Variation Applied to 35 kHz Waveform; for Single 255 V 50 Hz Energization Cycle

The same RMS voltage value of 1.8 mV measured for the 35 kHz LV to MV waveform of Figure 6.4 was applied in the simulation. The simulated waveform's upper envelope is plotted in Figure 7.8. The upper envelope of the measured 35 kHz waveform given in Figure 6.5 is also plotted in Figure 7.8, for comparison purposes. A correlation coefficient of 0.98 was obtained from the comparison.

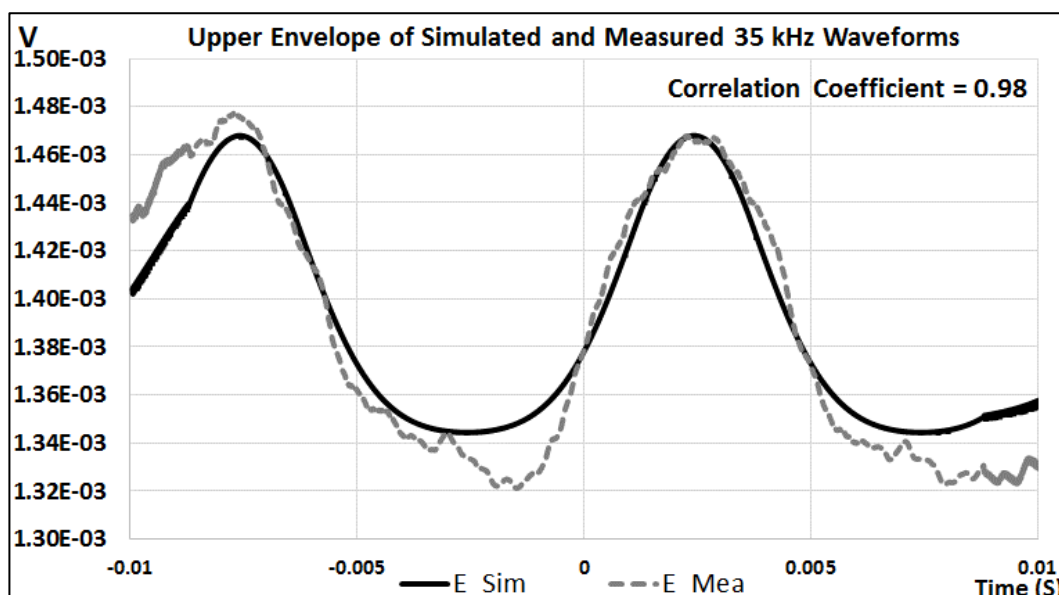


Figure 7.8 – Plots of Upper Envelopes for Simulated and Measured 35 kHz Waveform

Figure 7.8 reveals that the maximum voltage magnitude of the simulated and measured 35 kHz waveforms, at 255 V 50 Hz energization, occur at approximately the same point, i.e. approximately halfway between the zero crossing points and the peaks of the 50 Hz voltage waveform, i.e. at the 45° and 225° points of the 360° cycle. This indicates that the simulation model for capturing the signal variations due to transformer energization replicates the segments for the occurrence of the maximum signal magnitude variations, to a good extent.

The 10-Cycle RMS plots for the simulated and measured waveforms are given in Figure 7.9.

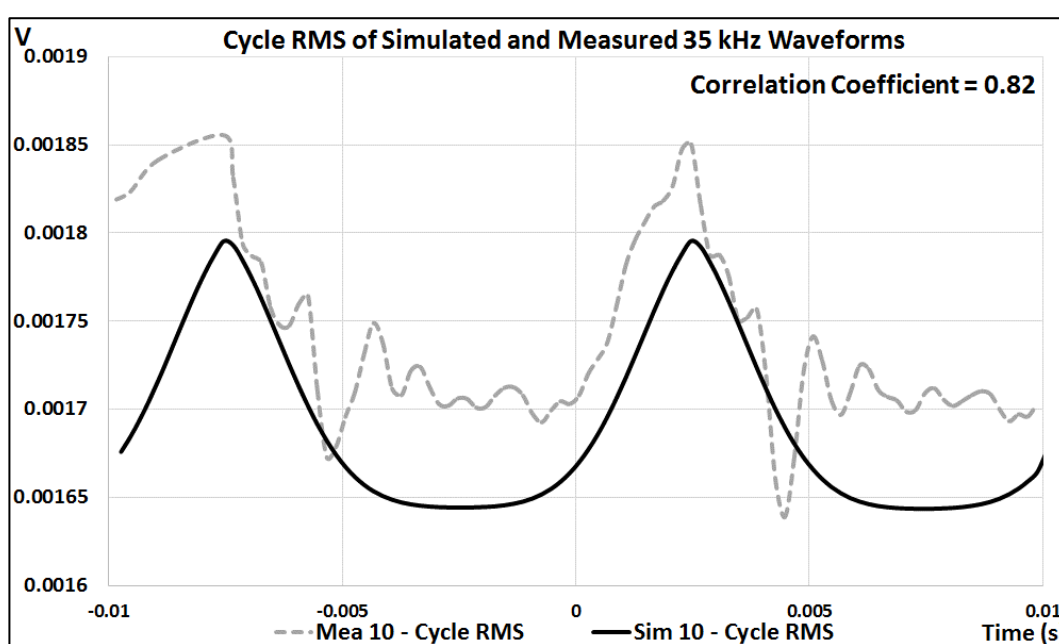


Figure 7.9 – Plots of 10-Cycle RMS Values for Simulated and Measured 35 kHz Waveform



The plots of Figures 7.7, 7.8 and 7.9 serve as verifications of the capability of the energized through-transformer PLC simulation model to reproduce the time-variance of the measured waveforms. Therefore, the model can be considered verified.

## 7.4 MV Line Models

The results for the determination of the SWER and Two-wire MV line FRFs are provided in Section 7.4.1, while the results for the determination of the SWER and Two-wire MV line ILs are provided in Section 7.4.2.

### 7.4.1 SWER and Two-wire MV Line FRFs

The magnitude and phase plots of the FRFs obtained from simulations of the SWER, and Two-wire MV line of length 100 m and 1 km are shown in Figures 7.10 and 7.11.

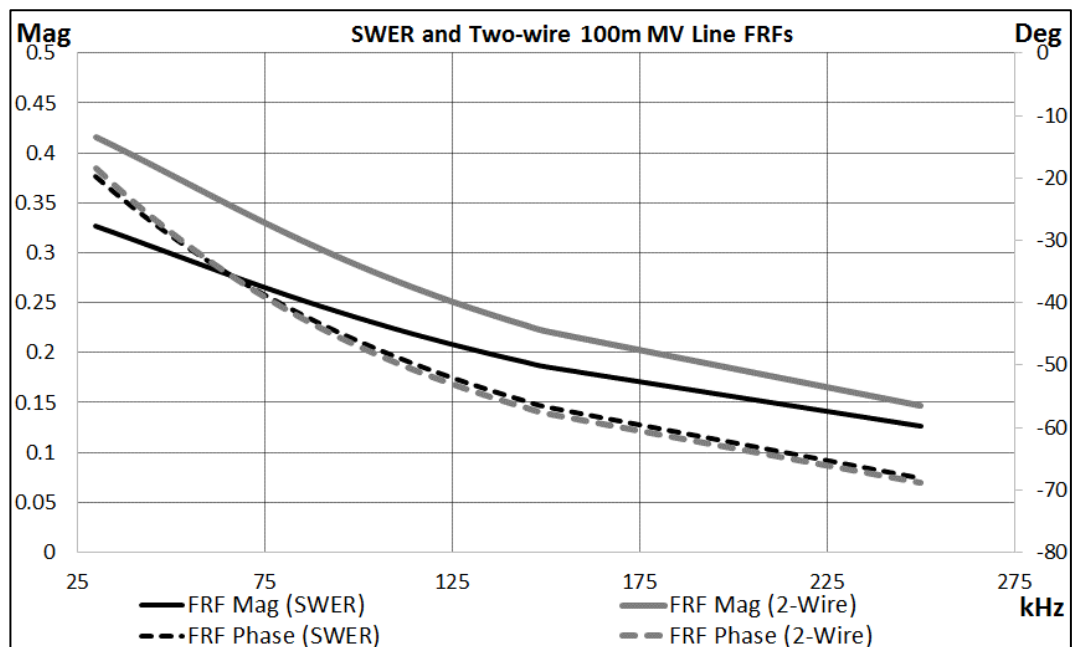


Figure 7.10 – Simulated FRFs of 100m SWER and Two-wire MV Lines

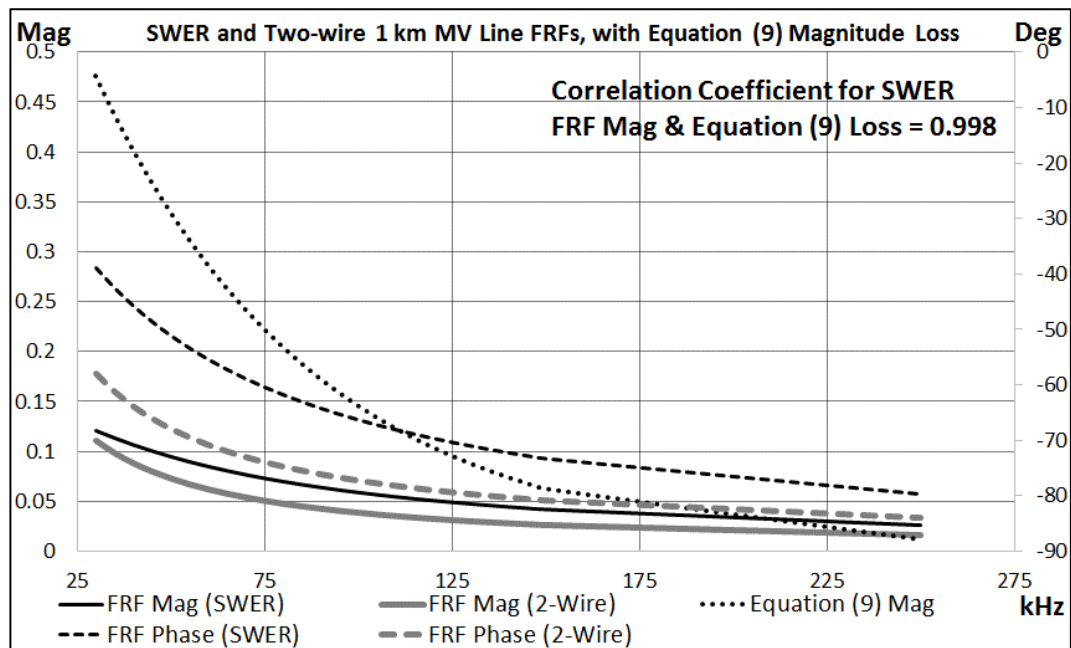


Figure 7.11 – Simulated FRFs of 1 km SWER and Two-wire MV Lines, Compared with Equation (9) Magnitude Loss

The magnitude response of both lines, for both lengths, are exponentially decaying, as was found for previous work reviewed in Section 3.2. This has been demonstrated by evaluating equation (8) to obtain power line loss for frequencies from 30 kHz to 250 kHz. The results are also plotted in Figure 7.11. It can be seen that the plot trends for the reviewed work and the SWER line FRF magnitude are similar, as indicated by the correlation coefficient of 0.99.

The magnitude plots for the 100m line length show that the Two-wire line attenuation is less than that of the SWER line, at the lower end of the spectrum, due to the added impedance of the earth return path. However, the Two-wire attenuation increases with frequency and tends to be equal to that of the SWER line, beyond 250 kHz. The phase plots for the 100m line length show that the line capacitance is very similar for both lines.

The magnitude plots for the 1 km line length show that the Two-wire line attenuation is now more than that of the SWER line. The phase plots for the 1 km line length show that the SWER line now has less capacitance than the Two-wire line. The plots also show that the magnitude response of the lines converge to a common average value, with distance.

#### 7.4.2 SWER and Two-wire MV Line ILs

Figures 7.12 and 7.13 summarize the results of the IL calculation for the 100 m and 1 km SWER and Two-wire MV lines.

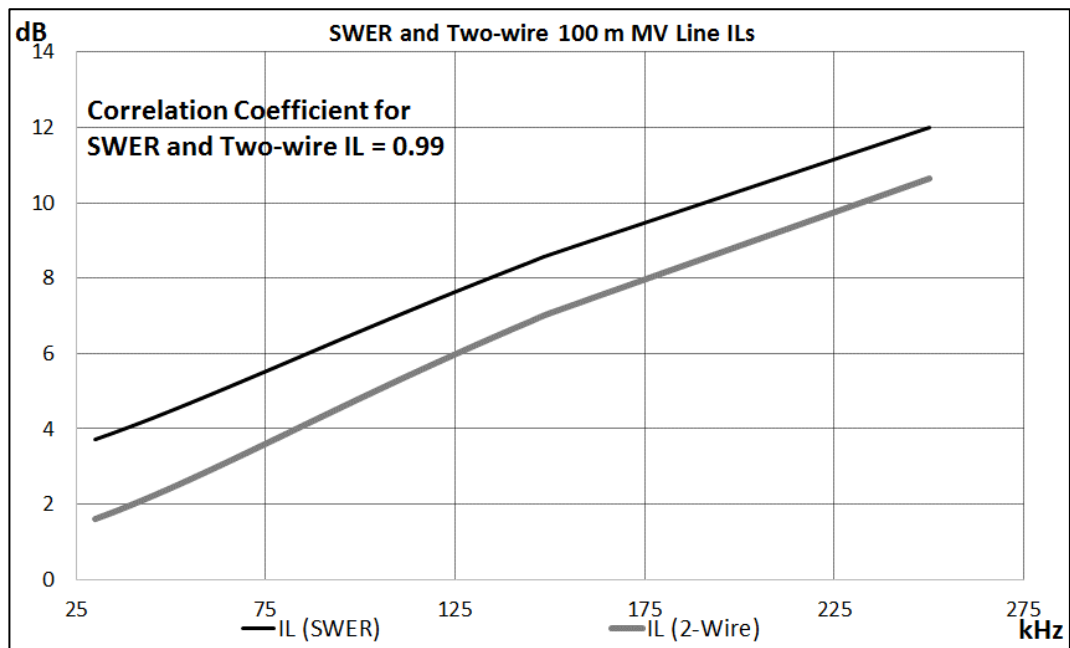


Figure 7.12 – Simulated ILs of 100 m SWER and Two-wire MV Lines

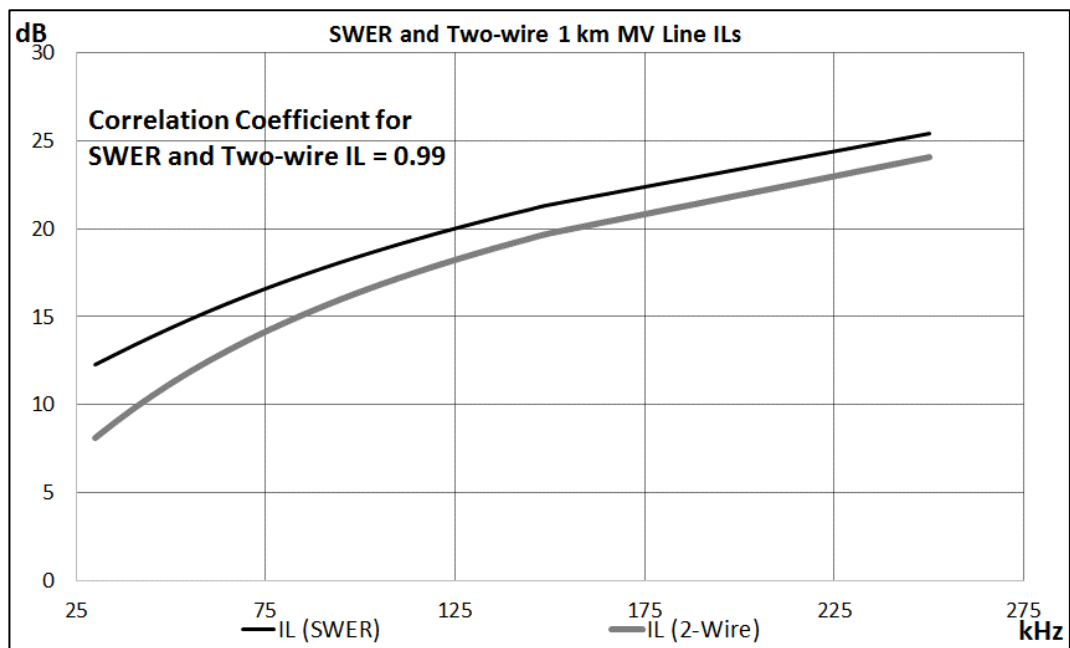


Figure 7.13 – Simulated ILs of 1 km SWER and Two-wire MV Lines

The line FRF and IL results for both line lengths show that the SWER line loss characteristics are comparable with those of the 2-wire line, with an approximately constant additional loss of 2 dB for the SWER MV line, compared with the Two-wire MV line, for both line lengths. This approximately constant loss difference is due to the close correlation of the plots, which gives a value of 0.99.

The final MV line NB-PLC models obtained also have bandwidth specifications in accordance with the original FRFs, which is between 30 kHz and 250 kHz.

## 7.5 MV Line NB-PLC Simulation

The results of PLC carrier simulation, not shown, reveal that the SWER line performs satisfactorily in terms of attenuation, at various frequencies and lengths. However, the phase shifts increase significantly with frequency. This indicates that bit errors may be significant, due to the displacements of the received bits from their specified symbol mapping positions [177, 178]. BPSK has a larger margin of error of up to approximately  $90^\circ$  due to its widely spaced symbol positions, followed by QPSK with approximately  $45^\circ$ , then 8PSK and 16 QAM with approximately  $22.5^\circ$ .

### 7.5.1 BERs for 100 m SWER MV line Simulation

Charts of the simulation BERs of the SWER MV line PLC model of length 100 m, for the various modulation methods, are provided in this section. The BER charts are virtually the same as those obtained from simulations of the Two-wire MV line model and therefore were not provided. Similarly, the BERs for the 1 km SWER line were virtually the same as those for the 100m SWER line, and therefore were also not provided.

The Bit Error Ratios (BERs) for the SWER channel, for a length of 100m, is shown in the charts of Figure 7.14.

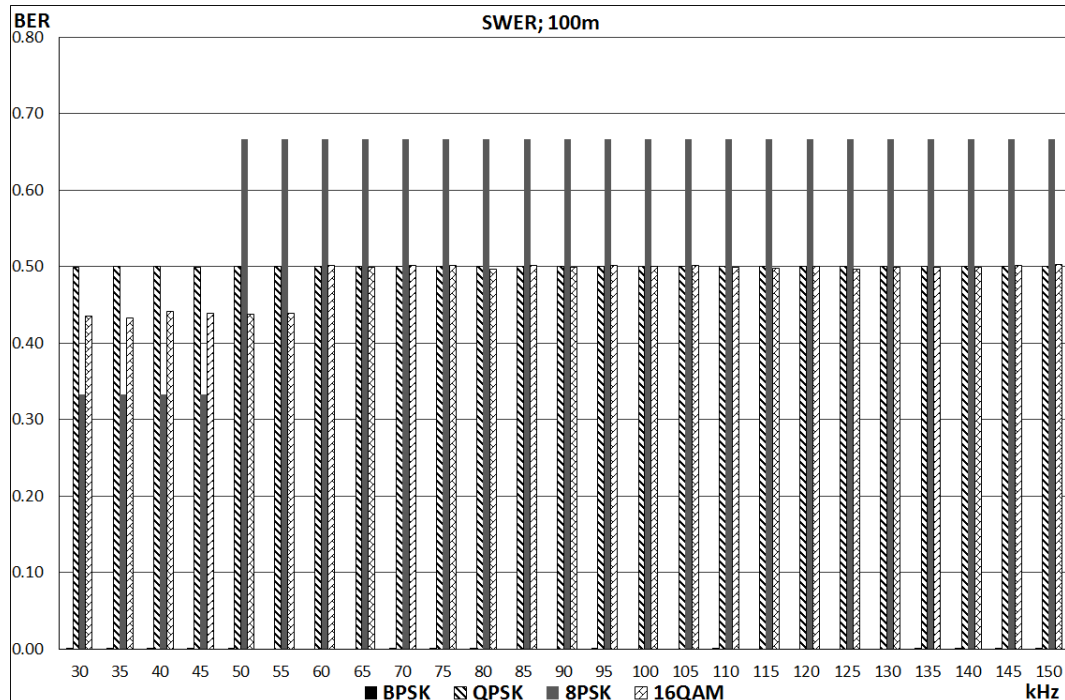


Figure 7.14 – BER for SWER Channel;  $l = 100\text{m}$

The charts show consistency in BER across the bandwidth, especially for BPSK and QPSK with values of 0 and 0.5 respectively. Between 60 kHz and 150 kHz, 16QAM is consistently 0.5, while 8PSK is approximately 0.67. Between 30 kHz and 60 kHz, the

values are lower at approximately 0.44 and 0.33 for 16QAM and 8PSK respectively. There is an increase in bit error with increased frequency as expected, but only for 8PSK and 16QAM. Moreover, the BERs of 8PSK are significantly higher than those of 16QAM, at 50 kHz and beyond.

These results are the statistical values for BER, where the energy per bit to noise power spectral density ratio ( $E_b/N_0$ ) varies. The maximum phase shift at 150 kHz is approximately  $-80^\circ$  as previously mentioned in Section 8.2, which is still within the tolerance for BPSK. Therefore,  $E_b/N_0$  may be considered minimal, giving a consistent BER value of zero when equation (1) is applied.

Between 30 and 150 kHz, the phase angle is between  $-60^\circ$  and  $-80^\circ$ , which is within the tolerance of  $45^\circ$ , i.e.  $90^\circ - 60^\circ = 30^\circ$ , for QPSK. This creates a phase offset which statistically mimics a channel with low  $E_b/N_0$ , of the order  $\leq 0.005$  when equation (1) is applied. This BER value allows approximately half of the bits to be accurately decoded. This same angle of  $30^\circ$  is however beyond the tolerance for 8PSK, thereby leading to higher error rates from about 50 kHz and beyond, for this modulation method.

The same situation applies to the other modulation BERs, with the  $E_b/N_0$  for 8PSK and 16QAM progressing from a relatively noisy to a very noisy channel, with increased frequency. Even though the phase offset tolerance for 8PSK and 16QAM are approximately the same, in some situations the BER for 8PSK is higher than that for 16QAM, under the same channel conditions. This is because of the larger number of symbols and by extension, bits that are available for demodulation in 16QAM. This leads to random statistical occurrences of correctly decoded bits that are higher than those for 8PSK.

The BERs for the SWER channel, for a length of 1000m, were virtually the same as those for the 100m length. The difference was that the 8PSK values increased from 0.33 to 0.67 between 30 kHz and 40 kHz, while the 16QAM values increased from 0.44 to 0.5 between 30 kHz and 55 kHz, thereby making all the BER values consistent throughout the bandwidth.

The BERs for the Two-wire channel, for a length of 100m, are virtually the same as those for the SWER line, for the same length. This is with the exception of the 8PSK value at 45 kHz, which increases from 0.33 to 0.67. The BERs for the Two-wire channel, for a length of 1000m, are exactly the same as those for the SWER line, for the same length. Therefore, the results for both the SWER and Two-wire MV line channels reveal that

though magnitude attenuation is relatively low at a maximum of -6 dB per 100m, significant phase impairments exist throughout the bandwidth.

## 7.6 Unenergized Through-transformer Channel NB-PLC Simulation

The Bit Error Ratios (BERs) for the various modulations for the unenergized 1 kVA and 15 kVA through-transformer PLC channel models in the LV to MV and MV to LV direction are given in Section 7.6.1, while the average bit power results for the channels are provided in Section 7.6.2.

### 7.6.1 BERs for Unenergized Through-transformer Channel Simulation

BERs for the various modulations for the unenergized 1 kVA and 15 kVA through-transformer PLC channel models in the LV to MV and MV to LV direction are given in the charts of Figures 8.6 to 8.9.

The BER values for the unenergized 1 kVA through-transformer channel in the LV to MV direction are summarized in the charts of Figure 7.15.

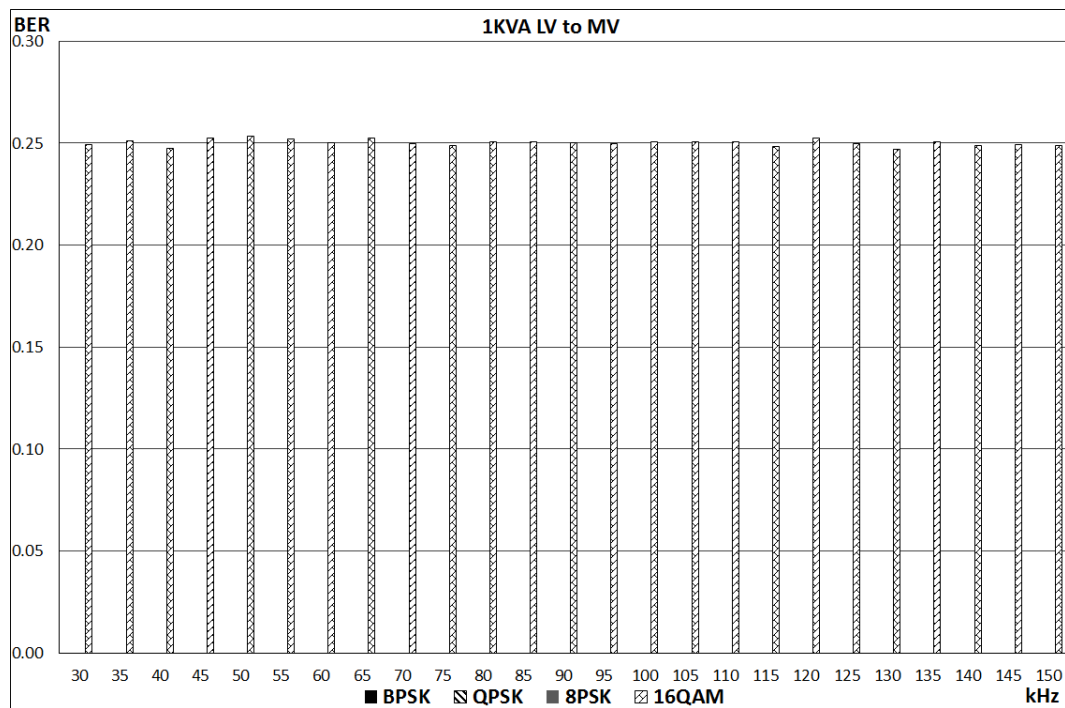


Figure 7.15 – BER for Unenergized 1 kVA Through-transformer Channel, LV to MV Direction

The charts reveal that all modulations result in approximately zero BER, with the exception of 16QAM at approximately 0.25, throughout the bandwidth.

The BER values for the unenergized 1 kVA through-transformer channel in the MV to LV direction are summarized in the charts of Figure 7.16.

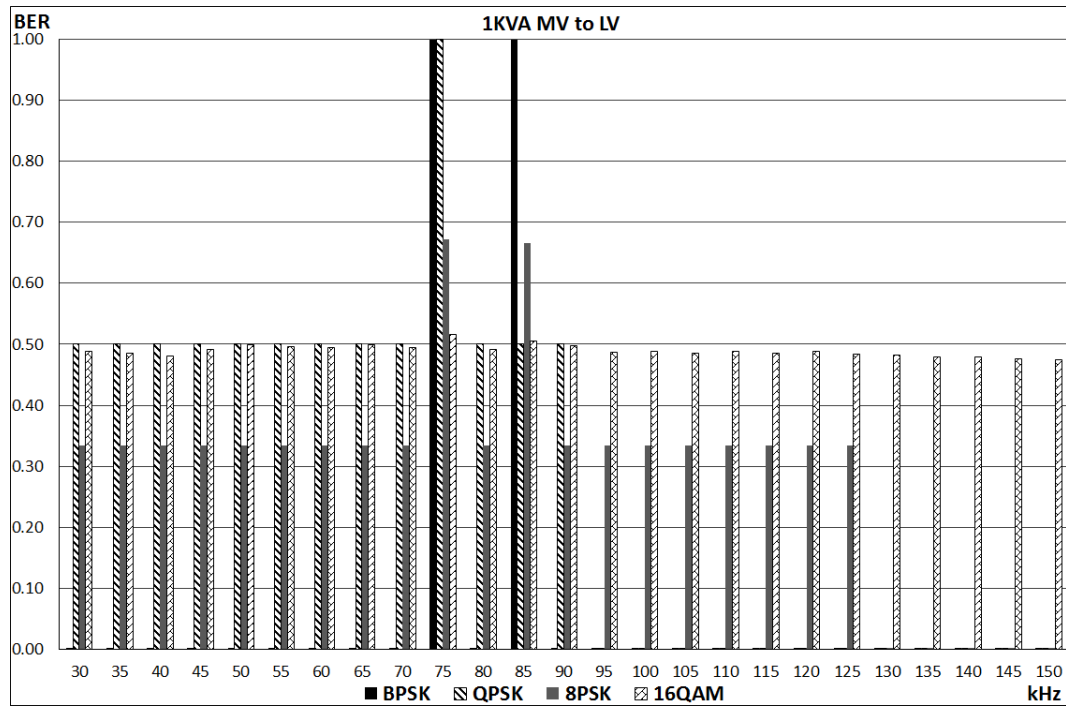


Figure 7.16 – BER for Unenergized 1 kVA Through-transformer Channel, MV to LV Direction

The charts show consistency in BER across the bandwidth for 16QAM, with a value of approximately 0.5. The BERs for BPSK are also consistent throughout the bandwidth at 0, with the exception of the maximum values of 1.0 at 75 kHz and 85 kHz. The BERs for QPSK are also consistent between 30 kHz and 90 kHz at approximately 0.5, with the exception of the maximum value of 1.0 at 75 kHz. Beyond 90 kHz, the QPSK BER is zero.

Similarly, the BERs for 8PSK are also consistent between 30 kHz and 125 kHz at approximately 0.33, with the exception of the values of 0.67 at 75 kHz and 85 kHz. Beyond 125 kHz, the 8PSK BER is zero. The BER values do not show any specific pattern, but it is clear that BPSK and QPSK modulation does not perform well at 75 kHz and 85 kHz, due to the channel characteristics at those frequencies, as shown in Figure 7.14. However, BPSK and QPSK perform excellently at frequencies between 95 kHz and 150 kHz. 8PSK also performs excellently between 130 kHz and 150 kHz.

The BER values for the unenergized 15 kVA through-transformer channel in the LV to MV direction are summarized in the charts of Figure 7.17.

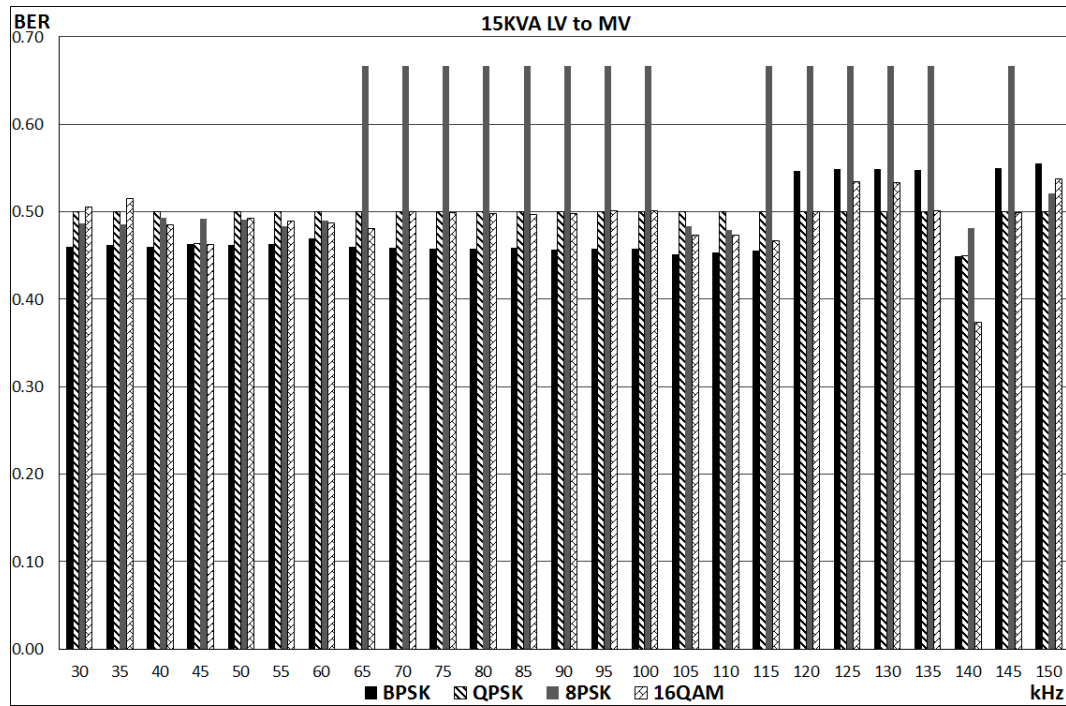


Figure 7.17 – BER for Unenergized 15 kVA Through-transformer Channel, LV to MV Direction

The charts show a generally high BER for all modulation methods, with reasonable consistency in BER across the bandwidth for BPSK, QPSK, and 16QAM, with a value of approximately 0.5. The BERs for 8PSK are also consistent between 65 kHz and 100 kHz, and 115 kHz to 135 kHz, at 0.67, and 0.5 elsewhere. However, outliers at lower values exist at the 140 kHz block, going as low as 0.36 for 16QAM. The charts show that the 15 kVA LV to MV channel characteristics of Figure 7.8 are generally unfavourable for PLC due to its high phase shift characteristics, especially using 8PSK modulation.

The BER values for the unenergized 15 kVA through-transformer channel in the MV to LV direction are summarized in the charts of Figure 7.18.



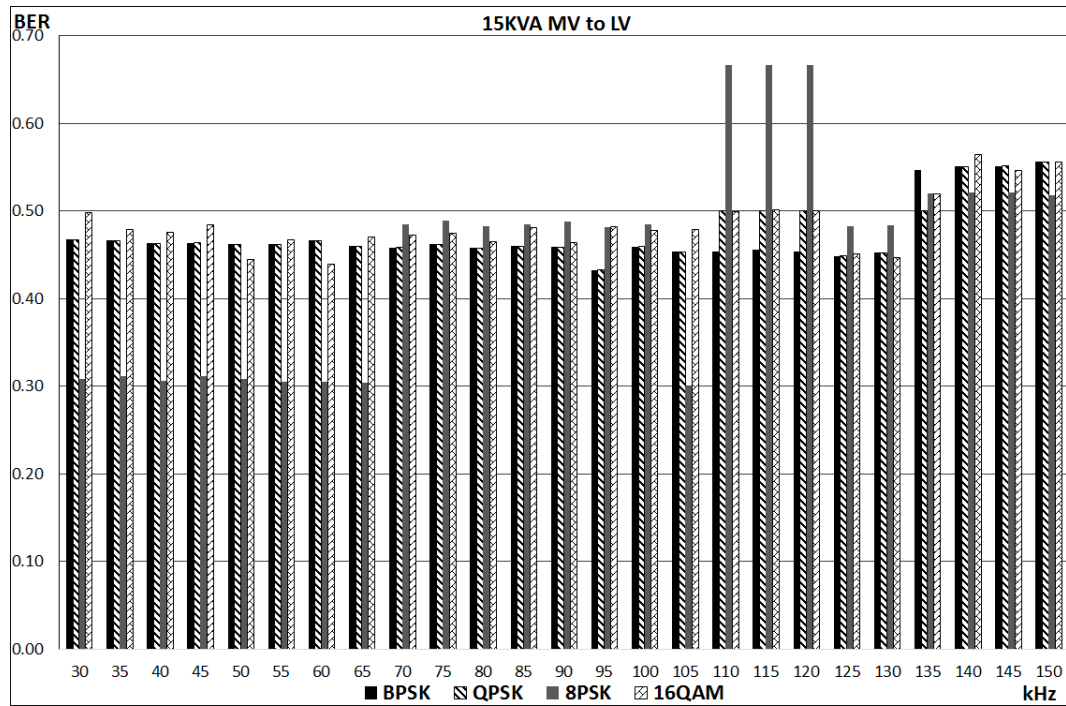


Figure 7.18 – BER for Unenergized 15 kVA Through-transformer Channel, MV to LV Direction

The charts once more show a generally high BER for all modulation methods, with reasonable consistency in BER across the bandwidth for BPSK and QPSK at approximately 0.45. The BER values for 8PSK increase with increased frequency, from 0.3 between 30 kHz and 65 kHz, 0.48 between 70 and 100 kHz, 0.67 between 110 kHz and 120 kHz, and approximately 0.5 between 125 kHz and 150 kHz. The charts show that the 15 kVA MV to LV channel characteristics of Figure 7.10 are also generally unfavourable for PLC, especially in the higher frequency range.

## 7.6.2 Unenergized Through-transformer Channel Average Received Bit Power

The average received bit power plots for the 1 kVA unenergized through-transformer PLC channels are shown in the plots of Figure 7.19.

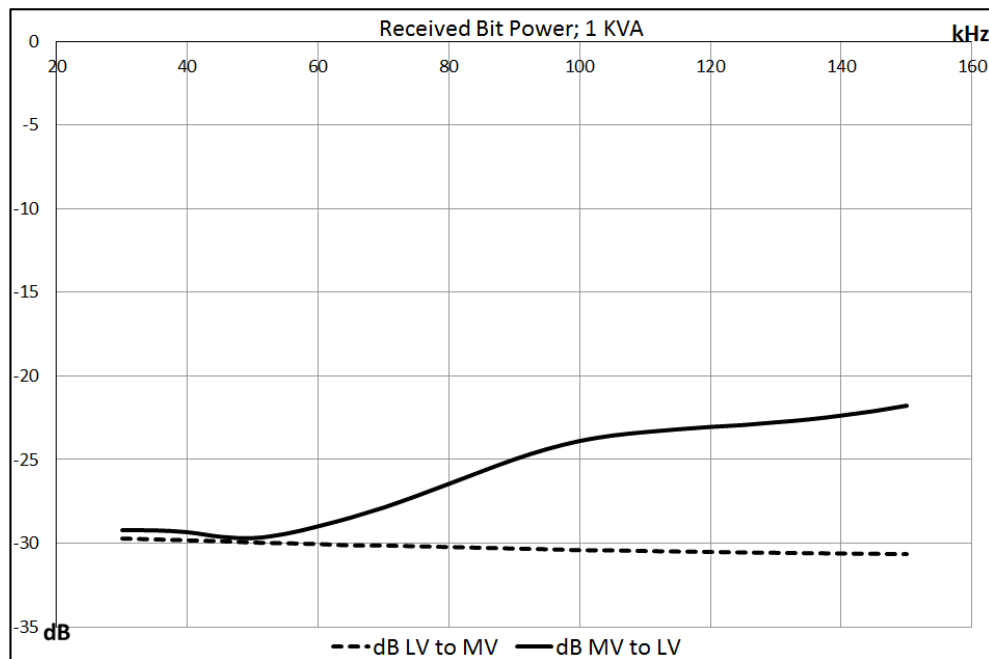


Figure 7.19 – Average Received Bit Power for Unenergized 1 kVA Transformer; input = 1W

The plots show that the channel has consistent but higher losses of -30 dB in the LV to MV direction, compared with decreasing losses of between -30 and -22 dB in the MV to LV direction, across the bandwidth for all modulation methods.

The average received bit power plots for the 15 kVA unenergized through-transformer channels are shown in the plots of Figure 7.20.

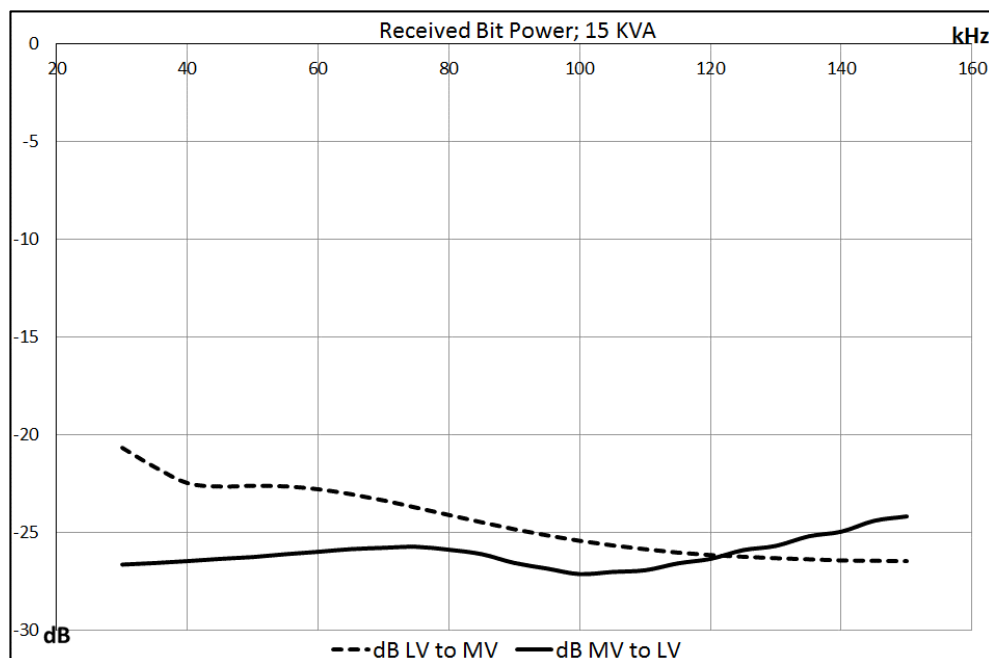


Figure 7.20 – Average Received Bit Power for Unenergized 15 kVA Transformer; input = 1W

The plots show that the channel has increasing losses of between -21 and -27 dB in the LV to MV direction, compared with gradually decreasing losses of between -27 and -24

dB in the MV to LV direction, across the bandwidth, for all modulation methods.

The average received bit power and the BER results for the unenergized transformer channels, particularly those for the 1 kVA transformer in the LV to MV direction, show how much the phase shifts associated with a communication channel affect signals based on phase shift modulation techniques [69]. The 1 kVA LV to MV channel has the least phase shift property, as shown in the Bode plot of Figure 7.12 with values between  $-5^\circ$  and  $-7.5^\circ$  throughout the bandwidth for a total variation of  $2.5^\circ$ . This is insignificant compared with those for the 15 kVA LV to MV and MV to LV channels shown in the Bode plots of Figures 7.8 and 7.10, and that of the 1 kVA MV to LV channel shown in the Bode plot of Figure 7.14.

## **7.7 Energized Through-transformer Channel NB-PLC Simulation**

The results of the simulation of the 1 kVA energized through-transformer channel magnitude and phase angle variations, using the energized through-transformer PLC simulation model developed in Section 6.4, are provided in this section. The incremental complex phase correlation coefficients, or simply phase correlations, are provided in Section 7.7.1, while the incremental BERs are provided in Section 7.7.2.

### **7.7.1 Incremental Complex Phase Correlation**

The incremental complex phase difference correlation coefficients, or simply phase correlation values, for the energized transformer channels are identical for all the modulation methods. In other words, they varied only with respect to energization levels. This is expected, as the complex phase differences are based on the phase variations of the through-transformer channel with energization. The correlation values for the 1 kVA through-transformer LV to MV PLC channel are summarized in the charts of Figure 7.21.

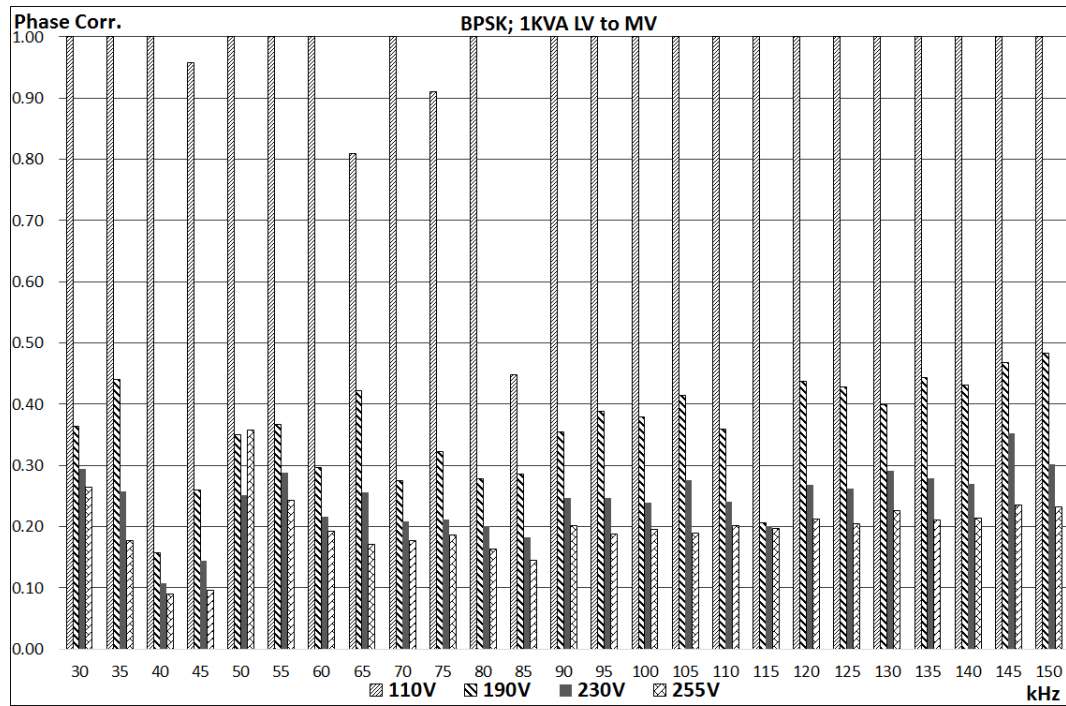


Figure 7.21 – Incremental Phase Angle Correlation for Signals Passing through Energized 1 kVA Transformer; LV to MV Direction

The charts show that, at 110 V energization, the incremental phase correlations are generally equal to 1, with a number of exceptions. This means that at this energization level, the complex phase differences between the channel input and output PLC signals in the LV to MV direction are very minimal throughout the bandwidth, with the exception of the 65 kHz and 85 kHz values of 0.8 and 0.45 respectively. The correlation value at 45 kHz of approximately 0.95 is above 0.9 and may be considered as satisfactory correlation.

The incremental complex phase difference correlations at 190 V are at an average of 0.35, which is poor. The severe outliers are found at 40 kHz and 115 kHz with values of approximately 0.15 and 0.2 respectively. The correlations at 230 V are at an average of 0.25, which is also poor. The severe outliers are found at 40 kHz and 45 kHz with values of approximately 0.1 and 0.15 respectively. The correlations at 255 V are the worst at an average of 0.15. The severe outliers are found at 40 kHz and 45 kHz with values of approximately 0.08.

The incremental complex phase difference correlation values for the 1 kVA transformer in the MV to LV direction were also found to be identical for all the modulation methods simulated. The values are summarized in the charts of Figure 7.22.

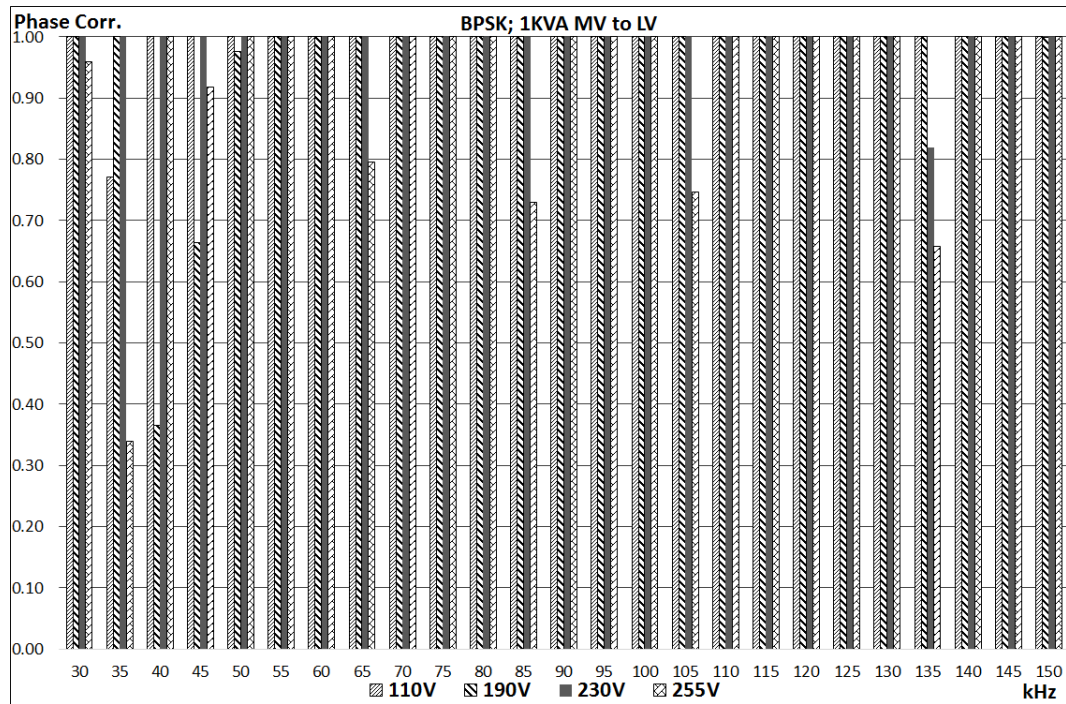


Figure 7.22 – Incremental Phase Angle Correlation for Signals Passing through Energized 1 kVA Transformer; MV to LV Direction

The charts show that the incremental complex phase differences between the channel input and output signals in the MV to LV direction are very minimal throughout the bandwidth, for all energization levels. The blocks that do not contain 1.0 correlations are at 35 kHz, 40 kHz, 45 kHz, 65 kHz, 85 kHz, 105 kHz and 135 kHz. Of these blocks, the correlation outlier at 110 V energization is found at 35 kHz, with a value of approximately 0.77. The outliers at 190 V are found at 40 kHz and 45 kHz with values of approximately 0.35 and 0.65 respectively. The outlier at 230 V energization is found at 135 kHz, with a value of approximately 0.8, while those at 255 V are found at 35 kHz, 65 kHz, 85 kHz, 105 kHz and 135 kHz with values of approximately 0.35, 0.8, 0.73, 0.75 and 0.66 respectively.

### 7.7.2 Incremental BER

The incremental BER values for BPSK modulated data passing through the energized 1 kVA transformer in the LV to MV direction are summarized in the charts of Figure 7.23.

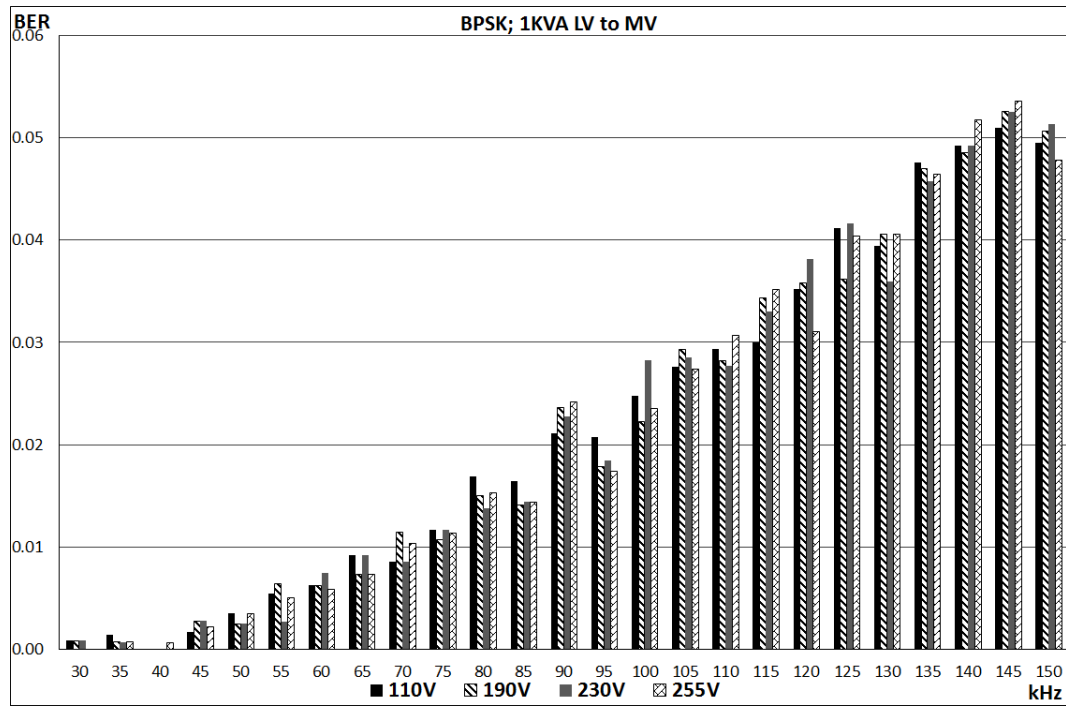


Figure 7.23 – Incremental BER for BPSK Signals Passing through Energized 1 kVA Transformer; LV to MV Direction

The charts show an increase in bit error with increased frequency, as expected. They also show that there are differences in bit error with energization, at some frequencies. These differences with energization are not consistent, i.e. the highest and lowest BER values are not associated with any particular energization values. However, outliers within each frequency block exist, these are found at 55 kHz for the 230 V value, 100 kHz for the 230 V value, 120 kHz for the 255 V value, 125 kHz for the 190 V value, and 130 kHz for the 230 V value.

The incremental BER values for QPSK modulated data passing through the energized 1 kVA transformer in the LV to MV direction are summarized in the charts of Figure 7.24.

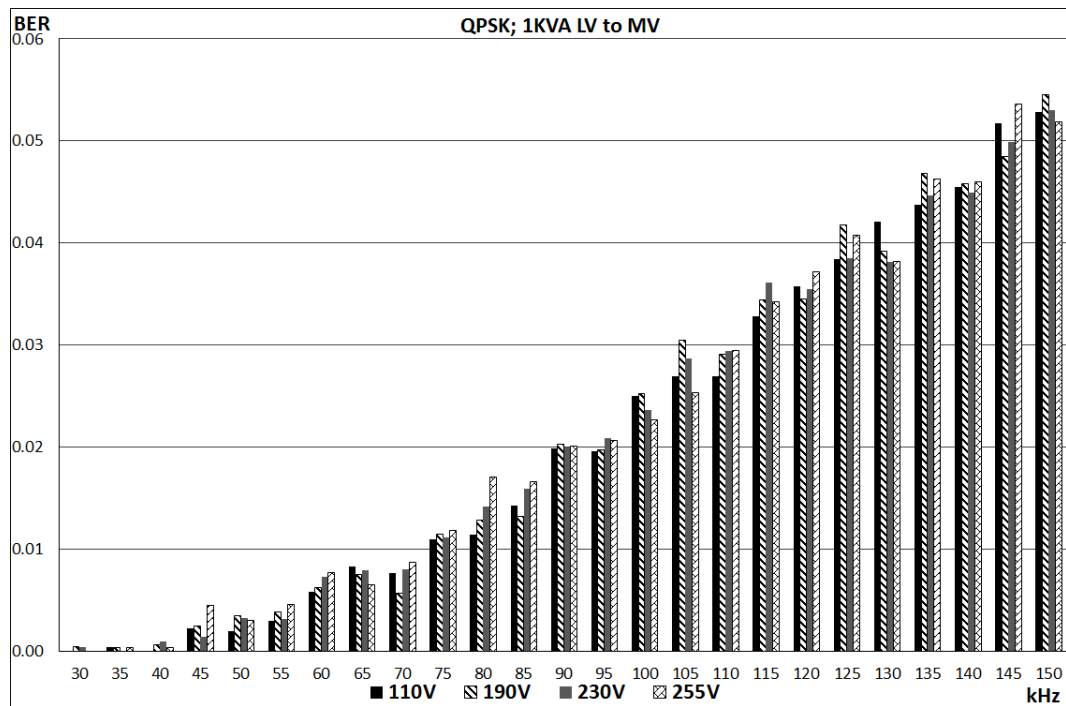


Figure 7.24 – Incremental BER for QPSK Signals Passing through Energized 1 kVA Transformer; LV to MV Direction

The charts show BER values similar to those for BPSK modulation, as expected. An outlier exists at 45 kHz for the 255 V value.

The incremental BER values for 8PSK modulated data passing through the energized 1 kVA transformer in the LV to MV direction are summarized in the charts of Figure 7.25.

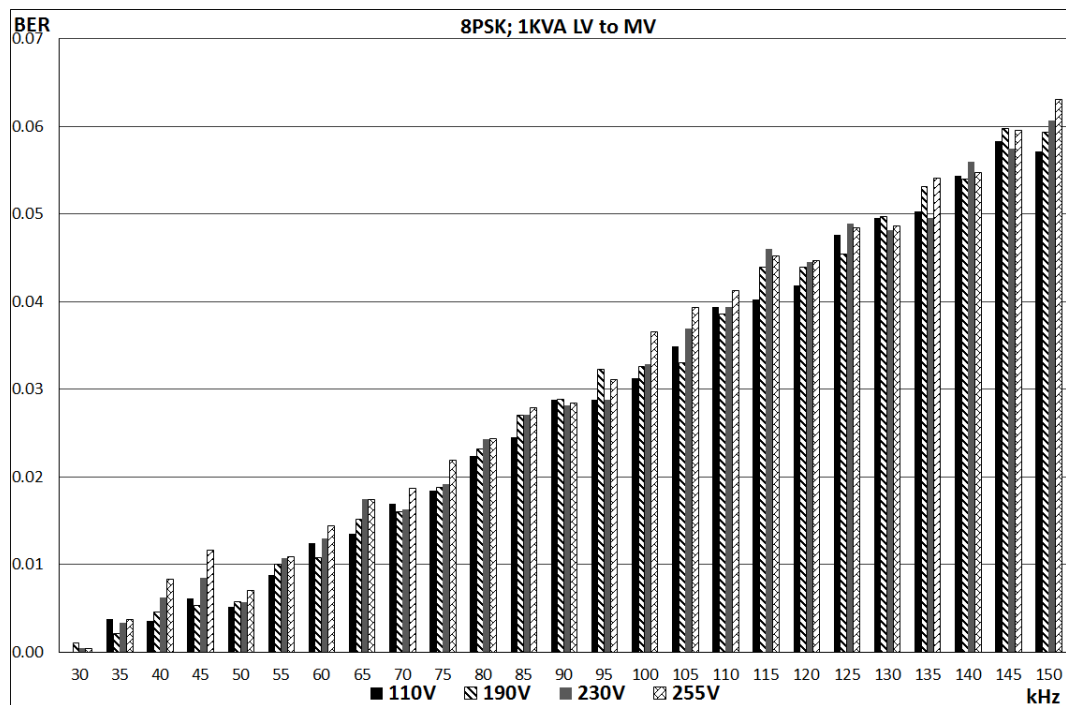


Figure 7.25 – Incremental BER for 8PSK Signals Passing through Energized 1 kVA Transformer; LV to MV Direction



The charts show higher BER values compared with those for BPSK and QPSK, as expected. The outliers are at 35 kHz for the 190 V value, 45 kHz for the 255 V value, 75 kHz for the 255 V value, 100 kHz for the 255 V value, 105 kHz for the 190 V value, and 135 kHz for the 230 V value.

The incremental BER values for 16QAM modulated data passing through the energized 1 kVA transformer in the LV to MV direction are summarized in the charts of Figure 7.26.

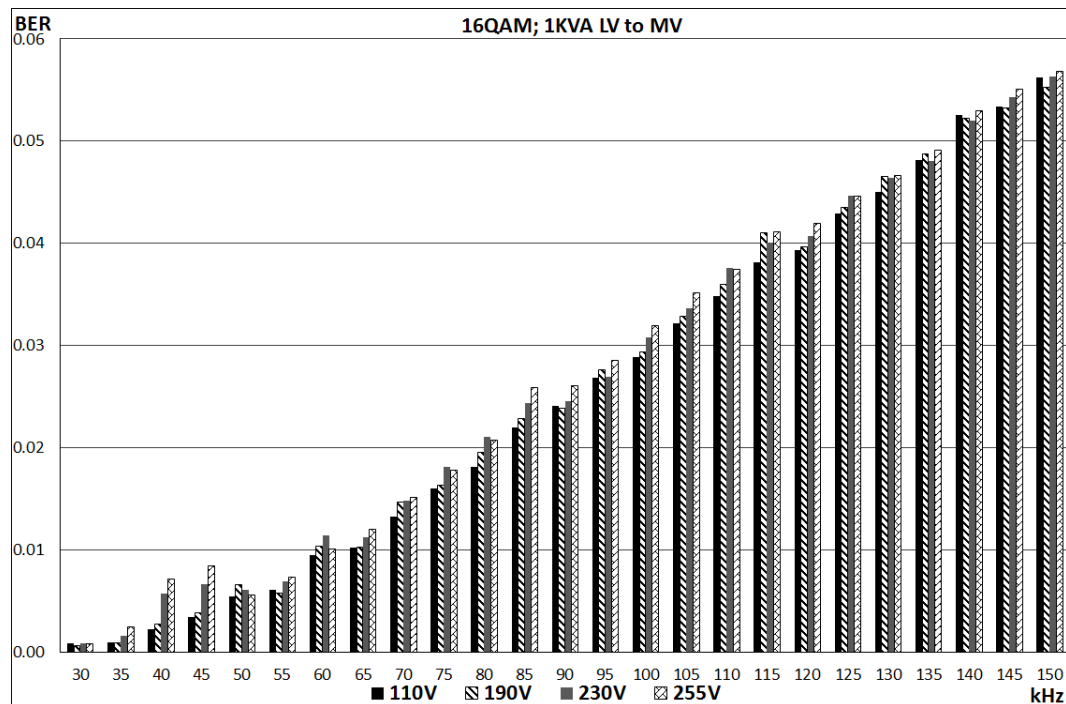


Figure 7.26 – Incremental BER for 16QAM Signals Passing through Energized 1 kVA Transformer; LV to MV Direction

The charts show BER values similar to those for BPSK and QPSK. However, the differences in bit error with energization are consistent, with the BER generally increasing with energization across the bandwidth. The outliers are at 35 kHz to 45 kHz for the 230 V and 255 V values.

The incremental BER values for modulated signals passing through the energized 1 kVA transformer in the MV to LV direction are summarized in Appendix I. They all show the existence of outliers at particular frequencies. They also show that the BER increases with frequency, with the values for BPSK, QPSK, and 16QAM being similar. The BERs for 16QAM modulation were also found to be consistent with energization level.

However, each given MV to LV direction chart of a particular modulation differs from its corresponding chart for the LV to MV direction, with significantly lower BER values



across energization levels at particular frequencies. These differences in values for the MV to LV and LV to MV BERs are not very significant for the BPSK and QPSK modulated signals but are more observable for 8PSK and 16QAM modulated signals.

The plots of the average incremental BER for the 8PSK and 16QAM signals passing through the energized 1 kVA transformer are shown in Figure 7.27. Zero average incremental BER represents the BER for the unenergized transformer, assuming near-perfect channel mitigation.

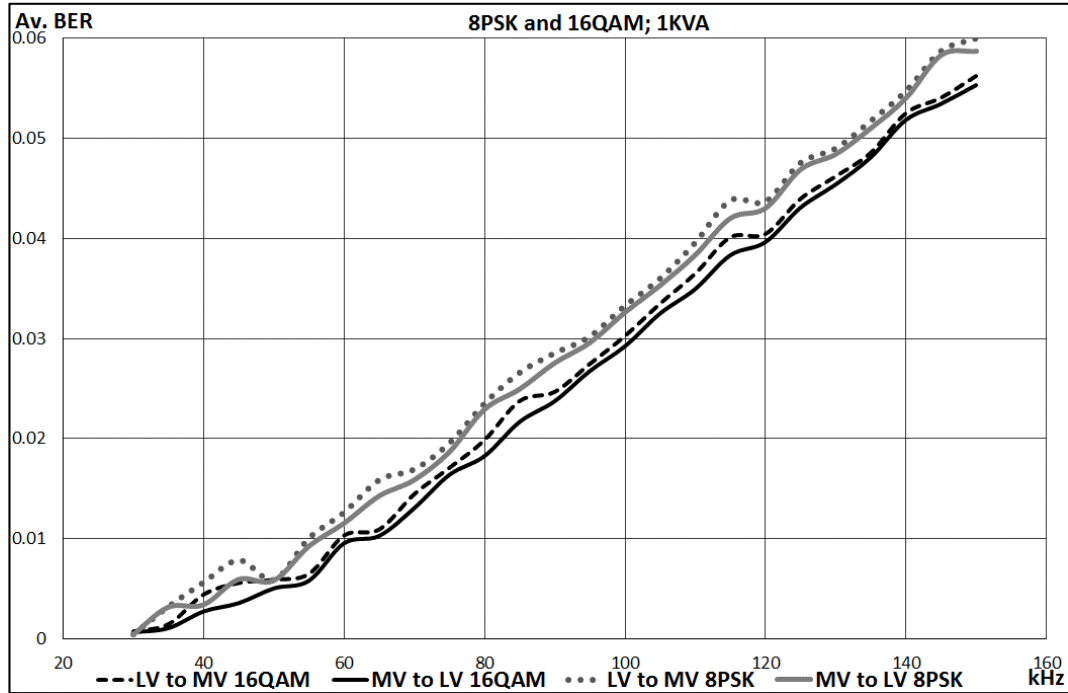


Figure 7.27 – Average Incremental BER for 8PSK and 16QAM Signals Passing through Energized 1 kVA Transformer

The plots show that the average BER values are higher for 8PSK modulation, compared with those for 16QAM. Statistically, this is expected for high  $E_b/N_0$  channels that exhibit significant phase shifts, as previously found for the MV line channels. More importantly, the plots show that the 8PSK and 16QAM average incremental BERs in the LV to MV direction are consistently higher than those for the MV to LV direction.

## 7.8 Conclusion

This chapter presented the results of the characterization of the transformers and MV lines, in the form of FRFs, as well as results that verify the PLC simulation model of energized through-transformer channels of distribution transformers. As best as can be determined, this method has not been previously identified and demonstrated in relation to PLC simulations of energized through-transformer channels, and therefore forms the

third original and significant contribution to knowledge, through the research outlined in this thesis.

The results obtained from simulations of SWER and Two-wire MV lines, and 1 kVA and 15 kVA through-transformer PLC channels, were also presented in this chapter. The results revealed that low channel phase values were generally the main determinant for error-free data transfer, especially with 8PSK modulation. It was also found that the PLC data throughput for SWER MV lines was indistinguishable from that of regular single phase Two-wire MV line of similar construction, thereby establishing the suitability of SWER MV lines for PLC implementation. Improvements to the BER rates recorded for the SWER MV line may be obtained by applying suitable mitigation strategies.

This chapter also presented results obtained from NB-PLC simulations of the energized through-transformer channels of the 1 kVA transformer. The results show differences in data throughput for each level of energization, and for each modulation method.

In terms of actual PLC implementation, the implications of the PLC throughput results obtained in this chapter are analysed and explained in Chapter Eight.

# Chapter Eight – Discussion and Analysis

## 8.1 Introduction

This chapter provides discussions and subsequent analysis of the results obtained from the characterization and simulation of the MV line and through-transformer channels for NB-PLC purposes, as detailed in Chapters Five to Seven. A discussion and analysis of the results obtained from the SWER MV line characterization process, which is centred on the developed earth path impedance characterization method, is provided in Section 8.2 together with a derivation of an expression for empirical earth path impedance estimation. A discussion on the SWER and Two-wire MV line PLC simulation results, which led to an evaluation of PLC on SWER MV lines, is provided in Section 8.3.

A discussion of the results obtained from the characterization of the 0.5 kVA, 1 kVA and 15 kVA through-transformer channels is provided in Section 8.4, while a discussion and analysis of the effects of energization levels of distribution transformers on PLC signal throughput is provided in Section 8.5. A discussion on the suitability of through-transformer channels for MV/LV PLC implementation is provided in Section 8.6, a discussion of the general feasibility of continuous MV/LV PLC on distribution grids is provided in Section 8.7, and the conclusion is given in Section 8.8.

## 8.2 Derivation of Expression for Empirical Earth Path Impedance

The requirement for accurate determination of long power transmission lines is responsible for the development of equations that improve the accuracy of the estimation of transmission line characteristics of power lines consisting of aerial conductors, such as (11) to (18). This improvement is achieved by considering the influence of the earth plane in electromagnetic field formulations [179, 180]. This consideration is necessary because the earth plane exists everywhere in tandem with the power line, and hence is convenient for serving as a relatively low impedance path to safely drain fault and phase sequence currents back to the 50 Hz power source. Hence, the general earth mass is termed 'earth return,' in the power system domain.

Although the presence of return current is inevitable in the daily operation of power systems, its magnitude in comparison with the magnitude flowing in the aerial conductors is negligible at low distances. However, the influence of the field interactions between the aerial conductors and earth plane increases with distance, leading to significant losses

due to field radiation. The field formulations represented by equations (11) to (18) are therefore based on voltage interactions between the conductors and the imperfect earth plane, rather than on actual current flow through the earth path. This is understood from the nature and underlying theory of the equations, which are based on field theory of images of current-carrying conductors, and hence yield only an inductive term for the contribution of the earth path to loop inductance, or a capacitive term for the contribution of the earth path to shunt admittance. This is evidenced by equations (15) and (16).

Therefore, these power system equations for estimating the contribution of the earth path to the total line impedance of aerial conductors may be used in applications outside power systems where the contribution of the earth path to the total resistance and inductance of the line is all that is required. As the earth path is capacitive in nature, this capacitive term, which is not available in most of these equations, will be missing. In addition, the characteristics of the earthing system are not provided for in these equations.

In the case of PLC on SWER, because of the reference to the term ‘earth return’ in the equations, as evidenced by (14), it could be assumed that these equations will be sufficient to provide accurate results when an analytical approach is used to characterise earth path impedances for PLC purposes. Therefore, exclusive use of these equations as a basis for modelling line-to-earth path PLC channels is erroneous, as was shown in the literature review. Unfortunately, this error can easily be made, as was done in [154].

Earth path characterization strategies based on soil parameter estimation are possible. The estimation of resistivity alone will lead to the exclusion of the capacitive reactance of the earth path, which results in phase errors at the lower end of the NB-PLC spectrum, as shown. An overestimation of soil resistivity and permittivity is also likely, to compensate for the absence of the grounding system impedances, as was done in [181].

Even though a phase-to-earth path PLC channel may be less popular than a phase-to-phase one [23], an accurate earth path model for PLC applications is nonetheless important, because it is still considered as a viable option in regular 2/3/4-wire systems [154, 182]. For PLC on SWER systems, the earth return path is the only practical one readily available [144, 145, 150, 183]. Therefore, so long as a proper earth path model is not used in situations where phase-to-earth PLC is being considered, the results obtained may be misleading.

The study on earth path impedances outlined in this thesis also found that soil relative permittivity has much less influence than resistivity, in agreement with previous work

[158]. This is an advantage because it reduces the number of variables required for obtaining earth path models based on the developed method. Equations (22) to (25) demonstrate how the total impedance of an earth path, with the earthing system and superfluous material considered, may be correlated with the measured voltage drop along a section of the earth path, to obtain the impedance of a given path within the section. The measurement platforms need to be similar in terms of instrumentation, depths, and lengths [166], to apply the same scaling factor  $F$  to another earth path. However, it is not necessary to replicate the platform in multiple locations, if a location with earth characteristics average to the various installation locations is selected at the onset.

A major determining factor for earth path impedance is soil ionic and moisture retention properties. Since this varies seasonally, a fixed earth path impedance measurement platform similar to the one described in this paper may be used to obtain  $K$  or  $F$  together with low frequency soil resistivity and relative permittivity measurements when required. These measurements may be correlated with previously measured scaling factors.

The results provided in Chapter Five show that there are conflicting approaches to the use of equations (11) to (18). In addition, the differences in earthing systems and the fact that soil properties vary with weather, type, and superfluous content, make it imperative to establish the high-frequency electrical characteristics of a typical earth path. This is best achieved by the methods described in this thesis, rather than staking significant resources on developing a PLC channel model based solely on existing analytical equations.

The lossy capacitor model of the earth path impedance, which forms the basis of the earth path characterization method, provides a means of formulating a transfer function representation of a general earth path. This is useful for situations where the earth path capacitance and resistance values of all the earth path components are known.

Considering only the impedance of the lossy capacitor earth path model portion of the hybrid SWER line shown in Figure 4.4, if the input voltage  $V_{in}$  of the SWER line is designated as unity, the per-unit length transfer function of the empirically determined earth path impedance, based on the lossy capacitor earth path model, will be:

$$TF_{EarthEmp} = \frac{V_{out}}{V_{in}} = 1 - i[R_{SE} + Z_P] \quad (32)$$

where  $Z_P$  is the per-unit length parallel RC combination of  $C_E$  and  $R_{LOSS}$ , given by:

$$Z_P = \frac{R_{LOSS}(1 - j\omega C_E R_{LOSS})}{\omega^2 C_E^2 R_{LOSS}^2 + 1} \quad (33)$$

Equation (32) allows for the per-unit length transfer function of the additional earth path impedance to be estimated by obtaining the individual values of soil capacitance, earthing system resistances, and all other superfluous impedances associated with a particular earth path, through measurements with specialised equipment [44, 45, 166]. This transfer function may then be merged with the transfer function of the aerial conductor, which may be analytically determined in a straightforward manner using equations (11) to (15).

Equation (32) is therefore important because, in practical situations, the probability of the presence of superfluous material within an earth path that is expected to run for lengths of kilometres at a time for PLC purposes, is high. These equations, therefore, represent tangible expressions of the relationship between existing equations used for analytical SWER line characterization for PLC applications such as equations (11) to (15), which have been shown to provide limited accuracy, and the consideration of practical factors that influence earth path impedances.

Equation (32) may be regarded as a fitting function for obtaining an accurate per-unit length SWER line model when different cables are being considered for a SWER MV line with similar earthing systems and soil characteristics as those encountered in the earth path characterization experiment.

Therefore, being a tangible mathematical expression, (32) is a bonafide representation of the first original and significant contribution.

### **8.3 Evaluation of PLC on SWER MV Lines**

The purpose of carrying out the comparisons between data throughput on a SWER MV line and a Two-wire MV line of the similar construction was to take advantage of the availability of vast amounts of literature on PLC on regular Two-wire lines. These may be used to evaluate the performance of a typical SWER MV line. The comparison of the FRF magnitudes of the SWER and Two-wire MV lines with that of a typical long-distance power line reviewed in literature, as shown in Figure 7.11, reveals that the power lines all share a basic exponential decaying loss trend.

It was stated in Section 7.5 that the BERs of the SWER MV line are essentially the same as those for the Two-wire MV line of similar construction, up to 1 km length. The comparison between the SWER and Two-wire FRFs provided by Figures 7.10 and 7.11 reveals that the phase properties of the lines are similar. However, there is an indication that the SWER line phase properties may be improved in practical applications. An average height of 3.5 m above the earth surface was used for the experiments, while a

minimum regulatory height of 7 m is specified for SWER MV lines. This increase in height will, therefore, translate to a reduction in line capacitance.

The PLC simulation results provided in Chapter Seven in conjunction with those for the earth path characteristics provided in Chapter Five, indicate that SWER narrowband characteristics are generally good enough to achieve PLC, but will degrade with increasing frequency, necessitating the use of repeaters at closer intervals if long distance communication is desired at higher narrowband frequencies. Since specialised earthing systems such as three-dimensional earthing grids are routinely used to reduce earthing impedance in power grids [156, 184], the application of the developed earth path characterization method, which is based on single earth rod pairs, is also useful for estimating the upper threshold of the earth path impedance.

#### **8.4 Effect of Insulation Dielectric Polarization on Distribution Transformer High Frequency Impedance**

From previous work detailed in the literature review, it is known that signal propagation between power transformer primary and secondary windings occur mainly through the capacitive path. Topologically, this path is parallel to the inductive path [185].

The plots of the 1 kVA LV to MV maximum phase angle variation between the input and output voltages shown in Figure 6.11 reveal that there is a generally consistent increase in phase angle with transformer energization across the bandwidth. Parallel LC circuit analysis establishes that a positive increase in phase angle at a particular frequency of observation indicates either a decrease in capacitive reactance or an increase in inductive reactance, provided the initial and final LC resonance frequencies do not cross the frequency of observation [186].

If the high inductive reactances of distribution transformers at high frequencies are considered, then it is not likely that a significant amount of the test signals will pass through the inductive path. Therefore, the inductive path of the 1 kVA transformer may be assumed to have a fixed reactance value at each frequency point regardless of energization, in relation to the high frequency signals. As mentioned in Chapter Six, this assumption is necessary to provide simplicity for the analysis of the signal variations.

Therefore, a fixed, high value of inductance leads to the conclusion that the phase angle variation observed at each frequency point is mainly due to changes in the capacitive reactance of the shunt paths. These changes in shunt capacitive reactance are heavily

influenced by the cyclic dielectric polarization of the transformer insulation, in accordance with instantaneous transformer energization, as explained in Section 2.8.2 and reviewed in Section 3.4.

By virtue of the high inductive reactance at high frequencies, it is unlikely that the inductive-capacitive combination of the through-transformer channel will reach resonance within the bandwidth of interest. As a result, a positive increase in phase angle, in conjunction with fixed inductive reactance at a frequency of observation that is lower than the LC resonant frequency, can only be achieved by a capacitive reactance decrease. This capacitive reactance decrease is responsible for the observed general increase in output voltage shown in Figures 6.8 and 6.9, with increased transformer energization.

These all signify a decrease in the impedance of the through-transformer channel impedance. Based on the experimental design, it is therefore established that the observed input and output voltage variations and the accompanying phase shifts shown in Figures 6.6 to 6.11 are mainly due to the cyclic dielectric polarization of the 1 kVA transformer insulation, which occurs in direct proportion to transformer energization levels. Dielectric polarization has the effect of varying the amount of available charge carriers within the oil-paper insulation medium, which translates to varying capacitance, with a commensurate variation in capacitive reactance [62].

The input voltage variations shown in Figures 6.6 and 6.7 are due to the dielectric polarization effects that influence the capacitive reactance of the shunt paths between the live and neutral terminals of the secondary (LV) side of the transformer. This means that the shunt path at the LV terminal exhibits minimal capacitive reactance at 30, 50, 85 and especially 115 kHz, as shown in the figures. This effect is reflected in the minimum, and especially the maximum, output voltage variation plots of Figures 6.8 and 6.9 respectively. It is also reflected in the maximum phase angle variation plots of Figure 6.11, as the general increase in phase angle is not applicable for the 255 V plot at 50 kHz, and the 190 V, 230 V and 255 V plots at 115 kHz.

The maximum output and phase angle variation results, given in Figures 6.9 and 6.11 respectively, show that up to 109 % RMS magnitude variation at approximately 35 kHz, and 8.5° phase angle variation at approximately 40 kHz, can occur with signals passing through the 1 kVA transformer in the LV to MV direction, when energized at the nominal 50 Hz 230 V. This variation is dynamic, i.e. it is in accordance with the instantaneous value of the energizing voltage, and will most probably affect data signals based on phase angle modulation techniques, depending on the quality of the PLC equipment [12, 31].



The analysed results of the energized through-transformer PLC channel simulation provided in Section 8.5 will fully establish this.

The results from the 1 kVA and 15 kVA through-transformer channel experiments are fully supported by those from the 0.5 kVA through-transformer channel experiments. Figure 6.3 shows that the attenuation at all the energization levels are approximately equal, at 60 kHz, 85 kHz, and 115 kHz. These are points of minimum attenuation, where the through-transformer channel has a low inductive reactance, making the differences due to dielectric polarization less distinct. However, at 70 kHz and 100 kHz, which represent points of maximum attenuation, the through transformer channel has a high inductive reactance, and therefore the differences due to dielectric polarization are more distinct. The points of maximum attenuation at 130 kHz and 150 kHz, and the point of minimum attenuation at 140 kHz indicate that major resonance may have occurred at approximately 120 kHz due to increased distributed capacitive reactance, making these points capacitive-dominant [63].

It has also been established from the results of through-transformer FRF determination provided in Chapter Seven, that the practice of bonding reduces the capacitive reactance and by extension, the impedance of through-transformer paths. However, there is a possibility that bonding increases the scope of the high frequency signal variation, due to the availability of more capacitive shunt paths.

By virtue of the prevailing conditions on power grids, PLC equipment that has been manufactured to high standards to withstand the harsh conditions on power grids, ought to handle the scale of signal variations reported in this chapter [187]. However, these results were obtained from brand new transformers, operating under controlled laboratory conditions, which are conducive to the objective of experimental observations. Consequently, if it is considered that the dielectric properties of transformer insulation degrade over time, then there is a possibility that these observed effects could be significant for older transformers, regardless of their size [188].

If the resonance phenomena of transformer windings at high frequencies are also factored into this situation, the PLC signal will encounter regions of loss and gain in the time domain, which may not be easily estimated analytically [83]. Therefore, the high frequency signal variation results provided in Chapter Six have demonstrated the advantage of empirical measurements on energized distribution transformers, for the purpose of through-transformer PLC channel characterization.

The input voltage variation results summarized in Figures 6.6 and 6.7 reveal that the input voltage variations, and by extension the impedance, across distribution transformer primary or secondary terminals, could be significant at particular frequencies and energization levels. This means that high frequency signals passing through a PLC interface that is connected to a distribution transformer port in an around-transformer configuration, as shown in Figures 2.4 and 2.5, can also be affected by the transformer's dielectric polarization status. Consequently, it is imperative to consider that these variations encountered by high frequency signals impinging on distribution transformers have the potential to affect PLC on distribution grids generally.

## **8.5 Implications of Insulation Dielectric Polarization on Through-transformer PLC**

The applied magnitude variation values for the energized 1 kVA transformer for the LV to MV direction shown in Figure 7.15 go up to a maximum of 1.12, while those for the MV to LV direction shown in Figure 7.17 go up only to a maximum of 1.035, which is significantly lower. Based on the magnitude variations, there is a higher amount of signal in the LV to MV direction, which should result in lower BER values. This discrepancy is explained by the phase angle variation values for the LV to MV direction shown in Figure 7.16, with a maximum value of  $5^\circ$ , which are significantly higher than those of the MV to LV direction shown in Figure 7.18 with a maximum value of  $-2.7^\circ$ .

The effects of these phase angle variations are represented by the incremental complex phase difference correlation values for the 1 kVA transformer in the LV to MV and MV to LV direction, shown in Figures 8.12 and 8.13 respectively. The complex phase differences of the signals in the MV to LV direction were found to be consistently much less than those of the signals in the LV to MV direction, thereby leading to the conclusion that the amount of phase angle variation of the energized through-transformer PLC channels have a larger influence on the PLC signal incremental BER, compared with the magnitude variations. This is generally the case for PSK and QAM modulated signals.

Figure 7.27 demonstrates that a difference of approximately  $7^\circ$  in average phase variation values between the LV to MV and MV to LV direction negatively affects PLC data integrity more than a difference of approximately 5% in average voltage magnitudes for both directions, at 40 kHz. This confirms that phase impairments generally affect PLC based on phase modulation more than magnitude impairments [189]. Therefore, the implications of transformer insulation dielectric polarization on through-transformer PLC

is that, although there is a reduction in impedance with increased transformer energization and dielectric polarization, this reduction comes with a commensurate amount of phase angle variation. The extent of impedance reduction depends on the physical dimensions and material characteristics of the distributed capacitances and inductances of the transformer insulation system and windings respectively, and the interactions between the reactances they exhibit at particular frequencies.

As these interactions between inductive and capacitive reactances of distribution transformers at high frequencies are very complex, as evidenced by resonance behaviour of their impedance characteristics, only a generalisation of the effects of dielectric polarization on through-transformer PLC data throughput may be made from the scope of research presented in this thesis. This generalisation is that the dielectric polarization of distribution transformer insulation is inversely proportional to the cyclic impedance of its through-transformer channels and directly proportional to the bit error ratio of the through-transformer channels. This is expressed as:

$$P(t)_{TRANS} = \frac{k_1}{Z_{LV2MV}} = k_3 BER_{LV2MV} \quad (34)$$

$$P(t)_{TRANS} = \frac{k_2}{Z_{MV2LV}} = k_3 BER_{MV2LV} \quad (35)$$

Polarization  $P(t)$  is given by equation (5),  $Z_{LV2MV}$  refers to the LV to MV channel impedance,  $Z_{MV2LV}$  refers to the MV to LV channel impedance,  $BER_{LV2MV}$  refers to the LV to MV bit error ratio, and  $BER_{MV2LV}$  refers to the MV to LV bit error ratio.

$k_1$  and  $k_2$  represent constants containing variables of the physical and material composition of the transformer, specific to the LV to MV and MV to LV directions respectively, and  $k_3$  represents the constant containing variables of the modulation method used to produce the PLC data. These constants are also frequency-dependent.

To reiterate, the phenomenon of dielectric polarization is well known. However, its effects on through-transformer PLC data throughput has not been previously studied. The discussion and analysis provided in this chapter have shown that this phenomenon is of general and considerable interest for PLC implementation, because even though the 15 kVA transformer did not show significant variation, it is likely that transformers of similar rating and construction, which are routinely found on SWER grids, may have insulation that has degraded over time. Such transformers may negatively affect PLC implementation on distribution grids, generally.

If the fact that SWER grids suffer from voltage regulation issues [47, 190] is factored into the discussion, then the importance of determining the extent of signal variations due to this phenomenon when considering through-transformer PLC on SWER grids becomes clear. The possibility that larger errors than those reported in this thesis may occur in the field becomes apparent. Therefore, the need to carry out empirical tests on energized transformers, or determine the extent of dielectric polarization of transformer insulation through some other means, before considering through-transformer PLC, has been established by the PLC simulation results provided.

Therefore, being tangible mathematical expressions, (34) and (35) are bonafide representations of the second original and significant contribution.

## **8.6 Suitability of Through-transformer Channels from Unenergized and Energized PLC Simulation Data Throughput**

The average incremental BER values for BPSK and QPSK modulated signals in the LV to MV and MV to LV direction were found to be the same or lower than those for 8PSK and 16QAM, due to the relative immunity of BPSK and QPSK to PLC channel phase variations, compared with 8PSK and 16QAM modulated signals [191]. Therefore, the main determinant to what modulation method may best suit PLC through distribution transformers that exhibit signal variation due to dielectric polarization will be its unenergized PLC channel characteristics.

If the BERs of the unenergized through-transformer channels are high, such as those of the 15 kVA transformer shown in Figures 8.8 and 8.9, it may be better to utilise low order modulation methods such as BPSK and QPSK, regardless of how much variation the energized channel exhibits. However, if the BERs of the unenergized through-transformer channels are low, it may be better to use high order modulation, specifically 16QAM. 8PSK modulation may be used when the phase angle variations are minimal, and the magnitude variations are significant enough to cause substantial BER with 16QAM modulation because 8PSK does not perform well under phase impairments [192]. This is also the case for energized through-transformer PLC channels, as shown in Figure 7.27.

The 1 kVA and 15 kVA unenergized through-transformer average received bit power plots, shown in Figures 8.10 and 8.11, indicate that some signal processing and amplification may be necessary to achieve favourable  $E_b/N_0$  values through these PLC channels. In that case, either of the through-transformer PLC configurations for high-loss channels, shown in Figure 2.7, may be used in conjunction with suitable repeaters. The

decision on where to locate repeaters, in relation to PLC interfaces and distribution transformers, is also an important consideration for grid-wide implementation of PLC [171].

## **8.7 Feasibility of Continuous PLC on Distribution Grids**

The results from the simulation of the MV line PLC channels have revealed that the main obstacle to achieving reliable PLC on typical SWER MV line is its phase shift characteristics. It may be difficult to apply any physical changes to the line, due to the line spacing specifications and inherent capacitive nature of the earth path. However, micro-mitigation strategies for correcting channel impairments are routinely applied in modern digital communication [193]. Therefore, it may be safely concluded that PLC, using popular digital modulation and error correction techniques such as those found in Orthogonal Frequency Division Multiplexing (OFDM) communication, can be implemented on SWER lines, to achieve reliable data transfer for distances of up to 1 km [192].

The nature of SWER MV lines places additional constraints on safety, due to the danger of line to earth faults from grid apparatus. This danger will extend to any extra installations between the MV and LV sections of SWER grids, such as the implementation of the around-transformer configuration shown in Figures 2.4 and 2.5, for the purpose of PLC implementation on SWER grids. Also, the SWER system has been firmly established as a low-cost option for power supply to rural communities, and therefore the primary consideration for PLC implementation on SWER grids ought to also be based on low-cost approaches. Therefore, it will be a huge advantage to achieve through-transformer PLC on SWER grids.

Passing PLC signals directly through transformers is a first choice for implementing cost-effective MV to LV PLC in distribution grids. However, this strategy should be encouraged only if reliable, and reasonably efficient communication throughput can be achieved. This suggests that lower costs and benefits ought to be adequately balanced by determining the suitability of applying the through-transformer strategy, on a case-by-case basis.

The results from the simulation of the unenergized through-transformer PLC channels have revealed that both magnitude and phase shifting characteristics of the through-transformer paths are possible obstacles to achieving reliable PLC through distribution transformers. The results also show that through-transformer PLC channels have regions

of relatively low BER, mainly due to low phase values from resonance phenomena. This then establishes that resonance phenomena may be used as an advantage for achieving through-transformer PLC on a variety of distribution transformers [171].

The procedures for PLC interface design and implementation described in Section 4.4.1 may be used as a guide to select and match appropriate line traps, coupling capacitors, filters and communication units to the impedances of the power grid components. The specific impedances to be matched are the characteristic impedances of the MV lines for PLC interfaces, for the MV grid sections, and the impedances of the secondary terminals of the transformers, for the LV grid sections. In recent times, coupler and line trap technology enables low insertion/extraction losses and high blocking impedances respectively in an efficient manner, to minimise the need for repeaters [194, 195]. This then signifies that if low-loss PLC interface components can be properly matched, the low-cost configurations shown in Figure 2.6 may be adequate for achieving efficient through-transformer PLC.

The BERs for the unenergized 1 kVA LV to MV and MV to LV PLC channels show that if the 1 kVA transformer existed on a distribution grid, achieving PLC through it using the configuration of Figure 2.6 may be feasible. In the LV to MV direction, the charts of Figure 7.15 show approximately zero BER for BPSK, QPSK, and 8PSK throughout the bandwidth, while in the MV to LV direction, the charts of Figure 7.16 show zero BER for BPSK, QPSK and 8PSK between 130 kHz and 150 kHz.

This situation provides the perfect opportunity to apply the communication macro-mitigation strategy of tone masking [31]. A tone mask for the MV to LV direction may be implemented anywhere between 130 kHz and 150 kHz, while another one for the LV to MV direction may be implemented anywhere between 30 kHz and 130 kHz, thereby making full duplex communication possible, if required [12].

The BERs for the 15 kVA LV to MV and MV to LV channels show that if the 15 kVA transformer existed on a distribution grid, achieving PLC through it using the through-transformer configurations of Figures 2.6 or 2.7 may not be feasible. The charts of Figures 8.8 and 8.9 show rather high BER values for all modulation methods, which point to the need for signal conditioning throughout the bandwidth in both directions. In this case, therefore, the around-transformer configuration shown in Figure 2.4 may be considered.

If the conditions on both the MV and LV lines are unfavourable, the around-transformer configuration of Figure 2.5 may be considered. This configuration also provides the

opportunity for tone masking, enabling couplers **1** and **3** to be combined to form a single hybrid PLC coupling unit. The configuration of Figure 2.5 for high-loss channels, therefore, best suits the conditions for achieving PLC across the MV/LV grid boundary represented by the 15 kVA transformer.

The Bode plot of the 15 kVA LV to MV channel shown in Figure 7.8 reveals that the region with the lowest magnitude attenuation exists between 30 kHz and 60 kHz, while the region with the lowest phase values, in this low attenuation area, is between 40 kHz and 45 kHz. This corresponds to the lower frequency region in Figure 7.17 where the BERs for QPSK and 16QAM show values of up to 0.5.

Therefore, an amplify and forward (AF) repeater may be used to boost BPSK, QPSK and 16QAM modulated signals in the LV to MV direction between 30 kHz and 45 kHz, and also boost 8PSK modulated signals in the MV to LV direction between 50 kHz and 65 kHz. These areas give relatively low BERs of 0.33. Alternatively, a decode and forward (DF) repeater may be used to reconstruct the actual data rather than boost the weak modulated signals, to ensure that errors are not propagated [53, 98].

## **8.8 Conclusion**

The originality and significance of the various aspects of the research outlined in this thesis have been demonstrated by the discussions and analysis provided in this chapter. A discussion on, and analysis of, the results from the SWER MV line characterization provided for the synthesis of a fitting function. This function may be used to merge empirically determined earth path capacitances and their lossy shunt resistances, earthing system resistances, and other incidental impedances, to analytically determined powerline parameters over a lossy earth plane. An evaluation of the potential for PLC on SWER grids was also provided.

The effect of the dielectric polarization process of the distribution transformer insulation system, on the transformer's general high frequency impedance characteristics, was also discussed. This was followed by a discussion on, and analysis of, its implications for through-transformer PLC. This analysis resulted in general expressions for this effect on through-transformer PLC data throughput, expressed as BER. The determination of the suitability of through-transformer channels, and the feasibility of continuous PLC implementation between MV and LV sections of distribution grids, from PLC simulation results, was also discussed.

## Chapter Nine – Conclusion

This thesis has presented a number of approaches to characterising and modelling power grid components, namely MV lines and distribution transformers, for the purpose of carrying out PLC simulations and implementations on MV and LV grid sections. Specifically, a SWER MV line was characterised and modelled, resulting in an original and significant contribution to knowledge.

Through-transformer PLC channel characterization experiments were also carried out, with the results being used to model unenergized and energized through-transformer channels of single phase MV/LV transformers. The transformer characterization and modelling efforts resulted in two more original and significant contributions to knowledge.

Section 10.1 describes the original and significant contributions made through the research described in this thesis, while Section 10.2 provides a few recommendations for further research.

### 9.1 Original and Significant Contributions of Research to Knowledge

Previous work on developing SWER line models for PLC applications revealed that analytical methods that were used to characterise SWER lines did not provide accurate representations, thereby creating a knowledge gap for PLC implementation on SWER MV grids. Therefore, experiments to characterise and model a SWER MV line were carried out. These experiments lead to the first original and significant contribution to knowledge made through the research outlined in this thesis, which is the development of a hybrid empirical/analytical method for characterising earth path impedances in the lower NB-PLC frequency region. The method directly results in a hybrid SWER MV line model. The contribution is important because it provides a means of balancing accuracy with speed in the process of characterising earth path impedances for the purpose of implementing line-to-earth PLC on distribution grids, such as SWER grids.

Apart from the cost implications, implementing an around-transformer MV/LV PLC configuration is a significant safety hazard, due to the possibility of line to earth faults occurring via the bypass channel. Therefore, the research outlined in this thesis also involved experiments to characterize through-transformer channels, by the propagation of high frequency signals through energized 0.5 kVA, 1 kVA and 15 kVA 11 kV/230 V transformers. These experiments led to the identification of cyclic variation of high



frequency signals passing through distribution transformers, in accordance with the transformer energization levels. This cyclic variation has been found to be due to the dielectric polarization of distribution transformer insulation.

The dielectric polarization of distribution transformer insulation has not been previously studied in relation to PLC through distribution transformers. Therefore, the second original contribution to knowledge made through the research outlined in this thesis is the determination of the relationship between the dielectric polarization of the insulation system of distribution transformers and the quality of through-transformer PLC. The contribution is important because voltage regulation is a significant problem in certain types of distribution grids, including SWER grids. Frequent voltage fluctuations may lead to commensurate changes in data throughput, which may result in degraded PLC performance, as has been shown in the thesis.

The successful implementation of micro and macro PLC channel mitigation strategies are a function of the accuracy of models of the grid components used in carrying out the research efforts. The models should be capable of faithfully replicating the characteristics of the energized power grid components, in relation to the applied PLC signals. Therefore, the third original and significant contribution to knowledge made through the research outlined in this thesis is a method for developing simulation models of energized through-transformer channels, for the purpose of PLC simulation.

## **9.2 Research Shortcomings and Challenges**

A few shortcomings and challenges were faced in the course of carrying out the research outlined in this thesis. The most significant of these were:

1. The current source used for constant current injection into our platforms had a compliance voltage of only approximately 25 volts RMS. This limited the magnitude of constant current waveforms attainable, when high impedances were encountered. However, it was considered a good choice because it had excellent performance for high reactance loads, such as transformer windings.
2. Tektronix AC/DC probes were used to measure the constant current waveforms. Unfortunately, those class of probes were found to have low sensitivity at current levels lower than 10 mA. This limited the maximum frequency that could be attained for the transformer measurements to 150 kHz, rather than 250 kHz.

3. There were no voltage probes available to measure ac voltages higher than 5 kV RMS, and so no voltage measurements could be performed on the primary side of the transformers while they were energized. However, this was a minor limitation.

### **9.3 Recommendations for Further Research**

A few recommendations for further research are provided in this section, covering earth path characterization, through-transformer PLC channel characterization and modelling, and optimization of PLC on power grids.

#### **9.3.1 Earth Path Characterization**

The scaling factors derived from the measurement platform used in the earth path characterization method contains length and depth variables. The relationship between the scaling factors  $F$  and  $K$  and the variables  $x$ ,  $L$ ,  $d'$  and  $d$  as described by equations (22) to (25) can be determined by additional experimentation. Assuming a homogeneous earth path, the length variables  $x$  and  $L$  may be easily correlated, based on existing equations for geometric factors of measurement arrays. The patterns between injection rod depth  $d$  and measurement rod depth  $d'$ , as shown in Figures 5.6 and 5.7, can be explored deeper.

This will be well suited for PhD research, as practical soils are stratified into many layers, each with unique properties. This will cause multi-path effects during high frequency signal propagation, which will be dependent on path lengths, current injection depths and earthing system configurations.

#### **9.3.2 Aerial Conductor Characterization**

Additional research on aerial conductors is also necessary. This is because some aerial conductors are specified as low-loss, mostly due to their smooth-bodied spiralling construction. More experimentation is required to establish concrete correlations between conductors of different design and construction and their high frequency characteristics.

#### **9.3.3 Through-transformer PLC**

There is an advantage to achieving reliable and cost-effective PLC signal transfer between MV and LV grid sections by passing the signals through distribution transformers. This provides sufficient motivation to study further how distribution transformers affect PLC signals passing through them. The transformers used in the experiments described in this thesis were brand new and hence contained uncontaminated oil-paper insulation. Since the transformers could exhibit the observed signal variation, there is a high probability

that other transformers with some amount of contamination in their insulation system could produce more signal variation.

As the capacitive shunt paths are the primary channels for PLC signal transfer through distribution transformers, the relationship between the physical and electrical properties of distribution transformers and the mechanism of dielectric polarization of the insulating medium, which is usually oil-paper but could be natural or forced convection air and paper, needs to be further studied. Specifically, quantifiable variables and equations need to be developed for estimating the amount of variation PLC signal may experience while passing through distribution transformers.

This may be done by exploring the flexibility of using spice simulators with white box transformer models, especially those represented as lumped n-sections of R-L-C-M parameters. In such a case, the C components may be specified as fractional capacitors, whose values may be scaled in accordance with the transformer insulation dielectric polarization process. Alternatively, the direct relationship between the insulation permittivity and impedance may be explored, which may then be applied in expanding equation (34) and (35) further. This offers the advantage of including the inherent resonance effects of the through-transformer paths in the analysis.

This will also be well suited for PhD research, as the number and complexity of the variables are significant.

### **9.3.4 Transformer Characterization and Modelling**

Studies on distribution transformers, which may also include transformer co-optimization for power and PLC applications, will require the characterization and modelling of energized distribution transformers with as much detail as possible. A constraint encountered during the course of this research was obtaining a simple but accurate means of creating static models of the variations measured and quantified empirically. The variations may be classified as non-linear. However, the common tools available in MATLAB system identification toolbox may not be adequate on their own to estimate the measured behaviour.

The practice of electrical bonding of transformer LV terminals to the transformer tank and earth is common worldwide. The results provided in this thesis shows that there are differences between the high frequency characteristics of transformers with bonded and unbonded LV terminals. Therefore, the effect of this practice on transformer

characteristics needs to be further investigated through adequate through-transformer channel characterization and modelling.

### **9.3.5 Grid-wide PLC Optimization**

As a consequence of developing accurate transformer and line models, optimization of PLC interface components for proper impedance matching with grid components, and implementation of micro and macro mitigation strategies, can be explored. The high frequency impedances of the primary and secondary ports of distribution transformers vary significantly, depending on the type and rating. As it is unlikely that the same type of transformer will be used throughout a distribution grid, an opportunity exists for grid-wide improvement of PLC networks. This may be done by optimizing the high frequency impedances of the PLC interfaces, transformer ports, and repeaters with the high frequency impedances of the MV and LV lines connected to them. This will enable further reduction of the costs associated with PLC on a modern smart grid.

## References

- [1] H. C. Ferreira, L. Lampe, J. Newbury, and T. G. Swart. (2010). *Power Line Communications : Theory and Applications for Narrowband and Broadband Communications over Power Lines (1 ed.)*. Available:  
<http://AUT.ebib.com.au/patron/FullRecord.aspx?p=530034>
- [2] G. Ledwich, P. Martino, F. Calderon, and C. Gaunt, "International practices in Rural Electrification CIGRE SC-C6 working group (Coli 2007)," *IWD Topic E*, 2007.
- [3] D. F. Barnes, *The Challenge of Rural Electrification: Strategies for Developing Countries*: Earthscan LLC, 2010.
- [4] H. Rudnick, J. Mutale, D. Chattopadhyay, and R. Saint, "Studies in Empowerment: Approaches to Rural Electrification Worldwide," *IEEE Power and Energy Magazine*, vol. 12, pp. 35-41, 2014.
- [5] A. Zomers, "Remote Access: Context, Challenges, and Obstacles in Rural Electrification," *IEEE Power and Energy Magazine*, vol. 12, pp. 26-34, 2014.
- [6] N. Hosseinzadeh, J. E. Mayer, and P. J. Wolfs, "Rural Single Wire Earth Return distribution networks – Associated problems and cost-effective solutions," *International Journal of Electrical Power & Energy Systems*, vol. 33, pp. 159-170, 2// 2011.
- [7] N. Hosseinzadeh and S. Mastakov, "Load Modelling for Medium Voltage SWER Distribution Networks," in *Australasian Universities Power Engineering Conference, 2008. AUPEC '08.* , 2008, pp. 1-6.
- [8] C. W. Holland, "Single wire earth return for remote rural distribution-reducing costs and improving reliability," *Maunsell Ltd., Auckland, New Zealand*, 2005.
- [9] N. Hosseinzadeh, J. E. Mayer, and P. J. Wolfs, "Rural Single Wire Earth Return distribution networks – Associated problems and cost-effective solutions," *International Journal of Electrical Power & Energy Systems*, vol. 33, pp. 159-170, 2/5/2011.
- [10] Sagemcom. (July 2017). *Smart Grid Suite*. Available:  
<http://www.sagemcom.com/smart-city/smart-grid/>
- [11] J. Duplex, S. p. Gosswiller, and S. b. Fagnoni, "A better knowledge of electricity consumption for residential customers through the Linky smart meter," 2013.
- [12] A. J. Viterbi and J. K. Omura, *Principles of digital communication and coding*: Courier Corporation, 2013.
- [13] B. Hamilton and M. Summy, "Benefits of the Smart Grid [In My View]," *IEEE Power and Energy Magazine*, vol. 9, pp. 104-102, 2011.

- [14] S. M. Amin and B. F. Wollenberg, "Toward a smart grid: power delivery for the 21st century," *IEEE Power and Energy Magazine*, vol. 3, pp. 34-41, 2005.
- [15] EPRI. (July 2017). *Report to NIST on the Smart Grid Interoperability Standards Roadmap (10 August 2009 ed.)* [Report]. Available: [http://collaborate.nist.gov/twiki-sggrid/pub/SmartGridInterimRoadmap/InterimRoadmapFinal/Report\\_to\\_NISTAugust10.pdf](http://collaborate.nist.gov/twiki-sggrid/pub/SmartGridInterimRoadmap/InterimRoadmapFinal/Report_to_NISTAugust10.pdf)
- [16] P. Shah and K. Gehring, "Smart Solutions to Power the 21st Century: Managing Assets Today for a Better Grid Tomorrow," *IEEE Power and Energy Magazine*, vol. 14, pp. 64-68, 2016.
- [17] K. Bhat, V. Sundarraj, S. Sinha, and A. Kaul, "IEEE Cyber Security for the Smart Grid," *IEEE Cyber Security for the Smart Grid*, pp. 1-122, 2013.
- [18] C. Gellings, "Estimating the costs and benefits of the smart grid: a preliminary estimate of the investment requirements and the resultant benefits of a fully functioning smart grid," *Electric Power Research Institute (EPRI), Technical Report (1022519)*, 2011.
- [19] S. Canale, A. D. Giorgio, A. Lanna, A. Mercurio, M. Panfili, and A. Pietrabissa, "Optimal Planning and Routing in Medium Voltage PowerLine Communications Networks," *IEEE Transactions on Smart Grid*, vol. 4, pp. 711-719, 2013.
- [20] A. Cataliotti, D. D. Cara, G. Marsala, A. Ragusa, and G. Tinè, "Electromagnetic immunity analysis of a new interface device with power line communication for smart grid and energy storage applications," in *2013 IEEE 17th International Symposium on Power Line Communications and Its Applications*, 2013, pp. 214-219.
- [21] "IEEE Standard for Power-Line Carrier Line-Tuning Equipment (30 kHz to 500 kHz) Associated with Power Transmission Lines," *IEEE Std C93.4-2012*, pp. 1-67, 2013.
- [22] "IEEE Approved Draft Standard for the Requirements for Power-Line Carrier Line Traps (30-500 kHz)," *IEEE PC93.3/D17.4, August 2016*, pp. 1-45, 2016.
- [23] E. T. Association, *Power System Protection, Volumes 1: principles and components. sl: The Institution of Electrical Engineers, 1995.*
- [24] D. Deka, S. Backhaus, and M. Chertkov, "Estimating distribution grid topologies: A graphical learning based approach," in *2016 Power Systems Computation Conference (PSCC)*, 2016, pp. 1-7.
- [25] M. D. Piantè and A. M. Tonello, "On Impedance Matching in a Power-Line-Communication System," *IEEE Transactions on Circuits and Systems II: Express Briefs*, vol. 63, pp. 653-657, 2016.
- [26] "IEEE Guide for Power-Line Carrier Applications," *ANSI/IEEE Std 643-1980*, p. 0\_1, 1981.

- [27] W. h. Choi and C. y. Park, "A simple line coupler with adaptive impedance matching for Power line Communication," in *2007 IEEE International Symposium on Power Line Communications and Its Applications*, 2007, pp. 187-191.
- [28] N. H. Slaughter and W. V. Wolfe, "Carrier telephony on power lines," *Journal of the A.I.E.E.*, vol. 43, pp. 377-381, 1924.
- [29] P. A. A. F. Wouters, P. C. J. M. v. d. Wielen, J. Veen, P. Wagenaars, and E. F. Steennis, "Effect of cable load impedance on coupling schemes for MV power line communication," *IEEE Transactions on Power Delivery*, vol. 20, pp. 638-645, 2005.
- [30] L. Wang, C. You, C. Ge, and X. Zhu, "Narrow-band bandpass filter with enhanced Q and selectivity based on coupled negative resistance," in *2012 4th International High Speed Intelligent Communication Forum*, 2012, pp. 1-3.
- [31] T. T. Ha, *Theory and design of digital communication systems*: Cambridge University Press, 2010.
- [32] N. Won and J. Lerdworatawee, "Noise figure of digital communication receivers-revisited," *IEEE Transactions on Circuits and Systems I: Regular Papers*, vol. 51, pp. 1330-1335, 2004.
- [33] A. Majumder and J. C. J, "Power line communications," *IEEE Potentials*, vol. 23, pp. 4-8, 2004.
- [34] M. Lecours, M. Tetu, A. Chefaoui, J. Ahern, and A. Michaud, "Phase measurements and characterization of mobile radio channels," *IEEE Transactions on Vehicular Technology*, vol. 45, pp. 105-113, 1996.
- [35] M. Lont, D. Milosevic, G. Dolmans, and A. H. M. v. Roermund, "Implications of I/Q Imbalance, Phase Noise and Noise Figure for SNR and BER of FSK Receivers," *IEEE Transactions on Circuits and Systems I: Regular Papers*, vol. 60, pp. 2187-2198, 2013.
- [36] K. Bullington, "Phase and amplitude variations in multipath fading of microwave signals," *The Bell System Technical Journal*, vol. 50, pp. 2039-2053, 1971.
- [37] S. Mukherjee and S. K. Mohammed, "Constant-Envelope Precoding With Time-Variation Constraint on the Transmitted Phase Angles," *IEEE Wireless Communications Letters*, vol. 4, pp. 221-224, 2015.
- [38] D. K. v. Alphen and W. C. Lindsey, "Higher-order differential phase shift keyed modulation," *IEEE Transactions on Communications*, vol. 42, pp. 440-448, 1994.
- [39] M. Hoch, "Comparison of PLC G3 and PRIME," in *2011 IEEE International Symposium on Power Line Communications and Its Applications (ISPLC)*, 2011, pp. 165-169.
- [40] F. Chiti, R. Fantacci, D. Marabissi, and A. Tani, "Performance Evaluation of an Efficient and Reliable Multicast Power Line Communication System," *IEEE Journal on Selected Areas in Communications*, vol. 34, pp. 1953-1964, 2016.

- [41] F. H. Juwono, Q. Guo, Y. Chen, L. Xu, D. D. Huang, and K. P. Wong, "Linear Combining of Nonlinear Preprocessors for OFDM-Based Power-Line Communications," *IEEE Transactions on Smart Grid*, vol. 7, pp. 253-260, 2016.
- [42] R. H. Galloway, W. B. Shorrock, and L. M. Wedepohl, "Calculation of electrical parameters for short and long polyphase transmission lines," *Electrical Engineers, Proceedings of the Institution of*, vol. 111, pp. 2051-2059, 1964.
- [43] R. G. Olsen and T. A. Pankaskie, "On the Exact, Carson and Image Theories for Wires at or Above the Earth's Interface," *IEEE Power Engineering Review*, vol. PER-3, pp. 20-20, 1983.
- [44] B. K. Sternberg and T. M. Levitskaya, "Electrical parameters of soils in the frequency range from 1 kHz to 1 GHz, using lumped-circuit methods," *Radio Science*, vol. 36, pp. 709-719, 2001.
- [45] N. M. Nor, A. Haddad, and H. Griffiths, "Performance of earthing systems of low resistivity soils," *IEEE Transactions on Power Delivery*, vol. 21, pp. 2039-2047, 2006.
- [46] P. Wolfs, "Capacity improvements for rural single wire earth return systems," in *Power Engineering Conference, 2005. IPEC 2005. The 7th International*, 2005, pp. 1-306.
- [47] J. Mayer, N. Hossein-Zadeh, and P. Wolfs, "Modelling of Voltage Regulation Issues in SWER systems using PSCAD/EMTDC," *AUPEC 2006 Proceedings*, 2006.
- [48] V. Krishnan, "Transformer bypass circuit," in *International Symposium on Power Line Communications and Its Applications, 2005.*, 2005, pp. 275-277.
- [49] B. Nikfar and A. J. H. Vinck, "Relay selection in cooperative power line communication: A multi-armed bandit approach," *Journal of Communications and Networks*, vol. 19, pp. 1-9, 2017.
- [50] K. M. Rabie and B. Adebisi, "Enhanced Amplify-and-Forward Relaying in Non-Gaussian PLC Networks," *IEEE Access*, vol. 5, pp. 4087-4094, 2017.
- [51] X. Cheng, R. Cao, and L. Yang, "Relay-Aided Amplify-and-Forward Powerline Communications," *IEEE Transactions on Smart Grid*, vol. 4, pp. 265-272, 2013.
- [52] G. Artale, A. Cataliotti, V. Cosentino, D. Di Cara, R. Fiorelli, P. Russotto, *et al.*, "Medium Voltage Smart Grid: Experimental Analysis of Secondary Substation Narrow Band Power Line Communication," *IEEE Transactions on Instrumentation and Measurement*, vol. 62, pp. 2391-2398, 2013.
- [53] B. P. Lathi, *Modern Digital and Analog Communication Systems 3e* Osece: Oxford university press, 1998.
- [54] A. A. Amarsingh, H. A. Latchman, and D. Yang, "Narrowband Power Line Communications: Enabling the Smart Grid," *IEEE Potentials*, vol. 33, pp. 16-21, 2014.



- [55] J. T. Logan, "Remote Metering and Automatic Load Control," *Transactions of the American Institute of Electrical Engineers*, vol. 55, pp. 40-47, 1936.
- [56] G. A. Burns and T. R. Rayner, "Remote control of power networks," *Electrical Engineers, Journal of the Institution of*, vol. 79, p. 95, 1936.
- [57] C. F. Bolton and R. H. Abell, "Transmission and distribution," *Electrical Engineers, Journal of the Institution of*, vol. 78, pp. 439-460, 1936.
- [58] AIEE, "Guide to Application and Treatment of Channels for Power-Line Carrier [includes discussion]," *Transactions of the American Institute of Electrical Engineers Power Apparatus and Systems, Part III.*, vol. 73, 1954.
- [59] H. P. Barker, "The centralized control of public lighting and off-peak loads by superimposed ripples," *Electrical Engineers, Journal of the Institution of*, vol. 83, pp. 823-836, 1938.
- [60] D. Dzung, I. Berganza, and A. Sendin, "Evolution of powerline communications for smart distribution: From ripple control to OFDM," in *2011 IEEE International Symposium on Power Line Communications and Its Applications (ISPLC)*, 2011, pp. 474-478.
- [61] R. M. D. Carlo, M. C. Bruzzone, C. Sarzanini, R. Maina, and V. Tumiatto, "Copper contaminated insulating mineral oils-testing and investigations," *IEEE Transactions on Dielectrics and Electrical Insulation*, vol. 20, pp. 557-563, 2013.
- [62] C. J. F. Böttcher, O. C. van Belle, P. Bordewijk, and A. Rip, *Theory of Electric Polarization* vol. 2. Amsterdam: Elsevier Science Ltd, 1978.
- [63] J. H. Harlow, *Electric Power Transformer Engineering*. Boca Raton: CRC press, 2012.
- [64] J. JURČIK and M. GUTTEN, "Analysis transformer insulation by PDC method," *Przegld Elektrotechniczny*, vol. 89, pp. 169--171, 2013.
- [65] R. Hollertz, L. Wågberg, and C. Pitois, "Effect of composition and Morphology on the dielectric response of cellulose-based electrical insulation," *IEEE Transactions on Dielectrics and Electrical Insulation*, vol. 22, pp. 2339-2348, 2015.
- [66] B. M. Hansen, J. R. Ovesen, and K. Kolte, "Characteristics Measurements Using TDR and Modelling of the Transmission Channel," in *2007 IEEE International Symposium on Power Line Communications and Its Applications*, 2007, pp. 319-323.
- [67] K. Razavian, M. Umari, and A. Kamalid, "Error correction mechanism in the new G3-PLC specification for powerline communication," in *ISPLC2010*, 2010, pp. 50-55.
- [68] S. Souissi, O. B. Rhouma, and C. Rebai, "Generation of cyclostationary noise for narrowband powerline channel emulation," in *2015 IEEE 5th International Conference on Consumer Electronics - Berlin (ICCE-Berlin)*, 2015, pp. 413-417.
- [69] A. Das, *Digital Communication: Principles and System Modelling*: Springer, 2010.

- [70] B. Hahn and D. T. Valentine, *Essential MATLAB for Engineers and Scientists*. Saint Louis, UNKNOWN: Elsevier Science, 2016.
- [71] E. Bjerkan, "High frequency modeling of power transformers: stresses and diagnostics," Norwegian University of Science and Technology, 2005.
- [72] B. S. Blanchard, W. J. Fabrycky, and W. J. Fabrycky, *Systems engineering and analysis* vol. 4: Prentice Hall Englewood Cliffs, New Jersey, 1990.
- [73] R. G. Sargent, "Verification and validation of simulation models," in *Proceedings of the 37th conference on Winter simulation*, 2005, pp. 130-143.
- [74] R. G. Sargent, "A historical view of hybrid simulation/analytic models," in *Proceedings of the 26th conference on Winter simulation*, 1994, pp. 383-386.
- [75] A. J. Van Der Schaft, J. M. Schumacher, A. J. van der Schaft, and A. J. van der Schaft, *An introduction to hybrid dynamical systems* vol. 251: Springer London, 2000.
- [76] W. Sui, *Time-Domain Computer Analysis of Nonlinear Hybrid Systems*. Boca Raton: CRC Press, 2001.
- [77] R. Sanfelice, D. Copp, and P. Nanez, "A toolbox for simulation of hybrid systems in Matlab/Simulink: Hybrid Equations (HyEQ) Toolbox," in *Proceedings of the 16th international conference on Hybrid systems: computation and control*, 2013, pp. 101-106.
- [78] B. Gustavsen, "A Hybrid Measurement Approach for Wideband Characterization and Modeling of Power Transformers," *IEEE Transactions on Power Delivery*, vol. 25, pp. 1932-1939, 2010.
- [79] B. S. Guru and H. R. Hiziroglu, *Electric machinery and transformers* vol. 726: Oxford University Press New York, 2001.
- [80] C. W. T. McLyman, *Transformer and inductor design handbook* vol. 121: CRC press, 2004.
- [81] P. Ahmadi, B. Maundy, A. S. Elwakil, and L. Belostotski, "High-quality factor asymmetric-slope band-pass filters: A fractional-order capacitor approach," *IET Circuits, Devices & Systems*, vol. 6, pp. 187-197, 2012.
- [82] M. S. Sarafriz and M. S. Tavazoei, "Realizability of Fractional-Order Impedances by Passive Electrical Networks Composed of a Fractional Capacitor and RLC Components," *IEEE Transactions on Circuits and Systems I: Regular Papers*, vol. 62, pp. 2829-2835, 2015.
- [83] K. Bandara, C. Ekanayake, and T. K. Saha, "Modelling the dielectric response measurements of transformer oil," *IEEE Transactions on Dielectrics and Electrical Insulation*, vol. 22, pp. 1283-1291, 2015.

- [84] F. Ferranti and Y. Rolain, "A local approach for the modeling of linear parameter-varying systems based on transfer function interpolation with scaling coefficients," in *2015 IEEE International Instrumentation and Measurement Technology Conference (I2MTC) Proceedings*, 2015, pp. 606-611.
- [85] U. S. D. o. Energy. (2009, July 2017). *The Smart Grid: An Introduction*. Available: [https://energy.gov/sites/prod/files/oeprod/DocumentsandMedia/DOE\\_SG\\_Book\\_Single\\_Pages%281%29.pdf](https://energy.gov/sites/prod/files/oeprod/DocumentsandMedia/DOE_SG_Book_Single_Pages%281%29.pdf)
- [86] Y. Bamberger, J. Baptista, D. Botting, B. M. Buchholz, R. Charnah, M. Chebbo, *et al.*, "Strategic Research Agenda for Europe's Electricity Networks of the Future," 2007.
- [87] U. S.-E. C. t. S. G. Deployment, A. C. o. t. U. States, and U. S. D. o. Commerce, *Report to U.S. and EU Leaders: U.S.-EU Cooperation Toward Smart Grid Deployment*: Atlantic Council of the United States, 2009.
- [88] G. Ledwich, "International Practices in Rural Electrification," vol. Rural Electrification, CIGRE, Ed., ed. Brussels: CIGRE 2007.
- [89] D. F. Barnes, *The challenge of rural electrification: strategies for developing countries*: Earthscan, 2007.
- [90] R. Ferguson, W. Wilkinson, and R. Hill, "Electricity use and economic development," *Energy Policy*, vol. 28, pp. 923-934, 11// 2000.
- [91] G. Foley, *Electricity for rural people*. London: Panos Publications, 1990.
- [92] M. B. Jagadeesha Joish, Nirmal Nair, "ICT Practices in New Zealand Distribution Utilities - Discussion Paper on Smart meters, Communication Technologies & Ripple Control," October 2014.
- [93] K. Mets, J. A. Ojea, and C. Devellder, "Combining Power and Communication Network Simulation for Cost-Effective Smart Grid Analysis," *IEEE Communications Surveys & Tutorials*, vol. 16, pp. 1771-1796, 2014.
- [94] A. Sanz, P. J. Pinero, J. M. Idiago, S. Esteban, and J. I. Garcia, "Narrowband power line communications evaluation in complex distribution networks," in *Smart Grid Communications (SmartGridComm), 2014 IEEE International Conference on*, 2014, pp. 266-271.
- [95] G. E. Ott, L. N. Walker, and D. T. Y. Wong, "Hybrid simulation for long term dynamics," *IEEE Transactions on Power Apparatus and Systems*, vol. 96, pp. 907-915, 1977.
- [96] W. V. Wolfe and J. D. Sarros, "Problems in Power-Line Carrier Telephony And Recent Developments to Meet Them," *Transactions of the American Institute of Electrical Engineers*, vol. 48, pp. 107-113, 1929.

- [97] C. A. Boddie and R. C. Curtis, "The Transmission of High-Frequency Currents for Communication over Existing Power Networks," *Transactions of the American Institute of Electrical Engineers*, vol. 48, pp. 227-235, 1929.
- [98] J. Anatory, M. M. Kissaka, and N. H. Mvungi, "Powerline Communications: The Effects of Branches on Network Performance," in *2006 IEEE International Symposium on Power Line Communications and Its Applications*, 2006, pp. 70-75.
- [99] T. Zheng, X. Yang, and B. Zhang, "Broadband transmission characteristics for power-line channels," *IEEE Transactions on Power Delivery*, vol. 21, pp. 1905-1911, 2006.
- [100] R. S. Mello and M. A. Grivet, "Modeling, simulation and estimation of PLC channels," in *Telecommunications Symposium, 2006 International*, 2006, pp. 201-206.
- [101] B. Adebisi, A. Khalid, Y. Tsado, and B. Honary, "Narrowband PLC channel modelling for smart grid applications," in *Communication Systems, Networks & Digital Signal Processing (CSNDSP), 2014 9th International Symposium on*, 2014, pp. 67-72.
- [102] T. A. Papadopoulos, B. D. Batalas, A. Radis, and G. K. Papagiannis, "Medium Voltage Network PLC Modeling and Signal Propagation Analysis," in *2007 IEEE International Symposium on Power Line Communications and Its Applications*, 2007, pp. 284-289.
- [103] T. A. Papadopoulos, C. G. Kaloudas, A. I. Chrysochos, and G. K. Papagiannis, "Application of Narrowband Power-Line Communication in Medium-Voltage Smart Distribution Grids," *IEEE Transactions on Power Delivery*, vol. 28, pp. 981-988, 2013.
- [104] C. Cano, A. Pittolo, D. Malone, L. Lampe, A. M. Tonello, and A. G. Dabak, "State of the Art in Power Line Communications: From the Applications to the Medium," *IEEE Journal on Selected Areas in Communications*, vol. 34, pp. 1935-1952, 2016.
- [105] E. Takmaz, "Impedance, attenuation and noise measurements for power line communication," in *2016 4th International Istanbul Smart Grid Congress and Fair (ICSG)*, 2016, pp. 1-4.
- [106] N. Zaraneh, A. S. Descamps, C. Batard, and N. Ginot, "Modeling of a communication channel on a PWM electrical network," in *2016 International Symposium on Power Electronics, Electrical Drives, Automation and Motion (SPEEDAM)*, 2016, pp. 588-593.
- [107] J. N. Murphy and H. E. Parkinson, "Underground mine communications," *Proceedings of the IEEE*, vol. 66, pp. 26-50, 1978.
- [108] M. Kitayama, J. Abe, and S. Tanabe, "Transmission characteristics simulation on power line communications," *Electronics and Communications in Japan*, vol. 92, pp. 46-55, 2009.
- [109] R. Aquilue, M. Ribo, J. R. Regue, J. L. Pijoan, and G. Sanchez, "Scattering Parameters-Based Channel Characterization and Modeling for Underground Medium-Voltage

- Power-Line Communications," *IEEE Transactions on Power Delivery*, vol. 24, pp. 1122-1131, 2009.
- [110] F. de Leon and A. Semlyen, "Complete transformer model for electromagnetic transients," *IEEE Transactions on Power Delivery*, vol. 9, pp. 231-239, 1994.
  - [111] K. Razazian, M. Umari, A. Kamalizad, V. Loginov, and M. Navid, "G3-PLC Specification for Powerline Communication: Overview, System Simulation and Field Trial Results," in *IEEE International Symposium on Power Line Communications and Its Applications; ISPLC 2010* 2010, pp. 313-318.
  - [112] T. Tran-Anh, P. Auriol, and T. Tran-Quoc, "High frequency power transformer modeling for Power Line Communication applications," in *PSCE '06. 2006 IEEE PES Power Systems Conference and Exposition, 2006.* , 2006, pp. 1069-1074.
  - [113] R. Lefort, B. Taquet, R. Vauzelle, V. Courtecuisse, A. M. Poussard, and N. Idir, "High Frequency MV/LV transformer modelling for Power Line Communication applications," in *Power Line Communications and its Applications (ISPLC), 2014 18th IEEE International Symposium on*, 2014, pp. 30-35.
  - [114] A. Pinomaa, A. Poluektov, J. Ahola, and A. Kosonen, "Analysis of channel characteristics and modeling of a transformer for PLC-based loss-of-mains concept," in *2016 International Symposium on Power Line Communications and its Applications (ISPLC)*, 2016, pp. 230-235.
  - [115] W. C. Black and N. E. Badr, "High-frequency characterization and modeling of distribution transformers," in *2010 IEEE International Symposium on Power Line Communications and Its Applications (ISPLC) 2010*, pp. 18-21.
  - [116] A. Mukherjee and A. K. Samantaray, *Bond graph in modeling, simulation and fault identification*: IK International Pvt Ltd, 2006.
  - [117] M. Melit, B. Nekhoul, D. Sekki, and K. Kerroum, "Modeling of the transmission of power line communication signal through the power electric transformer," *annals of telecommunications-Annales des télécommunications*, vol. 67, pp. 447-454, 2012.
  - [118] A. Cataliotti, V. Cosentino, D. Di Cara, and G. Tine, "Oil-Filled MV/LV Power-Transformer Behavior in Narrow-Band Power-Line Communication Systems," *IEEE Transactions on Instrumentation and Measurement*, vol. 61, pp. 2642-2652, 2012.
  - [119] C. Males, V. Popa, A. Lavric, and I. Finis, "Performance Evaluation of Power Line Communications over Power Transformers," in *2012 20th Telecommunications Forum (TELFOR)*, 2012, pp. 627-630.
  - [120] A. Cataliotti, V. Cosentino, S. Guaiana, D. Di Cara, N. Panzavecchia, and G. Tine, "Experimental investigation on PLC signal crossing of power transformers," in

*Instrumentation and Measurement Technology Conference (I2MTC) Proceedings, 2014 IEEE International*, 2014, pp. 1235-1239.

- [121] R. Lefort, R. Vauzelle, V. Courtecuisse, N. Idir, and A. M. Poussard, "Influence of the MV/LV transformer impedance on the propagation of the PLC signal in the power grid," *IEEE Transactions on Power Delivery*, vol. PP, pp. 1-1, 2016.
- [122] Y. El Haj, L. Albasha, A. El-Hag, and H. Mir, "Feasibility of data communication through distribution transformers for Smart Grid applications," in *Innovative Smart Grid Technologies - Asia (ISGT Asia), 2014 IEEE*, 2014, pp. 143-146.
- [123] A. Dabak, I. H. Kim, B. Varadarajan, and T. Pande, "Channel Modeling for MV/LV AMI Applications in the Frequency Range< 500kHz," in *Workshop on Power Line Communications*, 2011.
- [124] G. Liang, S. Gao, Y. Wang, Y. Zang, and X. Liu, "Fractional transmission line model of oil-immersed transformer windings considering the frequency-dependent parameters," *IET Generation, Transmission & Distribution*, vol. 11, pp. 1154-1161, 2017.
- [125] Y. Zhu, S. Li, and D. Min, "Origin of dielectric processes in aged oil impregnated paper," *IEEE Transactions on Dielectrics and Electrical Insulation*, vol. 24, pp. 1625-1635, 2017.
- [126] J. Liu, L. Zhou, Y. Luo, X. Huang, and G. Wu, "Dielectric frequency response of oil-paper composite insulation with transient moisture distribution," *IEEE Transactions on Dielectrics and Electrical Insulation*, vol. 20, pp. 1380-1387, 2013.
- [127] J. Blennow, C. Ekanayake, K. Walczak, B. Garcia, and S. M. Gubanski, "Field experiences with measurements of dielectric response in frequency domain for power transformer diagnostics," *IEEE Transactions on Power Delivery*, vol. 21, pp. 681-688, 2006.
- [128] M. K. Pradhan and K. J. H. Yew, "Experimental investigation of insulation parameters affecting power transformer condition assessment using frequency domain spectroscopy," *IEEE Transactions on Dielectrics and Electrical Insulation*, vol. 19, pp. 1851-1859, 2012.
- [129] E. I. Amoiralis, M. A. Tsili, and A. G. Kladas, "Transformer Design and Optimization: A Literature Survey," *Power Delivery, IEEE Transactions on*, vol. 24, pp. 1999-2024, 2009.
- [130] D. P. Carroll, "Digital and hybrid computer simulation of power systems," *Simulation*, vol. 21, pp. 9-15, 1973.
- [131] R. C. Degeneff, M. R. Gutierrez, and M. Vakilian, "Nonlinear, lumped parameter transformer model reduction technique," *IEEE Transactions on Power Delivery*, vol. 10, pp. 862-868, 1995.
- [132] M. Vakilian, R. C. Degeneff, and M. Kupferschmid, "Computing the internal transient voltage response of a transformer with a nonlinear core using Gear's method. Part 1: Theory," *IEEE Transactions on Power Delivery*, vol. 10, pp. 1836-1842, 1995.

- [133] M. Vakilian and R. C. Degeneff, "A method for modeling nonlinear core characteristics of transformers during transients," *Power Delivery, IEEE Transactions on*, vol. 9, pp. 1916-1925, 1994.
- [134] F. de Leon and A. Semlyen, "Reduced order model for transformer transients," *IEEE Transactions on Power Delivery*, vol. 7, pp. 361-369, 1992.
- [135] F. de Leon and A. Semlyen, "Efficient calculation of elementary parameters of transformers," *Power Delivery, IEEE Transactions on*, vol. 7, pp. 376-383, 1992.
- [136] F. de Leon and A. Semlyen, "Detailed modeling of eddy current effects for transformer transients," *Power Delivery, IEEE Transactions on*, vol. 9, pp. 1143-1150, 1994.
- [137] S. D. Mitchell and G. H. C. Oliveira, "A hybrid modelling methodology for analysing the effect of system transients within power transformers," in *2012 22nd Australasian Universities Power Engineering Conference (AUPEC)*, 2012, pp. 1-6.
- [138] B. A. Mork, F. Gonzalez, D. Ishchenko, D. L. Stuehm, and J. Mitra, "Hybrid Transformer Model for Transient Simulation - Part I: Development and Parameters," *IEEE Transactions on Power Delivery*, vol. 22, pp. 248-255, 2007.
- [139] B. Mork, F. Gonzalez, D. Ishchenko, D. Stuehm, and J. Mitra, "Hybrid Transformer Model for Transient Simulation: Part II - Laboratory Measurements and Benchmarking," in *2007. IEEE Power Engineering Society General Meeting*, 2007, pp. 1-1.
- [140] E. Bjerkan. (July 2017). *High Frequency Modelling of Power Transformers - A Guide to Significant Articles*. Available: <http://www.elkraft.ntnu.no/~eilertb/PhD/Review.pdf>
- [141] D. Gay, A. Thompson, M. T. O. Amanulla, and P. Wolfs, "Monitoring of Single Wire Earth Return systems using Power Line Communication," in *AUPEC 2009. Australasian Universities Power Engineering Conference, 2009.*, 2009, pp. 1-5.
- [142] Z. Zhang, Z. Yang, and A. P. Taylor, "The Feasibility of the SWER System in New Zealand as a Low Bit Rate Communications Channel," in *International Conference on Software Technology and Engineering (ICSTE 2012)*, 2012.
- [143] C. J. Kikkert and G. D. Reid, "Radiation Losses from a Single Wire Earth Return Power Line with Bends," in *ATNAC 2008. Australasian Telecommunication Networks and Applications Conference, 2008.*, 2008, pp. 158-162.
- [144] C. J. Kikkert and G. D. Reid, "Radiation and attenuation of Single Wire Earth return power lines at LF frequencies," in *ISPLC 2009. IEEE International Symposium on Power Line Communications and Its Applications, 2009.*, 2009, pp. 68-72.
- [145] C. J. Kikkert, "MV to LV transformer PLC bypass coupling networks for a low cost Smart Grid rollout," in *2011 IEEE PES Innovative Smart Grid Technologies Asia (ISGT)*, 2011, pp. 1-6.

- [146] C. J. Kikkert. (July 2017). *Modelling Power Transformers at Power Line Carrier Frequencies*. Available:  
[https://researchonline.jcu.edu.au/16323/1/Cornelis\\_Kikkert\\_Thursday.pdf](https://researchonline.jcu.edu.au/16323/1/Cornelis_Kikkert_Thursday.pdf)
- [147] C. J. Kikkert, "Modeling Power Transformers for the Design of SWER Line Coupling Networks," in *2010 First IEEE International Conference on Smart Grid Communications (SmartGridComm)*, 2010, pp. 120-125.
- [148] C. J. Kikkert, "Power transformer modelling and MV PLC coupling networks," in *2011 IEEE PES Innovative Smart Grid Technologies Asia (ISGT)*, 2011, pp. 1-6.
- [149] C. J. Kikkert, "An On-line PLC frequency Impedance Analyzer," in *IEEE International Conference on Smart Grid Communications; SmartGridComm 2013* 2013, pp. 606-611.
- [150] C. J. Kikkert, "Effect of couplers and line branches on PLC communication channel response," in *2011 IEEE International Conference on Smart Grid Communications (SmartGridComm)*, 2011, pp. 309-314.
- [151] R. A. Chipman, *Theory and problems of transmission lines*: McGraw-Hill New York, 1968.
- [152] L. L. Grigsby, *Power Systems. Electric Power Engineering Handbook*: CRC Press, 2007.
- [153] F. Rachidi and S. Tkachenko, *Electromagnetic Field Interaction with Transmission Lines: From Classical Theory to HF Radiation Effects*. Boston: WIT, 2008.
- [154] J. Anatory and N. Theethayi, "On the Efficacy of Using Ground Return in the Broadband Power-Line Communications - A Transmission-Line Analysis," *IEEE Transactions on Power Delivery*, vol. 23, pp. 132-139, 2008.
- [155] M. K. A. Elrahman, "An Advanced Technique for Earthing System Analysis," *IEEE Transactions on Power Delivery*, vol. 28, pp. 268-275, 2013.
- [156] M. S. M. Yunus, N. M. Nor, N. A. Etobi, and K. Ramar, "Performance of Earthing Systems for Different Earth Electrode Configurations," *IEEE Transactions on Industry Applications*, vol. 51, pp. 5335-5342, 2015.
- [157] R. L. Smith-Rose, "Electrical measurements on soil with alternating currents," *Electrical Engineers, Journal of the Institution of*, vol. 75, pp. 221-237, 1934.
- [158] N. Wagner, K. Emmerich, F. Bonitz, and K. Kupfer, "Experimental Investigations on the Frequency- and Temperature-Dependent Dielectric Material Properties of Soil," *IEEE Transactions on Geoscience and Remote Sensing*, vol. 49, pp. 2518-2530, 2011.
- [159] D. Martin and T. Saha, "A review of the techniques used by utilities to measure the water content of transformer insulation paper," *IEEE Electrical Insulation Magazine*, vol. 33, pp. 8-16, 2017.



- [160] J. Faiz and M. Soleimani, "Dissolved gas analysis evaluation in electric power transformers using conventional methods a review," *IEEE Transactions on Dielectrics and Electrical Insulation*, vol. 24, pp. 1239-1248, 2017.
- [161] A. M. Novikov, *Research Methodology : From Philosophy of Science to Research Design*, 1 ed. Hoboken: CRC Press, 2013.
- [162] J. F. Nunamaker, Jr. and M. Chen, "Systems development in information systems research," in *Proceedings of the Twenty-Third Annual Hawaii International Conference on System Sciences, 1990.*, 1990, pp. 631-640 vol.3.
- [163] A. Baghini, *Handbook of power quality*: John Wiley & Sons, 2008.
- [164] H. Zhao, S. Fortin, and F. P. Dawalibi, "Analysis of Grounding Systems Including Freely Oriented Plates of Arbitrary Shape in Multilayer Soils," *IEEE Transactions on Industry Applications*, vol. 51, pp. 5189-5197, 2015.
- [165] P. Llovera, J. A. LLiso, V. Fuster, and A. Quijano, "Improved Methodology for High-Frequency Low-Current Measurement of Grounding Rod Impedance," *IEEE Transactions on Power Delivery*, vol. 23, pp. 1954-1960, 2008.
- [166] J. D. Cooper, *Soil Water Measurement: A Practical Handbook*: John Wiley & Sons, 2016.
- [167] W. A. Thue, *Electrical power cable engineering*: CRC Press, 2011.
- [168] R. Alipio and S. Visacro, "Modeling the Frequency Dependence of Electrical Parameters of Soil," *IEEE Transactions on Electromagnetic Compatibility*, vol. 56, pp. 1163-1171, 2014.
- [169] S. Sivanagaraju, *Electric power transmission and distribution*: Pearson Education India, 2008.
- [170] Transpower. (July 2017). *Clearances and Conductor Spacings*. Available: <https://www.ea.govt.nz/dmsdocument/4121>
- [171] B. Nkom, A. P. R. Taylor, C. Baguley, B. C. Seet, and T. T. Lie, "A unified approach to characterizing medium to low voltage powerline communication channels," in *2016 IEEE International Conference on Power System Technology (POWERCON)*, 2016, pp. 1-6.
- [172] K. Yamamoto, S. Sumi, S. Sekioka, and J. He, "Derivations of Effective Length Formula of Vertical Grounding Rods and Horizontal Grounding Electrodes Based on Physical Phenomena of Lightning Surge Propagations," *IEEE Transactions on Industry Applications*, vol. 51, pp. 4934-4942, 2015.
- [173] P. Golden, H. Dedieu, and K. S. Jacobsen, *Fundamentals of DSL Technology*: CRC Press, 2005.

- [174] D. Cavka, N. Mora, and F. Rachidi, "A Comparison of Frequency-Dependent Soil Models: Application to the Analysis of Grounding Systems," *IEEE Transactions on Electromagnetic Compatibility*, vol. 56, pp. 177-187, 2014.
- [175] W. Sui, *Time-domain computer analysis of nonlinear hybrid systems*: CRC press, 2010.
- [176] "IEEE Standard for Low-Frequency (less than 500 kHz) Narrowband Power Line Communications for Smart Grid Applications," *IEEE Std 1901.2-2013*, pp. 1-269, 2013.
- [177] Q. Wang and P. Y. Kam, "Optimum Detection of Two-Dimensional Carrier Modulations With Linear Phase Noise Using Received Amplitude and Phase Information and Performance Analysis," *Journal of Lightwave Technology*, vol. 34, pp. 2439-2451, 2016.
- [178] O. Bialer and D. Raphaeli, "Analysis of Optimum Detector of Trellis Coded MPSK in Phase Noise Channels," *IEEE Transactions on Communications*, vol. 59, pp. 130-140, 2011.
- [179] J. A. B. Faria, "Dubanton's and Wait's Approximations of the Earth Return Impedance Used for Evaluating Transmission-Line Wave Propagation Parameters," *IEEE Transactions on Power Delivery*, vol. 30, pp. 2600-2601, 2015.
- [180] J. Lee, B. Zhang, J. Zou, and M. n. Ju, "Efficient Evaluation of Earth Return Impedances of Arbitrary Conductor Arrangements With a Horizontally Multilayered Soil," *IEEE Transactions on Electromagnetic Compatibility*, vol. 59, pp. 266-274, 2017.
- [181] F. d. I. Rosa and S. T. Mak, "A Look into Steady State and Transient Performance of Power Lines Integrating Single Wire Earth Return Circuits," in *2007 IEEE Power Engineering Society General Meeting*, 2007, pp. 1-6.
- [182] Y. Ozawa, T. Arai, and R. Kohno, "Spread spectrum data transmission system using the earth returning circuit on a low-voltage distribution line," in *Spread Spectrum Techniques and Applications Proceedings, 1996., IEEE 4th International Symposium on*, 1996, pp. 1097-1101 vol.3.
- [183] C. J. Kikkert and G. Reid, "Radiation and Attenuation of Communication Signals on Power Lines," in *7th International Conference on Information, Communications and Signal Processing, ICICS 2009.*, 2009, pp. 1-5.
- [184] J. Nahman and D. Jelovac, "High-voltage/medium(low)-voltage substation earthing systems," *IEE Proceedings C - Generation, Transmission and Distribution*, vol. 134, pp. 75-80, 1987.
- [185] R. Lefort, R. Vauzelle, V. Courtecuisse, N. Idir, and A. M. Poussard, "Influence of the MV/LV Transformer Impedance on the Propagation of the PLC Signal in the Power Grid," *IEEE Transactions on Power Delivery*, vol. 32, pp. 1339-1349, 2017.
- [186] K. Okada and T. Sekino, "Impedance Measurement Handbook," *Agilent Technologies*, vol. 128, pp. 5950-3000, 2003.

- [187] N. Shlezinger and R. Dabora, "On the Capacity of Narrowband PLC Channels," *IEEE Transactions on Communications*, vol. 63, pp. 1191-1201, 2015.
- [188] M. Dong, M. Ren, F. Wen, C. Zhang, J. Liu, C. Sumner, *et al.*, "Explanation and analysis of oil-paper insulation based on frequency-domain dielectric spectroscopy," *IEEE Transactions on Dielectrics and Electrical Insulation*, vol. 22, pp. 2684-2693, 2015.
- [189] P. K. Vitthaladevuni and M. S. Alouini, "Effect of imperfect phase and timing synchronization on the bit-error rate performance of PSK modulations," *IEEE Transactions on Communications*, vol. 53, pp. 1096-1099, 2005.
- [190] G. Bakkabulindi, "Planning Models for Single Wire Earth Return Power Distribution Networks," KTH Royal Institute of Technology, 2012.
- [191] S. Galli and T. Lys, "Next generation Narrowband (under 500 kHz) Power Line Communications (PLC) standards," *China Communications*, vol. 12, pp. 1-8, 2015.
- [192] E. Biglieri, "Coding and modulation for a horrible channel," *IEEE Communications Magazine*, vol. 41, pp. 92-98, 2003.
- [193] G. Kaddoum and N. Tadayon, "Differential Chaos Shift Keying: A Robust Modulation Scheme for Power-Line Communications," *IEEE Transactions on Circuits and Systems II: Express Briefs*, vol. 64, pp. 31-35, 2017.
- [194] P. A. Janse van Rensburg, M. P. Sibanda, and H. C. Ferreira, "Integrated Impedance-Matching Coupler for Smart Building and Other Power-Line Communications Applications," *Power Delivery, IEEE Transactions on*, vol. 30, pp. 949-956, 2015.
- [195] M. P. Sibanda, P. A. J. van Rensburg, and H. C. Ferreira, "A Compact Economical PLC Band-pass Coupler With Impedance Matching," in *17th IEEE International Symposium on Power Line Communications and Its Applications; ISPLC 2013*, 2013, pp. 339-344.

## Appendix A – Design Procedure for Line Traps [21, 22, 176]

If the PLC channel has an impedance  $Z_0$  at the centre frequency, while the communications unit, filters and coupling units have a combined impedance of  $Z_0^*$  (complex conjugate of  $Z_0$ ) as transformed by the impedance matching circuit, then the schematic diagram of A.1 will represent the arrangement at each PLC interface shown in Figure 2.2.

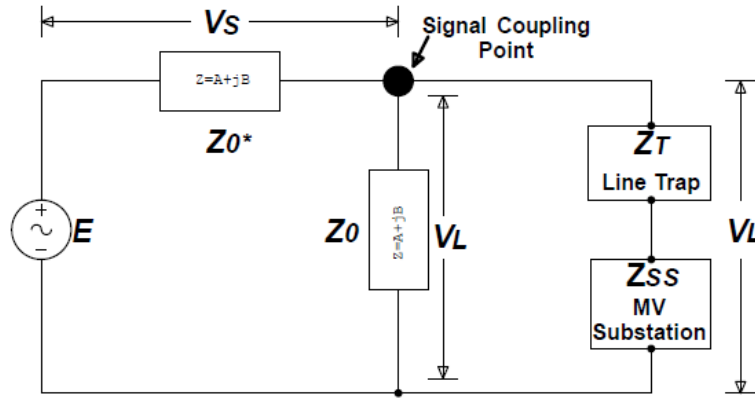


Figure A.1 – Grid Component Impedances at PLC Centre Frequency

With the line trap disconnected from the coupling point of Figure A.1, there will be maximum power transfer of the PLC signal into the PLC channel. The high frequency voltage across the PLC channel is:

$$V_{L1} = \frac{E}{2} \quad (1)$$

For the same value of  $E$ , with  $Z_C = Z_T + Z_{SS}$ ,

$$E = V_S + V_{L2} = I(Z_0 + Z_X) \quad (2)$$

where: 
$$Z_X = \left( \frac{Z_0 \times Z_C}{Z_0 + Z_C} \right) \quad (3)$$

From (2), 
$$I = \frac{E}{(Z_0 + Z_C)} \text{ and therefore } V_{L2} = \frac{E}{(Z_0 + Z_X)} \times Z_X \quad (4)$$

Extracting the impedance terms from (4) yields

$$Z = \frac{Z_X}{(Z_0 + Z_X)} \quad (5)$$

Substituting (3) into (5) and solving yields

$$Z = \frac{Z_C}{(Z_0 + 2Z_C)} \quad (6)$$

Substituting (6) into (4) yields

$$V_{L2} = E \times \frac{Z_C}{(2Z_C + Z_0)} = \frac{E}{2} \times \frac{Z_C}{(Z_C + 0.5Z_0)} \quad (7)$$

The power transferred into the PLC channel for first and second cases is:

$$P_{L1} = \frac{V_{L1}^2}{Z_0} \quad \text{and} \quad P_{L2} = \frac{V_{L2}^2}{Z_0} \quad (9)$$

If a 50% signal power loss (0.5 of transmitter output power) on the line is acceptable, a damped line trap can be designed for a gradual roll-off from the centre frequency. The necessary damping resistance value, considering the pre-determined power loss, can be found through a ratio of powers in relation to the characteristic impedance of the PLC channel. The ratio is:

$$\frac{P_{L2}}{P_{L1}} = \frac{V_{L2}^2}{V_{L1}^2} = \frac{1}{2} = 0.5, \quad \text{which gives:} \quad \frac{V_{L2}}{V_{L1}} = \frac{1}{\sqrt{2}} = \sqrt{0.5} \quad (10)$$

Putting (1) and (7) into (10) yields

$$\frac{Z_C}{(Z_C + 0.5Z_0)} = \frac{1}{\sqrt{2}} = \sqrt{0.5} \quad (11)$$

Solving (11) for  $Z_C$  gives:

$$Z_C = 1.21 Z_0 \quad (12)$$

If a different ratio of powers is desired, the ratio value can be placed directly into equation (11) to obtain the corresponding value of  $Z_C$  required. The magnitude value of  $Z_C$  is the minimum resistive value  $R_{Tmin}$  that needs to be designed into the line trap for the desired damping within a specified bandwidth [23]. The bandwidth is estimated with the following formula:

$$\text{Bandwidth (BW)} = \frac{L(2\pi f_0)^2}{R_s} \times \left| \sqrt{\left(\frac{R_s}{R_{Tmin}}\right)} - 1 \right| \quad (13)$$

where  $f_0$  is the PLC bandwidth centre frequency, and  $R_s$  and  $L$  are the shunt resistance and inductance of the line trap respectively. From (13), the maximum value of the bandwidth will occur when  $R_s = 2R_{Tmin}$ . When this condition is achieved, (13) becomes:

$$BW = \frac{(2\pi f_0)^2 L}{2R_{Tmin}} \quad (14)$$

$$BW = f_u - f_l \quad (15)$$

$$f_0 = \sqrt{(f_l \times f_u)} \quad (16)$$

where  $f_l$  and  $f_u$  are the lower and upper frequencies of the bandwidth.

Equations (14), (15) and (16) allow for a line trap design with either inductance  $L$ ,  $BW$ ,  $f_l$  or  $f_u$  as the unknown variable. However, inductance  $L$  is usually the variable of interest.

The schematic diagram of the simple damped line trap is shown in Figure A.2.

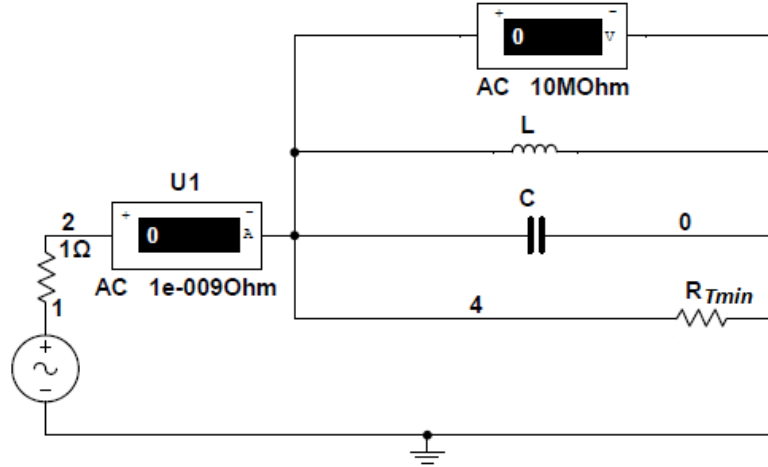


Figure A.2 – Schematic Diagram of Simple Damped Line Trap

This design can be improved by the use of a series LC combination, also resonant at the centre frequency, in the shunt damping arm of the line trap. A simple way of selecting the series L and C values is to consider that the Q factors of the planned series and existing parallel resonant circuits should closely match. Therefore, for the parallel RLC circuit in figure A.2,

$$Q = R_{Tmin} \sqrt{\frac{C_P}{L_P}} \quad (17)$$

For a series RLC circuit,

$$Q = \frac{2\pi f_0 L_S}{R_{Tmin}} \quad (18)$$

Equation (18) is first solved for  $L_S$ , after which the matching resonance capacitor  $C_S$  at the centre frequency specified by (16) is determined. These new L and C values form the component values for the series resonance circuit. The schematic diagram of the improved damped line trap is shown in Figure A.3.

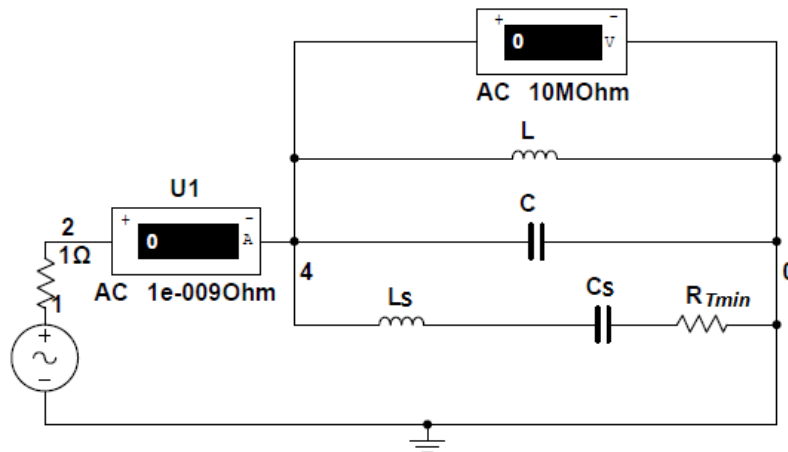


Figure A.3 – Schematic Diagram of Improved Damped Line Trap

## Appendix B – Design Procedure for Couplers [21, 22, 176]

### Coupling and Filtering Unit

A Constant-k T-section model shown in Figure B.1 is a good choice for implementing a simple PLC bandpass filter and coupling unit. It has two series capacitors of value  $2C_1$  each, which will ensure adequate attenuation of low frequency signals.

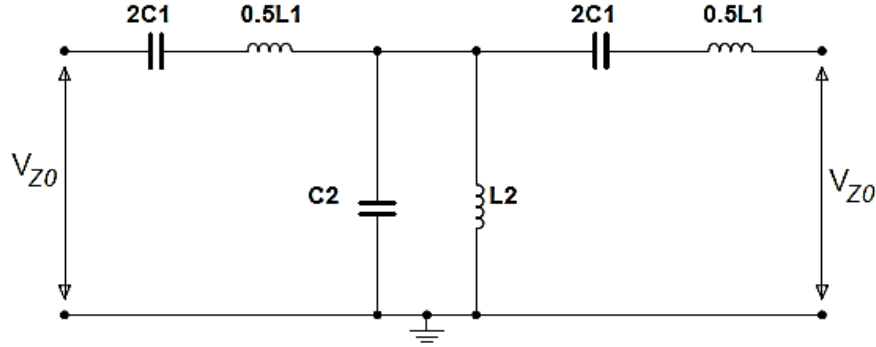


Figure B.1 – Schematic Diagram of Constant-k Bandpass T-Filter

The T-section model also has a shunt inductor  $L_2$  between the two series capacitors, which provides a critical drain path for the residual 50 Hz power that inevitably passes through the coupling capacitor [23]. For best performance, the source and load impedances should be equal; this value is usually also referred to as the characteristic impedance  $Z_0$ . The T-sections may be cascaded for improved performance, and also to perform impedance matching using appropriate component values. The caveat for this filter type is that it has poor performance for deviations of the  $L$  and  $C$  component values, and the source and load impedances from the nominal value of  $Z_0$ .

Equations (15) and (16) of Appendix A are used to determine the appropriate frequency values to apply in the filter equations while keeping  $Z_0$  of the PLC channel, and the bandwidth of the line trap design of Appendix A, consistent. A single T-section filter can then be designed using component values calculated using equations (1) to (4).

$$L_1 = \frac{Z_0}{\pi(f_u - f_l)} \text{ H} \quad (1)$$

$$L_2 = \frac{Z_0(f_u - f_l)}{4\pi(f_u \times f_l)} \text{ H} \quad (2)$$

$$C_1 = \frac{(f_u - f_l)}{4\pi(f_u \times f_l)Z_0} \text{ F} \quad (3)$$

$$C_2 = \frac{1}{\pi(f_u - f_l)Z_0} \text{ F} \quad (4)$$

### Impedance Matching Unit

For the purpose of interfacing this filter with the communications module which is usually rated at  $50\ \Omega$  impedance, it is necessary to carry out impedance matching. A transformer offers a simple way to implement impedance matching in a circuit, and in this case, it also has the added advantage of providing electrical isolation between the power system and the communications module, as a safety precaution. The impedances at the primary and secondary ports of an impedance matching transformer are related through:

$$\sqrt{\frac{Z_{sec}}{Z_{pri}}} = \frac{N_{sec}}{N_{pri}} \quad (5)$$

The combined coupling and filtering unit can then be integrated with the impedance matching transformer to form the complete coupling, filtering, and impedance matching unit. This is usually simply referred to as a coupler.



## Appendix C – LV Neutral Terminal Bonding to Distribution Transformer Tank

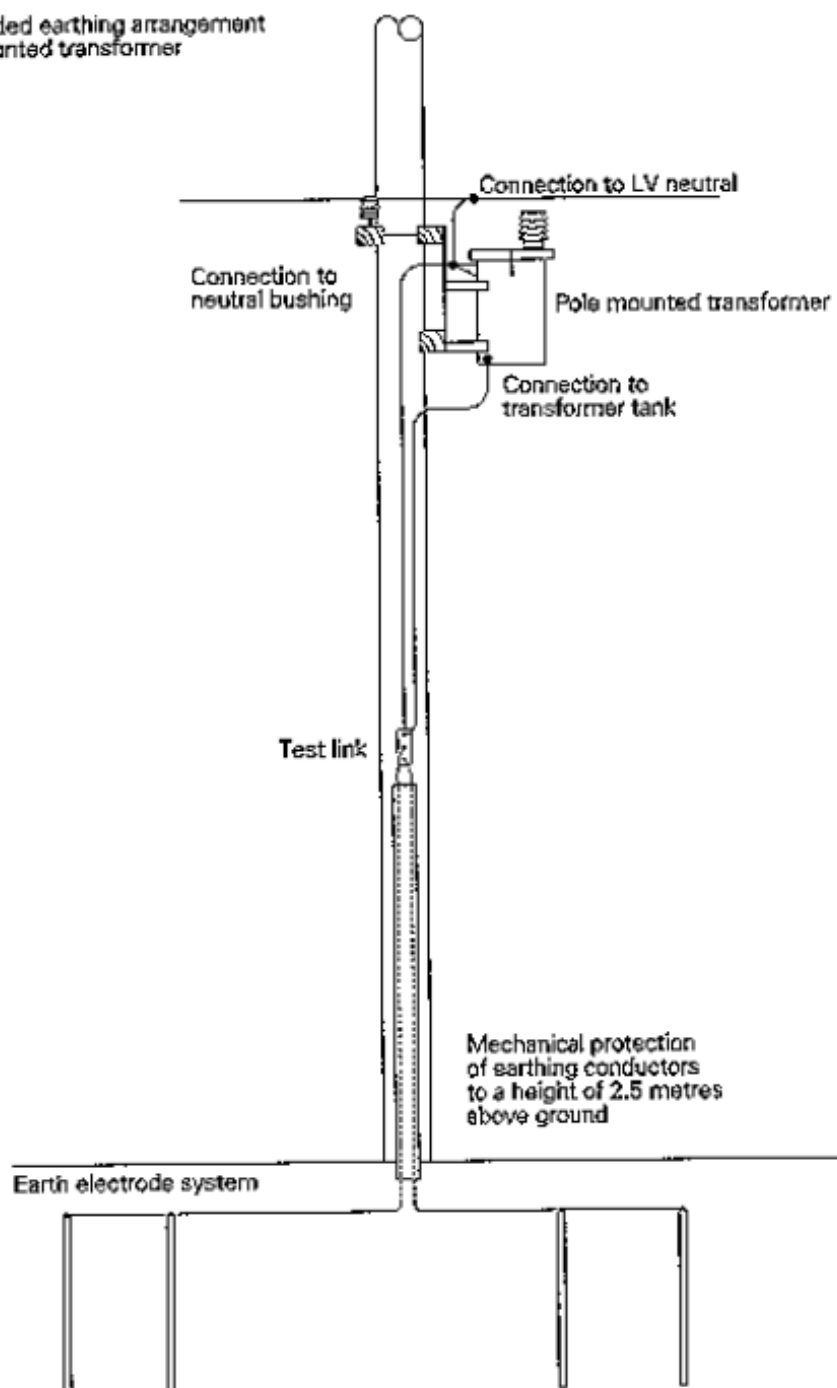
NZECF 35

20

Figure 5

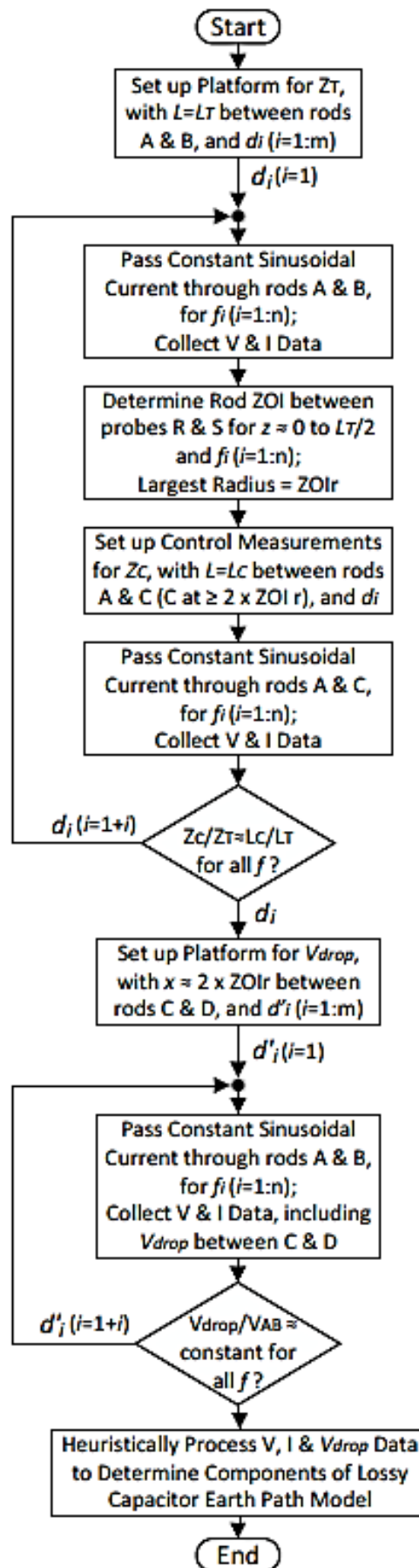
(refer to clause 6.5.3)

Recommended earthing arrangement  
for pole mounted transformer



1 April 1993

## Appendix D – Flowchart of Experimental Procedure for Earth Path Characterization Method



## Appendix E – Squirrel and Flounder Aerial Conductor Datasheets

### Squirrel

1/31/2017

ACSR Bare Aerial Conductors - Nexans

### Characteristics

#### CONSTRUCTION CHARACTERISTICS

Reinforcement members material type	Galvanized steel
Conductor material	aluminum / Steel Core

#### DIMENSIONAL CHARACTERISTICS

Stranding No./mm Steel	1/2.11
Stranding No./mm Ali	6/2.11
Equivalent Aluminium Cross Section Area	20.7mm <sup>2</sup>
Nominal overall diameter	6.33mm
Approximate weight	0.09kg/m

#### MECHANICAL CHARACTERISTICS

Minimum breaking load	7.49kN
-----------------------	--------

1/31/2017

ACSR Bare Aerial Conductors - Nexans

#### ELECTRICAL PERFORMANCE DATA

Nexans ref.	Modulus of Elasticity (GPa)	Coefficient of Linear Expansion (x 10 <sup>-6</sup> / °C)	Calculated DC Resistance at 20°C (0hm/km)	Reactance at 50Hz with 300mm Spacing (0hm/km)	Current Rating Still Air (Amps)	Current Rating 1 m/s (Amps)
Magpie	136	13.9	2.23	0.349	59	113
Squirrel	83	19.3	1.37	0.322	75	145
Gopher	83	19.3	1.09	0.315	86	167
Ferret	83	19.3	0.677	0.299	117	223



## ENERGY CABLES

### Electric Utility Cables

#### Aerial ACSR / 1350

#### Smooth Body



APPLICATION		
Bare overhead reticulation for medium spans, normally at low and medium voltages ■ ACSR = Aluminium Conductor Steel Reinforced.	STANDARD CONDUCTOR	BS 215 Part 2:1970 Aluminium Alloy 1350 + Galvanised Steel wire
	STRAND CONSTRUCTION	As Below

#### TECHNICAL SPECIFICATIONS

CODE NAME	CONDUCTOR ALUMINIUM		STEEL	NOMINAL OVERALL DIAMETER mm	APPROX. MASS kg/km	MAXIMUM PACK SIZE metres
	NOMINAL AREA mm <sup>2</sup>	No./mm	No./mm			
POLLOCK	20	6/2.59	1/3.00	6.17	113	2000
FLOUNDER	20	6/2.31	1/3.78	6.70	146	2000
WHITING	25	6/2.59	1/3.35	6.91	142	2000
LAMPREY	40	6/3.28	1/ 4.24	8.97	226	1500

\* Also available with Aluminium Clad Steel Reinforced wires.

#### TECHNICAL SPECIFICATIONS - Continued

TECHNICAL SPECIFICATIONS - Continued								
CONDUCTOR CODE NAME	ELECTRICAL CHARACTERISTICS						INDUCTIVE REACTANCE TO 0.4M Ω/km	SINGLE PHASE VOLTAGE DROP @ 0.4M SPACING mV/A.m
	EQUIVALENT ELECTRICAL AREAS		MAXIMUM DC RESISTANCE @20°C Ω/km	MAXIMUM AC RESISTANCE @75°C Ω/km	CURRENT RATINGS @ 75°C (a)			
	ALUMINIUM mm²	COPPER mm²			WINTER NIGHT A	SUMMER NOON A		
MULLET	10	8	2.154	2.780	130	110	0.343	5.60
HERRING	10	8	2.154	2.780	132	112	0.338	5.60
POLLOCK	20	13	1.534	1.751	174	147	0.328	3.56
FLOUNDER	20	13	1.354	1.751	178	150	0.323	3.56
WHITING	25	16	1.074	1.390	202	170	0.321	2.85
LAMPREY	40	26	0.674	0.873	274	230	0.305	1.84
HAKE	60	40	0.425	0.533	365	305	0.296	1.22

(a) Wind Speed 1m/sec, emissivity 0.5, absorptance 0.5. Air temperature 10°C for winter night, 25°C for summer noon. Intensity of solar radiation 1000 W/m<sup>2</sup> for summer noon. Angle of wind to conductor axis is 60°. For current ratings at different conductor operating temperatures, refer to the graph on next two pages.

Calculation based on IEEE Std 738 – 1993.

CONDUCTOR CODE NAME	PHYSICAL PROPERTIES						
	NOMINAL OVERALL DIAMETER mm	TOTAL CROSS SECTIONAL AREA mm <sup>2</sup>	CALCULATED MINIMUM BREAKING LOAD kN	APPROX. MASS kg/km	% STRENGTH OF EQUIVALENT DIAMETER 8/1 STRANDING	FINAL MODULUS OF ELASTICITY GPa	COEFFICIENT OF LINEAR EXPANSION 1° x 10 <sup>-6</sup>
MULLET	4.9	17.66	7.67	71	150	88.7	17.9
HERRING	5.3	20.36	10.7	91	200	113.5	15.2
POLLOCK	6.2	28.23	14.5	113	150	84.5	18.4
FLOUNDER	6.7	32.38	16.4	146	200	100.2	16.4
WHITING	6.9	35.46	14.8	142	150	88.9	17.7
LAMPREY	9.0	59.51	23.1	226	150	88.9	17.7
HAKE	10.4	78.64	23.8	273	100	77.2	19.6

## Appendix F – Transformer Magnitude and Phase Angle Variation Plots for Less Significant Cases

The MV to LV minimum output RMS voltage magnitude variation values for the various energization levels of the 1 kVA transformer, specified as percentages, are summarized in Figure F.1.

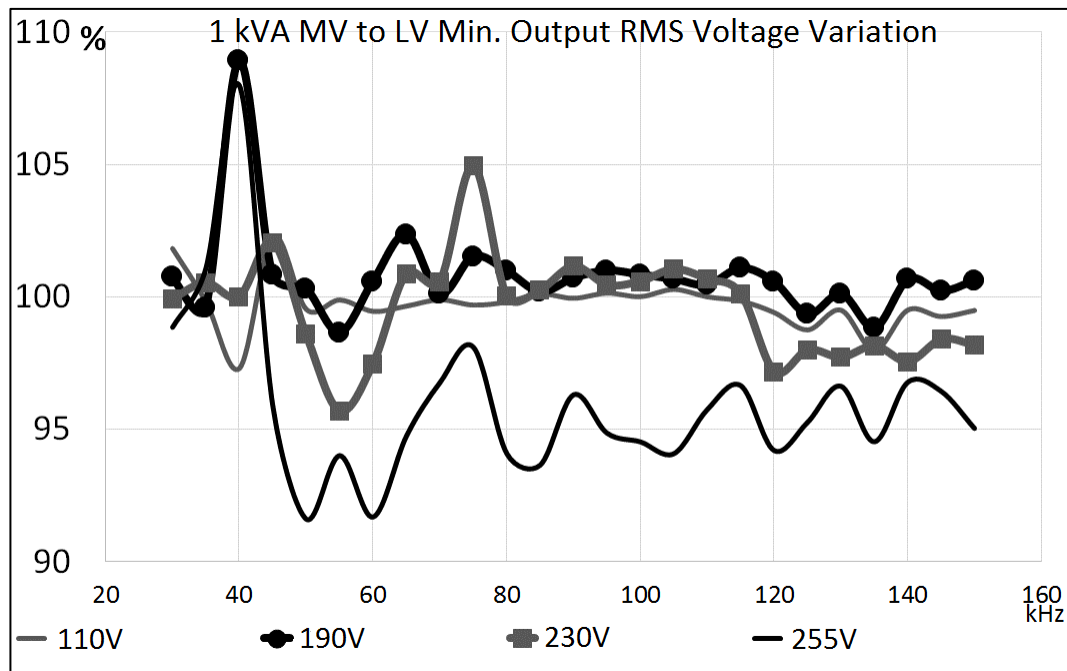


Figure F.1 – 1 kVA MV to LV Minimum Output RMS Voltage Magnitude Variation

The plots show distinct peaks of high values at 40 kHz for the 230 V and 255 V values, and low values from this frequency to 150 kHz for the 255 V plot. This shows impedance decrease and increase, respectively. These impedance changes can be attributed to the transformer oil polarization effects that affect the capacitive reactance of the shunt paths that exist between the live and neutral terminals of the primary (MV) side of the 1 kVA transformer. The same situation holds for the rest of the plots of Figure F.1, with distinct peaks trending at 65 kHz and 75 kHz.

The MV to LV maximum output RMS voltage magnitude variation values for the various energization levels of the 1 kVA transformer, expressed as percentages, are summarized in Figure F.2.

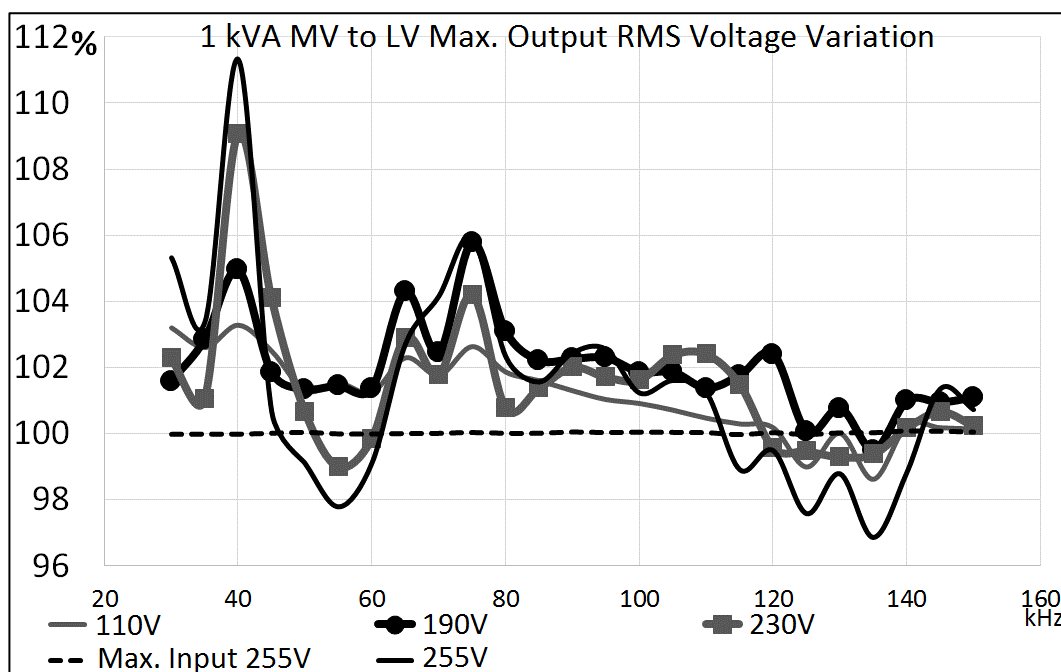


Figure F.2 – 1 kVA MV to LV Maximum Output RMS Voltage Magnitude Variation (Maximum Input RMS Voltage Magnitude Variation Included for Comparison)

The plots show that the peaks at 40 kHz, 65 kHz, and 75 kHz show more variation effects, with values of approximately 11%, 4.5%, and 6% respectively for the 190 V plot, at these frequencies. The 255 V plot also shows a general increase in variation across the bandwidth.

The MV to LV minimum phase angle variation values for the various energization levels of the 1 kVA transformer, expressed as angle degrees, are summarized in Figure F.3.

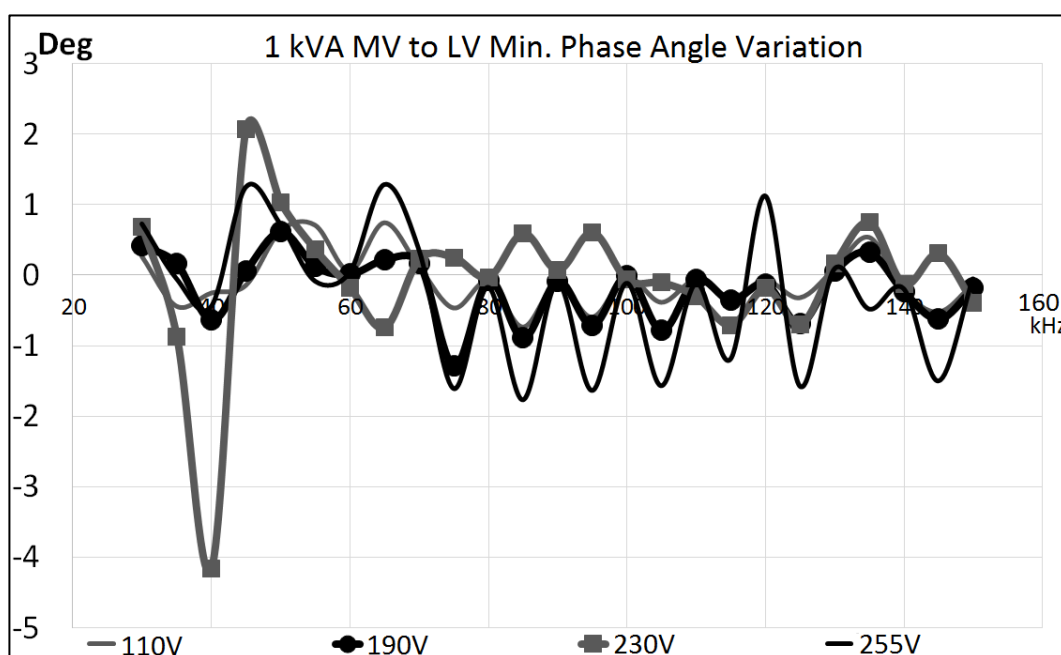


Figure F.3 – 1 kVA MV to LV Minimum Phase Angle Variation

A prominent peak of  $-4^\circ$  occurs at 40 kHz for the 230 V plot, which is significant. The rest of the plots do not show any significant increase or decrease in phase values.

The MV to LV maximum phase angle variation values for the various energization levels of the 1 kVA transformer, expressed as angle degrees, are summarized in Figure F.4.

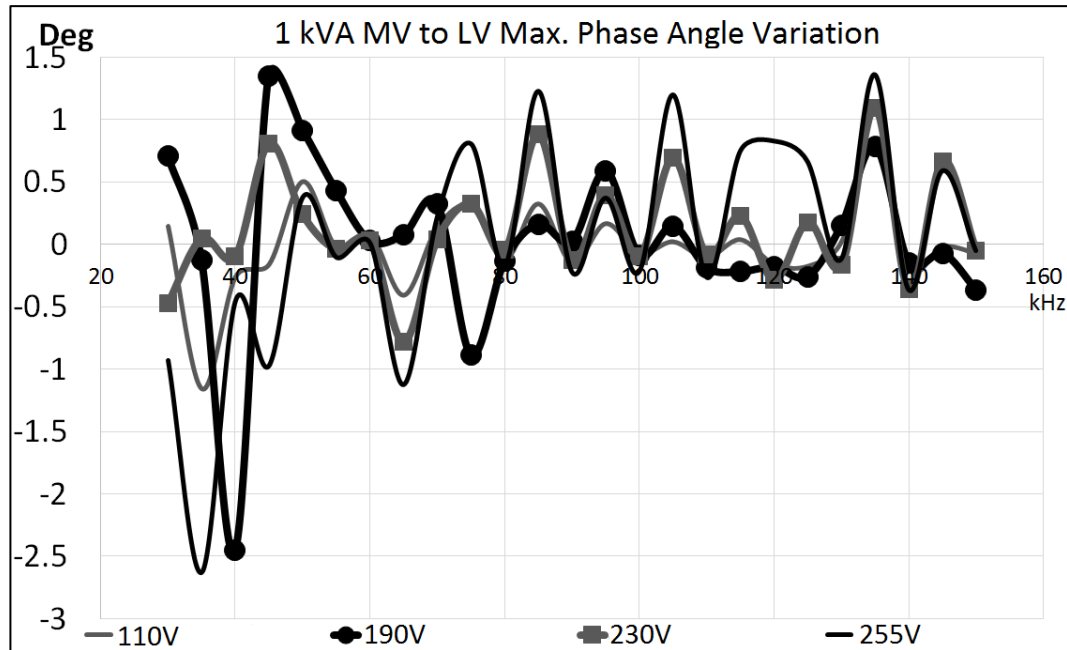


Figure F.4 – 1 kVA MV to LV Maximum Phase Angle Variation

The plots show random minimal variations with distinct oscillatory patterns, which do not reveal anything much in particular, with the exception of a relatively large negative peak at 35 kHz of approximately  $-2.6^\circ$  for the 255 V plot. This peak may be related to the 40 kHz peak in the minimum phase variation plot of Figure F.3, in terms of phase shifting.

The LV to MV minimum output RMS voltage magnitude variation values for the various energization levels of the 15 kVA transformer, specified as percentages, are summarized in Figure F.5.

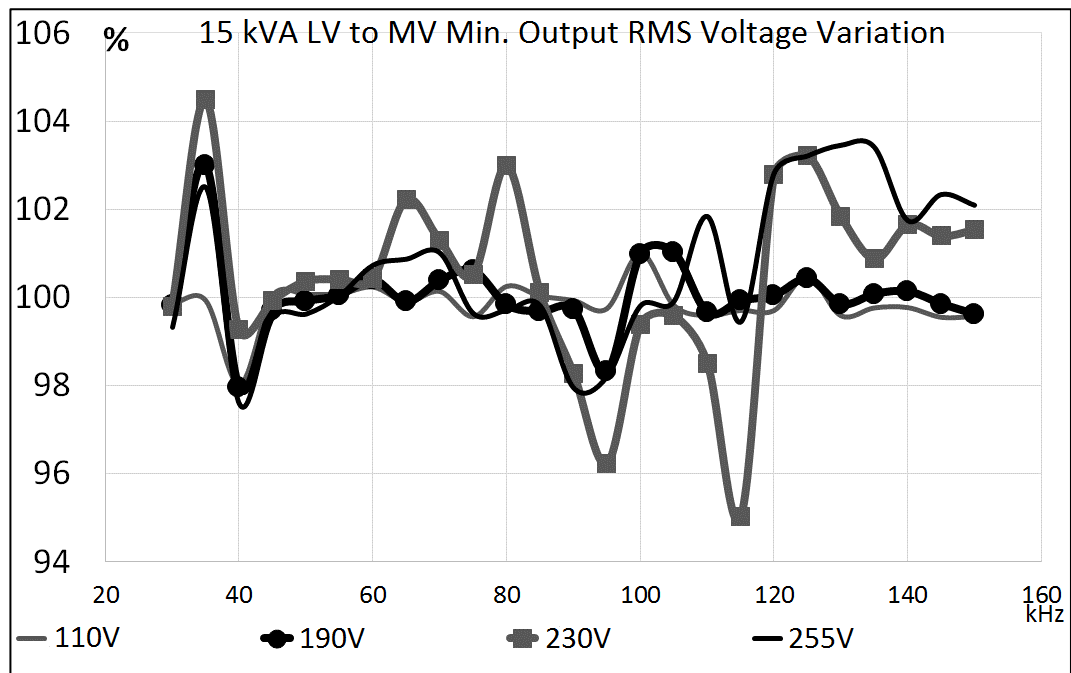


Figure F.5 – 15 kVA LV to MV Minimum Output RMS Voltage Magnitude Variation

The plots show distinct positive peaks at 35 kHz, 80 kHz and 125 kHz, and negative ones at 95 kHz and 115 kHz. These all imply impedance decrease and increase respectively.

The LV to MV maximum output RMS voltage magnitude variation values for the various energization levels of the 15 kVA transformer, specified as percentages, are summarized in Figure F.6.

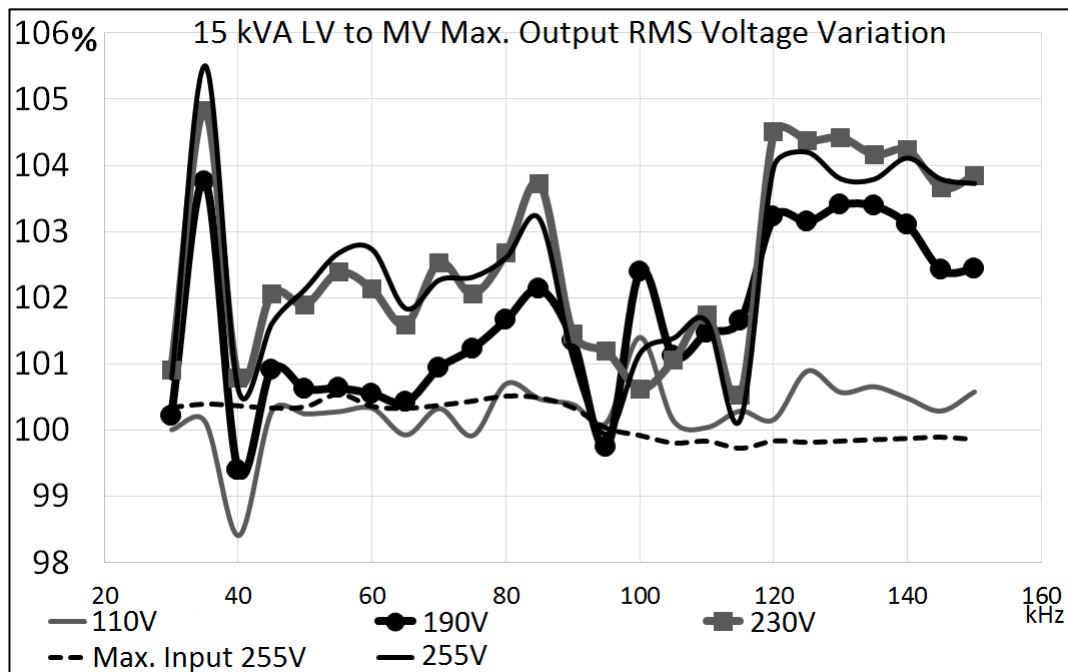


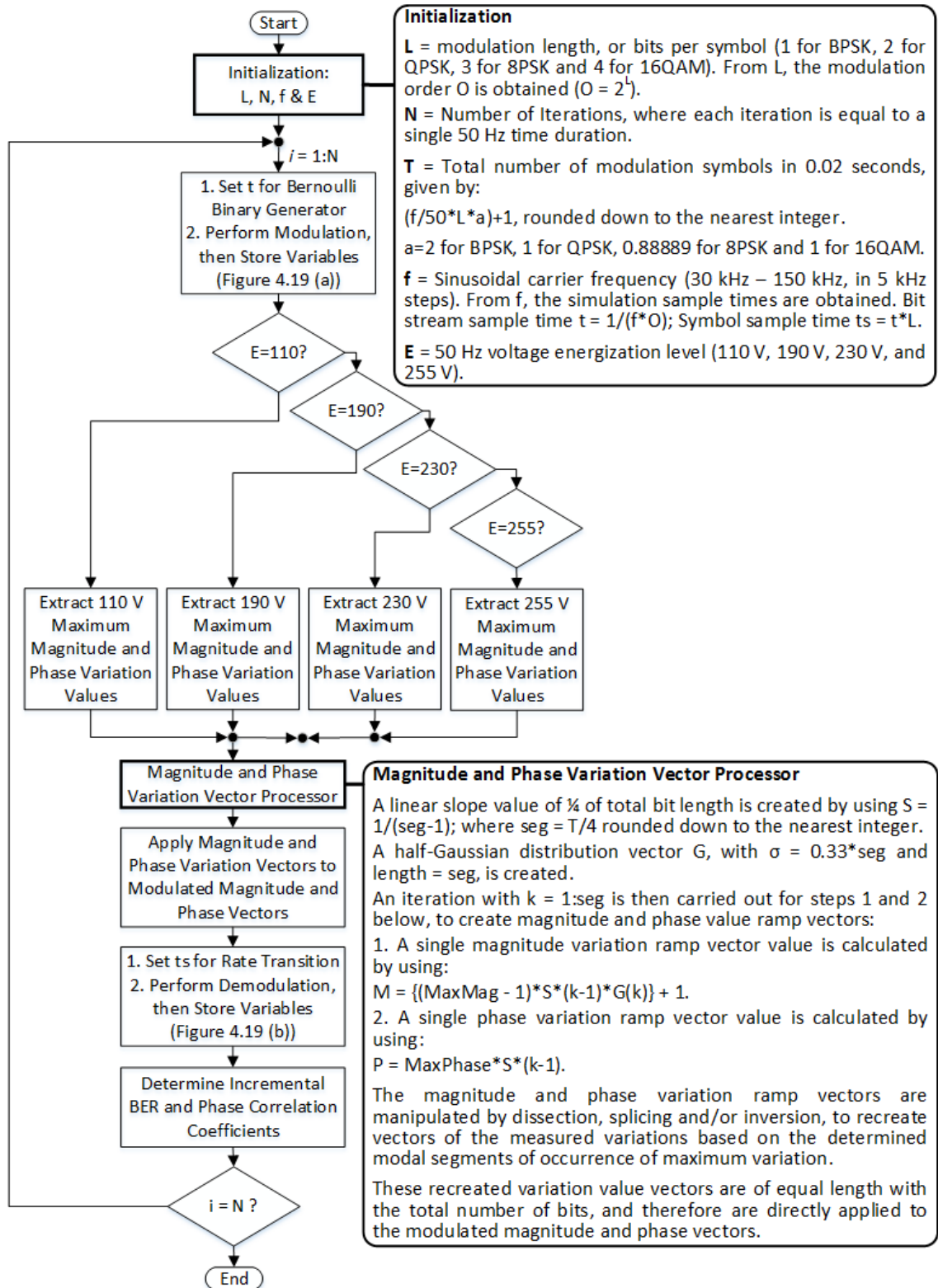
Figure F.6 – 15 kVA LV to MV Maximum Output RMS Voltage Magnitude Variation (Maximum Input RMS Voltage Magnitude Variation Included for Comparison)



The plots are similar to those of the 1 kVA transformer LV to MV maximum output RMS voltage magnitude variation plots shown in Figure 6.9, with all the peaks of the energizations showing a general increase in magnitude. This indicates an impedance reduction for most of the bandwidth.

Distinct positive peaks occur at 35 kHz, as was found for the 15 kVA LV to MV minimum output RMS voltage magnitude variation plots shown in Figure F.5, with other positive peaks at 60 kHz and 85 kHz, for the 230 V and 255 V plots. Also, all the plots, with the exception of the 110 V plot, have plateaus with an average value of 3.5%, between 120 kHz and 150 kHz, showing a consistent decrease in impedance within this frequency range.

## Appendix G – Flowchart of Energized Through-transformer PLC Simulation Model Program



## Appendix H – Timing Performance of Energized Through-transformer PLC Simulation Program

Profile Summary			
Generated 18-Jul-2017 02:09:28 using performance time.			
Function Name	Calls	Total Time	Self Time*
<a href="#">DirectSim_Energized</a>	1	1.827 s	0.337 s
<a href="#">run</a>	1	0.620 s	0.006 s
<a href="#">Scale_Energized</a>	1	0.602 s	0.284 s
<a href="#">WiredSource_coreBlockCommand</a>	17	0.534 s	0.006 s
<a href="#">WiredSource_coreBlockCommand&gt;localStart</a>	4	0.470 s	0.001 s
<a href="#">ScopeBlock.mdlStart</a>	4	0.469 s	0.057 s
<a href="#">WiredSource.mdlStart</a>	4	0.288 s	0.001 s
<a href="#">WiredSource.connectToPorts</a>	4	0.287 s	0.012 s
<a href="#">UnifiedScope.installDataSource</a>	4	0.211 s	0.006 s
<a href="#">...llback&gt;@(~,~)fcn(this,varargin{:})</a>	8	0.127 s	0.002 s
<a href="#">ConstellationVisual.onDataSourceChanged</a>	4	0.125 s	0.007 s
<a href="#">State&gt;State_TrapEvents</a>	40	0.113 s	0.024 s
<a href="#">...ConstellationDiagramBlockCfg.mdlStart</a>	4	0.091 s	0.001 s
<a href="#">...this.onStateEventHandler(varargin{:})</a>	8	0.087 s	0.001 s
<a href="#">commbkrectgamdemod</a>	21	0.086 s	0.004 s
<a href="#">Source.onStateEventHandler</a>	8	0.086 s	0.005 s

## Appendix I – 1 kVA MV to LV Incremental BER Charts

Through visual inspection, the incremental BER's for the energized 1 kVA transformer for the MV to LV direction do not show significant differences with those for the LV to MV direction shown in Figures 7.23 to 7.26. Therefore, they are placed here for reference purposes only. The analysed BER differences in both directions are shown in Figure 7.27.

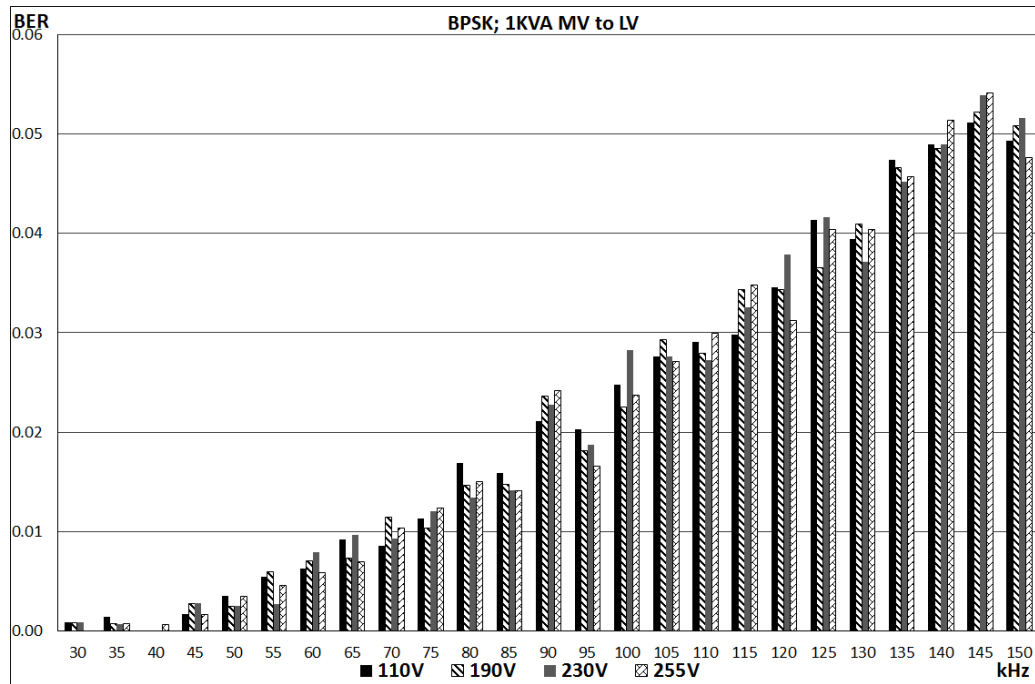


Figure I.1 – Incremental BER for BPSK Signals Passing through Energized 1 kVA Transformer; MV to LV Direction

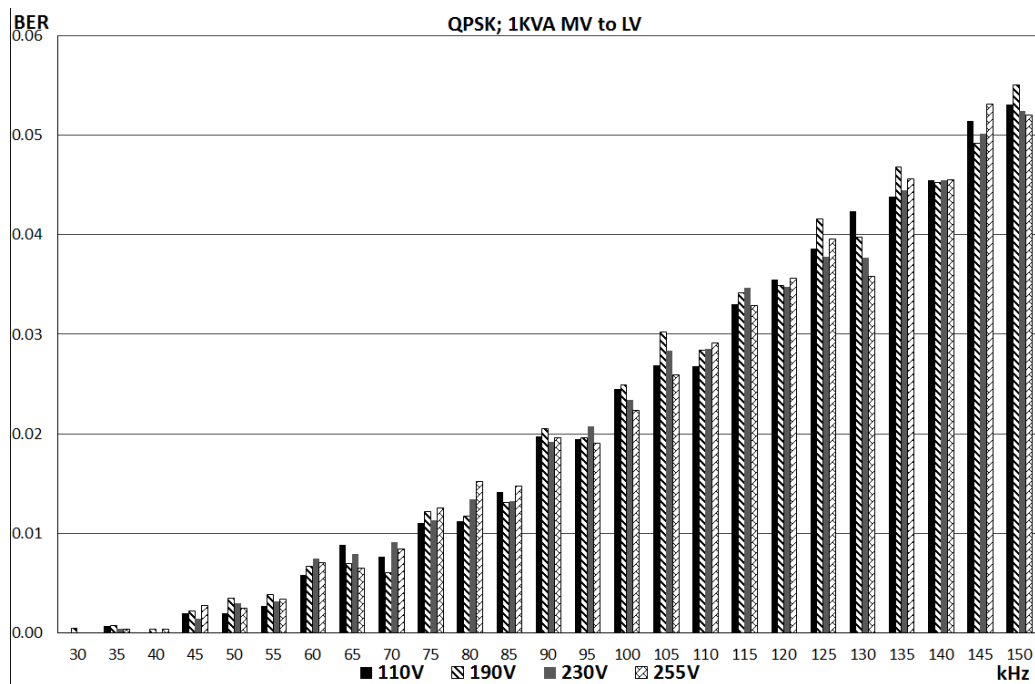


Figure I.2 – Incremental BER for QPSK Signals Passing through Energized 1 kVA Transformer; MV to LV Direction

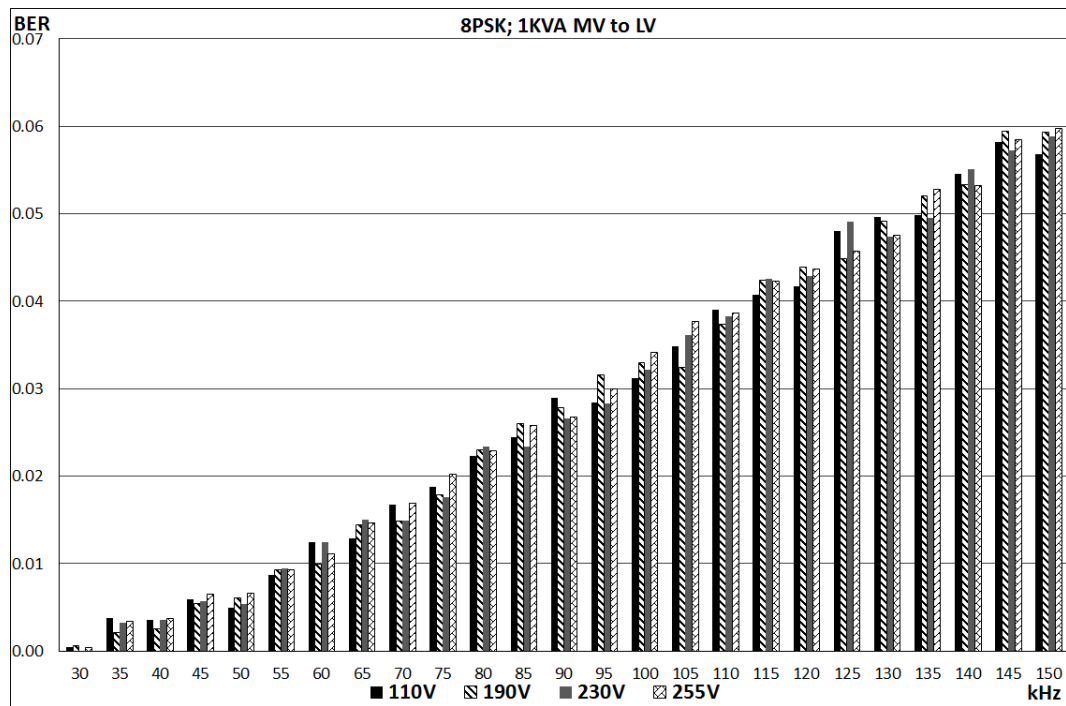


Figure I.3 – Incremental BER for 8PSK Signals Passing through Energized 1 kVA Transformer; MV to LV Direction

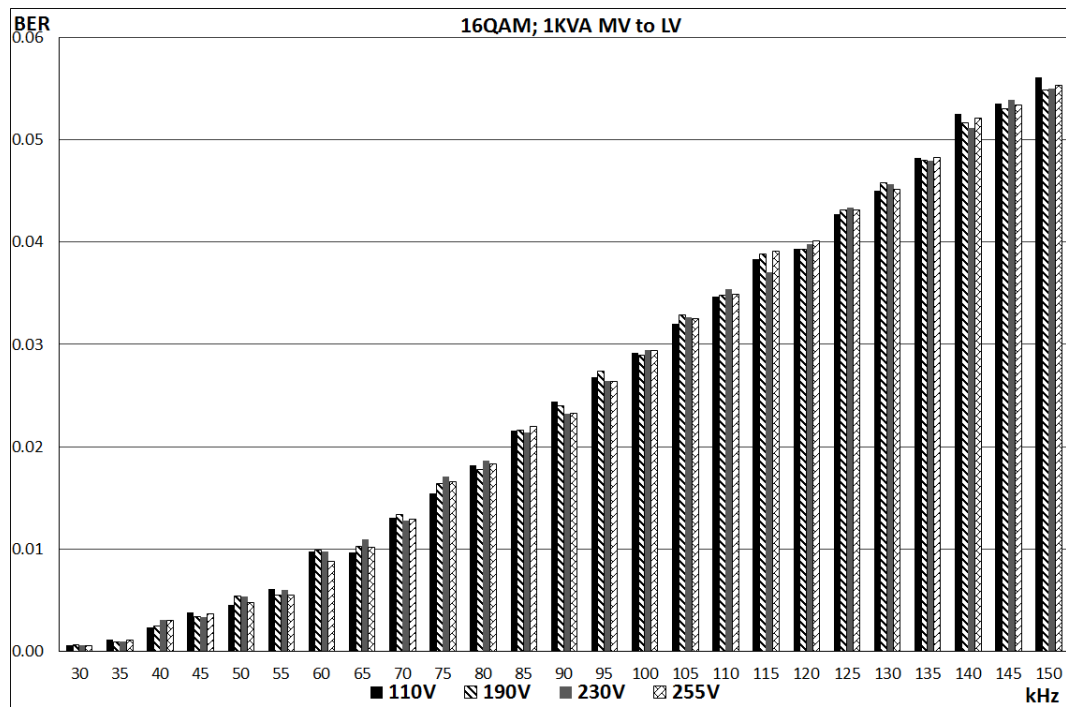


Figure I.4 – Incremental BER for 16QAM Signals Passing through Energized 1 kVA Transformer; MV to LV Direction